Numerical Studies of Topological phases

Thesis by

Scott Geraedts

In Partial Fulfillment of the Requirements

for the Degree of

Doctor of Philosophy

California Institute of Technology

Pasadena, California

2015

(Defended May 27, 2015)

Abstract

The topological phases of matter have been a major part of condensed matter physics research since the discovery of the quantum Hall effect in the 1980s. Recently, much of this research has focused on the study of systems of free fermions, such as the integer quantum Hall effect, quantum spin Hall effect, and topological insulator. Though these free fermion systems can play host to a variety of interesting phenomena, the physics of interacting topological phases is even richer. Unfortunately, there is a shortage of theoretical tools that can be used to approach interacting problems. In this thesis I will discuss progress in using two different numerical techniques to study topological phases.

Recently much research in topological phases has focused on phases made up of bosons. Unlike fermions, free bosons form a condensate and so interactions are vital if the bosons are to realize a topological phase. Since these phases are difficult to study, much of our understanding comes from exactly solvable models, such as Kitaev's toric code, as well as Levin-Wen and Walker-Wang models. We may want to study systems for which such exactly solvable models are not available. In this thesis I present a series of models which are not solvable exactly, but which can be studied in sign-free Monte Carlo simulations. The models work by binding charges to point topological defects. They can be used to realize bosonic interacting versions of the quantum Hall effect in 2D and topological insulator in 3D. Effective field theories of "integer" (non-fractionalized) versions of these phases were available in the literature, but our models also allow for the construction of fractional phases. We can measure a number of properties of the bulk and surface of these phases.

Few interacting topological phases have been realized experimentally, but there is one very important exception: the fractional quantum Hall effect (FQHE). Though the fractional quantum Hall effect we discovered over 30 years ago, it can still produce novel phenomena. Of much recent interest is the existence of non-Abelian anyons in FQHE systems. Though it is possible to construct wave functions that realize such particles, whether these wavefunctions are the ground state is a difficult quantitative question that must be answered numerically. In this thesis I describe progress using a density-matrix renormalization group algorithm to study a bilayer system thought to host non-Abelian anyons. We find phase diagrams in terms of experimentally relevant parameters, and also find evidence for a non-Abelian phase known as the 'interlayer Pfaffian'.

Acknowledgements

The success of my PhD relied on support from a whole bunch of people. Especially I'd like to thank my office mate and friend Paraj Titum. I'd also like to thank my advisor, Lesik Motrunich, and also Roger Mong. Finally I'd like to thank my parents for their constant support.

Contents

Chapter 1

Introduction

During the course of my graduate research, I have worked on two sets of projects. In the first, I developed a set of analytical and numerical tools for studying a certain class of statistical mechanics models. These models potentially have a number of applications, but the application I focused on was topological phases of bosons. In the end I was able to produce numerically tractable models of topological phases in one, two and three dimensions. This series of projects occupied the majority of my time during my degree. More recently, I have been working on projects related to the numerical study of the fractional quantum Hall effect. What these two sets of projects have in common is that they are both studies of topological phases of matter. Therefore this thesis begins with a discussion and motivation for the study of topological phases.

1.1 Introduction to Topological Phases

A central concept is condensed matter physics is that of phase transitions, which are locations in parameter space where the free energy is not analytic. From this we can arrive at the definition of a 'phase of matter': two states of a material are in the same phase if there is a path in parameter space that connects them and that does not cross a phase transition or break a symmetry. It has long been known that different phases of matter can have qualitatively different properties. This understanding was put on a firmer footing by Landau[1], who pointed out that these qualitatively different properties arise because different phases have different symmetries. One example is a paramagnetic phase with full spin-rotation symmetry that can have a ferromagnetic phase with less symmetry, for example the ferromagnetic phase my have spin rotation symmetry about only one axis. Liquids have continuous translational symmetry while crystals have only a discrete translational symmetry. Given a material known to undergo a phase transition, the task of the condensed matter physicist was to determine the symmetry which was breaking across the transition.

This understanding was expanded by the discovery of the Integer quantum Hall effect (IQHE) in 1980.[2] In the IQHE, each Hall plateau corresponds to a different phase of matter (different plateaus cannot be turned into each other without undergoing a phase transition), but all the phases have the same symmetry. What is different between the different phases turns out to be a topological invariant known as the Chern number. We

call the Chern number a topological invariant because it is the result of integrating a function (in this case the Berry curvature) over a topologically non-trivial manifold (in this case a torus). An interesting property of topological invariants is that they are independent of the metric of the manifold, and care only about its topology. Because of this, two systems in the same phase will have identical values for the topological invariant, even if their microscopic physics is different.

There are many general statements that can be made about symmetry-breaking transitions in condensed matter physics. Examples of such general properties include the fact that the breaking of a symmetry can be detected by an order parameter, and that properties at a critical point are determined by critical exponents independent of the microscopic details of the system. We also know about the point groups, which tell us all the different ways to break spatial symmetries, and that breaking continuous symmetries leads to Goldstone modes. These general facts help us to understand symmetry-breaking transitions.

Since the discovery of phases that are described by topological invariants and not symmetry breaking, an important area of research has been to establish similar general principles. Much progress has been made in this direction over the past several years, and in the remainder of this section, I will describe a number of these properties which will be used throughout this work.

The concept of entanglement is crucial to the study of topological phases. One way to quantify the entanglement in a system is by the 'conditional mutual information'[3]. This is defined by imagining a system broken into three parts A,B and C, as shown in Fig. 1.1. The conditional mutual information is a function of the entanglement between the different parts of the system, and it represents how much information subsystem A has about the state of subsystem B. An example of a system with a large mutual information would be a system containing a large number pairs of spin-1/2 particles, each of which forms a spin singlet. If one component from each pair were in A and the other in B the system would have large mutual information. As early as 1935 it was realized by Einstein[4] that systems like this have highly counterintuitive physics, and so it should be no surprise that most of the matter around us has very mutual information.

With this in mind, we can divide all gapped states of matter into two classes: short-ranged entangled (SRE) and long-ranged entangled (LRE). In an SRE phase the entanglement between two spatially separated subsystems A and B (i.e., the conditional mutual information) decreases to zero as the separation between the subsystems increases, while for an LRE system this quantity decreases to a constant called the topological entanglement entropy [5, 6]. We will see that long-ranged entangled matter can have a variety of very interesting (and perhaps even useful) properties. Topological phases can have either short- or long-ranged entanglement, and these two cases will be discussed separately.

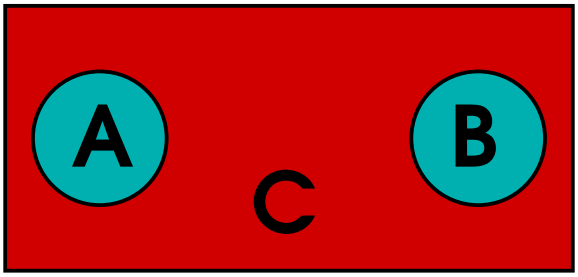

Figure 1.1: The setup for defining conditional mutual information.

1.1.1 Short-ranged Entangled Topological Phases

Even in the absence of long-ranged entanglement, topological phases of matter can still have exotic properties. In addition, short-ranged entangled phases are arguably simpler to understand than their long-ranged cousins, and so they are a good place to begin any study of topological phases.

The integer quantum Hall effect was the first example of an SRE topological phase to be discovered. More recently other SRE topological phases have been discovered, such as the quantum spin Hall effect[7] and the topological insulator(TI)[8, 9]. [1] Like the integer quantum Hall effect, these recently-discovered phases have topological invariants, which can be computed by integrating the Berry curvature over the Brillioun zone[10, 11]. Unlike the IQHE, these topological invariants are *only quantized in the presence of time-reversal symmetry*. This means that these topological phases only exist when this symmetry is present. This turns out to be a general property of non-chiral SRE topological phases: [2] they become topologically trivial if certain symmetries are broken. These phases are often called 'symmetry protected topological phases' (SPTs).

The topological invariants in the quantum spin Hall effect and the topological insulator are coefficients of total derivative terms. Therefore there is no bulk measurement which can distinguish these phases from topologically trivial phases with the same symmetry. There is, however, exotic edge physics that takes place on the edge of these phases that can distinguish them from topologically trivial matter. For example, the quantum spin Hall effect has two counterpropagating edge modes (each carrying opposite spin). This cannot happen in a purely one-dimensional system with time-reversal symmetry [12]. The topological insulator has a single Dirac cone, which cannot happen in a two-dimensional time-reversal-invariant system. This is another general property of SRE topological systems: they can host edge physics which cannot exist in a system of one lower dimension.

One may also ask what other SRE topological phases are possible, besides the ones given above. Answers to this question take the form of 'classification tables', which, given a symmetry and number of dimensions, tell us how many topological phases there are. Classification tables for free fermion systems[13, 14] as well as bosons[15, 16, 17] have been produced, which classify many possible cases, though a complete classification is still an area of active research. Such classification tables provide a roadmap in the search for more examples of SRE topological phases.

1.1.2 Long-ranged entanglement

Like the SRE topological phases discussed above, LRE topological phases can have exotic physics. Unlike SRE phases, LRE phases do not require symmetry to exist. They also have other novel properties, in particular *fractionalization*. This means that the gapped quasiparticles in a LRE phase can carry fractions of

[1] The term 'topological insulator' is used in the literature to describe a number of different phases. In this thesis I will use it exclusively to describe the 3D 'strong' TI.

[2] Chiral phases like the IQHE do not have this property.

the quantum numbers (such as charge). Much of the physics of LRE phases was first developed during the study of the fractional quantum Hall effect (FQHE).[1] For example, a filling $\nu = 1/3$ FQH system has quasiparticles carrying $1/3$ charge[18]. The spin of the quasiparticles can also become fractionalized. In an SRE system all quasiparticles must be either bosons or fermions, so their exchange statistics are ± 1. In an LRE system (in two dimensions) exchange statistics can take complex values, for example in a $\nu = 1/3$ FQH system the exchange statisitics is $e^{\pi i/3}$, or $1/3$ the value for fermions. From the anyonic statistics of the quasiparticles we can also show that LRE topological phases have a ground state degeneracy when put on a topologically non-trivial surface(e.g., a torus). This is because the operations of taking a quasiparticle around the different cycles of the torus do not commute.

1.2 Tractable Models of Interacting Topological Phases

We can see that many general properties of topological phases have been determined. Note that though those properties hold in general, the concepts were first established for specific examples of topological phases, such as the fractional quantum Hall effect, quantum spin Hall effect, and topological insulator. To learn more about topological phases, we may need to study other specific examples. In particular, we may be interested in topological phases which have strong interactions, because (with the exception of the FQHE) most of the topological phases studied are phases of free fermions. Including interactions will likely change the results derived for non-interacting systems. For example, non-interacting topological phases can become topologically trivial when interactions are added[19]. Interacting topological phases may be feasible experimentally, such as by fabricating materials out of atoms with strong Coulomb interactions[20]. We hope that by considering interactions we can find new topological phases that contain fundamentally novel physics.

Strongly interacting systems are hard to study, since powerful techniques such as Fermi liquid theory do not apply. Therefore one may wish to simplify the system as much as possible. One way to simplify the problem is to consider bosons, which are easier to work with because they have trivial exchange statistics. Since bosons in the absence of interactions will form a (topologically trivial) Bose-Einstein condensate, any topological phase of bosons will have interactions playing an important role. We also may find it convenient to study the simpler case of SRE topological phases first before moving onto the more complicated LRE phases.

In 2012 Chen et al.[15, 16] classified a number of short-ranged entangled bosonic topological phases; that is, they attempted to determine how many such phases exist for a given dimension and with a certain symmetry. Their classification was proven to be correct for one-dimensional phases, although it was later found to not include all possible phases in two and higher dimensions[21, 17]. Such classification tables tell us how many bosonic, interacting, SRE topological phases exist, but they do not tell us about the properties of those phases, and for that we must turn to other techniques.

One way to learn more about a specific interacting topological phase is to construct an exactly solvable

model that realizes it. Such exactly solvable models have contributed much to the study of topological phases, with examples including the Haldane chain, Kitaev's toric code[22], and models of Levin and Gu[23] and Walker and Wang[24, 25]. One cannot, however, rely solely on exactly solvable models, since for some topological phases of interest (especially those with continuous symmetries) we do not know how to construct such a model.

Another approach to topological phases that has acheived much success is to consider an effective field theory that describes the topological phase. An effective field theory is a low-energy description that is independent of the microscopic details of the system. Therefore, unlike band theory these methods can be generalized to interacting systems. As we will soon see, effective field theories can be a powerful tool with which to understand topological phases. When one has an effective field theory describing a topological phase, one still does not know whether or not it corresponds to any microscopic model, and what the properties of such microscopic models may be. In Chapters 3 and 4 I will present microscopic models which realize the effecive field theories for two phases of recent interest: the bosonic quantum Hall effectin 2D and the bosonic topological insulator in 3D. The models are strongly interacting and not exactly solvable, but they can be handled using Monte Carlo simulations.

1.2.1 Integer and Fractional Quantum Hall Effect for Bosons

Chen et al. predicted that for two-dimensional phases of bosons with $U(1)$ (charge conservation) symmetry, an integer number of SRE topological phases exist (i.e., there are an infinite number of phases, each of which has a topological invariant that takes integer values). This is of course the same symmetry and dimension as the well-studied integer quantum Hall effect, like the IQHE there is an integer classification of the possible phases. Inspired by this similarity, Lu and Vishwanath [21] applied techniques developed to study the quantum Hall effect to the bosonic case.

Specifically, Lu and Vishwanath described two-dimensional bosonic topological phases using Chern-Simons theory. This effective theory contains a topological term, the Chern-Simons term, which has a coefficient that is quantized to take integer values. The coefficient of this term is a topological invariant which labels the different phases. An action for a Chern-Simons theory takes the following form (in units with $\hbar = c = 1$)[1]:

$$S = -\frac{1}{4\pi}\epsilon^{\mu\nu\lambda}K_{IJ}a_{I\mu}\partial_\nu a_{J\lambda} + \frac{e}{2\pi}\epsilon^{\mu\nu\lambda}q_I\partial_\nu a_{I\lambda}A^{\text{ext}}_\mu. \tag{1.1}$$

This is an action which contains N species of charged quasiparticles, which are described by gauge fields $a_{I\mu}$ which satisfy

$$j_{I\mu} = \epsilon^{\mu\nu\lambda}\partial_\nu a_{I\lambda}, \tag{1.2}$$

where $j_{I\mu}$ is the number current of the quasiparticles. In these equations $\epsilon^{\mu\nu\lambda}$ is a Levi-Civita symbol, μ is a direction in $(2+1)$-dimensional space, I, J label the quasiparticle species and repeated indices for both directions and quasiparticle species are assumed to be summed over. These equations are coupled to the

Maxwell gauge field A^{ext} by the second term in Eq. (1.1), where the vector q_I gives the charge of each quasiparticle. K_{IJ} is an integer-valued $N \times N$ matrix. The first term in the action is the Chern-Simons term. It gives the quasiparticles exchange statistics: if quasiparticle I is exchanged with quasiparticle J, the action acquires a phase of

$$\theta_{\text{exchange}} = \pi \left(K^{-1}\right)_{IJ}. \tag{1.3}$$

We can also get the Hall conductivity from this action: integrating out all of the quasiparticle fields a_I gives

$$S = \frac{e^2}{4\pi} q_I \left(K^{-1}\right)_{IJ} q_J \epsilon^{\mu\nu\lambda} A^{\text{ext}}_\mu \partial_\nu A^{\text{ext}}_\lambda, \tag{1.4}$$

and noting that the electric current $\mathcal{J}_\mu = \partial S / \partial A^{\text{ext}}_\mu$, we get

$$\mathcal{J}_x = \sigma_{xy} E_y, \quad \sigma_{xy} \equiv \frac{e^2}{h} q_I K^{-1}_{IJ} q_J, \tag{1.5}$$

where we have restored units of $\hbar$. A Chern-Simons theory can be completely defined by writing down its 'K-matrix' K_{IJ} and 'charge vector' q_I. From Eq. (1.3) it can be seen that if $|\det K| > 1$ the quasiparticles can have anyonic statistics (they are neither bosons nor fermions). In this case there is a ground state degeneracy of $|\det K|$.

From Eq. (1.3) we see that for a conventional quantum Hall system of fermions we need at least one of the diagonal elements of the K-matrix to have odd-integer values. Lu and Vishwanath studied bosonic systems, which means that they restricted to the case where diagonal elements of the K-matrix had even integer values. Furthermore, they studied short-ranged entangled topological phases, which have no ground-state degeneracy, and therefore $|\det K| = 1$. The simplest such K-matrix is

$$K = \begin{bmatrix} 0 & 1 \\ 1 & 0 \end{bmatrix}, \quad q = \begin{bmatrix} 1 \\ 1 \end{bmatrix}. \tag{1.6}$$

The phase described by Eqs. (1.6) and (1.1) has $\sigma_{xy} = 2$ and was named the 'Integer Quantum Hall effect for bosons'. Note that by changing q the Hall conductivity can take any even integer value, so that there is an integer classification of the phases, as predicted by Chen et al.[15, 16]. The K-matrix is 2×2, and therefore it describes two species of bosons. If these bosons are separately conserved, the system has total symmetry $U(1) \times U(1)$, while we are really interested in systems with only $U(1)$ symmetry. It is often convenient to assume that in addition to Eq. (1.1) there is tunnelling between the two species, so that only the total number of bosons is conserved, this breaks one of the $U(1)$ symmetries but should not qualitatively change the physics. The remaining $U(1)$ symmetry represents the conservation of the total boson charge.

Chern-Simons theory can also be used to understand edge states[1]. The number of edge modes in a given theory is equal to the number of eigenvalues of the K-matrix, and their direction is given by the sign of the eigenvalue. By diagonalizing Eq. (1.6) we can see that the boson IQHE has two modes travelling in

opposite directions. There is still a quantized Hall conductivity since one mode carries a charge of 2 while the other mode is neutral. Note that the edge is protected by the $U(1)$ charge-conservation symmetry—if this symmetry is broken the two edges can scatter into each other and open a gap, leading to a topologically trivial phase. This is an example of how symmetry protects the topology of short-ranged entangled phases.

A system whose ground state can be decribed by the effective theory in Eqs. (1.6) and (1.1) is a boson IQHE. An obvious question therefore is are there physical systems that can be described by this effective theory, and what are their characteristics? This question was addressed in Ref. [26], which considered two species of bosons in a magnetic field with some interactions. They performed a 'flux attachment' procedure, familiar from studies of the conventional quantum Hall effect. By attaching one unit of flux from each species of boson to the opposite species, [3] and taking a mean-field limit where the flux is distributed uniformly, they can cancel the magnetic field from the Hamiltonian. They then have bosons which see no magnetic field, and they condense these bosons, leaving them with an effective action described by Eq. (1.6) and (1.1).

Ref. [26] tells us that binding bosons to fluxes can realize the boson IQHE. It still does not give us a microscopic model that realizes this physics. In essence, the question of 'what interactions give the correct Chern-Simons theory?' has been replaced by the question 'what interactions allow us to take the mean-field limit of the flux attachment, and then condense the resulting composite bosons?' These questions will be answered in Chapter 3. We will construct a microscopic model that realizes the physics of binding bosons to fluxes, and we will show that this model realizes the boson IQHE.

Such microscopic models are convenient for a number of reasons. They provide a pathway towards possible experimental realizations, by explicitly showing what kind of interactions can lead to a desired phase. At a more basic level, they show that the boson IQHE can be realized in a local Hamiltonian, which is not guaranteed by earlier works. Finally, such models allow us to potentially do things like add disorder, spatial boundaries, or different kinds of interactions to the model, and study the behaviour of the boson IQHE under such different circumstances.

The models we have studied began as interesting $(2+1)$-dimensional statistical mechanics models consisting of two species of bosons. When bosons of opposite species are exchanged, the wave function gets an overall phase. This means that the bosons are 'mutual anyons'. One would expect that models with non-trivial statistics would contain complex Berry phases in their path integral, which would make Monte Carlo simulations impossible. It turns out that it is possible to eliminate this 'sign problem' through formal manipulations to get a model which can be simulated. We also developed sophisticated analytical tools which can be used to study these systems. This study frequently uses a useful duality for two-dimensional bosons; a two dimensional system of bosons can be equivalently described either in terms of the bosons themselves, or in terms of the vortices of the boson phases.

Such models can have many applications; for example, they can be used to study certain kinds of exotic critical points, but the application most relevant to this work is that these models can be used to realize

[3] Note that attaching a flux of a different species of bosons does not change statistics, unlike in the typical flux attachment procedure.

topological phases of bosons. Our models have two species of bosons (and therefore $U(1)\times U(1)$ symmetry), while the bosonic quantum Hall effect has only $U(1)$ symmetry, but we expect that breaking our symmetry to $U(1)$ by allowing a small amount of tunnelling would not change the system qualitatively. We realize the 'flux attachment' of Ref. [26] by representing one of the two species of bosons in terms of its vortices, while the other uses a conventional representation. We then introduce interacitons between the bosons and vortices, and condense the resulting bound states. By binding multiple vortices to each boson (which is equivalent to flux attachment in which multiple fluxes are bound to each boson) we were able to realize fractional boson quantum Hall effects, which had not been previously developed in the literature. Our work was the first to give a microscopic model that realized these topological phases. We were able to use these models to measure the Hall conductivity, as well as demonstrate the existence of two gapless edge modes. In the fractional case, we showed that the gapped quasiparticles of the system had fractionalized spin and charge.

1.2.2 Topological Insulator of Bosons

The bosonic quantum Hall effect is a highly-nontrivial state of matter containing both topological physics and strong interactions. Despite these obstacles, much progress has been made by using intuition developed in the study of the conventional electronic quantum Hall effect. Another topological phase where a lot of research has been performed is the topological insulator, and so one can try to use intuition gained from this study to construct a bosonic topological insulator.

The free fermion topological insulator is a three-dimensional system with both $U(1)$ (charge conservation) and $\mathbb{Z}_2^T$ (time reversal) symmetry. Many of the tools used to study TI's only work for free fermions, and therefore will not apply to this interacting case. As in the previous section, we want to use an effective field theory to study the system, since this should have the same form regardless of microscopic details such as whether or not there are interactions. The analog of Eq. (1.4) is the so-called 'magnetoelectric' term[11]:

$$S = \theta \frac{e^2}{8\pi^2} \epsilon^{\mu\nu\lambda\sigma} \partial_\mu A^{\text{ext}}_\nu \partial_\lambda A^{\text{ext}}_\sigma, \tag{1.7}$$

where units are such that $\hbar = 1$ and θ is a constant, which is quantized to either 0 or π for reasons to be explained shortly.

In the quantum Hall case, we can measure the coefficient of the topological term by measuring the Hall conductivity, and it would be convenient if θ could also be detected by some quantized bulk response. Unfortunately this is not the case, as Eq. (1.7) is a total derivative, and therefore does not contribute to any bulk physics. Instead, θ can be measured by studying the surface of the topological insulator. At the surface of the TI, θ changes in value by π. Since θ is varying in space, we can integrate Eq. (1.7) to get the following action, which is only non-zero on the two dimensional surface of the TI:

$$S^{\text{surface}} = \frac{e^2}{4\pi} \frac{\Delta\theta}{2\pi} \epsilon^{\mu\nu\lambda} A^{\text{ext}}_\mu \partial_\nu A^{\text{ext}}_\lambda. \tag{1.8}$$

By comparing to Eq. (1.4), we can see that [4]

$$\sigma_{xy}^{\text{surface}} = \frac{1}{2}\frac{e^2}{h}. \tag{1.9}$$

The topological insulator is a SRE topological phase, and therefore we would expect that its surface is SRE as well. We know that a two-dimensional SRE phase phase can have a quantized Hall conductivity, as this is the integer quantum Hall effect, which has Hall conductivity quantized to integer values. We have just shown that on the surface of the 3d topological insulator we have a 2d phase with a *half-integer* Hall conductivity. The fractional value is an example of how physics can exist on the 2d surface of a 3d topological phase which could not exist in a purely 2d system.

Thinking about the Hall conductivity on the surface of the TI allows us to see why θ is quantized to 0 or π. First, notice that under time-reversal symmetry, $\theta \to -\theta$. Second, note that we can (in a thought experiment) place an integer quantum Hall phase on top of a topological insulator without changing its bulk physics. This would change $\sigma_{xy}^{\text{surface}}$ by 1 and therefore by Eq. (1.9), it would change θ by 2π. But this procedure didn't change any bulk physics, and therefore θ in the bulk is only defined modulo 2π. Putting these two facts together tells us that in the presence of time-reversal symmetry, the only allowed values of θ are 0 and π. Without time-reversal symmetry the above arguments do not apply, and θ can take any value (it is no longer a topological invariant). This is another example of how breaking symmetry in a SRE topological phase makes the phase topologically trivial.

It has been pointed out [27] that technically there is a bulk measurement which can measure θ. This can be seen as follows. Imagine trying to measure the charge density which arises from the magnetoelectric term. To do this, one would differentiate the action with respect to A_0^{ext}, obtaining:

$$\rho \equiv \frac{\partial S}{\partial A_0^{\text{ext}}} = \theta \frac{e^2}{4\pi^2}\vec{\nabla}\cdot\vec{B}, \tag{1.10}$$

where B is the magnetic field. Since magnetic field is typically divergenceless, this shows that the magnetoelectric term makes no contribution to the charge density of the system, consistent with our picture that it should not contribute to the bulk physics. There is, however, an exception to this which occurs when a magnetic monopole is located inside a topological insulator. In this case the divergence of the magnetic field is equal to $2\pi/e$, [5] and we find that $\theta/2\pi = 1/2$ charge has bound to each magnetic monopole. This binding of fractional charge to magnetic monopoles is

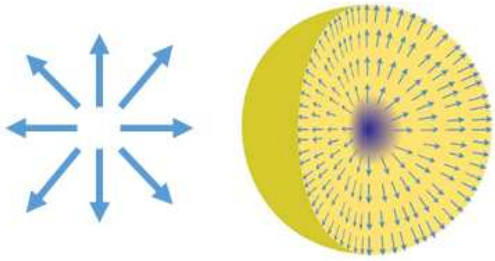

Figure 1.2: The left picture is a vortex, which in two dimensions is a point topological defect. The right is a hedgehog, which is a point topological defect in three dimensions.

[4] restoring units of $\hbar$.

[5] from the Dirac quantization condition

called the Witten effect, and it is another way to differentiate between a topological insulator and a trivial insulator. This is quite a remarkable result since we are studying a system without fractionalized excitations (it has only short-ranged entanglement), and yet we still have a fractional charge binding to the monopole.

The bosonic TI was first studied by Vishwanath and Senthil in 2013[28]. They produced effective field theories for the bulk of the bosonic TI which are consistent with Eq. (1.7). One important difference in the boson case is that for bosons the 'integer quantum Hall effect' has a Hall conductivity quantized to even integers (see Section 1.2.1). Therefore by the same arguments as for the fermionic case θ is 4π-periodic, and therefore in the presence of time reversal symmetry θ is quantized to be either 0 or 2π.

Ref. [28] also produced an effective field theory for the surface of the boson TI. As one would expect on the surface of a SRE topological phase, they found a number of different phenomena that cannot exist in a purely 2d system, and can only exist on the surface of a 3d topological phase. In the free fermionic topological insulator, the possible edge phases either are gapless (Dirac cones) or break one of the symmetries of the system (either charge conservation or time reversal). In studies of the bosonic quantum Hall effect it is convenient to enlarge the charge conservation symmetry to $U(1) \times U(1)$ (two species of bosons). The surface effective field theory of Ref. [28] can produce exotic superfluid phases which break at least one of these symmetries, and it can also realize a time-reversal symmetry broken phase which has a Hall conductivity quantized to an odd integer (impossible in a purely two-dimensional boson system). Most interestingly, they also find a surface phase that is gapped and breaks none of the symmetries of the system, but which contains LRE topological order.

The effective field theory of Ref. [28] is a powerful tool for describing topological phases, but it does not tell us whether a microscopic model described by this effective theory exists, and it gives us little intuition into what properties such a microscopic model might have. To answer these questions, we have constructed a microscopic model which realizes the boson TI, and this work is the subject of Chapter 4. The model uses many of the same techniques used to study the boson QHE in Chapter 3. In the boson QHE case, we were working in two dimensions, and we realized the phase of interest by binding bosons to point topological defects (vortices), and condensing the resulting bound states. In the boson TI, we will again bind bosons to point topological defects and condense the bound states. In this case the point topological defects are called hedgehogs (see Fig. 1.2). One way to model such hedgehogs is to introduce $SO(3)$ spins onto our lattice, and define a hedgehog as existing whenever the spins have a configuration like that in Fig. 1.2. This method provides intuition for understanding our setup, but unfortunately it does not allows us to make quantitatively accurate measurements. Alternatively, we can introduce hedgehogs into our model by starting with a set of boson variables, and describing these bosons with a parton description. The redundancy of this description introduces an internal gauge field, and we can identify monopoles of this gauge field with the hedgehogs. By binding these hedgehogs to a second species of bosons, we produce the boson TI. This is also a nice description because it is a model of two species of bosons, like that in Ref. [28]. Both of these methods of representing the hedgehogs can be studied in sign-free Monte Carlo simulations.

We can make a number of measurements on our model to determine that it is in fact a boson TI. We can study the surface of the model, and like Ref. [28] we find exotic superfluids which break one of the $U(1)$ symmetries. By explicitly breaking the time-reversal symmetry we can put the system into a phase with a Hall conductivity, and by measuring this Hall conductivity (and finding a value not allowed in a purely two-dimensional system) we can convincingly argue that the bulk of our system is in a topological phase. We can also find a surface phase which is gapped and breaks no symmetries, and we argue that it is therefore the long-ranged entangled phase of Ref. [28].

We can also measure the Witten effect, as described above for the fermionic TI and extended to the boson TI by Refs. [29, 30]. In our system we study two species of bosons which are coupled to different external gauge fields. The Witten effect in this setup is the statement that a monopole of one of the gauge fields will have a half-integer charge bound to it of the boson species coupled to the other gauge field. If the two external gauge fields were identified, we would get an integer charge bound to each monopole, which is what is predicted by Eq. (1.7) with $\theta = 2\pi$. We could cancel this integer charge by adding a boson to the monopole, but this would turn the monopole into a fermion, which is a manifestation of the 'statistical Witten effect'[29, 30].

Our models also allow us to bind multiple hedgehogs to each boson. We find that this leads to a model with gapped excitations that carry fractional charge, and therefore we call this the fractional topopological insulator of bosons, and it is an LRE topological phase. The model also contains gapped excitations which are quantum lines, and when a fractionally charged quasiparticle is exchanged with these lines the action is changed by an anyonic phase (i.e., a phase not 0 or π). We find that the surface of the fractional phase has a Hall conductivity quantized to a rational number (which is not possible without long-ranged entanglement), and it exhibits a Witten effect involving fractionally charged quasiparticles.

1.3 Topological Quantum Computing and Numerical Studies of the Fractional Quantum Hall Effect

In recent decades, the field of quantum computing has been a very active field of physics research. The excitement in this field comes from the fact that, in general, the amount of time it takes to find the ground state of a quantum Hamiltonian scales exponentially in the size of the system. Yet nature manages to use quantum mechanics to solve such systems efficiently, and this raises the question of what other computationally hard problems can be solved by a quantum mechanical system, or 'quantum computer'. Such quantum computers have many practical applications, such as their ability to factor large numbers. They are also exciting as an aid to condensed matter physicists, who could use them to find the ground states of model Hamiltonians.

Constructing such a quantum computer requires overcoming a large number of experimental challenges, perhaps the most daunting of which is the phenomena of decoherence. Imagine, for example, a quantum

computer constructed out of a number of cold atoms, which have an internal degree of freedom that we can model as a spin-1/2. The spin-1/2's form the 'qubits', and the states of the quantum computer are all wavefunctions of these spins. If we work in, for example, the z basis, a wavefunction is a linear superposition of a number of z-eigenstates, each of which has some spins pointing up and others down. Local perturbations can change the state of the computer either by flipping a spin or by changing the relative phases of the different eigenstates (these are called phase errors). This phenomenon is called decoherence, and it means that any information stored on a quantum computer will quickly be lost.

The problem of decoherence exists in classical computers as well, but it is somewhat simpler in that the only error is the flip of a bit. In this case 'error-correcting codes' can be used to redundantly store information. These error correcting codes can make classical computers essentially error-free. Error-correcting codes exist for quantum systems as well, but in a quantum computer there are more ways for errors to happen, and the result is that many spin 1/2's are needed to form a single error-protected qubit. Constructing a quantum computer with such a large number of physical degrees of freedom is an extremely difficult task.

A possible way to avoid this problem is by constructing a 'topological quantum computer' out of long-ranged entangled topological phases. The quantum information can be encoded by which of the degenerate ground states the system is in. Not only do LRE phases have such degenerate ground states, but these ground states cannot be changed into each other by a local perturbation. Therefore the information encoded in the ground states of topological quantum computer will be robust against local decoherence. For example, in a fractional quantum Hall system on a torus, a quasiparticle must be brought all the way around a cycle of the torus in order to change the ground state. The probably of this happening by purely local perturbations scales as e^{-L}, where L is the linear dimension of the system. This is exponentially small in the thermodynamic limit, making it difficult for local perturbations to change the state of the system, and therefore significantly increasing the time it takes for the system to decohere.

The fractionalized quasiparticles ('anyons') in the fractional quantum Hall effect can store quantum information in way that is robust against decoherence. However, in order to implement a 'universal' quantum computer one must act on a quantum state with both Abelian (commuting) and non-Abelian operations,[31] while the anyons in the FQHE can only implement the Abelian operations. To implement the non-Abelian operations we need more exotic quasiparticles known as non-Abelian anyons. These are particles for which the operation of exchanging them is not Abelian: exchanging particle A with particle B and then particle C is not the same as exchanging A with C and then B.

Theoretically, there are a number of different types of non-Abelian anyons. The simplest and best-known is the Ising anyon. Though it may be difficult to use the Ising anyon for universal quantum computation,[32] it can still be interesting for its applications to long-lived quantum memory[33], as well as for its unique physical properties. Techniques developed by realizing Ising anyons experimentally may also be useful for realizing their more complicated relatives. The Ising anyon is also called a '$\mathbb{Z}_2$ parafermion', because combining two of them gives something Abelian. This can be generalized to $\mathbb{Z}_k$ parafermions, for integer k.

For $k \neq 1, 2, 4$ these can be used for universal quantum computation[31, 34]. Another anyon which can be used for universal quantum computation is the Fibonacci anyon.

Since these non-Abelian anyons can be used for universal and fault-tolerant quantum computation, they are being actively sought-after experimentally. Many experimental proposals involve constructing heterostructures of phases such as superconductors, topological insulators, ferromagnets, and wires with strong spin-orbit coupling[35]. Most of these proposals are for realizing Ising anyons, and some proposals have even reported the possible detection of the Majorana zero modes which are bound to the Ising anyones[36, 37]. Experiments for realizing other anyons in heterostructures have also been proposed[38].

Another approach would be to find long-ranged entangled topological phases which have non-Abelian anyons as their gapped quasiparticles. In particular, Moore and Read[39] proposed that the quantum Hall effect at $\nu = 5/2$ can host Majorana fermions. Non-Abelian phases which can exist at other filling fractions have been proposed as well[40, 41]. Unfortunately, even if a given non-Abelian phase is consistent with a given filling fraction, this does not mean that that non-Abelian phase is the ground state for the systems prepared at that filling by experimentalists.

It is therefore an important problem to determine whether the quantum Hall states realized experimentally are indeed the sought after non-Abelian phases. This may be possible experimentally, but as the experiments are likely very difficult it is up to theorists to provide guidance as to which filling fractions are most likely to host non-Abelian phases, and under what conditions. Unfortunately, performing this task requires quantitatively estimating the energy of the possible ground states in the strongly interacting quantum Hall problem, and this is very difficult analytically.

In order to determine whether the non-Abelian phase is indeed the ground state of a realistic system we therefore turn to numerics. Particularly, these systems can be studied using density matrix renormalization group (DMRG) algorithms[42, 43]. DMRG is a variational method which works well for one-dimensional, gapped systems. To study a quantum Hall system, we put the system on a cylinder. The computing resources required to study the system scale as e^L, with L the circumference of the cylinder. Though this exponential growth is unfortunate, it is in only one of the two dimensions of the system, and this compares well with the rival method, exact diagonalization, which scales as e^{L^2}.

A promising place to look for non-Abelian quantum Hall phases is in quantum Hall bilayers: systems composed of two quantum wells, each of which hosts a quantum Hall effect. Such bilayers have been studied experimentally, primarily at fillings $1/2 + 1/2$ (each layer is at $\nu = 1/2$) and $1/4 + 1/4$[44]. One advantage of studying these bilayers is their tunability: experimentalists can change the distance between the two layers as well as the tunneling between the layers, and this can tune the system between different quantum Hall phases. One can hope that we can experimentally tune the bilayer system into a phase which hosts non-Abelian anyons.

In Chapter 5 I describe a DMRG study of a bilayer system at filling $1/3 + 1/3$. We obtain the phase diagram in terms of the tunable parameters of layer separation and interlayer tunnelling, and also investigate

the effects of finite layer width. We find transitions between a number of different Abelian phases, and we investigate the nature of these phase transitions. All of these phases have the same symmetry (there is no local order parameter that can distinguish them) and the same Hall conductivity, but we identify the phases using other properties related to their entanglement structure.

The phases that we find by modifying the experimentally tunable parameters are all Abelian. To find phases that host non-Abelian anyons we further modify the Coulomb interaction. Experimentally there are a number of ways to modify the Coulomb interaction, such as studying higher Landau levels, allowing mixing between the Landau levels, or changing the shape of the quantum wells. We find that by reducing the repulsion between electrons in different layers, we are able to tune the system into a non-Abelian phase. We measure a number of properties of this phase, and determine that it is a phase called the 'interlayer Pfaffian' which hosts a Majorana fermion.

1.4 Overview of All Projects and Their Relationships

Figure 1.3 shows a representation of all of the publications produced during my graduate research. Not all of the publications in this figure will be adequately covered in this report, but this figure has been included to show how the projects that I will discuss fit into the other research that I have done.

The papers are divided into three categories: orange (ovals), blue (rectangles), and green (hexagons). The orange category contains work done to develop the statistical mechanics models of bosons with mutual statistics. The paper marked A [45] in the figure was the first to study such models in sign-free Monte Carlo simulations. It was specialized to the case where the bosons has mutual π-statistics, and interacted within each species by on-site interactions. The paper marked B[46] was a related study of a system with only a single species of bosons, but these bosons had 'marginally long-ranged' $(1/r^2)$ interactions. The order of the Mott insulator-superfluid transition in this system was the subject of some controversy, and we definitively showed that the transition was second order while also developing the numerical techniques needed to handle bosons with arbitrary interactions. Paper C[47] also studied bosons with delta function interactions but generalized the mutual statistics of the two species to be any number. Finally, paper D[48] generalized our methods to any interaction and any mutual statistics. In particular we focused on the marginally-long-ranged case, where our analytical tools allowed for the complete establishment of the phase diagram. The results found for the various models studied in these papers will not be discussed in this report. However, the methods used to study these systems proved extremely useful throughout my graduate research, and so these methods are outlined in Chapter 2. Also, the results of paper C are featured in Section 3.5, where they are used to understand the phase diagram of bosonic quantum Hall phases.

The blue category takes the methods developed in the orange category and applies them to the problem of studying topological phases of bosons with local Hamiltonians. In Paper E[49], which is discussed in Chapter 3, the methods are applied to the bosonic topological insulator. We next wanted to apply the same

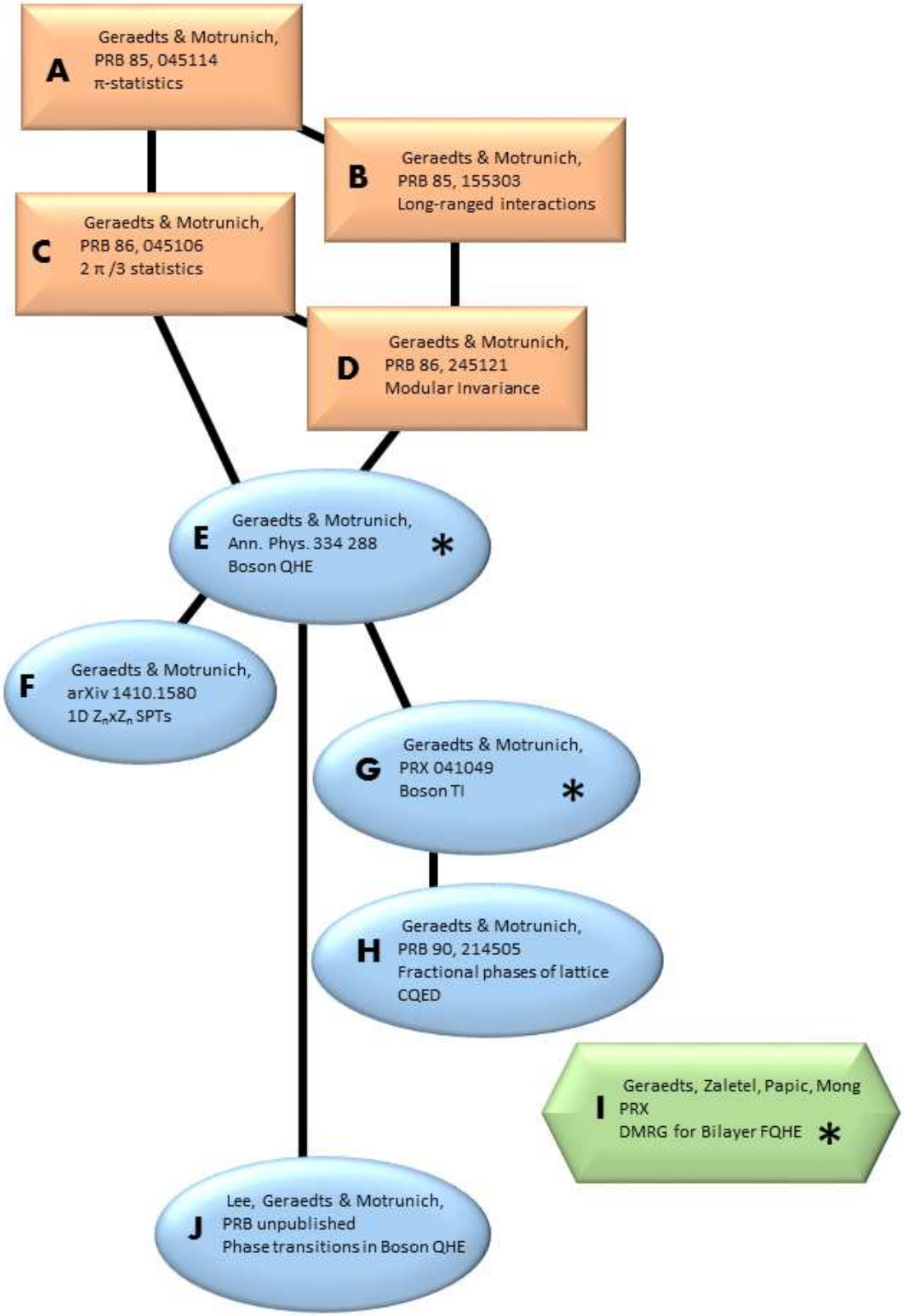

Figure 1.3: An overview of all the papers discussed in this work. The vertical direction is time, and black arrows mean that results of one paper were used in the next. Details for the various figures are described in the text. Asterisks indicate the publications that are described in detail in this thesis.

methods to three-dimensional topological phases. To gain some intuition for this we first went backward and developed an exactly solvable model for a class of one-dimensional topological phases, which is described in paper F[50]. In Paper G[51], which is discussed in Chapter 4, we successfully construct a model for the three-dimensional bosonic topological insulator. In paper H[52] we consider a variant of our model for the boson fractional topological insulator, which instead realizes a novel long-range entangled phase of a lattice gauge theory. Finally in paper J[53] we use the model of the boson QHE to study the transitions between different quantum Hall phases. All of the above work was done in collaboration with Lesik Motrunich.

The green category covers the work on the (fermionic) fractional quantum Hall effect accomplished using DMRG. This category contains only paper I[54], and is discussed in Chapter 5 This work was done in collaboration with Roger Mong, Michael Zaletel and Zlatko Papić.

Chapter 2

Methods for studying two species of bosons with mutual statistical interactions

Over the course of my graduate study I developed a set of powerful tools for studying a statistical mechanics model of two species of bosons, where the bosons have 'mutual statistics': interchanging bosons of different species changes the wave function by a phase. Models such as this can have many applications, and in particular these models will be used to construct bosonic versions of the quantum Hall effect in the next chapter. In this chapter I will pedagogically describe the methods that I have developed.

2.1 One species of bosons

Let us begin by considering a single species of bosons. The material in this section is not original, but it will be useful to understand a single species of bosons before we can move on to multiple species.

2.1.1 Trotter Decomposition

First consider a Bose-Hubbard model at integer filling. When the number of bosons per site is very large and we can consider the fluctuations in the boson number to be much smaller than the average boson number, we can describe the system by a 'quantum rotor model':

$$\hat{H} = t \sum_{\langle i,j \rangle} -\cos(\hat{\phi}_i - \hat{\phi}_j) + g \sum_i \hat{n}_i^2. \tag{2.1}$$

Here $\hat{n} \in \mathbb{Z}$ is the deviation of the boson number from its equilibrium value, while $\hat{\phi}$ are its conjugate variables such that

$$[\hat{n}_i, \hat{\phi}_j] = i\delta_{ij}. \tag{2.2}$$

The first term in this Hamiltonian is a hopping term which moves the bosons around, and when this term dominates the system is in a superfluid phase. The second term is a potential energy, which dominates in the Mott insulating phase.

We now wish to study the finite-temperature path integral of this system:

$$Z = Tr(e^{-\beta \hat{H}}). \tag{2.3}$$

To do this we perform a Trotter decomposition:

$$Z = Tr(\prod^{N} e^{-\delta\tau \hat{H}}). \tag{2.4}$$

Here $\delta\tau = \beta/N$, and breaking up the exponential into a product introduces an error of $O(\delta\tau^2)$, which is fine as long as N is large. We now insert decompositions of unity so that each $e^{-\delta\tau \hat{H}}$ becomes:

$$\langle \phi_i(\tau)|\, e^{-\delta\tau g \hat{n}_i^2}\, |n_i(\tau)\rangle \, \langle n_i(\tau)|\, e^{\delta\tau t \cos(\hat{\phi}_i - \hat{\phi}_j)}\, |\phi_i(\tau+\delta\tau)\rangle\,. \tag{2.5}$$

Here all of the possible states of $\hat{n}$ and $\hat{\phi}$ will need to summed over. Note that we have inserted N sets of states for both the $\hat{n}$ and $\hat{\phi}$ variables. The partition sum is made up of N of the above expressions, and each one has a different τ index. All N of the $\hat{n}$ and $\hat{\phi}$ bases will need to be summed over. In this step we also factored an exponential, which again introduces an error of $O(\delta\tau^2)$. Now all of the operators are diagonal in either the $|n\rangle$ or $|\phi\rangle$ bases, so they can all be factored out of the braket and they become classical variables. We are left with a bunch of $\langle\phi|n\rangle$ objects, and from Eq. 2.2 these give

$$\langle \phi_i(\tau)|n_j(\tau')\rangle = \delta_{ij} e^{in(\tau')\phi(\tau)}. \tag{2.6}$$

Therefore the path integral has become

$$\begin{aligned} Z &= \sum_{\{n,\phi\}} e^{-S} \\ S &= g\sum_{i,\tau} n_i(\tau)^2 - t\sum_{\langle i,j\rangle,\tau} \cos[\phi_i(\tau) - \phi_j(\tau)] + i\sum_{i,\tau} n_i(\tau)[\phi_i(\tau+\delta\tau) - \phi_i(\tau)]. \end{aligned} \tag{2.7}$$

We see that through the Trotter decomposition our quantum problem has turned into a classical problem. The cost of doing this is that we now have an additional imaginary-time direction τ to sum over. At this point it is convenient to formally replace the cosine term with a Villain potential:

$$e^{\cos(x)} \approx \sum_{p} e^{-(x-2\pi p)^2}. \tag{2.8}$$

This new potential obtained by summing over the p variables is in the same universality class as the cosine

potential. We then use the identity

$$\sum_p e^{-t(x-2\pi p)^2} = \sum_J e^{-\frac{J^2}{t}+iJx}. \tag{2.9}$$

Plugging the above into Eq. (2.7) for each of the cosines, we get

$$S = g\sum_r n(r)^2 + \frac{1}{t}\sum_r J_a(r)^2 + i\sum_r n(r)[\phi(r+\hat{\tau}) - \phi(r)] + i\sum_{r,a} J_a(r)[\phi(r+\hat{a}) - \phi(r)]. \tag{2.10}$$

Here a is a direction on the original spatial lattice, and the position index r can refer to either a spatial (a) or imaginary time (τ) index. If the original Hamiltonian was defined on a d dimensional square lattice, we can imagine the sum over τ as giving us a number of copies of this d dimensional lattice. Futhermore we can imagine links between the sites of the different lattices, turning the whole thing into a $d+1$ dimensional cubic lattice. The $(\phi(r+\hat{\tau}) - \phi(r))$ term is defined on these τ-direction links, and we can imagine the $n(r)$ variables living on these links as well, while the $J_a(r)$ variables live on the spatial links of the lattice in direction a. This partition sum for this action includes a sum over the J, n, and ϕ variables.

An this point we can also sum out the ϕ variables to get the following action:

$$S = \tilde{g}\sum_{r,\mu} J_\mu(r)^2, \tag{2.11}$$

which is subject to the constraint

$$\sum_\mu \nabla_\mu J_\mu = 0. \tag{2.12}$$

Th partition sum is over the J_μ variables subject to the constraint. Here we have relabelled the n variables as J_τ, and μ is a direction index which can run over both τ and the spatial directions. We have specialized to the case where the parameter $\tilde{g}$ is space-time isotropic (which means that $\tilde{g} \equiv g = 1/t$. The lattice derivative ∇_μ is defined as $\nabla_\mu x = x(r+\mu) - x(r)$, and the constraint comes from integrating over the ϕ variables. The J variables can be viewed as integer-valued conserved currents living on the links of the $d+1$ dimensional lattice, and they can be interpreted as the world-lines of the bosons introduced in Eq. (2.1). The constraint forces the bosons to be conserved. In Chapters 3 and 4 we will be using Eq. (2.11) frequently to represent a system of bosons.

2.1.2 Reformulations in terms of ϕ variables

Eq. (2.11) is one way to study a statistical mechanics model for a system of bosons, and it will be very useful throughout this thesis. There are also a number of other ways to reformulate the same model, which will also be useful at various points. One such reformulation can be obtained by starting with Eq. (2.7) combined with

Eq. (2.8), and summing over the n variables instead of the ϕ. Using Eq. (2.9) one obtains

$$S = \tilde{t} \sum_{r,\mu} (\nabla_\mu \phi(r) - 2\pi p_\mu(r))^2, \tag{2.13}$$

where the partition sum is over the ϕ and p_μ variables. The p_μ variables are integer-valued and live on the links of the lattice in the μ direction, and $\tilde{t} \equiv t = 1/g$. By comparing with Eq. (2.8) we see that the above equation is a classical XY model with cosine interactions between the XY spins.

We can obtain yet another reformulation by summing over the J variables in Eq. (2.7) directly [i.e. without using Eq. (2.9)] to get

$$\begin{aligned} S &= \sum_{r,\mu} V_{\text{Villain}}[\nabla_\mu \phi(r); \tilde{t}] \\ e^{-V_{\text{Villain}}(x;\tilde{t})} &= \sum_J e^{-\frac{1}{\tilde{t}} J^2 + i\alpha J}. \end{aligned} \tag{2.14}$$

This is again just a classical XY model, with the 'Villain potential' V_{Villain} taking the place of the cosine. In both of these reformulations we are representing a d-dimensional model of bosons using a classical $(d+1)$-dimensional model in terms of the phases of those bosons. These reformulations are very useful when studying these systems in Monte Carlo.

2.1.3 Reformulations in terms of vortices

Eq. (2.11) is an action in terms of the world-lins of the bosons in a Bose-Hubbard model. In this section we reformulation it in terms of the world-lines of the vortices of the bosons. This approach only works in $(2+1)$ dimensions, and is an application of the boson-vortex duality developed to study the Mott insulator-superfluid transition[55, 56, 57, 58, 59, 60, 47] . Unlike the reformulations in the previous subsection, this reformulation only works in $(2+1)$ dimensions, but we will see that it makes up for this by being an extremely powerful analytic tool.

The original degrees of freedom are conserved integer-valued currents $\vec{J}(r)$ residing on links of a simple 3D cubic lattice; $\vec{\nabla} \cdot \vec{J}(r) = 0$ for any r. To be precise, we use periodic boundary conditions and also require vanishing total current, $\vec{J}_{\text{tot}} \equiv \sum_r \vec{J}(r) = 0$ [1].

We define duality mapping as an exact rewriting of the partition sum in terms of new integer-valued currents $\vec{Q}(R)$. These new variables reside on links of a' dual' lattice whose positions are labelled by R. The sites of the dual lattice sit in the centers of the cubes of the original ('direct') lattice, i.e. $R = r + \hat{x}/2 + \hat{y}/2 + \hat{z}/2$. The $\vec{Q}$ variables also satisfy $\vec{\nabla} \cdot \vec{Q}(R) = 0$ for any R and $\vec{Q}_{\text{tot}} = 0$. These $\vec{Q}$ variables represent the worldlines of the vortices dual to the original bosons.

The derivation of this duality mapping is as follows. First, we would like to integrate out the $\vec{J}$ variables.

[1] Here I have changed to the very convenient notation in which all of the J_μ from Eq. (2.11) are grouped into a vector $\vec{J}$.

However, the $\vec{J}$ variables are integer-valued and constrained to be divergenceless with no total current. We enforce these constraints by adding new variables to our partition sum as follows. To enforce the divergenceless of the $\vec{J}$ variables we add the following term:

$$\delta_{[\vec{\nabla}\cdot\vec{J}](r)=0} = \int_{-\pi}^{\pi} d\phi(r) \exp\left[-i\phi(r)[\vec{\nabla}\cdot\vec{J}](r)\right]. \tag{2.15}$$

(We are ignoring overall constants here and below.) This introduces a 2π-periodic $\phi(r)$ variable on every site of the lattice. These variables correspond to the phases of the bosons. We enforce the constraint that there must be no total current (in our full system) by adding another term to the partition sum:

$$\delta_{\vec{J}_{\rm tot}=0} = \prod_{\mu=1}^{3} \int_{-\pi}^{\pi} d\gamma_{1\mu} \exp[-i\gamma_\mu \sum_r \delta_{r_\mu=0} \vec{J}_\mu(r)]. \tag{2.16}$$

This term introduces a 2π-periodic γ_μ variable for each direction μ on the lattice. This variable means that instead of periodic boundary conditions we have a fluctuating boundary condition such that across the boundary the ϕ variables differ by γ; here we chose the boundary plane perpendicular to the x direction to be at $x = 0$, and similarly for the other directions.

Now that the $\vec{J}$ variables are unconstrained, we can go from integer-valued $\vec{J}$ to real-valued j by using the following relation:

$$\sum_{\vec{J}_\mu(r)} [...] = \int_{-\infty}^{+\infty} dj_{1\mu}(r) \sum_{p_\mu(r)} \exp\left[-i2\pi p_\mu(r) j_{1\mu}(r)\right] [...].$$

This term introduces integer-valued $p_\mu(r)$ variables on every link on the lattice, and these variables are free of any constraint. In formal duality maps,[55, 56, 57, 58, 59, 60, 47] the physical meaning of the p variables is that their curl gives vorticity in the phase variables conjugate to $\vec{J}$, i.e., $\vec{Q} = \vec{\nabla} \times \vec{p}$.

Putting all of this together we obtain the following partition sum:

$$Z = \int_{-\infty}^{+\infty} \mathcal{D}j_\mu(r) \sum_{p_{r\mu}=-\infty}^{+\infty} \int_{-\pi}^{\pi} \mathcal{D}\phi(r) \int_{-\pi}^{\pi} \prod_{\mu=1}^{3} d\gamma_\mu \exp\left(-S[j] + i\sum_{r,\mu} j_\mu(r)[\nabla_\mu\phi(r) - 2\pi p_\mu(r) - \gamma_\mu \delta_{r_\mu=0}]\right), \tag{2.17}$$

where $S[j]$ is the original action of Eq. (2.11), now in terms of real valued variables.

Now consider Q variables such that $\vec{Q} = \vec{\nabla} \times \vec{p}$. Clearly there are multiple values of $\vec{p}$ that give the same $\vec{Q}$. Two such $\vec{p}$, given by $\vec{p}$ and $\vec{p}^0$, are related as follows:

$$p_\mu(r) = p^0_\mu(r) + \nabla_\mu N(r) + M_\mu \delta_{r_\mu=0}. \tag{2.18}$$

Here $N(r)$ is an integer-valued field and M_μ are integers. We can divide all possible configurations of $p_\mu(r)$ into classes, where two configurations are in the same class if they can satisfy the above equation. We can

separate the above sum over all $p_\mu(r)$ into a sum over classes (where each distinct class is denoted by a fixed member $p^0_\mu(r)$), as well as a sum over the members of each class, which corresponds to a sum over $N(r)$ and M_μ. We can then absorb the sums over $N(r)$ and M_μ into the definitions of $\phi(r)$ and γ_μ, which changes the limits on their integration to $(-\infty, +\infty)$. We can then interpret the integration over these variables as producing delta function constraints on the j variables. This gives the partition sum:

$$Z = \int_{-\infty}^{+\infty} \prod_{\mu=1}^{3} \mathcal{D}j_\mu(r) \sum_{\vec{Q}=\vec{\nabla}\times\vec{p}^0} \prod_{r\neq 0} \delta[\vec{\nabla}\cdot\vec{j}(r)=0]\delta[\vec{j}_{\rm tot}=0] \exp\left[-S(j) - 2\pi i \sum_{r,\mu} j_\mu(r) p^0_\mu(r)\right]. \quad (2.19)$$

Note that due to the U(1) symmetry of the action we can fix $\phi(r=0)=0$, $N(r=0)=0$, and so there is no delta function at $r=0$.

If we wish to obtain an action entirely in the Q variables, we can now integrate out the $\vec{j}$ fields. Let us first generalize Eq. (2.11) slightly to the form that will be used for the rest of this work. We will allow longer-ranged interactions between the currents. Futhermore, we will couple the currents to a fixed gauge field. For now we call this gauge field A, but it will take various meanings throughout this work. We also Fourier transform, defining:

$$\vec{J}(k) \equiv \frac{1}{\sqrt{\rm Vol}} \sum_r e^{-ikr} \vec{J}(r), \quad (2.20)$$

. where Vol is the volume of the system. This gives the following action:

$$S[\vec{J}] = \frac{1}{2}\sum_k v(k)|\vec{J}(k)|^2 + i\sum_k \vec{J}(k)\cdot\vec{A}(-k), \quad (2.21)$$

where $v(k)$ is a potential (which can be long ranged) and $\vec{A}$ is a fixed gauge field coupled to the $\vec{J}$ variables. With this action, the integrations over the j variables are Gaussian, with basic averages with respect to the quadratic piece in Eq. (2.21) given by

$$\langle j_\mu(k) j_{\mu'}(k')\rangle_0 = \frac{\delta_{k+k'=0}}{v(k)}\left(\delta_{\mu\mu'} - \frac{f_{k,\mu} f^*_{k,\mu'}}{|\vec{f}_k|^2}\right), \quad (2.22)$$

where

$$f_{k,\mu} \equiv 1 - e^{ik_\mu}. \quad (2.23)$$

We then obtain

$$S_{\rm dual}[\vec{Q}] = \frac{1}{2}\sum_k \frac{(2\pi)^2}{v(k)|\vec{f}_k|^2}|\vec{Q}(k) + \vec{B}(k)/2\pi|^2, \quad (2.24)$$

where $B_\mu(k) \equiv \epsilon^{\mu\nu\lambda} f_{k,\nu} A_\lambda$. [2] The relation between Eq. (2.21) and Eq. (2.24) will be called "duality map" in the remainder of this work.

Equations (2.11), (2.13), (2.14), and (2.24) are all equivalent ways to represent the same system of bosons,

[2] In real space $\vec{B} = \vec{\nabla}\times\vec{A}(k)$.

and each will be used at different times throughout the remainder of this thesis. Note also that we could have derived Eq. (2.24) by integrating out the ϕ variables (and constraining the bosons to not have zero total current in the periodic system) in Eq. (2.13). In this subsection demonstrates the method of performing the duality starting with Eq. (2.11) because going directly from the $\vec{J}$ to $\vec{Q}$ variables is in practice often the most convenient.

The single-component boson system described in this section has two phases: a superfluid and a Mott Insulator. In the superfluid the bosons are proliferated, while the vortices are gapped. In our $(2+1)$ dimensional stat-mech model, this manifests itself by either proliferation of $\vec{J}$ currents, or an absence of $\vec{Q}$ currents (depending on which formulation is being used). This happens when $v(k)$ is small so that the bosons (vortices) see a small (large) energy cost. On the other hand, in a Mott insulator the vortices are proliferated while the bosons are gapped, so there are either a lot of $\vec{Q}$ currents or an absence of $\vec{J}$ currents. This happens when the potential $v(k)$ seen by the bosons is large. The single-component of bosons are a $U(1)$ symmetry which comes from conserving the boson number, and the superfluid phase breaks this symmetry.

2.2 Two species of Bosons: Modular Transformations

In this section we use the techniques of the previous section to study models of two species of bosons with statistical interactions.[47, 48, 49] Consider the following action:

$$\begin{aligned} S &= \frac{1}{2}\sum_k \left[v_1(k)|\vec{J}_1(k)|^2 + v_2(k)|\vec{J}_2(k)|^2 \right] + i\sum_k \theta(k)\vec{J}_1(-k)\cdot\vec{a}_{J_2}(k) \\ &+ i\sum_k \left[\vec{J}_1(-k)\cdot\vec{A}_1^{\text{ext}}(k) + \vec{J}_2(-k)\cdot\vec{A}_2^{\text{ext}}(k) \right]. \end{aligned} \tag{2.25}$$

The first two terms of this action are just two copies of Eq. (2.21). Both $\vec{J}_1$ and $\vec{J}_2$ behave like the $\vec{J}$ of the previous section; however. in real space they are defined on different cubic lattices, as described previously. We will index the sites of lattice of $\vec{J}_1$ with the index r, and call it the direct lattice, while $\vec{J}_2$'s lattice will be indexed by R and called the dual lattice. The sites of the dual lattice are in the center of the cubes of the direct lattice.

Eq. (2.25) also contains an integer-valued gauge field $\vec{a}_{J_2}$, which is defined such that

$$\vec{J}_2(R) = [\vec{\nabla}\times\vec{a}_{J_2}(r)]. \tag{2.26}$$

This field lives on the links of direct (r) lattice, but taking the curl of something on the links of the direct lattice gives a variable defined on the links of the dual lattice. The third term in this action is defined such that when $\theta(k)$ is a constant, this action has a phase of $e^{i\theta}$ when loops of opposite species are linked. This linking in the $(2+1)$-dimensional spacetime corresponds to an exchange in the corresponding $2d$ problem, so the effect of this term is to encode mutual statistics between $\vec{J}_1$ and $\vec{J}_2$. When $\theta(k)$ is not constant this term gives

some additional interactions in addition to the statistical interactions. The $A^{\rm ext}$ are external Maxwell fields which will be used to compute linear reponses.

In this section we will show how to reformulate this action in terms of some new integer-valued currents $\vec{G}$, which represent the worldlines of some other kind of boson. We will obtain an action for the $\vec{G}$ bosons that is of the same form as Eq. (2.25), but with modified parameters $v(k)$ and $\theta(k)$. We will show how to write the $v(k)$, $\theta(k)$ for the $\vec{G}$ variables in terms of those for the $\vec{J}$ variables. The point of doing this is that depending on the choice of parameters, the $\vec{G}$ variables can be much easier to study than the $\vec{J}$ variables. We can also relate observables in the $\vec{J}$ variables (which can be hard to measure) to observables in the $\vec{G}$ variables (which can be easier to measure). These techniques were essential to solving the problems studied in Refs. [47, 48, 49].

We can use the duality transform from the previous section [see Eq. (2.24)] to go from the J_1 variables to dual Q_1 variables as follows:

$$\begin{aligned} S &= \frac{1}{2}\sum_k \frac{\left|2\pi\vec{Q}_1(k)+\theta(k)\vec{J}_2(k)+[\vec{\nabla}\times\vec{A}_1^{\rm ext}](k)\right|^2}{|\vec{f}_k|^2 v_1(k)} \\ &+ \frac{1}{2}\sum_k v_2(k)|\vec{J}_2(k)|^2 + i\sum_k \vec{J}_2(-k)\cdot\vec{A}_2^{\rm ext}(k). \end{aligned} \tag{2.27}$$

The $\vec{Q}_1$ variables represent the vortices of the bosons defined by $\vec{J}_1$, and like them they are divergenceless and therefore form closed loops.

We can now make the following change of variables:[48, 49]

$$\vec{F}_1 = a\vec{Q}_1 - b\vec{J}_2, \tag{2.28}$$

$$\vec{G}_2 = c\vec{Q}_1 - d\vec{J}_2. \tag{2.29}$$

This change of variables is valid if the matrix

$$\begin{pmatrix} a & b \\ c & d \end{pmatrix} \in PSL(2,\mathbb{Z}), \tag{2.30}$$

i.e., a, b, c, d are integers such that $ad - bc = 1$. Since the above matrix is an element of the modular group, we call this change of variables a modular transformation and will often refer to it simply (a, b, c, d). Here F_1 and G_2 are new integer-valued conserved currents, with all the same properties (divergenceless, zero total current) as the J and Q variables. We can therefore perform the duality transform to go from the $\vec{F}_1$ variables to dual G_1 variables, which gives us an action in terms of the G_1 and G_2 variables. This transformation, from J_1, J_2 variables to G_1, G_2 variables, is the generalization of the duality operation to modular transformations.

After performing this change we are left with the following action:

$$\begin{aligned} S &= \frac{1}{2}\sum_k v_{G1}(k)\left|\vec{G}_1(k)+\frac{c[\vec{\nabla}\times\vec{A}_2^{\rm ext}](k)}{2\pi}\right|^2+\frac{1}{2}\sum_k v_{G2}(k)\left|\vec{G}_2(k)+\frac{c[\vec{\nabla}\times\vec{A}_1^{\rm ext}](k)}{2\pi}\right|^2 \\ &+ i\sum_k \theta_G(k)\vec{G}_1(-k)\cdot\vec{a}_{G2}(k)-i\sum_k\frac{c[2\pi a-\theta_G(k)c]}{(2\pi)^2}[\vec{\nabla}\times\vec{A}_1^{\rm ext}](-k)\cdot\vec{A}_2^{\rm ext}(k) \\ &- i\sum_k\left[a-\frac{\theta_{\vec{G}}(k)c}{2\pi}\right]\left[\vec{G}_1(-k)\cdot\vec{A}_1^{\rm ext}(k)+\vec{G}_2(-k)\cdot\vec{A}_2^{\rm ext}(k)\right], \end{aligned} \tag{2.31}$$

where $\vec{G}_2=\vec{\nabla}\times\vec{a}_{G2}$ and

$$v_{G1/2}(k)=\frac{(2\pi)^2 v_{1/2}(k)}{[2\pi d+\theta(k)c]^2+v_1(k)v_2(k)|\vec{f}_k|^2c^2}, \tag{2.32}$$

$$\frac{\theta_G(k)}{2\pi}=\frac{[2\pi b+\theta(k)a][2\pi d+\theta(k)c]+v_1(k)v_2(k)|\vec{f}_k|^2ca}{[2\pi d+\theta(k)c]^2+v_1(k)v_2(k)|\vec{f}_k|^2c^2}. \tag{2.33}$$

Neglecting the $A^{\rm ext}$ terms, the above action has the same form as Eq. (2.25), but with different $v(k)$ and $\theta(k)$. Though the expressions for may look intimidating, with a proper choice of (a,b,c,d) they can in fact be quite easy to work with.

Often we are interested in measuring physical properties of the $\vec{J}$ variables, but find that the $\vec{G}$ variables are much easier to work with. In particular, we want to measure linear responses to applied electromagnetic fields. These responses are defined by:

$$C_{ab}^{\mu\nu}(k)=\langle J_{a\mu}(k)J_{b\nu}(-k)\rangle, \tag{2.34}$$

where μ,ν are lattice directions and a,b represent boson species. $C_{aa}^{\mu\mu}(k)\equiv\rho_{a\mu}(k)$ is the superfluid stiffness for species a, while $C_{12}^{xy}(k)$ is related to the cross-species Hall response: the current induced in bosons of species 1 to an applied field which couples to bosons of species 2. The following equations give the $C_{ab}^{\mu\nu}(k)$ of the $\vec{J}$ variables, in terms of the $C_{ab}^{\mu\nu}(k)$ of the $\vec{G}$ variables:

$$\begin{aligned} C_{11J}^{xx}(k)&=\frac{v(k)|f_k|^2c^2}{(\theta c+2\pi d)^2+|f_k|^2v(k)^2c^2} \\ &+\frac{[(\theta c+2\pi d)^2-|f_k|^2v(k)^2c^2]C_{11G}^{xx}(k)-4\sin\frac{k_z}{2}v(k)c(\theta c+2\pi d)C_{12G}^{xy}(k)}{[(\theta c+2\pi d)^2+|f_k|^2v(k)^2c^2]^2}\cdot(2\pi)^2, \end{aligned} \tag{2.35}$$

$$\begin{aligned} C_{12J}^{xy}(k)&=\frac{-2\sin\frac{k_z}{2}c(\theta c+2\pi d)}{(\theta c+2\pi d)^2+|f_k|^2v(k)^2c^2} \\ &+\frac{[(\theta c+2\pi d)^2-|f_k|^2v(k)^2c^2]C_{12G}^{xy}(k)+4\sin\frac{k_z}{2}v(k)c(\theta c+2\pi d)C_{11G}^{xx}(k)}{[(\theta c+2\pi d)^2+|f_k|^2v(k)^2c^2]^2}\cdot(2\pi)^2. \end{aligned} \tag{2.36}$$

The above expressions are especially easy to evaluate if the $\vec{G}$ variables are gapped, because in that

case in the thermodynamic limit the $C^{\mu\nu}_{abG} \to 0$. [3] In the next chapter we will have an action of the form Eq. (2.25) which is difficult to study, and we will determine its Hall conductivity by finding the (a, b, c, d) which produced gapped $\vec{G}$ variables. We can then read off the Hall conductivity from Eq. (2.36). We also took a different approach in Ref. [48], which is not covered by this report. We studied a model where $v(k)$ had the form $g/|f_k|$ for both the $\vec{J}$ and $\vec{G}$ variables, with only the constant g changing under the modular transformation. We were therefore able to use the above equations to produce the entire phase diagram, and find the Hall conductivity and superfluid stiffness in each phase.

2.3 Monte Carlo Techniques

In Refs. [45, 47, 48, 49] we studied actions of the form of Eq. (2.25) in Monte Carlo simulations. At first glance, this may not seem possible, as the third term in that equation contains a complex number. Actions which evaluate to complex numbers cannot be studied in Monte Carlo due to the 'sign-problem': since Monte Carlo algorithms populate states with probability e^{-S}, if S is not real the result will not be real, and thus cannot be a probability.

There are number of ways to reformulate Eq. (2.25) to avoid the sign problem. One is to simulate Eq. (2.27), which has no sign problem. This approach was taken in Ref. [48]. However, we can see that the $\vec{Q}_1$ variables have long-ranged interactions, and in systems with such interactions the time required for the simulations scales as L^6 (for a $(2+1)$-dimensional system with linear dimension L). It is often convenient to have only short-ranged interactions in our system, so that the Monte Carlo can run in a time proportional to L^3, and larger sizes can be studied. When the $\vec{J}$ bosons have only onsite interactions, this can be accomplished using the reformulations discussed in Sec. 2.1. In particular, we will represent one of the bosons (say $\vec{J}_1$) using Eq. (2.13) or Eq. (2.14). The model which has two species of bosons therefore has an action that is a combination of Eq. (2.11) for the $\vec{J}_2$ bosons and one of the Eqs. (2.13),(2.14), with $\nabla_\mu \phi(r) \to \nabla_\mu \phi(r) + \theta a_{2\mu}(r)$ for the J_1 bosons. This approach was used in Refs. [45, 47]. In Chapter 3 we will describe additional reformulations which work for systems with spatially varying θ.

All of our reformulations contain at least one species of conserved currents $\vec{J}$. These must be divergenceless, so we update them either by adding small loops to the system, or by using the directed geometric worm algorithm[61]. It is often convenient to have the symmetry $\vec{J}_1 \leftrightarrow \vec{J}_2$, and to do this in the various reformulations we also need to constrain the boson currents to not wind around the periodic boundary conditions.

In our simulations, we monitor the "internal energy per site," $\epsilon = S/\mathrm{Vol}$, where Vol is the volume of the system, which we take to have linear size L in all directions. From this, we can determine the specific heat per site:

$$C = (\langle \epsilon^2 \rangle - \langle \epsilon \rangle^2) \times \mathrm{Vol}. \tag{2.37}$$

[3] This is only true for correlators evaluated at $k = 2\pi/L$, with L the system size, which is the case we are interested in, as will be discussed in the next section.

We can locate phase transitions in our model by looking for singularities in the specific heat. In reformulations that contain boson phase variables ϕ, we also monitor the magnetization per spin:

$$m = \frac{\langle |\sum_R \phi(R)| \rangle}{\mathrm{Vol}}. \tag{2.38}$$

When the spins are disordered the magnetization is proportional to $1/\sqrt{\mathrm{Vol}}$, while in the ordered phase the magnetization remains non-zero in the thermodynamic limit. Therefore we can use measurements of the magnetization at different sizes to determine if the spins are ordered.

To study the behavior of the boson currents, we monitor current-current correlators, defined as:

$$C_{aa}^{\mu\mu} \equiv \rho_{Ja}(k) = \langle J_{a\mu}(k) J_{a\mu}(-k) \rangle \ , \tag{2.39}$$

where k is a wave vector, μ is a fixed direction, and $a \in \{1, 2\}$ is a boson species index.

In space-time isotropic systems, $\rho_J(k)$ is independent of the direction μ, and when we show numerical data we average over all directions to improve statistics. In an ensemble which would allow non-zero total winding number, $\rho_J(0)$ would be the familiar superfluid stiffness. In our model which is constrained to the case of zero total current, $J(k = 0) = 0$, so this measurment is not available in our simulations. Instead, we evaluate the correlators at the smallest non-zero k. For example, if μ is in the x direction in a $(2 + 1)$-dimensional system, we can take $k_{\min} = (0, \frac{2\pi}{L}, 0)$, and $(0, 0, \frac{2\pi}{L})$ and average over these; we exclude $(\frac{2\pi}{L}, 0, 0)$ because in our ensemble the net winding of the J_x current is zero, so the $J_x(k)$ evaluated at this wavevector is also zero. In reformulations containing vortex currents Q, we also monitor current-current correlators of the vortex currents, $\rho_Q(k)$, which are defined in the same way as for the boson currents.

In the phase where the J_μ are gapped, only small loops contribute to the current-current correlators and $\rho_J(k_{\min}) \sim k_{\min}^2 \sim 1/L^2$, while when the J_μ proliferate ρ_J is independent of the system size. Therefore we can use finite-size scaling of this quantity to determine the locations of phase transitions. For the vortex currents, $\rho_Q(k_{\min}) \sim k_{\min}^2$ in all phases, so we cannot use finite-size scaling of this quantity to find phase transitions; this originates from effective long-range interactions of these topological defects.

Chapter 3

Numerical Study of the Boson Integer and Fractional Hall Effects

3.1 Introduction

In this chapter we use the formalism developed in Chapter 2 to construct a model of a topological phase known as the bosonic quantum Hall effect. This is a phase that is constructed of interacting bosons, but which has a quantized Hall conductivity and gapless edge modes, and we will show that our model indeed has these properties. The bosonic integer quantum Hall effect has short-ranged entanglement, and is a symmetry-protected topological phase protected by $U(1) \times U(1)$ symmetry, while the fractional case has long-ranged entanglement and the same symmetry, and is a 'symmetry-enriched' topological phase [62].

Prior to our work, Ref. [63] used Chern-Simons approaches to provide understanding of the boson IQHE (for a review, see Ref. [3]). Several papers have proposed qualitative construction of such phases using Chern-Simons flux attachment[26] and slave-particle approaches.[64, 65, 66] However, prior to our work there have been no microscopic models producing such states. Our approach is different from Chern-Simons and slave-particle approaches, in that we work directly with physical degrees of freedom and do not introduce artificial fluxes or enlarge the Hilbert space. More specifically, we think directly in terms of charge and vortex degrees of freedom, which are all precisely mathematically defined in our lattice models. In this way, our work is close in spirit to pursuits to understand fractionalized phases of spins and bosons in terms of the vortex physics.[67, 68] The $U(1) \times U(1)$ structure allows us to provide an unambiguous and simple physical picture of the integer and fractional quantum Hall states of bosons. Thus, an elementary integer quantum Hall state is obtained when a vortex in one species binds a charge of the other species and the resulting composite object condenses; our approach provides a precise meaning of such a condensation. General integer quantum Hall states are obtained when a vortex in one species binds a fixed number of charges of the other species. On the other hand, fractional quantum Hall states are obtained when we have condensation of composite objects that are bound states of d vortices of one species and c particles of the other species. In this case we show that the system has a fractional quantum Hall response given by $\sigma_{xy} = 2c/d$ and has quasiparticles carrying

fractional charges of $1/d$ of the microscopic charges and non-trivial mutual statistics. Such d-tupled vortex condensation leading to charge fractionalization is reminiscent of the idea in Refs. [67, 68] of paired-vortex condensation leading to Z_2 fractionalized phases, although in the present case there is also binding of charges and the phase shows quantized Hall response.

This chapter is organized as follows. In Sec. 3.2 we describe how the results of Chapter 2 can be used to realize integer and fractional quantum Hall phases, and how these phases can be studied in Monte Carlo simulations. In Sec. 3.4 we present the results of these numerics, including evidence for gapless modes at the boundary of the quantum Hall states. In Sec. 3.5 we show the broader phase diagrams for our models. Finally, in Sec. 3.6 we present a local Hamiltonian which gives the action discussed in the rest of the chapter.

3.2 Explicit Models with Integer and Fractional Quantum Hall Effect

We start with the action for two species of bosons with statistical interactions given in Chapter 2, Eq. (2.25):

$$S = \frac{1}{2}\sum_k \left[v_1(k)|\vec{J}_1(k)|^2 + v_2(k)|\vec{J}_2(k)|^2 \right] + i\sum_k \theta(k)\vec{J}_1(-k)\cdot\vec{a}_{J2}(k). \tag{3.1}$$

The problem with using this action to realize boson QHE, or any phase, is that the θ term is non-local, and cannot be realized by a local Hamiltonian. We would like to make the action local. Note that the non-locality of the action is due to the explicit appearance of the gauge field $\vec{a}_{J2}$. Therefore the model can be made local if we set $\theta(k) = |f_k|^2 w(k)$, where $w(k)$ is some local interaction term. Since f_k is the Fourier transform of a lattice derivative, $|f_k|^2$ is equivalent to two derivatives in real space. Therefore when we transform the action to real space end up taking the curl of both $\vec{J}_1$ and a_{J2}, and from the definition of a_{J2} in Eq. (2.26) we get:

$$\begin{aligned} S &= \frac{1}{2}\sum_{r,r'} v_1(r-r')\vec{J}_1(r)\cdot\vec{J}_1(r') + \frac{1}{2}\sum_{R,R'} v_2(R-R')\vec{J}_2(R)\cdot\vec{J}_2(R') \\ &+ i\sum_{R,R'} w(R-R')[\vec{\nabla}\times\vec{J}_1](R)\cdot\vec{J}_2(R'). \end{aligned} \tag{3.2}$$

Now all of the terms are local. Note that $\vec{J}_1(r)$ and $\vec{J}_2(R)$ live on cubic lattices which are dual to each other, as described in Chapter 2.

The action in Eq. (4.1) is local, but it is also difficult to analyze. In order to study it, we want to transform to new variables $\vec{G}_1$, $\vec{G}_2$, which are gapped, as described in Chapter 2. To do this we need to find expressions for $v_1(k)$, $v_2(k)$, and $w(k)$, which can be transformed using a modular transformation with some (a, b, c, d)

to an action which is gapped. The expressions which can accomplish this are:

$$v_{1/2}(k) = \frac{\lambda_{2/1}}{\lambda_1\lambda_2 + \frac{c^2|\vec{f}_k|^2}{d^2(2\pi)^2}}, \tag{3.3}$$

$$\theta(k) = \frac{-c}{2\pi d}\frac{|\vec{f}_k|^2}{\lambda_1\lambda_2 + \frac{c^2|\vec{f}_k|^2}{d^2(2\pi)^2}}, \tag{3.4}$$

where λ_1 and λ_2 are constants and c, d are the same integers as in Eq. (2.29).

If we insert this expression into Eqs. (2.32) and (2.33) we get:

$$v_{Gi}(k) = \frac{1}{d^2\lambda_i}, \tag{3.5}$$

$$\theta_G = 2\pi\frac{b}{d}. \tag{3.6}$$

And when we insert these expressions into Eq. (3.8) in real space [1] we get:

$$\begin{aligned} S &= \frac{1}{2d^2\lambda_1}\sum_r \vec{G}_1(r)^2 + \frac{1}{2d^2\lambda_2}\sum_R \vec{G}_2(R)^2 + i\sum_r \theta_{\vec{G}}\vec{G}_1(r)\cdot\vec{a}_{G2}(r) \\ &- i\sum_r \frac{2\pi c}{d}[\vec{\nabla}\times\vec{A}_1^{\rm ext}](R)\cdot\vec{A}_2^{\rm ext}(R) - i\sum_r \frac{1}{d}\vec{G}_1(r)\cdot\vec{A}_1^{\rm ext}(r) - i\sum_R \vec{G}_2(R)\cdot\vec{A}_2^{\rm ext}(R), \end{aligned} \tag{3.7}$$

where we have used $ad - bc = 1$ where necessary.

For the case where the λ_i are small the $\vec{G}$ variables see a large energy potential and are gapped, and we can read off the Hall conductivity from the coefficient of the Chern-Simons term for the A fields. We find

$$\sigma_{xy}^{12}(k \to 0) = \frac{c}{d} \tag{3.8}$$

in units of e^2/h. From the $\vec{G}\cdot\vec{A}$ terms we can see that the $\vec{G}$ bosons carry

$$\text{charge} = \frac{1}{d}, \tag{3.9}$$

relative to $A_1^{\rm ext}$ and $A_2^{\rm ext}$, respectively. From the mutual statistics term we can see that they have mutual statistics $2\pi b/d$.

We see that when $d = 1$, the system has a Hall conductivity quantized to be an integer and excitations carrying integer charges. We propose that this is a realization of the bosonic integer quantum Hall effect.[63] When $d > 1$, we see that the Hall conductivity is quantized as a rational number and the $\vec{G}$ quasiparticles carry fractional charge and statistics. Therefore this phase is a fractional quantum Hall effect for bosons. Note that the Hall conductivity studied here is the 'cross-species Hall conductivity': the current of bosons coupled to the external field $A_2^{\rm ext}$ under an applied $A_1^{\rm ext}$ field. If these external fields are identified [reducing

[1] leaving out the $\vec{\nabla}\times\vec{A}$ terms in the G_1^2 terms, which turn out to be unimportant.

the symmetry of the system from $U(1) \times U(1)$ to $U(1)$], then the Hall conductivity is doubled, which gives a Hall conductivity quantized to an even integer, consistent with studies of the boson quantum Hall effect in the literature.

As an intermediate step in the change of variables procedure defined in Chapter 2, we obtain the following action [which is a specialization of Eq. (2.27)]:

$$S = \frac{1}{2} \sum_k \frac{(2\pi)^2 \lambda_1}{|\vec{f}_k|^2} |\vec{Q}_1(k)|^2 + \frac{1}{2} \sum_R \frac{1}{\lambda_2} |\vec{J}_2(R) - \eta(R) \vec{Q}_1(R)|^2.$$

Here $\eta(R) = c/d$ everywhere in the system, though later we will consider spatially varying $\eta(R)$. Studying this action at small λ_1 and λ_2 can tell us about the physics of the quantum Hall states.

First consider the situation where $c = 0$, which leads to $\eta(R) = 0$, and consider the limit of small λ_1, λ_2. We can see from Eq. (3.8) that σ_{xy}^{12} vanishes and therefore this system is not in a quantum Hall state. There is a small energy cost for loops in the $\vec{Q}_1$ variables, but a large energy cost for loops in the $\vec{J}_2$ variables. Therefore the $\vec{J}_2$ loops are gapped. The $\vec{Q}_1$ variables are 'condensed', which means that large loops of these variables can form. In general, since $\vec{J}_1$ and $\vec{Q}_1$ are related by a duality transformation, if one of them is gapped the other is condensed. Therefore the $\vec{J}_1$ variables are gapped in this phase. Since the physical $\vec{J}_1$ and $\vec{J}_2$ variables are gapped, the system is a trivial insulator. This situation is shown on the left side of Fig. 3.1. We could have arrived at this conclusion also more quickly by examining Eqs. (3.3)-(3.4) for $c = 0$, but it was convenient to develop the picture in the Q_1 and J_2 variables.

Now consider the case where $c \neq 0$, so that $\eta(R) = c/d$. Since the $\vec{G}$ variables are gapped we have a quantized Hall conductivity, and the system is in the bosonic quantum Hall state. Notice that composite objects with $\vec{J}_2 = c$ and $\vec{Q}_1 = d$ see a very small energy cost, and therefore large loops of such objects can form. On the other hand, both the $\vec{J}_2$ and $\vec{Q}_1$ variables see large potentials if they exist independently, so only small loops of these variables can form by themselves. This is illustrated on the right side of Fig. 3.1 (for $c = d = 1$). We can see that the boson quantum Hall effect can be well described by binding bosons of species 1 to vortices of species 2.

We would like to know what carries the charges that leads to the $\sigma_{xy}^{12} \neq 0$. By analogy with the fermionic Quantum Hall effect, we expect that the charges are being carried by edge states. We will examine the physics of the formation of edge states by including a boundary between the quantum Hall state and the trivial insulator in our system. This is accomplished by allowing $\eta(R)$ to vary in space. Therefore we have one region where $\eta(R) = c/d$, and we have another region where $\eta(R) = 0$. Note that we have defined $\eta(R)$ as varying on the dual lattice denoted by the index R. Before we allowed η to vary in space, we had a symmetry between the $\vec{J}_1$ and $\vec{J}_2$ variables in the case where $v_1 = v_2$. However, the different variables see the boundary differently and it breaks this symmetry.

Now consider what happens at the boundary of the quantum Hall state. For example, consider the case where $\eta(R) = 1$ in the region where it is non-zero. In the quantum Hall region we will have large loops

with ($\vec{J}_2 = 1$,$\vec{Q}_1 = 1$), while in the trivial insulating region we have large loops of only $\vec{Q}_1$ variables. This situation is illustrated in Fig. 3.1. The large loops of the $\vec{Q}_1$ variables can pass through the boundary. However, the $\vec{J}_2$ loops must be bound to the $\vec{Q}_1$ loops in one region and must disappear in the other region. The system must find a way to accomplish this while satisfying the constraint that all currents must be divergenceless. To do this, it exhibits behavior which would be energetically forbidden in the bulk. For instance, the J_2 currents could run along the edge, as seen in Fig. 3.1. In this case on the right edge, the J_2 currents run from places where the Q_1 variables cross the boundary from left to right to places where they cross from right to left. Alternatively, loops of the Q variables could be forbidden from crossing between the two regions, which means that vortices in the boson phase variables would be forbidden on the boundary. This unusual behavior leads to gapless modes on the boundary between a quantum Hall region and a trivial insulator. In Sec. 3.4 we will develop mathematical description of this behavior and will numerically find evidence for these gapless modes.

3.3 Monte Carlo Study of a Model with a Boundary

In order to further characterize these bosonic quantum Hall phases, we now seek to find gapless edge modes numerically using Monte Carlo simulations.[69] We include edges by allowing $\eta(R)$ to vary in space, in one direction, which we will label as the x-direction. In our large $L \times L \times L$ system, we will say that

$$\eta(R) = \begin{cases} c/d & \text{for } X_L \leq X < X_R \\ 0 & \text{otherwise} \end{cases}, \tag{3.10}$$

where X is the x-coordinate on the dual lattice. The quantum Hall behavior occurs in the region with non-zero η. We will take half of the system to be in the quantum Hall phase and the other half in the trivial insulator phase.

Note that the original action in terms of J_1, J_2 currents, Eq. (4.1), has a sign problem. There are a number of ways to reformulate the action to avoid this problem, some of which are described in Chapter 2. The remainder of this section will be devoted to developing several additional exact reformulations of Eq. (3.10) which work for spatially varying $\eta(R)$. These reformulations are also useful because they provide access to boson Green's functions.

Consider the following action:

$$\begin{aligned} S[\vec{\alpha}_1, \vec{\alpha}_2, \vec{J}_1, \vec{J}_2] = \frac{1}{2}\sum_r \lambda_1 \vec{\alpha}_1(r)^2 + \frac{1}{2}\sum_R \lambda_2 \vec{\alpha}_2(R)^2 + i\sum_R \frac{\eta(R)}{2\pi}[\vec{\nabla} \times \vec{\alpha}_1](R) \cdot \vec{\alpha}_2(R) \\ + i\sum_r \vec{J}_1(r) \cdot \vec{\alpha}_1(r) + i\sum_R \vec{J}_2(R) \cdot \vec{\alpha}_2(R). \end{aligned} \tag{3.11}$$

The new α_1 and α_2 variables are real-valued vector fields residing on links of the direct and dual lattices,

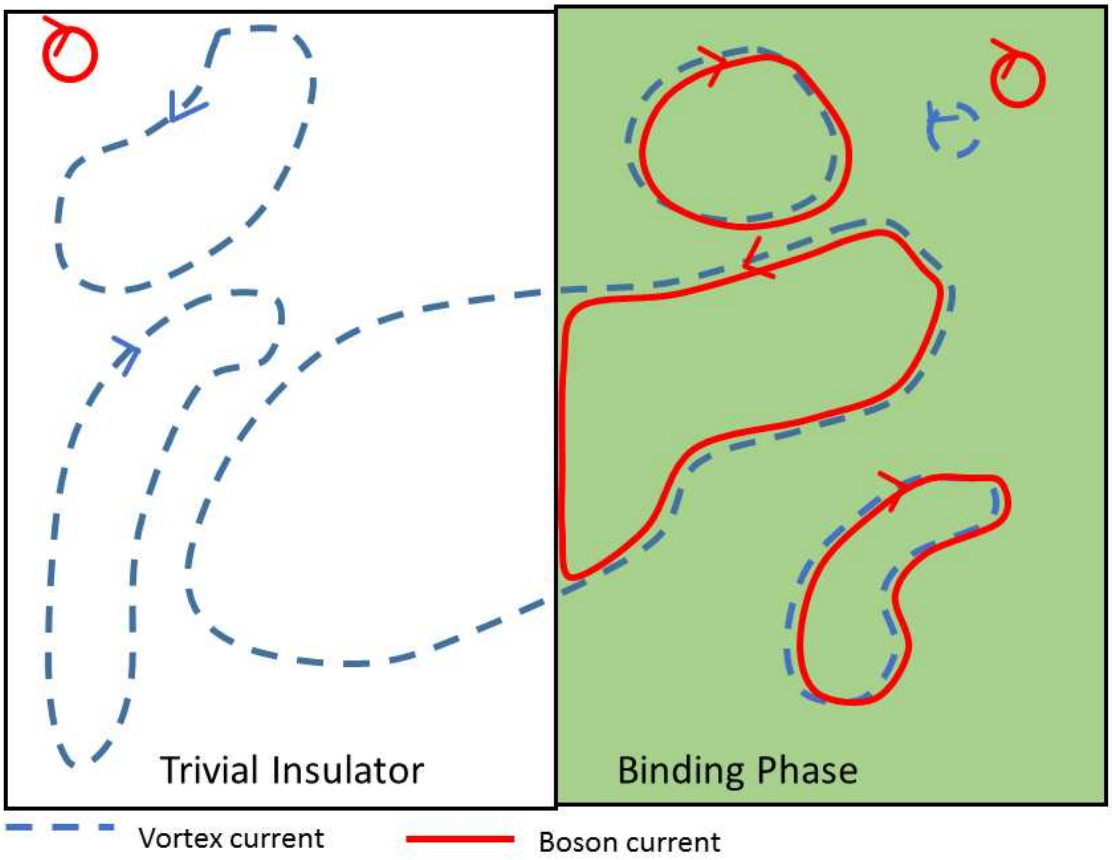

Figure 3.1: A sketch of the situation where $\eta(R)$ is allowed to vary in space, with $\eta(R) = 1$ in the quantum Hall region and $\eta(R) = 0$ in the trivial insulator region. In the trivial insulator region, loops of the $\vec{Q}_1$ variables can be large, while the $\vec{J}_2$ variables can only form small loops. In the quantum Hall region, large loops of composite objects with ($\vec{Q}_1 = 1$, $\vec{J}_2 = 1$) exist, while loops of only $\vec{Q}_1$ or only $\vec{J}_2$ variables are small. In order to have closed loops of the $\vec{J}_2$ variables, there must be behavior on the edge different from that in the bulk, which leads to the gapless edge supporting non-zero Hall conductivity. A similar situation also occurs in Chapter 4.

respectively. One can check that the partition sum which results from this action is the same as Eq. (4.1) if we integrate out both of these species of vector fields. Note that the α_1 and α_2 variables are not some gauge fields; rather, they are some local massive fields and are integrated over with no constraints. Section 3.6 shows that such an action can be realized as a path integral for a local Hamiltonian with bosons coupled to oscillator degrees of freedom.

In order to get a sign-free action that we can study efficiently in Monte Carlo, we start with Eq. (3.11) but perform different integrations. First, we integrate out the α_2 variables. Then, we integrate out the $\vec{J}_1$ variables using the techniques in Sec. 2.1.3, which gives:

$$Z = \sum_{\vec{J}_2}{}' \sum_{\vec{p}_1} \int_{-\pi}^{\pi} \mathcal{D}\phi_1 \int_{-\pi}^{\pi} \prod_{\mu=1}^{3} d\gamma_{1\mu} e^{-S[\phi_1,\gamma_1,\vec{p}_1,\vec{J}_2]}, \tag{3.12}$$

$$S[\phi_1,\gamma_1,\vec{p}_1,\vec{J}_2] = \frac{\lambda_1}{2} \sum_r \left[\vec{\omega}_1(r) - 2\pi\vec{p}_1(r)\right]^2 + \frac{1}{2\lambda_2} \sum_R \left[\vec{J}_2(R) - \eta(R)(\vec{\nabla}\times\vec{p}_1)(R)\right]^2 \tag{3.13}$$

Here the primed sum over J_2 variables is subject to the constraints of no divergence and zero total current; we have also defined

$$\omega_{1\mu}(r) = \phi_1(r+\hat{\mu}) - \phi_1(r) - \gamma_{1\mu}\delta_{r_\mu=0}, \tag{3.14}$$

and used $\vec{\nabla}\times\vec{\omega}_1 = 0$. This action is sign-free and all interactions are short-ranged, so it can be studied efficiently in Monte Carlo; it will allow us to detect gaplessness of the quantum Hall edge by looking at the spatial correlations of the ϕ_1 variables, which as usual represent the phases of the bosons of species 1. The action is not explicitly 2π-periodic in the ω_1 variables, but all physical measurements have the required periodicity. Specifically, the periodicity $\phi_1(r) \to \phi_1(r) + 2\pi N(r)$ and $\gamma_{1\mu} \to \gamma_{1\mu} + 2\pi M_\mu$, with integers $N(r)$ and M_μ, can be accounted for by shifting the summation variables $p_{1\mu}(r) \to p_{1\mu}(r) + \nabla_\mu N(r) - M_\mu\delta_{r_\mu=0}$, which does not change $\vec{\nabla}\times\vec{p}_1$ in the second term of Eq. (3.13). We will present Monte Carlo measurements of the $e^{i\phi_1}$ correlators at the edge in the next section.

We would also like to measure Greens functions of the type-2 bosons. To get a reformulation that provides access to the phase variables of the type-2 bosons, ϕ_2, we go back to Eq. (3.11) and integrate by parts on the second line as follows:

$$\sum_R \eta(R)[\vec{\nabla}\times\vec{\alpha}_1](R)\cdot\vec{\alpha}_2(R) = \sum_r (\vec{\nabla}\times[\eta(R)\vec{\alpha}_2(R)])(r)\cdot\vec{\alpha}_1(r)\ , \tag{3.15}$$

which already suggests that the two boson species will see the edge differently. We then integrate out the α_1 and $\vec{J}_2$ variables using similar methods to those above. The resulting action is:

$$\begin{aligned} S[\phi_2,\gamma_2,\vec{p}_2,\vec{J}_1] = {} & \frac{\lambda_2}{2}\sum_R [\vec{\omega}_2(R) - 2\pi\vec{p}_2(R)]^2 \\ & + \frac{1}{2\lambda_1}\sum_r \left[\vec{J}_1(r) - (\vec{\nabla}\times[\eta(R)\vec{p}_2(R)])(r) + \frac{1}{2\pi}(\vec{\nabla}\times[\eta(R)\vec{\omega}_2(R)])(r)\right]^2, \end{aligned} \tag{3.16}$$

where $\omega_{2\mu}(R)$ is defined similarly to Eq. (4.4). For the $\eta(R)$ in Eq. (3.10) we can calculate:

$$(\vec{\nabla} \times [\eta(R)\vec{\omega}_2(R)])(r) = \frac{c}{d}(\delta_{x+\frac{1}{2}=X_L} - \delta_{x+\frac{1}{2}=X_R}) \times [\omega_{2y}(R)\hat{z} - \omega_{2z}(R)\hat{y}],$$

which is non-zero only near the boundaries. In the last line $\omega_{2z}(R)$ is at the appropriate edge ($X = X_R$ or $X = X_L$) and is calculated on the dual lattice link perpendicular to the direct lattice link $\langle r, r+\hat{y}\rangle$ next to it, and similarly for $\omega_{2y}(R)$. Thus we have the extra boundary ω_2 term in Eq. (3.16), which comes from differentiating $\eta(R)$.

Note that the 2π-periodicity in the ω_2 variables is accounted for by the p_2 variables. A more subtle observation is that in the limit of $\lambda_2 = 0$, the ϕ_2 variables have periodicity of $2\pi/c$. Indeed, if we shift $\phi_2(R)$ by $2\pi N(R)/c$ with integer-valued $N(R)$, then $\vec{\omega}_2(R)$ is shifted by $2\pi\vec{\nabla}N(R)/c$. We can simultaneously shift the summation variables $\vec{p}_2(R)$ by $-b\vec{\nabla}N(R)$ and observe that $[\vec{\omega}_2(R) - 2\pi\vec{p}_2(R)]\eta(R)/(2\pi)$ is shifted by $\vec{\nabla}N(R)(ad/c)\eta(R)$, where we used $ad - bc = 1$. The latter shift is an integer-valued vector field [since $(ad/c)\eta(R)$ is an integer everywhere], and its curl can be absorbed into the redefinition of $\vec{J}_1(r)$, thus keeping the λ_1 term in Eq. (3.16) unchanged. We will need to keep this in mind when measuring correlation functions of the ϕ_2 variables.

In the case where $d = 1$ so that $\eta(R)$ is an integer everywhere, we can obtain one additional reformulation from Eq. (3.16). Consider making the following change of variables:

$$\vec{M}(r) = \vec{J}_1(r) - (\vec{\nabla} \times [\eta(R)\vec{p}_2(R)])(r). \tag{3.17}$$

This is an allowed change of variables since $\eta(R)\vec{p}_2(R)$ is an integer vector field and therefore its curl is a divergenceless integer field. Note that if $\eta(R)$ is not an integer, such a change of variables is not allowed since it will lead to a non-integer $\vec{M}$. After making this change of variables, we can perform a summation over $\vec{p}_2$ to arrive at the following action:

$$S[\phi_2, \gamma_2, \vec{M}] = \sum_{R,\mu} V_{\text{Villain}}[\omega_{2\mu}(R); \lambda_2] + \frac{1}{2\lambda_1}\sum_r \left[\vec{M}(r) + \frac{1}{2\pi}(\vec{\nabla} \times [\eta(R)\vec{\omega}_2(R)])(r)\right]^2, \tag{3.18}$$

where V_{Villain} is the Villain potential defined in Eq. (2.14), which we tabulate before the start of the simulations. Since this action contains fewer variables than the previous actions, it is more efficient to run in Monte Carlo.

3.4 Numerical Evidence for Gapless Edge

In order to determine the existence of gapless modes on the edge, we will measure correlators of the ϕ_1 and ϕ_2 variables.

A technical point: these variables are not translationally invariant because of the way in which we intro-

duced fluctuating boundary conditions to enforce a zero total current in the $\vec{J}$ variables. In particular, these variables appear as $\nabla_\mu \phi$ everywhere in the system, except at the cuts where we added the γ variables, where they appear as $\nabla_\mu \phi - \gamma_\mu$. Assuming here that r_μ takes values $0, 1, \ldots, L_\mu - 1$ and the fluctuating boundary condition is between $r_\mu = L_\mu - 1$ and $r_\mu = 0$, we can make a change of variables $\phi \to \tilde{\phi}$,

$$\tilde{\phi}(r) = \phi(r) + \sum_\mu \gamma_\mu r_\mu / L_\mu \, . \tag{3.19}$$

This gives $\nabla_\mu \phi(r) - \gamma_\mu \delta_{r_\mu = L_\mu - 1} = \nabla_\mu \tilde{\phi}(r) - \gamma_\mu / L_\mu$, and the action becomes translationally invariant along the edge in the $\tilde{\phi}$ variables, so we will use them to measure correlators.

In the $\tilde{\phi}_1$ variables, we measure the correlator

$$\chi_1(r - r') \equiv \langle e^{i\tilde{\phi}_1(r)} e^{-i\tilde{\phi}_1(r')} \rangle. \tag{3.20}$$

Gapless modes exist when $\chi_1(r - r')$ has algebraic decay along the edge. We have taken $r' = r + m\hat{\mu}$, where m is an integer such that $0 < m < L$ and $\hat{\mu}$ is a unit vector in either the y or z directions. When we present numerical data we have averaged over all directions and all sites on the edge. We can choose either edge to measure the correlators at; in this work we have measured at $X = X_R$. Since the edge is defined with respect to the dual lattice, it is not obvious where on the direct lattice to perform measurements of the edge states. If the sites of the direct lattice are indexed by (x, y, z), in our numerics we defined the sites of the dual lattice to be located at $(x + 1/2, y + 1/2, z + 1/2)$. Using this definition and Eq. (3.13) we can see that the edge effects will be most noticeable at $x = X_L - 1/2$ or $x = X_R - 1/2$, and so we measured the ϕ_1 correlators at $x = X_R - 1/2$.

We can gain some insight into the behavior of these correlators by comparing them to spin-wave theory with the action

$$S_{\text{edge, spin-wave}}[\phi_1] = \int dy dz \frac{\lambda_1}{2} \left[(\nabla_y \phi_1)^2 + (\nabla_z \phi_1)^2 \right] .$$

This is a good approximation to Eq. (3.13) in the limit of small λ_1 and λ_2, where vortices in the ϕ_1 variables (which are equivalent to $\vec{Q}_1$ variables) have a very large energy cost to cross the edge. Indeed, in the limit $\lambda_2 \to 0$ one can see that no vortices $\vec{Q}_1$ are crossing the plane where we measure the correlators, and the spin wave theory is appropriate on this plane. The spin-wave theory predicts the algebraic decay exponent of χ_1 to be

$$b_{\chi_1} \approx 1/(2\pi\lambda_1). \tag{3.21}$$

We expect our data to be consistent with this prediction at small λ_1 and λ_2. At larger λ_2 there will be more vortices Q_1 in our system, which increases the decay exponent of the ϕ_1 correlations, while at larger λ_1 in the bulk the correlations can also develop through the bulk terms. In our numerics taken at $\lambda_1 = \lambda_2$, the first effect dominates and the extracted power law exponent is larger than this spin wave prediction.

To detect gapless modes in the $\vec{J}_2$ variables, we measure the correlator:

$$\chi_2(R-R') \equiv \langle e^{ic\tilde{\phi}_2(R)} e^{-ic\tilde{\phi}_2(R')} \rangle. \tag{3.22}$$

The c in Eq. (3.22) is the same as the one defining the quantum Hall state with $\sigma_{xy}^{12} = 2c/d$. As discussed after Eq. (3.16), in the limit where λ_2 is very small we can change a ϕ_2 variable by $2\pi/c$ while also redefining $\vec{p}_2$ and $\vec{J}_1$ variables and incur only a very small energy cost. Therefore for $c > 1$ if we only measured correlators of $e^{i\phi_2(R)}$ we would not see any order since each ϕ_2 variable will be randomly distributed in one of c orientations, and it is the fluctuations around these orientations that will be power-law correlated. Thus, our direct analysis suggests that for $c > 1$ only c-tupled "molecular" states of type-2 bosons can propagate along the edge.

The χ_2 data can be compared to the following "spin-wave" reasoning. Consider for simplicity edges of the $\sigma_{xy}^{12} = 2$ quantum Hall state and reformulation Eq. (3.18). In this case we can easily see the mechanism which forbids vortices on the edge. In the limit of small λ_1, we expect the currents of $\vec{M}$ to be zero everywhere away from the edges, while they satisfy a conservation law on the edge, $\sum_{\mu=y,z} \nabla_\mu M_\mu = 0$. The action on the edge at $X = X_R$ has the structure

$$S_{\text{edge}}[\phi_2, M_y, M_z] = \frac{1}{2\lambda_1 (2\pi)^2} \sum_{R \in \text{edge}; \mu=y,z} [\nabla_\mu \phi_2 - 2\pi P_\mu]^2,$$

with $P_y \equiv M_z$ and $P_z \equiv -M_y$. For such a 2D XY model, the curl of the field (P_y, P_z) is the vorticity, but this curl is precisely $\sum_{\mu=y,z} \nabla_\mu M_\mu$, which is zero. Thus, in this limit, the action is like an XY model with completely prohibited vortices. Away from this limit, we expect the vortices to still be effectively prohibited, and the spin wave treatment is now justified. From examining Eqs. (3.18) and (3.16), we see that at small λ_1 and λ_2 such spin-wave theory predicts the exponent

$$b_{\chi_2} \approx 2\pi\lambda_1 d^2 \tag{3.23}$$

for the algebraic decay of $\chi_2(R-R')$.

We now present results for χ_1 and χ_2. In all the results in this section, we show data on the line in the parameter space where $\lambda_1 = \lambda_2 = \lambda$. All data was taken with a system size of $L = 20$. We know that we are in the quantum Hall phase when λ is small, because it is here that the $\vec{G}$ variables are gapped. In Sec. 3.5 we will present the phase diagrams of these models and will see that, for all $\eta \neq 0$, the system is in this quantum Hall state for $\lambda d^2 \lesssim 0.33$ (the precise value depends on c and d, but not very sensitively), while for $\eta = 0$ the system will be in a trivial insulator state in this parameter regime. Therefore at small λ the edge we are studying is between a trivial insulator and a quantum Hall insulator. We have measured the correlation functions for $\lambda d^2 = 0.07, 0.1, 0.15, 0.2, 0.25$ and seen algebraic decay. [We quote λd^2 because at larger d it takes smaller values of λ for the $\mathcal{G}$ variables to become gapped, as can be seen in Eq. (3.5).] We plot χ on a

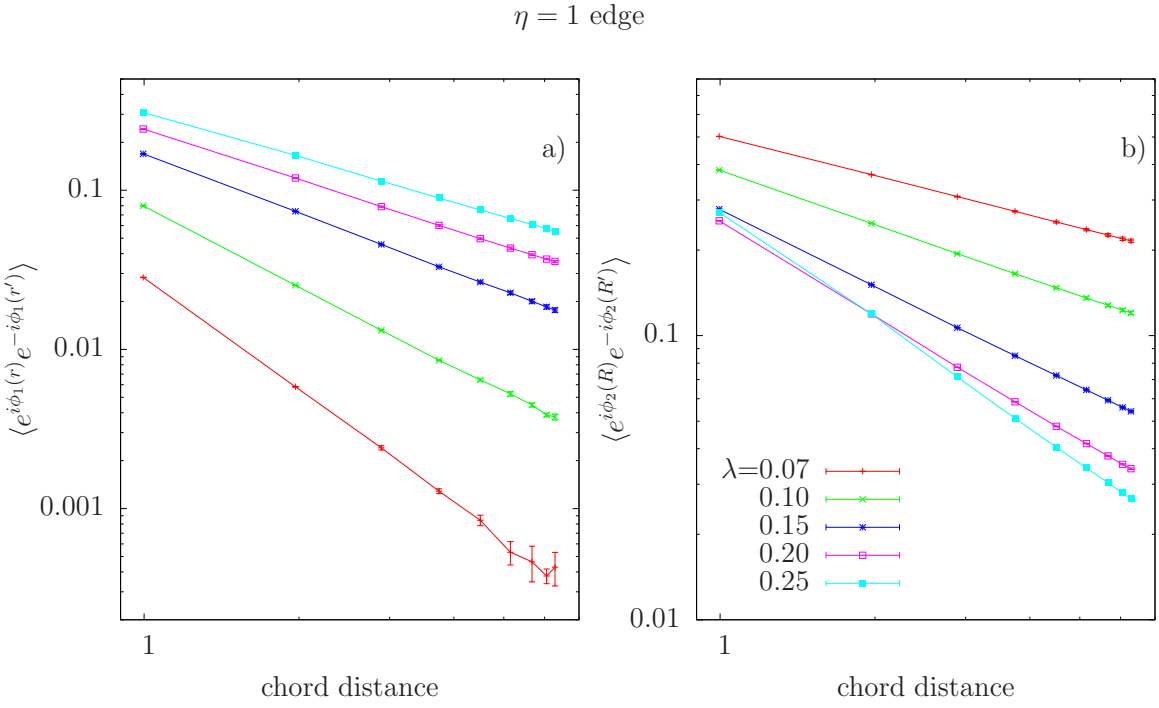

Figure 3.2: Correlation functions a) χ_1 and b) χ_2, plotted against the chord distance of Eq. (3.24), on a log-log scale, for $\eta = 1$ edge. Error bars come from comparing runs with different initial conditions. The straight lines imply that we have algebraic decay in the correlation functions and therefore the edge is gapless. The slope of these lines varies with λ, and the extracted exponents are shown in Fig. 3.4.

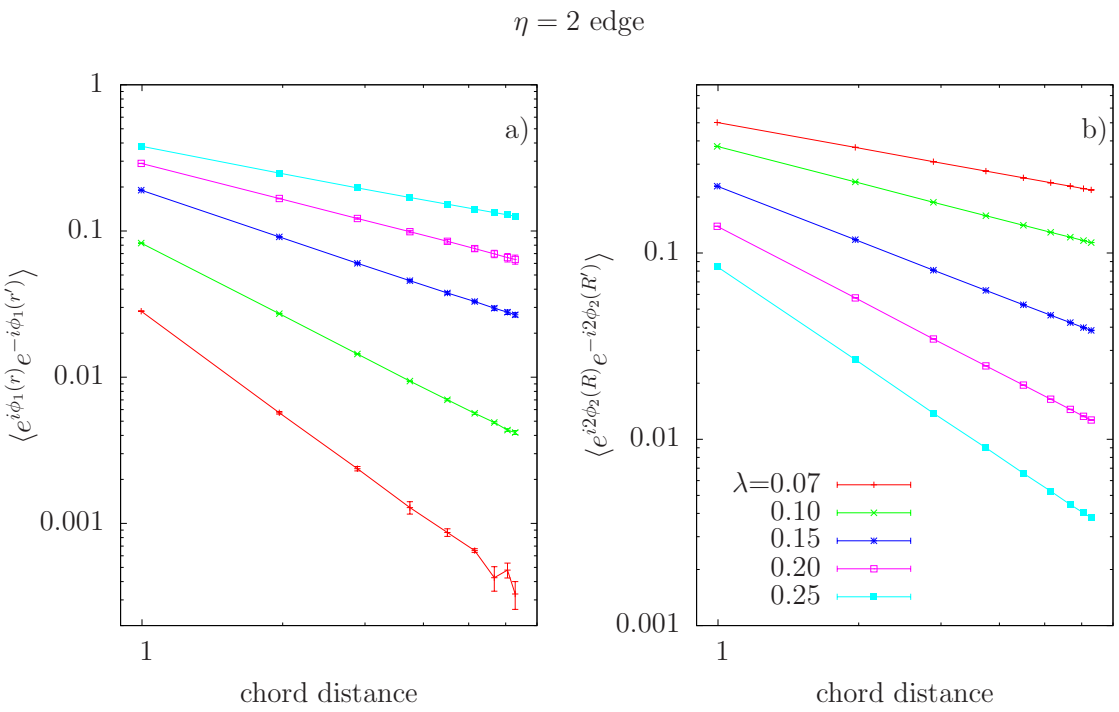

Figure 3.3: Same as Fig. 3.2, but for $\eta = 2$ edge. Once again, we see evidence for gapless modes. Note that in b) we measure pair-boson $e^{i2\phi_2}$ correlators on the edge, while single-boson $e^{i\phi_2}$ correlators decay exponentially.

log-log plot, so that if it decays algebraically we will see straight lines. Due to the finite size of the system the lines will not be perfectly straight. We compensate for this by replacing $R - R'$ with the 'chord distance' $D_{RR'}$:

$$D_{RR'} = \frac{L}{\pi} \sin\left[\frac{\pi|R - R'|}{L}\right], \tag{3.24}$$

which is often used in studies of (1+1)D systems. With this substitution the plots should exhibit straight lines, and we found that this works very well in the present cases.

In Fig. 3.2 we show χ_1 and χ_2 for the case where $\eta = 1$. The plot contains straight lines, which means that we do have algebraic decay. We can see that the slope of these lines, and therefore the decay exponents, depend on λ. In taking the data for this plot we used the reformulation given by Eq. (3.18) for the χ_2 measurements. This reformulation is more efficient than the one in Eq. (3.16), and allows us to obtain better statistics. However, we have compared the results of the two reformulations and found them to be consistent. Note that as λ is increased, χ_1 decays more slowly while χ_2 decays more quickly. This behavior suggests that ϕ_1 and ϕ_2 behave as conjugate variables.

Figure 3.3 shows the same measurements for $\eta = 2$. Again we see evidence of algebraic decay with exponents which depend on λ. As above, we used the reformulation in Eq. (3.18) for the χ_2 measurements. Note that for this data it is important to measure correlators of $\exp(i2\phi_2)$, as defined in Eq. (3.22). As expected, we found that single-boson correlators decay exponentially in this case, and only pair-boson correlators show

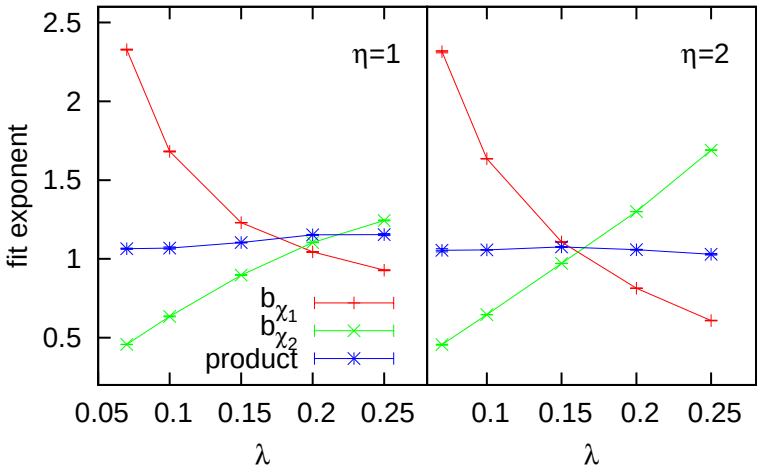

Figure 3.4: The exponents of the algebraic decay for $\eta = 1$ and $\eta = 2$, extracted using the fitting function in Eq. (3.25). We see that the b_{χ_1} exponent decreases with increasing λ while the b_{χ_2} exponent increases. The product of these exponents is also shown.

algebraic decay.

From the above data we can extract the exponents of the algebraic decay. We fit the above data to the function

$$\chi_1(r - r') = \frac{A}{\left[\frac{L}{\pi}\sin\left(\frac{\pi|r-r'|}{L}\right)\right]^{b_{\chi_1}}}, \tag{3.25}$$

with A and b_{χ_1} parameters of the fit. We analyzed χ_2 similarly. Figure 3.4 shows plots of these exponents for $\eta = 1$ and $\eta = 2$. The decay exponents for both χ_1 and χ_2 are slightly above the spin-wave prediction at small λ (e.g., within 10% for $\lambda = 0.07$). At large λ the fitted exponents differ significantly from the naive spin-wave predictions, though within an order of magnitude. In Ref.[49] we discuss a phenomenological understanding of the edge which predicts that the product of these exponents in the integer quantum Hall case should be equal to 1. We can see from Fig. 3.4 that the products we measured are approximately equal to one.

Figure 3.5 shows χ_2 for $\eta = 1/3$. The existence of straight lines in this plot implies that we have gapless modes in a fractional quantum Hall system. We acquired this data using the reformulation in Eq. (3.16). We were unable to measure χ_1 for the fractional cases because the decay exponents were too large. Recall that in order to have gapped $\mathcal{G}$ variables we need $\lambda d^2 \lesssim 0.33$; for $d^2 = 9$ this leads to a small λ, and the spin-wave theory estimate Eq. (3.21) tells us that this leads to large exponents for χ_1. The presence of the factor d^2 in the product $b_{\chi_1} b_{\chi_2} \approx d^2$, which we obtained here by the direct analysis, is an indirect manifestation of the fractionalization when parameter $d > 1$. Indeed, in Ref.'[49] we use a phenomenological model of the edge and the fractionalization of the particles to show that the product of these exponents should be equal to d^2, while if there is no fractionalization the product will be equal to 1. In our lattice model of the edge and the specific parameterizations of the potentials, we have found that the values of b_{χ_2} are numerically similar to those in the integer case, but the b_{χ_1} values are much larger. This implies that the product of the exponents is

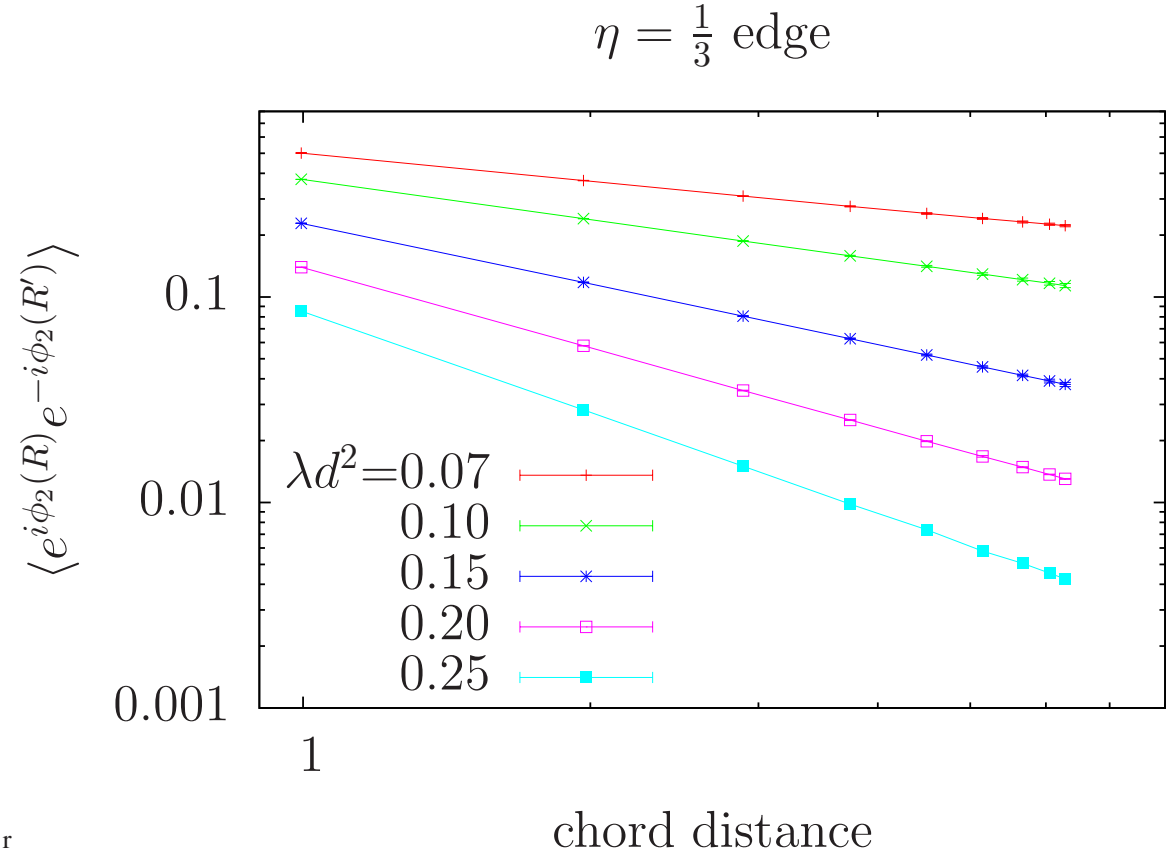

Figure 3.5: χ_2 correlation function for $\eta = 1/3$ edge, where $c = 1$ and $d = 3$. The straight lines indicate algebraic decay for this fractional case. We were unable to obtain data for χ_1 because it decayed too quickly.

greater than 1, providing indirect evidence for fractionalization.

3.5 Phase diagrams

In previous works[45, 47, 48] we have studied actions similar to that in Eq. (3.1). However, in those works we considered only the case where $\theta(k)$ was equal to a rational constant multiplied by 2π. These are precisely the actions of the $\vec{G}$ variables which appeared in Eq. (3.8), and from now on we will refer to them as "statistical" actions. The statistical variables are quasiparticles in the quantum Hall phases. In Refs. [45, 47] we did not attempt to connect the statistical actions to a physical system, and instead focused on their phase diagrams. Therefore we did not specify the "vacuum" of physical variables as it does not affect the dynamics of the phase transitions, but it is this vacuum which carries the quantized σ_{xy}^{12} as can be seen from Eq. (3.8). Furthermore, we can now also specify physical charges of the quasiparticles.

If we start with a statistical action with rational θ_G, we can invert the change of variables procedure in Sec. (3.2) with the correct choice of a, b, c, d to get an action with $\theta(k) \sim k^2$, as in Eq. (4.1), which we will from now on call the "physical" action. This is how we obtained the specific potentials in Eqs. (3.3) and

(3.4). We know from the previous works the phase diagrams of the statistical actions in terms of the variables $\vec{G}$. We can use the change of variables in this work to describe these phase diagrams in terms of the physical variables $\vec{J}$.

Recall that the specific potentials can be classified by the coefficients c and d. When changing from the physical variables $\vec{J}$ to the statistical variables $\vec{G}$, we need these coefficients as well as a and b, but these coefficients are not independent since they must satisfy $ad - bc = 1$. In particular, if we have one solution a_0, b_0 then this constraint tells us that

$$\begin{aligned} a &= a_0 + mc, \\ b &= b_0 + md, \end{aligned} \tag{3.26}$$

are also solutions if m is an integer. The statistical actions can be classified by their statistical angle, which for our specific potential choices is given by $\theta_G = 2\pi b/d$. Therefore each physical action can be related to multiple statistical actions by our change of variables. However, these statistical actions differ only in that θ_G can be different by an integer multiple of 2π. Such a shift will have no effect on the partition sum in the $\vec{G}$ variables. Therefore all of the statistical actions which can be related to a given physical action have the same behavior.

We can also see that multiple physical actions whose ratio c/d differ by an integer can also be mapped to the same statistical action: that is, the actions in terms of G particles are essentially the same except for the "background" quantum Hall conductivity σ_{xy}^{12} changing by an even integer. These physical actions are related to each other by adding an "integer quantum Hall layer" to the system without changing the properties of the fractionalized excitations.

To begin the discussion of the broader phase diagrams of our models, it is useful to consider also the action in terms of the dual variables $\vec{Q}_1$, $\vec{Q}_2$:

$$S = \frac{1}{2}\sum_k \frac{(2\pi)^2}{|\vec{f}_k|^2}\left[\lambda_1|\vec{Q}_1(k)|^2 + \lambda_2|\vec{Q}_2(k)|^2\right] + i\sum_k \frac{2\pi c}{d}\vec{Q}_1(-k)\cdot\vec{a}_{Q2}(k), \tag{3.27}$$

where $\vec{Q}_2 = \vec{\nabla}\times\vec{a}_{Q2}$. This action comes from dualizing the J_1, J_2 variables with the specific potentials in Eqs. (3.3) and (3.4). [Eq. (15) in Ref. [47] contains this action with general potentials.] This action can also be obtained by applying the modular transformation $(0,-1,1,0)$ to the original action. Note that the d in Eq. (3.27) corresponds to the parameter in Eqs. (3.3)-(3.4), and is not related to the modular transformation used to obtain this phase. The Q variables are vortices with the usual long-range intra-species interactions, $v_Q(k) \sim 1/k^2$ in momentum space, and we see that these vortices are gapped for large λ_1 and λ_2. The statistical angle in the third term of Eq. (3.27) is a rational number. However, this rational number is unique to the specific choices we made in Eqs. (3.3)-(3.4), and small short-range modifications of the model can lead to a different statistical angle for the $\vec{Q}$ variables. This is unlike the rational $\theta_{\vec{G}}$ in the quantum Hall insulators

which is robust to short-range modifications of the potentials. The difference comes from the qualitative difference when applying Eq. (2.32) to generic short-ranged $v(k) \sim \text{const}$ and $\theta(k) \sim k^2$ in the cases $d = 0$ (duality to only vortices) and $d \neq 0$ (more general modular transformation).

3.5.1 Models with $c/d = n$, $\sigma_{xy}^{12} = 2n$

We now turn to detailed descriptions of the phase diagrams. First we discuss the case where the conductivity in the quantum Hall phase is quantized as an even integer. In this case we start with a physical action with the potentials Eqs. (3.3)-(3.4) with parameters $c = n$, $d = 1$ for n an integer. We can get a statistical action by applying the modular transformation $(1, 0, n, 1)$, and this gives a statistical action with $\theta_{\vec{G}} = 0$ and a background Hall conductivity of $\sigma_{xy}^{12} = 2n$. Therefore in the statistical action we have a system of two uncoupled loops, which is a system that is well understood.[70, 61] In this system when $\lambda_i \lesssim 0.3325$, the variables $\vec{G}_i$ are gapped, and when λ_i is greater than this value the $\vec{G}_i$ are condensed. All phase transitions are second-order XY transitions. Figure 3.6 shows this phase diagram. Since we know the behavior of the $\vec{G}$ variables everywhere in the phase diagram, we can now deduce the behavior of the physical $\vec{J}$ variables. In the lower left corner phase we have seen that the $\vec{J}$ variables are in a quantum Hall phase.

To understand the rest of the phase diagram we must make more precise our earlier definitions of what makes a variable "gapped" or "condensed". When a variable is in a phase in which it is gapped, the energy cost for having large loops of that variable becomes arbitrarily large and only small loops are present. When a variable is condensed the energy cost for forming loops is small. A variable is condensed if and only if the variable dual to it is gapped. In some phases a variable will be neither condensed nor gapped in the above sense; instead the variable can be part of a composite object which is condensed or gapped. This is the situation for the J variables in the quantum Hall phases. We bring this out to indicate that there are more cases than just given by binary choice of J_i variable being gapped or condensed. In all cases, the precise meaning is provided by finding appropriate transformation that leads to a description in terms of gapped particles only.

With this in mind, we can interpret the rest of the phase diagram. We begin with the phase in the upper-right corner, where λ_1 and λ_2 are large. We can see that in this phase the potentials seen by the $\vec{Q}$ variables in Eq. (3.27) become arbitrarily large, so both of these species of variable are gapped. Therefore both species of $\vec{J}$ variable are condensed and this phase is a superfluid. The conductivities σ_{xx}^{11} and σ_{xx}^{22} diverge in this phase, while the Hall conductivity σ_{xy}^{12} is non-universal.

We now study the off-diagonal phases in Fig. 3.6. For simplicity we discuss the phase in the lower right corner where λ_1 is large but λ_2 is small (in fact λ_1 can become arbitrarily large in this phase). The upper left corner is similar to the lower right with the indices interchanged. From Eq. (3.3) we can see that when $\lambda_1 \to \infty$, $v_2(k) \to \frac{1}{\lambda_2}$. Since λ_2 is small in this phase, $v_2(k)$ can become arbitrarily large and the $\vec{J}_2$ variables must be gapped. In addition, we can see from Eq. (3.10) that the $\vec{Q}_1$ variables see an arbitrarily large potential and are therefore gapped, so the $\vec{J}_1$ variables are condensed. From the above results, we can conclude that this phase is a trivial insulator in the $\vec{J}_2$ variables and a superfluid in the $\vec{J}_1$ variables.

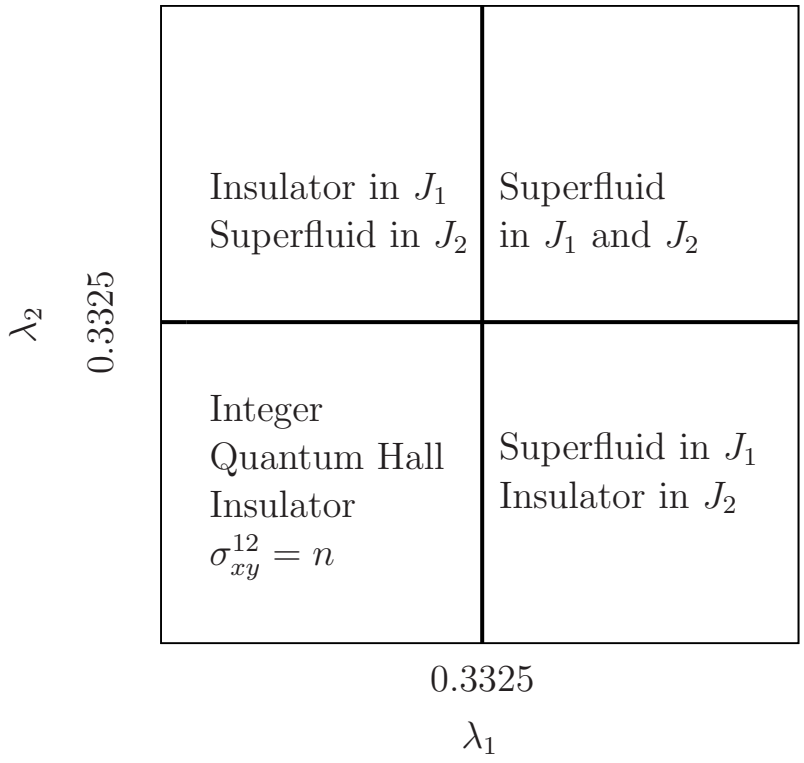

Figure 3.6: The phase diagram for the model with the potentials of Eqs. (3.3)-(3.4) and $c = n$, $d = 1$. In the lower left phase the $\vec{G}$ variables are gapped and we have the integer quantum Hall phase with $\sigma_{xy}^{12} = 2n$. In the upper right phase the $\vec{J}$ variables are condensed, and we have a superfluid. In the off-diagonal phases, one of the J variables is condensed and the other is gapped.

Finally, we note that the specific model, Eqs. (3.3)-(3.4), with $c = n, d = 1$ does not realize the trivial insulator phase with both J_1 and J_2 gapped. Of course, we can obtain such a phase by different modifications of the potentials, e.g., by adding large repulsive pieces to both v_1 and v_2, and it would be interesting to study such models in the future.

3.5.2 Models with $d \neq 1$

In Ref. [47] we studied a statistical action with $\theta_{\mathcal{G}} = 2\pi/3$. The phase diagram for this model is shown in Fig. 4.13. In the lower left corner the $\vec{G}$ variables are gapped and this is the fractional quantum Hall phase. Any physical action with $d = 3$ and $c = 1 + 3m$ (for m an integer) can be related to this statistical action by our modular transformation; here we will discuss the case where $c = 1$. In this case the change of variables needed to get from the $\vec{J}$ variables to the $\vec{G}$ variables is $(0, -1, 1, 3)$. The fractional quantum Hall phase will have $\sigma_{xy}^{12} = 2 \cdot \frac{1}{3}$ and excitations carrying respective fractional charges of $1/3$ and mutual statistics of $2\pi/3$.

We know from Ref. [47] that in the middle phase the variables dual to the $\vec{G}$ variables are gapped. We can also compute the action for the variables dual to the $\vec{G}$ variables and see that it has the same potential as the action for the $\vec{J}$ variables. The two actions also have values of $\theta(k)$ which differ only by an integer multiple of 2π. Such difference will translate to factors $e^{2\pi i}$ in the partition sum and therefore will not contribute. Therefore if the variables dual to the $\vec{G}$ variables are gapped then the $\vec{J}$ variables should also be gapped. Therefore this middle phase is a trivial insulator in the $\vec{J}$ variables. This can be confirmed by measuring the conductivity numerically in this phase.

In the upper right corner phase we can see from Eq. (3.27) that the Q variables are gapped, and therefore the $\vec{J}$ variables are condensed and this phase is a superfluid. In our previous work[47] we found that transition between the trivial insulator and the superfluid is a pair of XY transitions, while we found more complicated behavior at the fractional quantum Hall-trivial insulator transition.

The structure described in the previous paragraph holds for any set of physical variables which can be mapped to a statistical action with $\theta_G = 2\pi/m$, with m an integer. One exception is $m = 2$, where our specific model with $c = 1, d = 2$ has an additional symmetry in the G variables which prevents the existence of the middle phase, cf. Fig. 1 in Ref. [45]. This is discussed in detail in Refs. [45, 48], while here we note that generic perturbations to our original model will break this symmetry and open a sliver of the trivial phase in the phase diagram.

Finally, for more complicated fractions c/d, our model will have multiple phases in the middle of the phase diagram, resembling hierarchy of phases that we found in $U(1) \times U(1)$ loop models with marginally long-ranged interactions and modular invariance.[48] We expect that the "middle" phase at the largest λ is a trivial insulator, while the other phases are various quantum Hall states. For example, in our model Eqs. (3.3)-(3.4) with $c = 2, d = 5$, we found the following sequence of phases upon increasing $\lambda_1 = \lambda_2$: fractional quantum Hall insulators $\sigma_{xy}^{12} = 2 \cdot 2/5$ and $\sigma_{xy}^{12} = 2 \cdot 1/2$, trivial insulator $\sigma_{xy}^{12} = 0$, and superfluid. It would be interesting to explore such phase diagrams and phase transitions in more detail in the future.

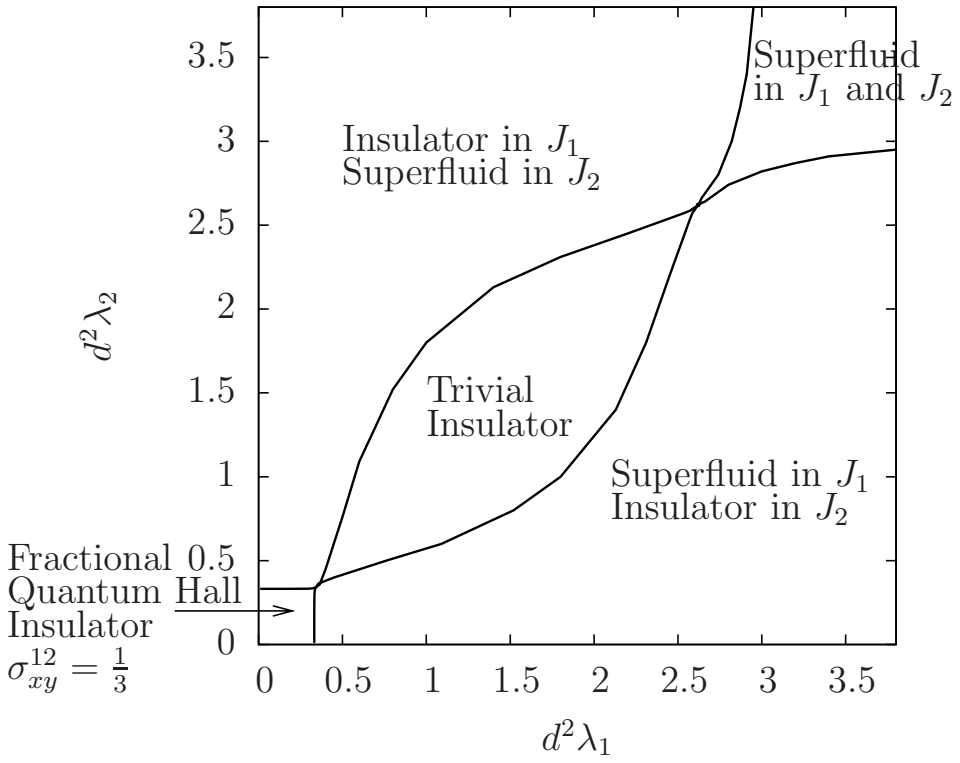

Figure 3.7: The phase diagram for the model with $c = 1, d = 3$. In the lower left phase the $\vec{G}$ variables are gapped and we have a fractional quantum Hall phase with $\sigma_{xy}^{12} = 2 \cdot \frac{1}{3}$. In the upper right phase the $\vec{J}$ variables are condensed, which implies a superfluid. In the middle phase the $\vec{J}$ variables are gapped and we have a trivial insulator. This figure is reproduced from Ref. [47], but the phases have been re-interpreted in terms of the physical variables discussed in this work.

3.6 Hamiltonian formulation

Throughout this chapter, we have worked with the Euclidean action formulation of the model. The action for the physical currents is local in (2+1)D space-time and is very convenient for analysis. However, it is natural to ask whether this action can be realized as a path integral of a local Hamiltonian in 2d.[71] Below we provide an example of such a Hamiltonian.

We first specify the physical Hilbert space. Our degrees of freedom reside on two inter-penetrating square lattices as shown in Fig. 3.8. We place quantum U(1) rotors on sites $\mathbf{r}$ of the first square lattice. The rotors are described by 2π-periodic phase variables $\hat{\phi}_1(\mathbf{r})$ and conjugate integer number variables $\hat{n}_1(\mathbf{r})$, with commutation relations $[\hat{\phi}_1(\mathbf{r}), \hat{n}_1(\mathbf{r}')] = i\delta_{\mathbf{r}\mathbf{r}'}$. We place another set of U(1) rotors, described by $\hat{\phi}_2(\mathbf{R})$ and $\hat{n}_2(\mathbf{R})$, on sites $\mathbf{R}$ of the second (dual) square lattice. Finally, we place harmonic oscillators, described by $\hat{\chi}_\ell$ and $\hat{\pi}_\ell$, on centers of links of the first square lattice, which are also centers of links of the second square lattice, e.g., $\ell =< \mathbf{r}, \mathbf{r}+\hat{\mathbf{x}} >=< \mathbf{R}, \mathbf{R}+\hat{\mathbf{y}} >$ as illustrated in Fig. 3.8. Here $\hat{\chi}_\ell$ are real-valued coordinate variables and $\hat{\pi}_\ell$ are conjugate momentum variables, $[\hat{\chi}_\ell, \hat{\pi}_{\ell'}] = i\delta_{\ell\ell'}$. Looking ahead, we will use a path integral containing both χ_ℓ and π_ℓ. We will view the coordinate variables as fields on the links of the first lattice,

$$\hat{\alpha}_{1j}(\mathbf{r}) \equiv \hat{\chi}_{\mathbf{r},\mathbf{r}+\hat{\mathbf{j}}} \, , \tag{3.28}$$

$\hat{\mathbf{j}} = \hat{\mathbf{x}}$ or $\hat{\mathbf{y}}$, while we will view the conjugate momentum variables as fields on the links of the second lattice,

$$\hat{\alpha}_{2j}(\mathbf{R}) = \epsilon_{jk}\hat{\pi}_{\mathbf{r},\mathbf{r}+\hat{\mathbf{k}}} \, . \tag{3.29}$$

Here $\epsilon_{xy} = -\epsilon_{yx} = 1$ is the 2d antisymmetric tensor and $< \mathbf{R}, \mathbf{R}+\hat{\mathbf{j}} >$ and $< \mathbf{r}, \mathbf{r}+\hat{\mathbf{k}} >$ are crossing links.[72] Note that in this chapter we adopt the following notation: spatial lattice sites are labeled with bold face, e.g., $\mathbf{r}, \mathbf{R}$. Spatial directions are labeled with Roman letters, e.g., j, k; space-time directions that appear later will be labeled with Greek letters, e.g., μ, ν. Oriented fields residing on spatial links are viewed as spatial vectors and are labeled with bold face, e.g., $\boldsymbol{\alpha}_1, \boldsymbol{\alpha}_2$.

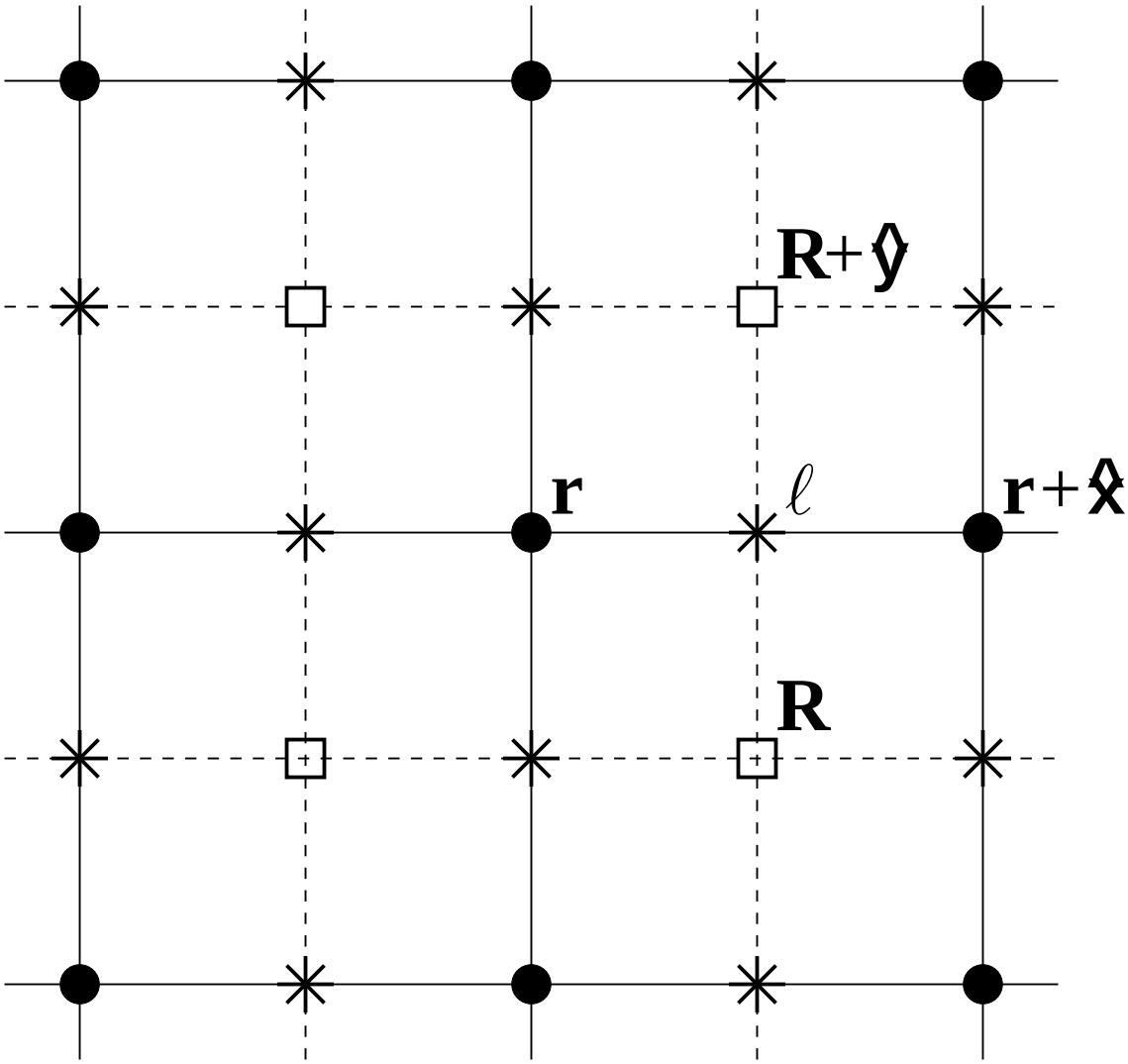

Figure 3.8: Our Hamiltonian Eq. (3.30) has U(1) rotors residing on sites $\mathbf{r}$ of the direct square lattice and U(1) rotors residing on sites $\mathbf{R}$ of the dual lattice. We also have harmonic oscillators residing on crosses ℓ of the links of the two lattices. The first and second U(1) systems are coupled to the oscillator position and momentum variables, respectively, as if the latter were gauge fields.[72] With appropriate choices of parameters and additional charge-flux couplings, we can induce condensations of bound states of charges and vortices leading to the quantum Hall states discussed in the main text.

Our Hamiltonian is:

$$\hat{H} = \hat{H}_{h1} + \hat{H}_{h2} + \hat{H}_{u1} + \hat{H}_{u2} + \hat{H}_{\chi} + \hat{H}_{\pi} \,, \tag{3.30}$$

$$\hat{H}_{h1} = -\sum_{\mathbf{r},j} h_1 \cos[\nabla_j \hat{\phi}_1(\mathbf{r}) - e_1 \hat{\alpha}_{1j}(\mathbf{r})] \,, \tag{3.31}$$

$$\hat{H}_{h2} = -\sum_{\mathbf{R},j} h_2 \cos[\nabla_j \hat{\phi}_2(\mathbf{R}) - e_2 \hat{\alpha}_{2j}(\mathbf{R})] \,, \tag{3.32}$$

$$\hat{H}_{u1} = \frac{1}{2}\sum_{\mathbf{r}} u_1 \left[\hat{n}_1(\mathbf{r}) + g_1(\boldsymbol{\nabla} \wedge \hat{\boldsymbol{\alpha}}_2)(\mathbf{r})\right]^2 \,, \tag{3.33}$$

$$\hat{H}_{u2} = \frac{1}{2}\sum_{\mathbf{R}} u_2 \left[\hat{n}_2(\mathbf{R}) + g_2(\boldsymbol{\nabla} \wedge \hat{\boldsymbol{\alpha}}_1)(\mathbf{R})\right]^2 \,, \tag{3.34}$$

$$\hat{H}_{\chi} = \sum_{\ell} \frac{\kappa\, \hat{\chi}_\ell^2}{2} \,, \quad \hat{H}_{\pi} = \sum_{\ell} \frac{\hat{\pi}_\ell^2}{2m} \,. \tag{3.35}$$

Here we introduced various parameters such as boson hopping amplitudes h_1 and h_2, on-site energies u_1 and u_2, and oscillator parameters κ and m. The hopping terms couple the boson phases and the oscillators as if the latter were "gauge fields." The on-site terms couple the boson numbers and appropriate fluxes of the "gauge fields": e.g., flux $\boldsymbol{\nabla} \wedge \hat{\boldsymbol{\alpha}}_1 \equiv \nabla_x \hat{\alpha}_{1y} - \nabla_y \hat{\alpha}_{1x}$ is associated with a plaquette of the first lattice, or, equivalently a site $\mathbf{R}$ of the dual lattice, and is coupled with the boson number $\hat{n}_2(\mathbf{R})$ on that site. The corresponding parameters e_1, e_2, g_1, g_2 will be chosen later. Here we emphasize that the model is local in the physical variables (i.e., it is not a gauge theory), in the same spirit as Kitaev's toric code model.

We develop imaginary-time path integral [similar to Sec. 2.1.1] by using Trotter decomposition and insertions of unity as follows:

$$\begin{aligned}
e^{-\delta\tau \hat{H}} &\approx e^{-\delta\tau(\hat{H}_{u1}+\hat{H}_{h2}+\hat{H}_{\pi})} e^{-\delta\tau(\hat{H}_{h1}+\hat{H}_{u2}+\hat{H}_{\chi})} \\
&= \mathbb{1}_{\tau+\delta\tau}\, e^{-\delta\tau(\hat{H}_{u1}+\hat{H}_{h2}+\hat{H}_{\pi})}\, \mathbb{1}_{\tau+\frac{\delta\tau}{2}}\, e^{-\delta\tau(\hat{H}_{h1}+\hat{H}_{u2}+\hat{H}_{\chi})}\, \mathbb{1}_{\tau} \,, \\
\mathbb{1}_{\tau} &= \int_{-\pi}^{\pi} D\phi_1(\mathbf{r},\tau) \sum_{n_2(\mathbf{R},\tau)=-\infty}^{\infty} \int_{-\infty}^{\infty} D\chi_\ell(\tau) \\
&\qquad \Big|\phi_1(\mathbf{r},\tau), n_2(\mathbf{R},\tau), \chi_\ell(\tau)\Big\rangle\Big\langle \phi_1(\mathbf{r},\tau), n_2(\mathbf{R},\tau), \chi_\ell(\tau)\Big| \,, \\
\mathbb{1}_{\tau_{\frac{1}{2}}\equiv\tau+\frac{\delta\tau}{2}} &= \sum_{n_1(\mathbf{r},\tau_{\frac{1}{2}})=-\infty}^{\infty} \int_{-\pi}^{\pi} D\phi_2(\mathbf{R},\tau_{\frac{1}{2}}) \int_{-\infty}^{\infty} D\pi_\ell(\tau_{\frac{1}{2}}) \\
&\qquad \Big|n_1(\mathbf{r},\tau_{\frac{1}{2}}), \phi_2(\mathbf{R},\tau_{\frac{1}{2}}), \pi_\ell(\tau_{\frac{1}{2}})\Big\rangle\Big\langle n_1(\mathbf{r},\tau_{\frac{1}{2}}), \phi_2(\mathbf{R},\tau_{\frac{1}{2}}), \pi_\ell(\tau_{\frac{1}{2}})\Big| \,.
\end{aligned}$$

Here we used one set of variables on "integer" time slices $\tau = \text{int} \times \delta\tau$ and conjugate variables on "half-integer" time slices $\tau_{\frac{1}{2}} \equiv \tau + \delta\tau/2$. We also arranged the Trotter decomposition so that the pieces of the Hamiltonian act as c-numbers on the kets of the above insertions of unity. Throughout, we omit normalization constants. The remaining inputs to complete the path integral formulation in the above variables are overlaps

such as

$$\begin{aligned}
\big\langle \chi_\ell(\tau+\delta\tau)\big|\pi_\ell(\tau_{\frac{1}{2}})\big\rangle\big\langle \pi_\ell(\tau_{\frac{1}{2}})\big|\chi_\ell(\tau)\big\rangle &= e^{i\pi_\ell(\tau_{\frac{1}{2}})[\chi_\ell(\tau+\delta\tau)-\chi_\ell(\tau)]} = e^{i\alpha_{2k}\epsilon_{kj}\nabla_\tau\alpha_{1j}}\ , \\
&\qquad \text{for } \ell =< \mathbf{r}, \mathbf{r}+\hat{\mathbf{j}} >, \\
\big\langle \phi_1(\mathbf{r},\tau+\delta\tau)\big|n_1(\mathbf{r},\tau_{\frac{1}{2}})\big\rangle\big\langle n_1(\mathbf{r},\tau_{\frac{1}{2}})\big|\phi_1(\mathbf{r},\tau)\big\rangle &= e^{in_1(\mathbf{r},\tau_{\frac{1}{2}})[\phi_1(\mathbf{r},\tau+\delta\tau)-\phi_1(\mathbf{r},\tau)]} = e^{iJ_{1\tau}\nabla_\tau\phi_1}
\end{aligned} \tag{3.36}$$

and similarly for the second rotor variables.

In the action, we have phase variables $\phi_1(\mathbf{r},\tau)$ residing on sites $(\mathbf{r},\tau)$ of a (2+1)D cubic lattice and $\phi_2(\mathbf{R},\tau_{\frac{1}{2}})$ residing on sites $(\mathbf{R},\tau_{\frac{1}{2}})$ of a dual cubic lattice (in the main text, such space-time points are labeled simply r and R). We also have boson number variables $n_1(\mathbf{r},\tau_{\frac{1}{2}})$ and $n_2(\mathbf{R},\tau)$, which we can view as residing on temporal links of the first and second (dual) cubic lattices, respectively, and write as temporal components of boson three-currents, $J_{1\tau}(\mathbf{r},\tau) \equiv n_1(\mathbf{r},\tau_{\frac{1}{2}})$ and $J_{2\tau}(\mathbf{R},\tau_{\frac{1}{2}}) \equiv n_2(\mathbf{R},\tau+\delta\tau)$. We introduce spatial current components using an approach familiar in treatments of XY models; namely, we interpret the cosine terms in $\hat{H}_{h1}$ and $\hat{H}_{h2}$ as so-called Villain cosines and write, e.g.,

$$e^{\delta\tau h_1\cos[\nabla_j\phi_1(\mathbf{r},\tau)-e_1\alpha_{1j}(\mathbf{r},\tau)]} \to \sum_{J_{1j}(\mathbf{r},\tau)=-\infty}^{\infty} e^{-\frac{J_{1j}^2}{2\delta\tau h_1}+iJ_{1j}[\nabla_j\phi_1-e_1\alpha_{1j}]}\ .$$

We can now integrate over the phase degrees of freedom and obtain current conservation conditions, $\vec{\nabla}\cdot\vec{J}_1 \equiv \sum_{\mu=x,y,\tau}\nabla_\mu J_{1\mu} = 0$, and similarly for the three-current $\vec{J}_2$. Here and below, arrows over symbols denote three-vectors such as $\vec{J}_1 = (J_{1x}, J_{1y}, J_{1\tau})$, while bold symbols refer to spatial parts such as $\boldsymbol{J}_1 = (J_{1x}, J_{1y})$.

We still have the oscillator variables, now labeled $\boldsymbol{\alpha}_1(\mathbf{r},\tau)$ and $\boldsymbol{\alpha}_2(\mathbf{R},\tau_{\frac{1}{2}})$ and residing on spatial links of the first and second cubic lattices. At this point, we could also integrate over these variables and obtain an action in terms of the boson three-currents only. To facilitate the integration and show the connection with the loop models in the main text, we will first write the on-site terms by introducing auxiliary fields labeled $\alpha_{1\tau}$ and $\alpha_{2\tau}$ residing on the temporal links of the first and second cubic lattices respectively, e.g.,

$$\begin{aligned}
& e^{-\frac{\delta\tau u_2}{2}\left[J_{2\tau}(\mathbf{R},\tau_{\frac{1}{2}})+g_2(\boldsymbol{\nabla}\wedge\boldsymbol{\alpha}_1)(\mathbf{R},\tau_{\frac{1}{2}})\right]^2} \\
&= \int_{-\infty}^{\infty} d\alpha_{2\tau}(\mathbf{R},\tau_{\frac{1}{2}}) e^{-\frac{\alpha_{2\tau}^2}{2\delta\tau u_2}-i\alpha_{2\tau}[J_{2\tau}+g_2(\boldsymbol{\nabla}\wedge\boldsymbol{\alpha}_1)]}\ .
\end{aligned}$$

For brevity, we often omit the lattice coordinates on the fields and imply precise geometric relation between objects on different lattices: e.g., an oriented plaquette on one lattice is also associated with a unique oriented bond on the other lattice crossing this plaquette.

Putting everything together, the final action takes the form

$$\begin{aligned} S[\vec{\alpha}_1, \vec{\alpha}_2, \vec{J}_1, \vec{J}_2] &= \sum \left[\frac{\delta\tau\kappa\, \boldsymbol{\alpha}_1^2}{2} + \frac{\alpha_{1\tau}^2}{2\delta\tau u_1} + \frac{\delta\tau \boldsymbol{\alpha}_2^2}{2m} + \frac{\alpha_{2\tau}^2}{2\delta\tau u_2} \right] + \sum \left[\frac{\boldsymbol{J}_1^2}{2\delta\tau h_1} + \frac{\boldsymbol{J}_2^2}{2\delta\tau h_2} \right] \\ &+ i \sum \left[(\nabla_\tau \boldsymbol{\alpha}_1) \wedge \boldsymbol{\alpha}_2 + g_1 \alpha_{1\tau} (\boldsymbol{\nabla} \wedge \boldsymbol{\alpha}_2) + g_2 \alpha_{2\tau} (\boldsymbol{\nabla} \wedge \boldsymbol{\alpha}_1) \right] \\ &+ i \sum \left[e_1 \boldsymbol{J}_1 \cdot \boldsymbol{\alpha}_1 + J_{1\tau} \alpha_{1\tau} + e_2 \boldsymbol{J}_2 \cdot \boldsymbol{\alpha}_2 + J_{2\tau} \alpha_{2\tau} \right]. \end{aligned}$$

Here the wedge operator is $\boldsymbol{v}_1 \wedge \boldsymbol{v}_2 \equiv \sum_{j,k} \epsilon_{jk} v_{1j} v_{2k} = v_{1x} v_{2y} - v_{1y} v_{2x}$. By rescaling $\boldsymbol{\alpha}_1 = \boldsymbol{\alpha}_1'/e_1$ and similarly for $\boldsymbol{\alpha}_2$, and choosing, e.g., $e_1 = e_2 = 1/g_1 = 1/g_2 = \sqrt{2\pi d/c}$, we obtain essentially the same action as in Eq. (3.11). The only difference is that there are additional local current interactions containing h_1 and h_2 couplings, and to make the actions identical we only need to take h_1 and h_2 large. In particular, the model is in the "c/d" Quantum Hall phase for sufficiently small κ and sufficiently large m and large u_1, u_2. Thus, we have provided a Hamiltonian realization for our Quantum Hall phases.

We can also carry out this derivation when the parameters $h_{1,2}, u_{1,2}, \kappa, m, e_{1,2}, g_{1,2}$ vary in space; in particular, we can study a boundary between Quantum Hall and trivial insulators. Note that there is significant freedom in how to vary the parameters to achieve different phases even within the specific model. For example, we can obtain a trivial insulator by taking $e_{1,2}$ and $g_{1,2}$ to be zero while also taking the hopping amplitudes $h_{1,2}$ to be small and on-site potentials $u_{1,2}$ large. Alternatively, we can take $e_{1,2}$ to be very large while $g_{1,2} \to 0$ and can reach the trivial insulator this way even when the bare hopping amplitudes $h_{1,2}$ are large (in this case, the boson propagation is scrambled by strong phase coupling to the oscillators). The latter route is closer to the model we used in the main text when discussing a boundary between Quantum Hall and trivial insulators. Such a boundary model in the present Hamiltonian approach will in general differ from that in the main text. Indeed, in the Chern-Simons-like piece for the rescaled $\vec{\alpha}_{1,2}'$ variables,

$$i \sum [\frac{(\nabla_\tau \boldsymbol{\alpha}_1') \wedge \boldsymbol{\alpha}_2'}{e_1 e_2} + g_1 \alpha_{1\tau} (\boldsymbol{\nabla} \wedge \frac{\boldsymbol{\alpha}_2'}{e_2}) + g_2 \alpha_{2\tau} (\boldsymbol{\nabla} \wedge \frac{\boldsymbol{\alpha}_1'}{e_1})] \,,$$

the spatially varying e and g couplings can appear non-trivially under spatial derivatives, and the action in general cannot be cast in the form of Eq. (3.10). However, we can find a pattern of couplings that will reproduce our boundary model in the main text: If we take $1/e_a = g_a = \sqrt{c/(2\pi d)}$ for $x \in [x_{aL}, x_{aR}]$ and $1/e_a = g_a = 0$ otherwise, and take the region $[x_{2L}, x_{2R}]$ to be inside the region $[x_{1L}, x_{1R}]$, we eliminate terms with non-desired derivatives of the couplings and can recast the Chern-Simons-like piece for the rescaled $\vec{\alpha}_{1,2}'$ variables into the form of Eq. (3.10) with $\eta(R) = c/d$ inside $[x_{2L}, x_{2R}]$ and zero outside. Thus, we have also provided a Hamiltonian realization of the boundary model used in the main text.

While we universally expect gapless boson correlations on the boundary, detailed aspects can be different for different realizations. In this paper, we have focused on the crude demonstration of the gaplessness for the specific boundary model in the main text. In future work, it would be interesting to examine different realizations and systematically explore all aspects of possible edge theories.

3.7 Discussion

In this chapter we have used the techniques of Chapter 2 to present physical $U(1) \times U(1)$ bosonic models which realize insulating phases with a quantized Hall conductivity that can take both integer and fractional values. In the fractional case, we also have excitations carrying fractionalized charges and non-trivial mutual statistics. We have shown how to study these models in Monte Carlo and found evidence for gapless edge modes. We have also presented broader phase diagrams of our models.

The action in Eq. (4.1) can be derived from a local Hamiltonian, as shown in Section 3.6. When we included an edge in our action by varying $\eta(R)$ in Eq. (3.10), we do not know precisely how that edge is realized in the physical Hamiltonian. It is possible that this method of including an edge changes the Hamiltonian near the edge in such a way as to create gapless modes which are not due to the bulk topological state of the system on one side. For example, a local strengthening of boson hopping along the edge could lead to gapless (1+1)D Luttinger liquid modes. Irrespective of the microscopic details, the edges that we studied do produce the quantum Hall σ_{xy}^{12}, so at least some of the observed properties are due to the topology of the bulk phases. Including edges using different methods, and confirming that the observed gapless properties are not artifacts of the method used in this work, is a possible subject of future research. There is, however, some evidence that our gapless modes are due to topological effects. In the $\eta = 1/3$ case we expect topological gapless modes to exist on the edge in the bottom left corner of the phase diagram, but not in the middle phase. This is precisely the behavior which we have observed, with gapless modes disappearing beyond $\lambda d^2 = 0.35$. In addition, we have observed gaplessness in both ϕ_1 and ϕ_2 variables (for the integer case where both signals could be detected), which is what we expect if the gapless modes are topological.

Our work allows the numerical study of interacting topological insulator phases, and therefore may be able to address many questions about such phases. For example, we could investigate the effect of disorder and other perturbations on the gapless edge states.

One immediate application is the study of transitions between different topological phases. We first observed unusual behavior at the fractional quantum Hall-trivial insulator transition in Ref. [47]. In a forthcoming work with undergraduate student Jong Lee, we will expand this study, as well as look at transitions between different fractional quantum Hall states.

Another possibility is to look at transitions between integer quantum Hall states and trivial insulators, which are of recent interest.[64, 65] Using the modular transformations developed in Section 2.2 we can show that the model of Eq. 3.1 with short-ranged interactions and $\theta = \pi$ contains precisely this transition, though a study of this transition in Ref. [45] revealed it to be first order. It might, however, be possible to modify the model slightly in order to realize a continuous transition.

More generally, it would be interesting to see what other interacting topological phases can allow unbiased numerical studies. Furthermore, since ideas in the present work do not rely on Chern-Simons construction specific to (2+1)D, they can be readily extended to studies of such phases in higher dimensions.[73, 74, 75, 76]

In the next chapter we will perform precisely this extension, and study a $(3+1)$ dimensional system of a bosonic topological insulator.

Chapter 4

Numerical Study of Bosonic Topological Insulator and Fractional Topological Insulator

4.1 Introduction

Among all the topological phases studied in recent years, the topological insulator (TI) is one of the most prominent.[8, 9] The TI is a three-dimensional phase of free fermions. Though it is insulating in the bulk, its topological behavior can be deduced from its unusual surface properties, in particular the odd number of Dirac cones it has on its surface. The topological insulator is an example of a symmetry-protected topological phase (SPT). Like all SPT's, it has short-ranged entanglement, which implies that it has only conventional excitations in the bulk and a unique ground state on any closed manifold. This is in contrast to intrinsically topologically ordered states like the fractional quantum Hall states. The relevant symmetries for the topological insulator are charge conservation and time-reversal, and if either of these symmetries is violated, the phase loses its topological properties.

One obvious extension of research into topological insulators is to consider the effects of interactions on their properties. This is, however, a difficult task. Many of the methods used to study TI's involve the properties of their band structure, and these methods obviously do not apply if interactions are strong. As an introduction to this difficult problem, one can try to study an analog of the topological insulator, constructed of interacting *bosons* instead of fermions. In bosonic systems we know that the non-interacting case would be a condensate, so we can be sure that the topological behavior is due to the interactions. In addition, certain theoretical techniques, like the Monte Carlo studies employed in this paper, work mainly for bosonic systems.

Vishwanath and Senthil in an inspirational paper[28] found effective field theories which can describe both the bulk and the surface of a three-dimensional "bosonic topological insulator" with charge conservation and time-reversal symmetry. They found exotic behavior on the surface which can be used to assert the topological behavior in the bulk.

In particular, Vishwanath and Senthil found three kinds of exotic phases on the surface of the bosonic TI. These surface phases cannot exist in a purely two-dimensional system, and their existence on the surface of a three-dimensional system shows that the system is topological. The first kind of phase is a superfluid, which spontaneously breaks charge conservation symmetry. There are actually several different types of superfluids which can exist on the surface. The gapped vortex excitations in these superfluids have properties which cannot exist in a purely two-dimensional system. Phase transitions between the different superfluids are predicted to be deconfined critical points. Another kind of surface phase appears when we break time-reversal symmetry on the surface. This phase has a Hall conductivity quantized to one-half of the elementary value possible in a purely two-dimensional bosonic system. Since the Hall conductivity in the bosonic integer quantum Hall effect is quantized to even integers, this surface phase is expected to have an odd integer Hall conductivity. Finally, it is possible to have a surface phase which breaks no symmetries but has a symmetry-enriched intrinsic topological order of a kind impossible in a purely two-dimensional system with these symmetries.

In the previous chapter we constructed two-dimensional bosonic topological phases by binding charges to point topological defects, which were vortices. In this chapter, we construct explicit models which realize the interacting bosonic analog of the topological insulator, once again by binding charges to point topological defects. However, in this three-dimensional case the relevant point topological defects are called hedgehogs. The models have both charge conservation $U(1)$ symmetry and a time reversal $\mathbb{Z}_2^T$ symmetry, to be discussed in the main text. We present two different models which realize this physics. In the first model, described in Section 4.2, the spins are represented by $SO(3)$ degrees of freedom with Heisenberg interactions. We introduce a term in our action which energetically binds hedgehogs to bosons, and we show that this term can lead to a phase (which we call the "binding phase") where these bound states are proliferated.

The charges which will bind to the hedgehogs are ordinary bosons in $(3+1)$-dimensions, and can be represented using the techniques developed in Chapter 2. We will need to develop new methods to represent the hedgehogs, but while doing this the intuition developed in Chapter 2 will be very useful.

In an independent work, Metlitski and Fisher also produced a construction which explicitly binds hedgehog-like "monopole" objects to bosons without enlarging the continuous symmetry and showed that it gives the three-dimensional bosonic TI,[29] while the present setting is a bit simpler to analyze and is amenable to Monte Carlo studies.

In order to show that the binding phase is indeed the bosonic topological insulator, we will attempt to find the phases predicted by Vishwanath and Senthil on its surface. Initially we find only superfluids on the surface. In our Monte Carlo simulations, we do not have simple access to properties of the gapped vortex excitations in these surface phases. Therefore we cannot determine whether the superfluids we observe are the exotic superfluids predicted by Vishwanath and Senthil, or more conventional superfluids. We find that the surface superfluids in our model are connected by a direct transition. If this transition were second-order, then it could be the predicted deconfined critical point. However, we cannot access large enough system sizes

to determine the order of the observed phase transition.

We can try to find other exotic surface phases by explicitly breaking the $\mathbb{Z}_2^T$ symmetry of our model on the surface. If the bulk of the system is in a topological phase, this will lead to a Hall conductivity quantized to an odd integer. In order to measure this Hall conductivity in our system, we need to introduce external gauge fields. In the model in Section 4.2, this is complicated by our definition of the hedgehog number, which is a discontinuous function of the Heisenberg spins. In this case, we do not know how to properly couple to the external gauge fields, which prevents us from measuring the surface Hall conductivity.

To remedy this, in Section 4.3 we introduce a second model which binds hedgehogs to bosons. In this model, we represent the spins with an easy-plane CP^1 model. We can identify hedgehogs with the monopoles of the internal compact gauge field of this CP^1 model. This formulation will allow us to make several measurements which demonstrate that our phase is a bosonic topological insulator.

One measurement that we can make is called the Witten effect[30, 29, 77, 78]. This is the binding of one-half of a boson charge to external monopoles in the spin sector. We introduce such external monopoles into the bulk of our system and find that each binds precisely half of a boson charge.

We then determine the surface phases of our model. We again find superfluids connected by a direct transition. We can also break the $\mathbb{Z}_2^T$ symmetry on the surface. In the CP^1 model, we can measure the surface Hall conductivity and we find it to be quantized to odd integers as predicted. We reiterate that this Hall conductivity cannot be observed in a purely two-dimensional model, and so we must be measuring the Hall conductivity on the surface of a topological phase. Finally, we also find a surface phase which breaks none of the symmetries of the model. We suspect that this phase has symmetry-enriched intrinsic topological order of the kind predicted by Vishwanath and Senthil[28], but we do not know how to test this using Monte Carlo.

In Chapter 3 we found that we can obtain symmetry-enriched phases with intrinsic topological order by binding multiple topological defects (vortices) to bosons. In Section 4.4 we consider such a binding in (3+1) dimensions. We find that binding of multiple hedgehogs to bosons leads to a bulk phase with intrinsic topological order, thus opening the study of bosonic SET phases in (3+1) dimensions.

4.2 Realizing the topological insulator by binding bosons to hedgehogs of $SO(3)$ spins

We first study the binding between bosons and topological defects by using hedgehogs of a Heisenberg model as our topological defects. We demonstrate the existence of a phase which can be loosely viewed as a condensate of bound states of bosons and hedgehogs, and explore its properties. This model provides an intuitive introduction to the physics of such binding. Additional properties of the resulting SPT phase will be considered in Section 4.3.

4.2.1 Model and its Bulk Phase Diagram

We study the following action, in (3+1)D Euclidean space-time:

$$S = S_{\text{spin}} + \frac{\lambda}{2}\sum_{r,\mu}[J_\mu(r) - Q_\mu(r)]^2. \tag{4.1}$$

S_{spin} is an action which controls fluctuations in the $SO(3)$ spins. The second term provides the binding interaction between bosons and hedgehogs. The bosons are represented by integer-valued conserved currents, $J_\mu(r)$, as in Chapters 2 and 3, though now they are defined on the links of a four-dimensional cubic lattice, where r is a site label on the lattice and $\mu \in (x, y, z, \tau)$ is a direction.

The $Q_\mu(r)$ variables in this $(3+1)$ dimensional model now represent the worldlines of hedgehogs (not vortices), which are also integer-valued conserved currents and will be defined shortly. When the real number λ is large, this term will bind bosons and hedgehogs together. We work with periodic boundary conditions and require no net boson charge and no net boson spatial currents, so that the J_μ space-time currents have zero total winding number; such conditions are automatically satisfied for the hedgehog currents Q_μ defined below. Imposing such conditions on the boson currents is just a convenient choice, which does not affect the bulk physics, but allows a precise change of variables involving both J and Q currents [see Eq. (4.6) below].

In this section we represent the spin degrees of freedom by $SO(3)$ unit vectors. For S_{spin}, we take the following action, which describes a Heisenberg model:

$$S_{\text{spin}} = -\beta\sum_{R,\mu}\vec{n}(R)\cdot\vec{n}(R+\hat{\mu}). \tag{4.2}$$

Here $\vec{n}(R) = (n_a, n_b, n_c)(R)$ are three-component unit vectors which represent the spins. They reside on a different lattice from the $J_\mu(r)$ variables above. This lattice has its sites labelled by R and located at the centers of the (hyper)cubes of the r-lattice in Eq. (4.1), i.e., the R and r lattices are dual to each other.

From these $\vec{n}(R)$, we can define the hedgehog currents $Q_\mu(r)$ using the prescription in the literature [79, 80, 81, 82] generalized to four dimensions. We summarize this prescription here. We first define variables $\alpha_\mu(R)$, which reside on links connecting the spins $\vec{n}_i \equiv \vec{n}(R)$ and $\vec{n}_j \equiv \vec{n}(R+\hat{\mu})$:

$$e^{i\alpha_\mu(R)} = \frac{1 + \vec{n}_i\cdot\vec{n}_j + \vec{n}_i\cdot\vec{N}_0 + \vec{n}_j\cdot\vec{N}_0 + i\vec{N}_0\cdot(\vec{n}_i\times\vec{n}_j)}{\sqrt{2(1+\vec{n}_i\cdot\vec{n}_j)(1+\vec{n}_i\cdot\vec{N}_0)(1+\vec{n}_j\cdot\vec{N}_0)}}. \tag{4.3}$$

Here $\vec{N}_0$ is a reference vector which we can choose arbitrarily. We then define placket "fluxes" $\omega_{\mu\nu} \in (-\pi, \pi]$ as follows:

$$e^{i\omega_{\mu\nu}(R)} = e^{i[\nabla_\mu\alpha_\nu(R) - \nabla_\nu\alpha_\mu(R)]}. \tag{4.4}$$

Here $\nabla_\mu\alpha_\nu(R) \equiv \alpha_\nu(R+\hat{\mu}) - \alpha_\nu(R)$. One can show that changing the reference vector $\vec{N}_0$ corresponds to a gauge transformation of the $\alpha_\mu(R)$ variables so that $\omega_{\mu\nu}(R)$ are independent of the reference vector.

Finally, we can define the hedgehog current:

$$Q_\mu(r) = \frac{1}{4\pi}\epsilon_{\mu\nu\rho\sigma}\nabla_\nu\omega_{\rho\sigma}, \tag{4.5}$$

with implied summation over repeated indices. Consider for example

$$Q_\tau[r = R + (\frac{1}{2}, \frac{1}{2}, \frac{1}{2}, -\frac{1}{2})] = \frac{\nabla_x\omega_{yz} + \nabla_y\omega_{zx} + \nabla_z\omega_{xy}}{2\pi}.$$

The right-hand-side is defined on a cube $[R, R+\hat{x}, R+\hat{y}, R+\hat{z}]$, and can also be associated with a point $R + (\hat{x} + \hat{y} + \hat{z})/2$ in the center of this cube. The ω variables are fluxes passing through the plaquettes of this cube, and the net flux out of the cube is guaranteed to be integer multiple of 2π. We then define hedgehog number to be the net outgoing flux divided by 2π. When all four dimensions are considered, the center of this cube can be equivalently associated with a link in the τ direction from a dual lattice site $r = R + (\hat{x} + \hat{y} + \hat{z} - \hat{\tau})/2$, and the hedgehog number becomes the τ-component, $Q_\tau(r)$, of the hedgehog four-current.

The bulk phase diagram of this model is shown in the inset in Fig. 4.1 and can be understood essentially analytically. Indeed, in the case where the entire system is in the same phase (i.e., the boson-hedgehog binding is applied everywhere), we can change to new variables in the partition sum

$$\tilde{J}_\mu(r) \equiv J_\mu(r) - Q_\mu(r)\ , \tag{4.6}$$

which satisfy the same conditions as the original boson currents. Expressed in these variables, the first and second terms in Eq. (4.1) decouple, and we can study them independently. At small β, the $\vec{n}$ spins are disordered, which also implies that the hedgehog currents are proliferated. As β is increased, the spins order. This means that there is a large energy cost for hedgehog currents to exist. We say that the hedgehog currents are gapped, and only small loops of them are present. We can determine the location of the spin-ordering phase transition by finding singularities in the heat capacity, or by performing finite-size scaling on the magnetization as described above. The value found by our numerics agrees with the literature on the 4D classical Heisenberg model.[83]

At small λ, the $\tilde{J}_\mu$ variables are proliferated. In our original variables, this means that the boson currents are effectively independent of the hedgehog currents and are condensed. At large λ, the $\tilde{J}_\mu$ variables are gapped. The boson currents are bound to the hedgehog currents. The result of this can be seen in Fig. 4.1, which shows the current-current correlators for the boson and hedgehog currents. For small λ, there is no relation between the bosons (red solid line) and the hedgehogs (blue dashed line). As λ is increased, the current-current correlators become essentially identical as the bosons and hedgehogs are bound together. We can determine the location of the phase transition in λ by studying singularities in the heat capacity, or by peforming finite-size scaling on $\rho_{\tilde{J}}$ as described above.

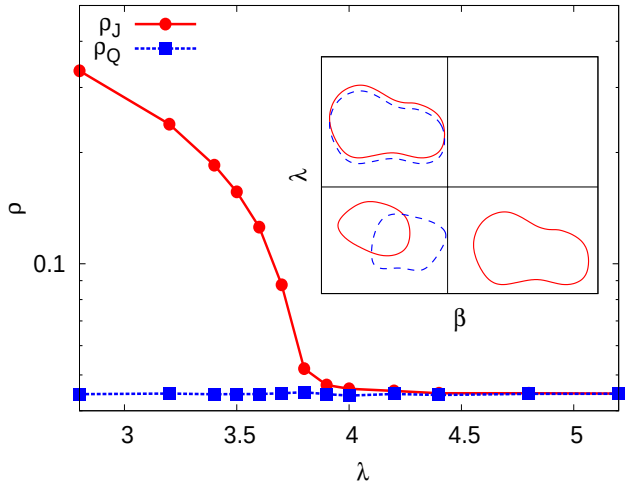

Figure 4.1: Inset: Bulk phase diagram for the model in Eqs. (4.1) and (4.2) with bosons and Heisenberg spins. The phase diagram is mathematically equivalent to a system of decoupled currents and spins, hence the straight line boundaries. At $\lambda = 0$, the system has a paramagnet-ferromagnet transition as β is increased, while the bosons are superfluid throughout. As λ is increased, the boson currents bind to the hedgehog currents. The loop pictures in the phases show a "snapshot" of the phase. Red solid loops mean that boson currents are proliferated in the phase, while blue dashed loops indicate proliferated hedgehog currents. The phase of interest is the "binding" phase in the upper left corner where bosons are bound to hedgehogs. The main figure shows the current-current correlations of the bosons and hedgehogs as λ is increased while $\beta = 0$, for a system of linear dimension $L = 6$. We see that the correlators become essentially equal as the system enters the upper left phase, indicating that bosons have bound to hedgehogs.

We can now summarize the phase diagram shown in the inset in Fig. 4.1. At small λ and β both the boson and hedgehog currents are proliferated and are not bound, while at large λ and β all currents are gapped. At small λ and large β the boson currents are condensed but the hedgehog currents are gapped. Finally, when λ is large and β is small the system is in the "binding" phase with "proliferated" bound states, which we will argue is a (3+1)D topological phase protected by the appropriate symmetries.

It is also helpful to think about the "easy-plane" regime for the spin variables, in which the spins, $\vec{n} = (n_a, n_b, n_c)$, are roughly in the ab-plane, with only small c components; we will denote the corresponding global symmetry of spin rotations in the ab-plane as $U(1)_{\text{spin}}$. In the easy-plane case we can define "vortices" of the XY spins (n_a, n_b) (i.e., phase windings of the complex order parameter $\sim n_a + in_b$). The vortices are defined on the plackets of the cubic lattice. Therefore in the (3+1)D space-time they are represented as two-dimensional "world-sheets." When dealing with vortices, one can gain intuition by thinking in terms of only the three spatial dimensions of our (3+1) dimensional space-time. In this picture the bosons and hedgehogs are represented by point particles, while the vortices are represented by lines. The next two paragraphs can be most easily understood by thinking in this picture.

Though ordinary XY spins are not defined at the core of a vortex, our spins have a c-component which can point either up or down at the vortex core. We can define two species of vortices, which we call the $\uparrow$ and $\downarrow$ species, depending on whether n_c is positive or negative at the core. This description is useful since

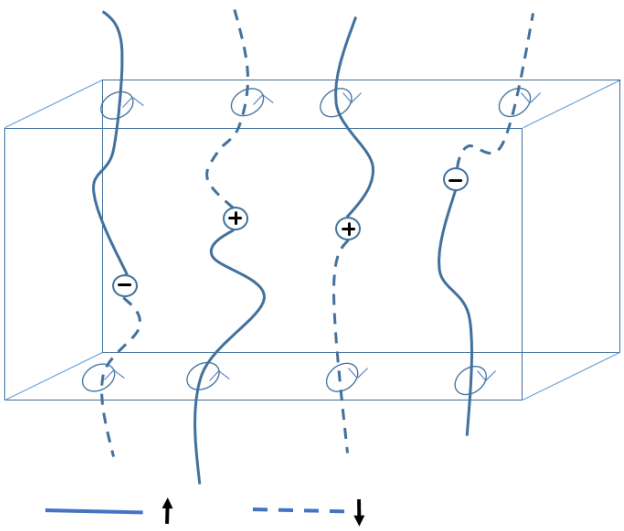

Figure 4.2: As discussed in the text, the easy-plane spin system has two species of vortex lines, $\uparrow$ and $\downarrow$, depending on n_c at the core. A hedgehog is a transition point between the two types of lines, with the sign of the hedgehog determined by the orientation of the type and vorticity of the vortex lines, as shown with examples. This figure shows only the spatial dimensions of the system, therefore the hedgehogs are point particles and the vortices are lines. Applying a Zeeman field to the surface means allowing only one type of vortex line through the surface. This leads to a correlation between the hedgehog number (and therefore the boson charge) and the vorticity at the surface, which is the origin of the Hall conductivity.

an $\uparrow$ vortex ending and continuing as a $\downarrow$ vortex is a hedgehog. Therefore our system can be thought of as a system of vortex lines having two different species. These vortex lines can change species, and the locations where this happens are hedgehogs.[84] This is illustrated in Fig. 4.2.

Hedgehog number can be either positive or negative, and this is determined by the properties of the vortex line the hedgehog is attached to. If, when looking along the line from the $\uparrow$ core to the $\downarrow$ core the vorticity is clockwise (counterclockwise), we define a positive (negative) hedgehog. This is pictured in Fig. 4.2.

4.2.1.1 Importance of Discrete Symmetry

The action in Eq. (4.1) has a $U(1)$ symmetry which comes from the conservation of the J_μ currents; this is boson charge conservation symmetry. It also has an $SO(3)$ symmetry from the spins. Both of these symmetries participate in the protection of the topological phase, in the sense that if they are broken it is possible to continuously connect the topological phase to a trivial phase. In addition, the action has a $\mathbb{Z}_2$ symmetry, which is obtained by reflecting the $\vec{n}$ spins in a plane in the spin space. To see how this affects the hedgehog current, we can examine Eq. (4.3), taking the reference vector $\vec{N}_0$ to be in the plane of reflection. We see that reflecting the spins changes the sign of the imaginary part of $e^{i\alpha_\mu}$, and therefore the hedgehog current changes sign under such a reflection. For our entire action to be invariant, we therefore need to combine such reflections with an operation which changes the sign of the boson currents. For concreteness

we will consider the $\mathbb{Z}_2$ symmetry corresponding to reflections of the $\vec{n}$ variables in the ab plane of the spin space. In this case the $\mathbb{Z}_2$ symmetry can be summarized as:

$$\begin{array}{ccc} n_a, n_b & \to & n_a, n_b \\ n_c & \to & -n_c \\ Q_\mu & \to & -Q_\mu \\ J_\mu & \to & -J_\mu \end{array} . \tag{4.7}$$

Note that it is also possible to reflect the $\vec{n}$ spins around a different plane, but this is not a distinct symmetry since it is simply the product of the above $\mathbb{Z}_2$ symmetry and an element of $SO(3)$.

By analogy with the electronic topological insulator, we would like the $\mathbb{Z}_2$ symmetry described above to be a "time-reversal" symmetry, i.e., it should be anti-unitary. The symmetry in Eq. (4.7) can be either a unitary or anti-unitary symmetry. Note that Eq. (4.1) is a real, (3+1)-dimensional action which is assumed to arise from the Trotter decomposition of the imaginary time propagator (i.e., Euclidean path integral) of a three-dimensional quantum Hamiltonian. The symmetry operations in Eq. (4.7) can be derived from the action of a symmetry operation on the quantum Hamiltonian. Therefore asking whether the symmetry in Eq. (4.7) is anti-unitary is the same as asking whether the symmetry of the quantum Hamiltonian which generates Eq. (4.7) is anti-unitary. This is a difficult question for us to answer as we do not know the quantum Hamiltonian which has Eq. (4.1) as its Euclidean path integral. Nevertheless, we take the perspective where we can check whether the original Hamiltonian has time reversal by complex-conjugating the action combined with the appropriate variable transformations, and in this way we can view the above symmetry of the action also as time reversal.

In the easy plane case, our system has $U(1)_{\text{boson}} \times U(1)_{\text{spin}}$ in addition to this discrete symmetry. We can think of the $U(1)_{\text{spin}}$ as also coming from a boson, and $n_a + in_b$ gives the phase degree of freedom of this boson. We can imagine allowing tunnelling between the two $U(1)$ symmetries. If we do this, then the discrete symmetry should act the same way on the two species, and we can see that the above symmetry changes the number of the bosons but not their phase. In a system consisting of one species of bosons, the symmetry which acts in this way is anti-unitary. From now on the symmetry described above will also be treated as anti-unitary and denoted by $\mathbb{Z}_2^T$.

The action in Eq. (4.1) is invariant under several $\mathbb{Z}_2$ symmetries, but for our purposes we will consider only the $\mathbb{Z}_2^T$ symmetry described above as important, as it protects the topological behavior. To see this we can break this symmetry and argue that the topological phase is destroyed. We break the $\mathbb{Z}_2^T$ symmetry by introducing a Zeeman field into our action:

$$S_{\text{Zeeman}} = -h \sum_R n_c(R). \tag{4.8}$$

Here h is the strength of the Zeeman field, which points in the c-direction. Note that the Zeeman field does not

break $U(1)_{\text{spin}}$ or $U(1)_{\text{boson}}$. In our picture of two species of vortices (Fig. 4.2), the Zeeman field forbids one of the species. Since the vortex lines cannot change species, hedgehogs are forbidden and the binding phase is destroyed. This can be made more precise if we replace the binding term in Eq. (4.1) with the following term:

$$\frac{\lambda}{2}\sum_{r,\mu}[J_\mu(r)-\eta Q_\mu(r)]^2\ , \tag{4.9}$$

where η is a real number. If we choose the parameters β and λ so that the system is initially in the binding phase, the introduction of η allows us to tune the system between the binding phase ($\eta=1$) and the trivial insulator ($\eta=0$). Without a Zeeman field, the system undergoes a phase transition as η is changed between 1 and 0. When a Zeeman field is applied, the hedgehogs are effectively forbidden, and so we can tune parameters h and η without going through a phase transition. Indeed, when $\eta=1$, the change of variables in Eq. (4.6) leads to decoupled $\tilde{J}$ currents and spins, so there is no phase transition when making h arbitrarily large to align all spins. We can then tune η to zero and finally reduce h back to zero, all without undergoing a phase transition. Thus, in the presence of the Zeeman field, the phase with $\eta=1$ is not distinct from the trivial insulator.

4.2.1.2 Binding of Multiple Bosons to a Hedgehog

The above methods also allow us to answer the question of what happens to the system if η in Eq. (4.9) is an integer larger than 1. In a $U(1)\times U(1)$ system in two dimensions, we studied the binding of multiple bosons to vortices (realized by taking integer η) and found that each number of bound bosons led to a different symmetry-protected topological phase.[49] There were therefore as many SPTs as there are integers, in agreement with the cohomology classification.[15, 16, 21] In the present three-dimensional case the classification of Chen et al.[15, 16] for $U(1)$ and $\mathbb{Z}_2^T$ symmetry predicts the existence of only a finite number of such symmetry protected topological phases, implying that not every value of η would lead to a distinct phase. Indeed, we find that all systems with η an even integer are topologically trivial, while when η is odd we have the same topological phase as $\eta=1$.

We can justify this claim by showing that $\eta=2$ can be continuously connected to $\eta=0$ which is a trivial insulator. This argument can then be extended to show that any two systems where η differs by 2 are in the same phase. Our argument is inspired by Ref. [85], except that here we are working with a microscopic model rather than a topological field theory. We start by considering two copies of our action, each with its own bosons and Heisenberg spins and with $\eta=1$:

$$\begin{aligned} S=&-\beta\sum_{R,\mu}\left[\vec{n}^{(1)}(R)\cdot\vec{n}^{(1)}(R+\hat{\mu})+\vec{n}^{(2)}(R)\cdot\vec{n}^{(2)}(R+\hat{\mu})\right]\\ &+\frac{\lambda}{2}\sum_{r,\mu}\left([J_\mu^{(1)}(r)-Q_\mu^{(1)}(r)]^2+[J_\mu^{(2)}(r)-Q_\mu^{(2)}(r)]^2\right), \end{aligned} \tag{4.10}$$

where the superscripts indicate which copy a variable is from. We now couple the two copies by adding the following terms:

$$\delta S = -A \sum_R \vec{n}^{(1)}(R) \cdot \vec{n}^{(2)}(R) - B \sum_r \cos[\Phi^{(1)}(r) - \Phi^{(2)}(r)]. \tag{4.11}$$

When A is large and positive, the first term above locks spins of the different copies together, $\vec{n}^{(1)} \approx \vec{n}^{(2)}$. The hedgehog variables therefore take on the same values, and either can be viewed as the hedgehog number of the whole spin system in this case: $Q \approx Q^{(1)} \approx Q^{(2)}$. On the other hand, when A is large and negative the spins of different types are locked in opposite directions, $\vec{n}^{(1)} \approx -\vec{n}^{(2)}$, and $Q^{(1)} \approx -Q^{(2)}$.

The Φ variables are 2π-periodic phases that can be thought of as conjugates to the J_μ variables. More precisely, in our path integral we sum over only the configurations of J_μ in which the currents are divergenceless. We can instead sum over all configurations of J_μ, and include the following term in our path integral:

$$\int_0^{2\pi} D\Phi(r) e^{-i \sum_r \Phi(r) (\sum_\mu \nabla_\mu J_\mu)(r)} , \tag{4.12}$$

which dynamically enforces the constraint that the boson currents be conserved. We introduce Φ variables for each copy of the boson currents, and the B term is tunnelling between the two copies. When B is large (of either sign) only the sum of $J^{(1)}$ and $J^{(2)}$ is conserved and can be identified as the current of the whole boson system (i.e., combining both copies).

When A and B are large and positive, we can expand the terms on the second line of Eq. (4.10), and take $J = J^{(1)} + J^{(2)}$, $Q = Q^{(1)} = Q^{(2)}$. In this case we obtain coupling between J and Q, which is effectively the same as in Eq. (4.9) with $\eta = 2$. On the other hand, when A is large and negative, but B is still large and positive, J is unchanged but its coupling to the hedgehogs vanishes as contributions from $Q^{(1)}$ and $Q^{(2)}$ cancel; this gives Eq. (4.9) with $\eta = 0$. We can continuously deform $A = 0$, $B = 0$ to $A = \infty$, $B = \infty$ without undergoing a phase transition. In addition, we can deform $A = 0$, $B = 0$ to $A = -\infty$, $B = \infty$ without undergoing a phase transition. This implies that we can tune from $\eta = 2$ to $\eta = 0$ without undergoing a phase transition, and so both of these cases are in the trivial insulating phase.

4.2.2 Phase Diagram on the Boundary Between the Binding Phase and a Trivial Insulator

By analogy to the fermionic topological insulator, we expect that one way to investigate the topological nature of our phase is to study the physics of its surface. In particular, a number of interesting phases have been predicted on the surface of the bosonic TI,[28] and if we can identify these phases on the surface of our binding phase, it will be a powerful argument that the binding phase is a bosonic TI.

We introduce a surface between the binding phase and a trivial insulator by allowing η in Eq. (4.9) to vary

spatially. We vary η in the z direction, so that:

$$\eta[r=(x,y,z,\tau)] = \begin{cases} 1, & z_L \leq z < z_R \\ 0, & \text{otherwise} \end{cases} . \tag{4.13}$$

This leads to the binding phase in the region $z_L < z < z_R$, while the trivial phase occupies the rest of the space. Note that there are two surfaces of the binding phase: one at z_L and one at z_R. The above geometry in our Monte Carlo setup with periodic boundary conditions corresponds to a four-dimensional torus which is divided into two parts along the z-direction.

On the surface, we can measure all of the quantities which we measured in the bulk, but we now only sum over the sites near the surface (and when averaging over directions we only use the $\hat{x}$, $\hat{y}$ and $\hat{\tau}$ directions).

The binding between hedgehogs and bosons in the bulk of the topological phase leads to exotic physics on the surface. In both the binding and trivial phases, hedgehog currents are proliferated, while boson currents are bound to the hedgehog currents in the binding phase and are absent in the trivial phase. The way this works is very similar to Fig. 3.1 in Chapter 3, except there is an additional dimension and vortex currents are replaced by hedgehog currents. Consider what happens when a hedgehog loop tries to cross the boundary between the phases. Since the boson currents must form closed loops, the above conditions cannot both be satisfied without something interesting happening on the surface. For example, we could have unbound boson currents on the surface, or hedgehogs could be effectively forbidden from crossing the surface. In order to study the surface physics and search for the exotic surface behavior predicted in Ref. [28], we first determine the surface phase diagram. To do this, we fix the values of β and λ in the bulk and tune them only on one of the surfaces, by setting:

$$\beta_\mu(X,Y,Z,T) = \begin{cases} \beta_{\text{surf}}, & Z = z_R - 1/2,\ \mu = \hat{x},\hat{y},\hat{\tau} \\ \beta_{\text{bulk}}, & \text{otherwise} \end{cases} \tag{4.14}$$

$$\lambda_\mu(x,y,z,\tau) = \begin{cases} \lambda_{\text{surf}}, & z = z_R,\ \mu = \hat{x},\hat{y},\hat{\tau} \\ \lambda_{\text{bulk}}, & \text{otherwise} \end{cases} . \tag{4.15}$$

Here we focused on the surface at z_R, and μ denotes link orientation for either β or λ terms. We show the surface phase diagram in the inset of Fig. 4.3. All data was taken with $\beta_{\text{bulk}} = 0$, $\lambda_{\text{bulk}} = 5.2$, parameters which put the bulk deep into the binding phase. The surface phase diagram contains three distinct phases. When λ_{surf} is small the bosons are in a superfluid phase, breaking their $U(1)$ symmetry. This is the scenario pictured in Fig. 3.1, where hedgehogs can cross the surface, and these crossings are connected by boson currents. If β_{surf} is also small the $SO(3)$ symmetry is unbroken as the spins are disordered. As β_{surf} increases at small λ_{surf}, the $SO(3)$ symmetry breaks, and so both symmetries are broken. Finally, at large λ_{surf} bosons see a large energy cost, and so the $U(1)$ symmetry is unbroken. This forbids hedgehogs from crossing the surface, leading to a system of $SO(3)$ spins with hedgehogs forbidden, which on the three-dimensional cubic

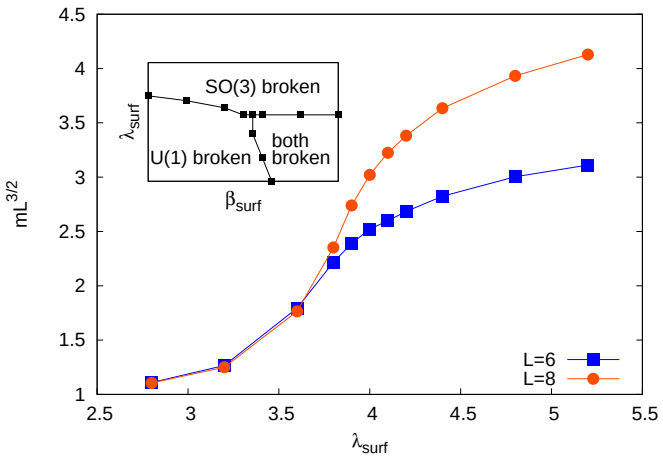

Figure 4.3: The inset shows the phase diagram of the surface of the binding phase, without a Zeeman field. It was obtained by tuning the bulk parameters deep into the binding phase and then varying β and λ *only on the surface*. We find that in this model our surface always spontaneously breaks a symmetry. At small $\beta_{\rm surf}$ and $\lambda_{\rm surf}$ the boson $U(1)$ symmetry is broken and the bosons condense into a superfluid, while at large $\lambda_{\rm surf}$ the spin $SO(3)$ symmetry is broken and the spins align into a ferromagnet. At small $\lambda_{\rm surf}$ and large $\beta_{\rm surf}$ both symmetries are broken. The main plot shows surface magnetization on a sweep in $\lambda_{\rm surf}$ for $\beta_{\rm surf} = 0$. We show $mL^{3/2}$, which is independent of system size in the disordered phase, and grows with system size in the ordered phase. We can clearly see that the $SO(3)$ symmetry is broken as $\lambda_{\rm surf}$ is increased past a value of approximately 4. All data in this section was taken with $\beta_{\rm bulk} = 0$, $\lambda_{\rm bulk} = 5.2$.

lattice is known to have magnetic order thus breaking the $SO(3)$ symmetry.[80, 82]

The locations of the phases and phase transitions in Fig. 4.3 were determined by studying singularities in the specific heat, as well as by studying the surface magnetization and current-current correlators. As an example of such data, in the main plot of Fig. 4.3 we show the magnetization, multiplied by the square-root of the volume of the surface ($L^{3/2}$). This quantity should be constant when the spins are disordered and should grow with system size when they are ordered. The data was taken with $\beta_{\rm surf} = 0$ and increasing $\lambda_{\rm surf}$. We can see that the spins order at $\lambda_{\rm surf} \approx 4$.

In order to use the current-current correlators to detect the breaking of the $U(1)$ boson symmetry on the surface, we must think through such measurements carefully. In a D-dimensional system of boson world-lines (space-time currents), the argument that $\rho_J(k_{\rm min}) \sim k_{\rm min}^2 \sim 1/L^2$ in the gapped phase relies on the conservation of the currents J. However, this is no longer true if we consider only the surface, as currents can enter and exit from the rest of the system. Therefore we instead measure the current-current correlators in the entire system (though only in the $\hat{x}$, $\hat{y}$, and $\hat{\tau}$ directions, which are parallel to the surface). When currents are gapped everywhere, this quantity will still be proportional to $1/L^2$. If we measured the current-current correlator only on the surface in the phase where the surface is a superfluid, we would expect the result to be independent of system size. Since we are measuring the correlator over the whole system, the result should be proportional to the fraction of the system which makes up the surface, which is $1/L$. In Fig. 4.4 we plot $\rho_J \cdot L^2$. We see that at large $\lambda_{\rm surf}$ this quantity is independent of system size, which tells us that the cur-

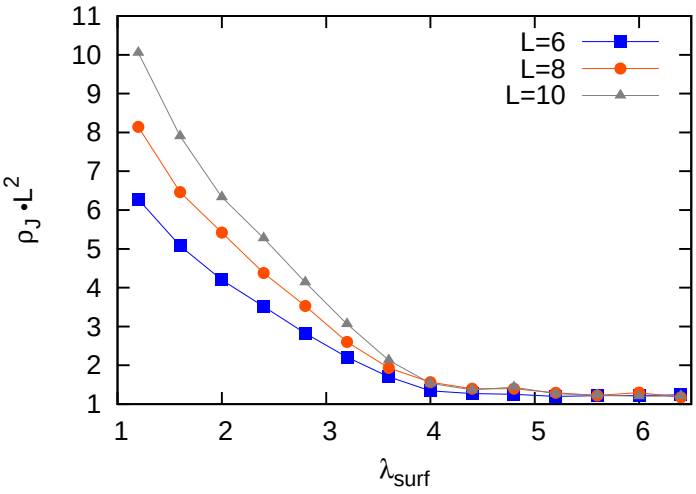

Figure 4.4: Current-current correlators of the entire system, multiplied by L^2, used to detect symmetry breaking of the bosons on the surface. This quantity is constant when the boson $U(1)$ symmetry is preserved and increases linearly with system size when it is broken on the surface. Parameters used are the same as in Fig. 4.3. We see that there is a phase transition at $\lambda_{\rm surf} \approx 4$.

rents are gapped everywhere and the surface is an insulator in the boson degrees of freedom. At small $\lambda_{\rm surf}$, $\rho_J \cdot L^2 \sim L$, which tells us that there is a region whose volume fraction is proportional to $1/L$ where the bosons are in a superfluid phase. We interpret this as evidence that there is a superfluid at the surface.

The surface phase where the $U(1)$ boson symmetry is broken is clearly a superfluid of bosons. In the easy-plane picture the spins can also be thought of as having a $U(1)$ symmetry which is broken when the spins are ordered, and so the phase where the spins order can also be thought of as a superfluid of new particles representing the spins. We can now ask whether these superfluids are trivial superfluids, or the exotic superfluids thought to exist on the surface of a bosonic TI.[28] The exotic properties have to do with the charge and statistics of gapped vortex excitations, and unfortunately we do not have access to these properties in our Monte Carlo. Therefore our surface superfluids cannot tell us whether the binding phase is a bosonic TI.

One predicted feature of the superfluids on the surface of the bosonic TI is that they are connected by a direct transition which is a deconfined critical point.[28] As shown in Figs. 4.3 and 4.4, our $SO(3)$ and $U(1)$ symmetries appear to break on the opposite sides of the same point, and so it looks that we also have a direct transition between these phases; however, we would need larger system sizes to see whether there is indeed a direct transition and whether it is continuous. Though this does not definitively show that the binding phase is topological, but it does provide evidence that we have an unusual field theory on the surface.

4.2.3 Surface with Zeeman Field

Another exotic phase predicted to exist on the surface of the bosonic TI is a phase which breaks $\mathbb{Z}_2^T$ symmetry and has a quantized Hall reponse. We can try to realize this phase by applying a Zeeman field on the surface

of our model to explicitly break the $\mathbb{Z}_2^T$ symmetry. We add a term similar to Eq. (4.8) to our action, but only on the surface of the model. We then expect that there is a surface phase which does not break any $U(1)$ symmetry—i.e., an insulator—but which has the surface Hall conductivity quantized to an odd integer, which is different from the even values expected in the (2+1)D bosonic integer quantum Hall effect. For easy-plane spins, we expect that a finite Zeeman field is needed to destroy the surface superfluids to reach this phase, while for SO(3) spins used here and starting in the spin-ordered phase, we expect to immediately transition to the quantum Hall insulator.[82]

In our Monte Carlo study, we actually apply Zeeman field h to both surfaces but take the fields on the two surfaces to have opposite signs. We take $\lambda = 5.2$ and $\beta = 0$ everywhere (including at the surfaces), which puts the bulk regions deep into the binding or trivial phases, respectively, while the surfaces start in the spin-ordered phase at $h = 0$.

Since the Hall conductivity in the surface system of spins and bosons will be due to correlations between the vorticity of the spins and the boson charges,[49] we will measure these correlations directly before moving on to the more complicated Hall conductivity measurement. In the absence of the Zeeman field, we can use the $\mathbb{Z}_2^T$ symmetry, which is reflection of the $\vec{n}$ variables in the ab-plane, to change the sign of hedgehog and hence the boson charge without changing the spin vorticity, and so such correlations vanish. This can be seen in Fig. 4.2, where, for example, on the top surface there is one clockwise vortex attached to a positive hedgehog (which is in turn bound to a positively charged boson), and another clockwise vortex is attached to a negative hedgehog. Applying a Zeeman field corresponds to only allowing one type of vortex ($\uparrow$ or $\downarrow$) to pass through the surface. In Fig. 4.2, this means that only solid lines are allowed to pass through the top surface. We can see that this leads to a correlation between the vorticity of the vortex on the surface and the charge of the boson it is binding nearby.

We can further think about Fig. 4.2 as depicting a slab of the binding phase. Opposite Zeeman fields on the two surfaces give us a quasi-two-dimensional slab on which vortices are bound to charges with definite relation between the vorticity and charge, and these bound states are proliferated. We have studied such a system in a previous work,[49] and found that its Hall conductivity is quantized to be equal to two. It is reasonable to assume that this conductivity is evenly distributed between the two surfaces, leading to the surface Hall conductivity equal to one on each surface. This intuitive argument reproduces the prediction of Ref. [28].

To measure correlations between vortices and bosons we first define the spin vorticity $V_{\mu\nu}(R)$ as

$$V_{\mu\nu}(R) = \frac{1}{2\pi}[\nabla_\mu s_\nu(R) - \nabla_\nu s_\mu(R)]\,, \tag{4.16}$$

where $s_\mu(R) \in (-\pi, \pi]$ measures the difference between the spin angles at $R + \hat{\mu}$ and R and brings it to $(-\pi, \pi]$:

$$s_\mu(R) \equiv \left[\tan^{-1}\left(\frac{n_b(R+\hat{\mu})}{n_a(R+\hat{\mu})}\right) - \tan^{-1}\left(\frac{n_b(R)}{n_a(R)}\right)\right] \bmod 2\pi.$$

We can then Fourier transform the vorticity as follows:

$$V_{xy}(k) = \frac{1}{\sqrt{L^3}} \sum_R{}' V_{xy}(R) e^{-ik\cdot R}. \tag{4.17}$$

The prime on the sum indicates we are summing over all sites at a fixed $z = z_R$. We measure $|\langle V_{xy}(k_{\min}) J_\tau(-k_{\min})\rangle|$, where $k_{\min} = (2\pi/L, 0, 0, 0)$, and the results are shown in Fig. 4.5.

We see that as soon as the Zeeman field is applied, the vortices and charges become correlated. Unlike the Hall conductivity, we do not expect these correlations to approach any universal value. We do note that the correlations on the two surfaces of the system are approximately equal, which is encouraging as we would expect the Hall conductivity on these surfaces to be equal as well. The differences between the correlations on the two surfaces is likely due to the fact that the surfaces are realized differently on a lattice, but we would expect that universal values such as the Hall conductivity would not have these differences.

In order to measure Hall conductivity, we need to couple both the bosons and spins to external probing gauge fields, and then use linear response theory to determine the conductivity. When we do this we run into a problem, which has to do with the way the hedgehog currents Q_μ were defined. We can see from Eq. (4.4) that $\omega_{\mu\nu}$ is a discontinuous function of spins since we required it to be brought to $(-\pi, \pi]$. When including the probing gauge fields, this causes the path integral to be a discontinuous function of the probing fields, which prevents us from taking the derivatives needed for linear response theory, and so we do not know how to calculate conductivity in this system. In the next section we will find a way around this problem, while in the present case we can only appeal to the intuitive argument presented above.

4.3 Realizing the topological insulator by binding bosons to hedgehogs of an easy-plane CP^1 model

The Heisenberg model discussed in the previous section allowed us to realize a "binding" phase of bosons and hedgehogs. However, in this model we were unable to find definitive evidence that the binding phase is in fact a symmetry-protected bosonic topological insulator, although our indirect arguments are compelling. In this section we introduce a new model, which includes the spin degrees of freedom in a CP^1 representation. This theory has spinor matter fields ("spinons") coupled to a compact gauge field and is a faithful representation of the microscopic spin system with short-range interactions (i.e., such a lattice "field theory" is "emergable" from a local microscopic Hamiltonian). We will see that this formulation allows us to make measurements, such as a Witten effect in the bulk and a quantized Hall conductivity on the surface, which indicate that the binding phase is a bosonic TI.

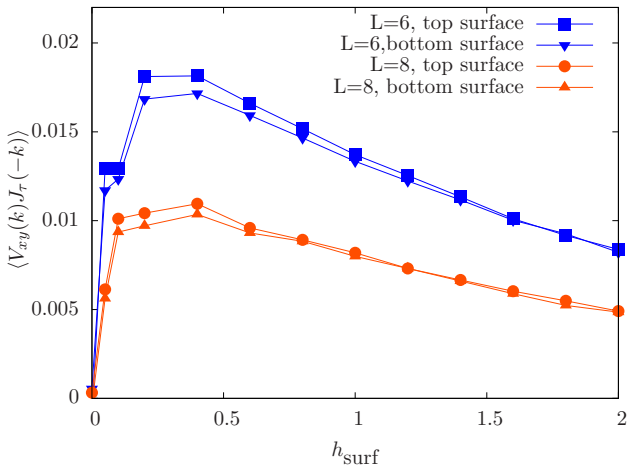

Figure 4.5: Spin vortex - boson charge correlators near the surface of the binding phase in the model Eqs. (4.1) and (4.2) using Heisenberg spins. The horizontal axis is the strength of the Zeeman field applied only near the surfaces (and of opposite sign on the two surfaces). We see that as soon as the Zeeman field is turned on, the correlator takes a non-zero value. The value is non-universal, but is approximately the same on the top and bottom surfaces. Data was taken with $\beta = 0$, $\lambda = 5.2$ everywhere and the binding phase occupying half of the system, cf. Eq. (4.13). Since we do not know how to properly couple external gauge fields to this system, we are unable to compute the Hall conductivity.

4.3.1 Bulk Phase Diagram

The following action represents the spins in the CP^1 representation:

$$S_{\rm spin} = -\beta \sum_{s=\uparrow,\downarrow} \sum_{R,\mu} [z_s^\dagger(R) z_s(R+\hat{\mu}) e^{-i a_\mu(R)} + c.c.] - K \sum_{R,\mu<\nu} \cos[\nabla_\mu a_\nu(R) - \nabla_\nu a_\mu(R)]. \quad (4.18)$$

Here the spins are represented by two complex bosonic fields $z_\uparrow$,$z_\downarrow$ ("spinons"), which satisfy $|z_\uparrow|^2 + |z_\downarrow|^2 = 1$. We can write the z fields as a spinor, $\mathbf{z} \equiv (z_\uparrow, z_\downarrow)^T$, and extract the spin $\vec{n} = \mathbf{z}^\dagger \vec{\sigma} \mathbf{z}$, where $\vec{\sigma} \equiv (\sigma_1, \sigma_2, \sigma_3)$ is a vector of Pauli matrices. The spinon fields are minimally coupled to a compact gauge field $a_\mu(R)$. The last term is a Maxwell-like term for the compact gauge field, which appears after partially integrating out the spinon fields. The variables in the above action live on a cubic lattice, where R gives the position on the lattice and μ, ν are directions.

The CP^1 model defined above actually has global $SO(3)$ symmetry, similar to the previous section. In this section we find it convenient to break the $SO(3)$ symmetry down to $U(1)$ explicitly by taking the "easy-plane" limit of the CP^1 model. We align all the spins $\vec{n}$ in the ab-plane, which corresponds to fixing the magnitude of $z_\uparrow$ and $z_\downarrow$, and allowing only phase fluctuations, i.e., $z_s \equiv \frac{1}{\sqrt{2}} e^{i\phi_s}$. The CP^1 model in the easy-plane limit becomes:

$$S_{\rm spin} = -\beta \sum_{s=\uparrow,\downarrow} \sum_{R,\mu} \cos[\nabla_\mu \phi_s(R) - a_\mu(R)] + \frac{K}{2} \sum_{R,\mu<\nu} [\nabla_\mu a_\nu(R) - \nabla_\nu a_\mu(R) - 2\pi B_{\mu\nu}(R)]^2 . \quad (4.19)$$

Here $\phi_\uparrow$ and $\phi_\downarrow$ are 2π-periodic variables which represent the phases of the spinon fields. We have also replaced the cosine in the Maxwell term by a quadratic "Villain" form, with $B_{\mu\nu}$ which are unconstrained, integer-valued dynamical variables residing on the plackets of the lattice. Upon summing over $B_{\mu\nu}$ in the partition sum, the third term generates a 2π periodic function of $\nabla_\mu a_\nu - \nabla_\nu a_\mu$, and therefore this does not change the universality class of the problem.

Using the Villain form of the Maxwell term is advantageous as it allows us to define the hedgehog current:

$$Q_\mu(r) = \frac{1}{2}\epsilon_{\mu\nu\rho\sigma}\nabla_\nu B_{\rho\sigma}. \tag{4.20}$$

Note that $Q_\mu(r)$ resides on the links of the lattice whose sites are labelled by r which, as in the previous section, is interpenetrating with the lattice labelled by R. The above definition is analogous to Eq. (4.5) with $B_{\rho\sigma} \leftrightarrow \omega_{\rho\sigma}/(2\pi)$. The $B_{\mu\nu}$ variables have the meaning of "Dirac strings" of the hedgehogs. Thus defined, the hedgehogs in the CP^1 model are actually monopoles of the compact gauge field a_μ. We will continue to call them hedgehogs in this work to avoid confusion with a different type of monopole introduced later.

We can again study the model described by Eqs. (4.1) and (4.19) in Monte Carlo. Equilibration becomes difficult in the regime where K and λ are large, and it is necessary to include composite updates which simultaneously change multiple variables. One such update is to change $B_{\mu\nu}$ while also changing J_μ so that there is no change in the second term in Eq. (4.1). Another update is to change both a_μ and $B_{\mu\nu}$ in such a way as to keep the K term in Eq. (4.19) small.

We can find phase transitions in this model by looking for singularities in the specific heat, which is defined in the same way as in the previous section. We can identify order in the bosonic degrees of freedom by studying the superfluid stiffness and order in the spins by studying the magnetization. In this easy-plane version of the model, the spin degree of freedom is an XY vector with components (n_a, n_b). Since $(n_a, n_b) = (\cos\phi_{\text{spin}}, \sin\phi_{\text{spin}})$ with $\phi_{\text{spin}} = \phi_\uparrow - \phi_\downarrow$, the magnetization is given by:

$$m = \frac{\left\langle \left| \sum_R e^{i[\phi_\uparrow(R) - \phi_\downarrow(R)]} \right| \right\rangle}{\text{Vol}}. \tag{4.21}$$

The phase diagram in this model is parameterized by β, K, and λ. As in the previous section, we can make the change of variables in Eq. (4.6) and find that the $\tilde{J}$ part of the problem decouples from the spin part. The behaviour of the bosons is the same as in the previous section. When λ is small, the physical bosons are essentially independent of the hedgehogs, and are in the superfluid phase. As λ is increased, they become bound to hedgehogs. The transition happens at $\lambda \approx 4$. The locations of the phase transitions in the spin degrees of freedom are independent of λ, though the nature of the various phases are not. In Fig. 4.6 we show the phase diagram in the β and K variables, for two cases: λ small and λ large. The phase diagram is consistent with the easy-plane CP^1 model in the literature.[60]

Let us first consider the case when λ is small. The bosons will be in a superfluid phase for any β and K.

The spin system has the following three phases: *i)* when β and K are small, the spin degrees of freedom are disordered and the hedgehogs are proliferated. The phase is therefore a conventional paramagnet in the spin degrees of freedom. *ii)* As K is increased, hedgehogs acquire a large energy cost, and become gapped. This phase was studied in Refs. [84, 82, 60]. It is known as the Coulomb phase[86] because it has an emergent gapless photon and gapped excitations that carry charge $1/2$ and interact via a Coulomb interaction. *iii)* Finally, the phase at large β has a large energy penalty for spin fluctuations, and so the spins order. This phase is a conventional ferromagnet in the spin degrees of freedom.

In the case when λ is large, the spin parts of the Coulomb and ferromagnetic phases do not change, since both of these phases suppress hedgehogs. These phases are now trivial insulators in the boson degrees of freedom. On the other hand, in the paramagnetic phase the hedgehogs are proliferated and the bosons become bound to them. This is the binding phase, which we will argue is a topological phase protected by the $U(1)_{\rm spin} \times U(1)_{\rm boson}$ and $\mathbb{Z}_2^T$ symmetries.

4.3.1.1 Symmetries When The Spins Are Represented By An Easy-plane CP^1 Model

When representing our spins with an easy-plane CP^1 model we have explicitly broken the $SO(3)$ symmetry from the previous section down to a $U(1)$ symmetry which corresponds to spin rotations in the easy plane. This complicates our discussion of the discrete symmetries of the model. In the previous section all reflections of $\vec{n}$ were related to each other by an operation in $SO(3)$, but in the easy-plane case, e.g., reflections in the ab plane $(n_a, n_b, n_c) \rightarrow (n_a, n_b, -n_c)$ are now distinct from reflections in the ac plane $(n_a, n_b, n_c) \rightarrow (n_a, -n_b, n_c)$. The result of this is that there are now two $\mathbb{Z}_2^T$ symmetries which protect the topological phase, in the sense that as long as any one of these symmetries is preserved, the topological phase cannot be continuously connected to a trivial phase. The first $\mathbb{Z}_2^T$ symmetry is the same as that in the previous section; in the variables of Eq. (4.19) it reads:

$$\begin{array}{ccc} \phi_\uparrow & \rightarrow & -\phi_\downarrow \\ \phi_\downarrow & \rightarrow & -\phi_\uparrow \\ a_\mu & \rightarrow & -a_\mu \\ B_{\mu\nu} & \rightarrow & -B_{\mu\nu} \\ J_\mu & \rightarrow & -J_\mu \\ i & \rightarrow & -i \end{array} . \tag{4.22}$$

This symmetry corresponds to a reflection in the ab plane.

The second $\mathbb{Z}_2^T$ symmetry is a combination of reflections in the ab and ac planes and acts on spins as

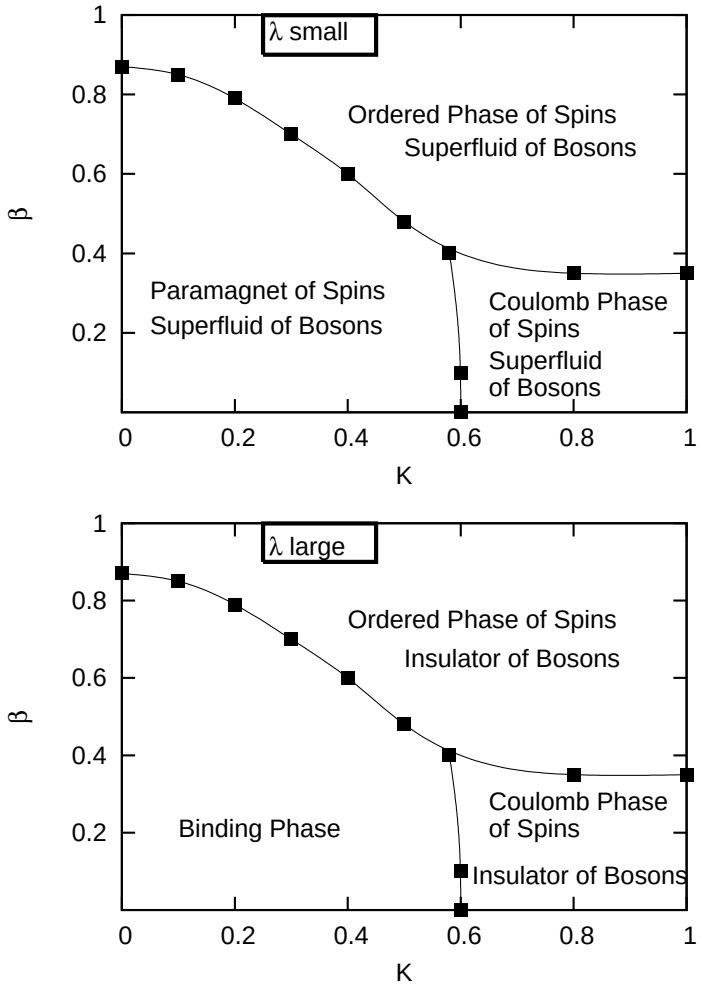

Figure 4.6: Bulk phase diagram in the β and K variables for the model defined in Eqs. (4.1) and (4.19) where the spins are described by an easy-plane CP^1 model. The top panel shows the phases at small λ, while the bottom panel shows large λ. The locations of the phase boundaries are independent of λ, but the nature of the phases are not. Symbols indicate points where the phase transitions were identified numerically from singularities in the heat capacity. The candidate for the topological phase is the binding phase, which occurs at large λ, small β, and small K.

$(n_a, n_b, n_c) \to (n_a, -n_b, -n_c)$. In the CP^1 representation, this symmetry is given by:

$$\begin{array}{ccc} \phi_\uparrow & \to & \phi_\downarrow \\ \phi_\downarrow & \to & \phi_\uparrow \\ a_\mu & \to & a_\mu \\ B_{\mu\nu} & \to & B_{\mu\nu} \\ J_\mu & \to & J_\mu \\ i & \to & -i \end{array} . \tag{4.23}$$

Note that a symmetry which consists only of a reflection in the ac plane does not protect the topological phase, as under this symmetry we can still apply the Zeeman field in the c direction and connect to a trivial phase as in Sec. 4.2.1.1. Note also that we cannot apply fields in the ab plane as this would violate the $U(1)_{\text{spin}}$ symmetry.

If either of the above $\mathbb{Z}_2^T$ symmetries are preserved, the topological phase cannot be connected to a trivial phase. A system with only the first symmetry has a total symmetry of $U(1)_{\text{spin}} \times U(1)_{\text{boson}} \times \mathbb{Z}_2^T$, while if we consider the second symmetry the direct product in front of $\mathbb{Z}_2^T$ is replaced with a semidirect product. (see Sec. 4.5 for further discussion of these symmetries) The Zeeman field introduced in the previous section (and used again below) breaks both of these symmetries.

Note that in the presence of separate $U(1)_{\text{spin}}$ and $U(1)_{\text{boson}}$ symmetries, we could in principle consider unitary symmetries given by Eqs. (4.22), (4.23), by simply omitting the complex conjugation. However, if we imagine introducing a tunnelling between the two $U(1)$ symmetries, which would reduce the total symmetry to $U(1) \times \mathbb{Z}_2^T$ [or $U(1) \rtimes \mathbb{Z}_2^T$], the discrete symmetry should then treat both spin and boson variables in the same way. We find that this condition is satisfied as long as the above symmetries are understood as anti-unitary; hence we will refer to these symmetries as $\mathbb{Z}_2^T$.

4.3.2 Observation of a Witten effect

The CP^1 representation allows us to make a bulk measurement which can detect whether our system is a bosonic topological insulator. This measurement, predicted in both the fermionic[27] and bosonic[30, 29, 77, 78] TIs, is called a Witten effect, and is the tendency of an external magnetic monopole in a TI to bind a charge of one-half. In order to justify our claim that the binding phase is a bosonic TI, we now demonstrate that our system exhibits a Witten effect.

The first step in measuring a Witten effect in our Monte Carlo is to add external $U(1)$ gauge fields to the system. These external fields correspond to the $U(1)_{\text{spin}}$ and $U(1)_{\text{boson}}$ symmetries of the system. We will fix configurations for these fields before performing the simulations, which corresponds to putting our system in some external electromagnetic field. These external gauge fields are distinct from the internal, dynamical gauge field a_μ. Similarly, the external monopoles introduced in this section are different from the hedgehogs

(which are monopoles of the field a_μ) discussed previously. We will introduce magnetic monopoles in the $U(1)_{\rm spin}$ gauge field and will measure $U(1)_{\rm boson}$ charge. The Witten effect is the statement that the external monopoles of the $U(1)_{\rm spin}$ gauge field will bind half of a charge of the $U(1)_{\rm boson}$ symmetry.

Let us first consider the gauge field coupled to the spin degrees of freedom. Here it is convenient to think in terms of a parton description. This is a description of a spin model by using the easy-plane CP^1 model in which the phases $\phi_\uparrow$ and $\phi_\downarrow$ represent the phases of different types of bosonic "partons". These partons each represent one-half of a physical boson. Each parton carries a unit charge under the internal gauge field a. The physical boson carries unit charge under the external gauge field, which we denote A_1. The partons carry half a charge under this gauge field, with one parton carrying positive charge and the other negative. To modify Eq. (4.19) to reflect this, we add $\pm A_{1\mu}/2$ inside the cosines on the first line. Partially integrating out the parton fields then gives compact Maxwell terms in the field combinations $a_\mu + A_{1\mu}/2$ and $a_\mu - A_{1\mu}/2$, with equal couplings due to the $\mathbb{Z}_2^T$ symmetry. We can write each in the Villain form, which introduces two integer-valued placket variables $B^+_{\mu\nu}$ and $B^-_{\mu\nu}$. We can expand and recombine these quadratic terms to get separate terms for the a and A_1 fields, leading to the following action:

$$\begin{aligned} S &= -\beta \sum_{R,\mu} \cos[\nabla_\mu \phi_\uparrow(R) - a_\mu(R) - \frac{1}{2} A_{1\mu}(R)] - \beta \sum_{R,\mu} \cos[\nabla_\mu \phi_\downarrow(R) - a_\mu(R) + \frac{1}{2} A_{1\mu}(R)] \\ &+ \frac{K}{2} \sum_{R,\mu<\nu} [\nabla_\mu a_\nu(R) - \nabla_\nu a_\mu(R) - 2\pi B_{\mu\nu}(R)]^2 \\ &+ \frac{K}{8} \sum_{R,\mu<\nu} [\nabla_\mu A_{1\nu}(R) - \nabla_\nu A_{1\mu}(R) - 2\pi M_{\mu\nu}(R)]^2 \\ &+ \frac{\lambda}{2} \sum_{r,\mu} [J_\mu(r) - Q_\mu(r)]^2 + i \sum_{r,\mu} J_\mu(r) A_{2\mu}(r). \end{aligned} \tag{4.24}$$

Here $B_{\mu\nu} = (B^+_{\mu\nu} + B^-_{\mu\nu})/2$, and $M_{\mu\nu} = B^+_{\mu\nu} - B^-_{\mu\nu}$. Note that $B_{\mu\nu}$ and $M_{\mu\nu}$ are not completely independent variables but satisfy the conditions that $B_{\mu\nu}$ is $1/2 \times$ integer, $M_{\mu\nu}$ is integer, and

$$2B_{\mu\nu}(R) = M_{\mu\nu}(R) \mod 2. \tag{4.25}$$

The variables $M_{\mu\nu}$ can be interpreted as the Dirac strings of the external monopoles. We can see that when we introduce external monopoles of odd integer strength, the internal hedgehog variables become half-integer valued—this is a crucial observation for the discussion of the Witten effect.[29] Note that in the case of no external field A_1 and no external monopoles, the $B_{\mu\nu}$ variables are integer-valued and Eq. (4.24) reduces to Eq. (4.19). Note also that the coupling we wrote for $(\nabla_\mu A_{1\nu} - \nabla_\nu A_{1\mu} - 2\pi M_{\mu\nu})^2$ [the "Maxwell term" for the external gauge field on the fourth line of Eq. (4.24)] is special to the preceding spinon-generated argument, while it is expected to be renormalized up by the rest of the universe; in fact, we will assume that the A_1 field is essentially externally controlled and is static.

We introduce a monopole into our system by making a specific choice for the external variables $A_{1\mu}$ and

$M_{\mu\nu}$. First, we choose a configuration of $M_{\mu\nu}$ which will lead to a pair of external monopoles. In our system with periodic boundary conditions, it is not possible to have only a single monopole. We will place external monopoles at coordinates $(x, y, z) = (0, 0, 0)$ and $(0, 0, L/2)$, on the lattice labelled by r. The external monopoles will have opposite charges, with the positively-charged one at the origin. All configurations of external gauge fields will be constant in the τ direction. In order to place external monopoles at these locations, we set $M_{xy}(R) = 1$ whenever $X = -1/2$, $Y = -1/2$, and $1/2 \leq Z \leq L/2 - 1/2$ (the $1/2$'s come from the R lattice being displaced from the r lattice by half a lattice spacing). All other $M_{\mu\nu}$ are set to zero. By Eq. (4.25), we must also constrain B_{xy} to be odd half-integers on this Dirac string. Now that we have specified the $M_{\mu\nu}$ values which introduce external monopoles, we choose values for the $A_{1\mu}$ variables to minimize the action of the Maxwell term on the fourth line of Eq. (4.24).

In our simulations we will set $A_{2\mu} = 0$ everywhere, so that it does not affect the system. It will be used only when computing linear responses.

There are in fact multiple configurations of the variables $M_{\mu\nu}$ which give the same configuration of external monopoles. The physics of the system is independent of which configuration of $M_{\mu\nu}$ we choose because the various configurations are related by the following gauge transformation:

$$\begin{array}{rcc} M_{\mu\nu}(R) & \rightarrow & M_{\mu\nu}(R) + \nabla_\mu \kappa_\nu(R) - \nabla_\nu \kappa_\mu(R) \\ B_{\mu\nu}(R) & \rightarrow & B_{\mu\nu}(R) + \frac{1}{2}[\nabla_\mu \kappa_\nu(R) - \nabla_\nu \kappa_\mu(R)] \\ A_{1\mu}(R) & \rightarrow & A_{1\mu}(R) + 2\pi\kappa_\mu(R) \\ a_\mu(R) & \rightarrow & a_\mu(R) + \pi\kappa_\mu(R) \end{array} , \tag{4.26}$$

where $\kappa_\mu(R)$ is an integer-valued field living on the links of the lattice labelled by R. One can use Eqs. (4.20) and (4.24) to check that this transformation does not change the action, including the configurations and energetics of the external monopoles and gauge fields, so our results are independent of the specific choice of the Dirac string $M_{\mu\nu}$.

Having introduced external monopoles into our system, we can begin to see why they should bind half a charge of the bosons. The argument goes as follows. First, when modifying the Dirac string variables $M_{\mu\nu}$ to insert external monopoles, we were also forced to modify the variables $B_{\mu\nu}$ in such a way as to introduce one-half of a hedgehog at the same locations as the external monopoles. However, we saw in the previous section that hedgehog-boson 'molecules', which have similar bare long-range interactions as just hedgehogs (i.e., carry hedgehog number), are proliferated in the binding phase. Therefore the $1/2$-hedgehog which we introduced will be screened by a "cloud" of hedgehog-boson molecules drawn from the rest of the system. This screening is analogous to Debye screening in a plasma. The screening cloud will carry a hedgehog number of one-half, but with opposite sign to the first hedghog, leading to a total hedgehog number of zero. Since in the binding phase hedgehogs are bound to charges, the cloud also carries a boson charge of one-half. Therefore we find that half of a boson charge has bound to the external monopole. We have tested this intuition by direct Monte Carlo simulations.

The above discussion is complicated by two degeneracies in Eq. (4.24). First, there is a degeneracy between $Q_\tau(0,0,0,\tau) = 1/2$ and $Q_\tau(0,0,0,\tau) = -1/2$: e.g., when $M_{xy} = 1$ on the Dirac string, B_{xy} can be either $+1/2$ or $-1/2$ with the same energy. This degeneracy is a result of the symmetry in Eq. (4.23). In what follows it can be helpful to neglect variations in the τ direction and think about $Q_\tau(0,0,0,\tau)$ as a stationary hedgehog charge at the origin. Because of this degeneracy the statistical mechanics has each of the two states equally probable, which in an infinitely long simulation would lead to zero net hedgehog charge, and no observation of the Witten effect. Second, if we were able to fix the hedgehog number in one of these two states, for example $Q_\tau(0,0,0,\tau) = 1/2$, we have another degeneracy, between $J_\tau(0,0,0,\tau) = 0$ and $J_\tau(0,0,0,\tau) = 1$. This leads to an average boson charge of $1/2$ at the location of the monopole. This charge cancels the boson charge from the screening cloud, leading to no observation of the Witten effect.

Despite these degeneracies, we may still observe a Witten effect if the degenerate states are metastable, and the Monte Carlo is stuck in one of the two states. For example, in order to get from $Q_\tau = +1/2$ to $Q_\tau = -1/2$ one needs to modify all of the $B_{\mu\nu}$ on the Dirac string, and the $\phi_{\uparrow,\downarrow}$ and a_μ variables nearby. Such a move would be quite unlikely (and impossible in the limit of an infinite separation between the monopoles). Similarly, to get from $J_\tau = 0$ to $J_\tau = 1$ one needs to insert a boson loop which passes from one monopole to another, and such a step is highly unlikely with local updates.

The results of our numerics shows that even at the small system sizes that we can access, degeneracy in the J variables is always broken. However, the degeneracy in the Q variables is unbroken, and so we do not observe a Witten effect. Let us consider the Q degeneracy more carefully. One of the two degenerate states has $Q = +1/2$ bound to a positive external monopole at $r = 0$, and $Q = -1/2$ bound to a negative external monopole at $r = L/2$. The other state as $Q = -1/2$ bound to a positive external monopole at $r = 0$, and $Q = +1/2$ bound to a negative external monopole at $r = L/2$. Note that to change between the two degenerate states we need to modify variables along a string connecting the two external monopoles, and the probability of this happening reduces exponentially with distance, so in the thermodynamic limit this degeneracy would certainly break, even though on our small systems it does not.

We will break this degeneracy in our system by decreasing the probability that the system will flip between degenerate states. To do this we add the following "biasing" term:

$$\delta S_{\text{bias}} = \gamma \sum_\tau \left[J_\tau(0,0,0,\tau) - J_\tau(0,0,L/2,\tau) \right], \tag{4.27}$$

where γ is some small real number. We have scanned the system by increasing γ from zero and seen no phase transitions, implying that these small γ do not change the phase we are in. It would be surprising if the above biasing term affected the bulk physical properties of the system, as we are only making a modification to a fraction of the system proportional to L^{-3}. In addition, though this term breaks the symmetry in Eq. (4.22), it preserves the symmetry in Eq. (4.23), and the topological phase is protected as long as either of these symmetries is preserved.

We hope that the above term reduces the probability of switching between degenerate states, so that we can observe a Witten effect. From our numerical results we can see that the above term indeed does this for a large range of γ. Therefore we have broken the problematic degeneracies and removed the obstacle to measuring the Witten effect. We would like to stress that the Witten effect is ordinarily defined for a single monopole, in the thermodynamic limit. The problems we have with degeneracies are artifacts of the fact that we are trying to measure a Witten effect in a finite-size system with two external monopoles. If the action were defined on an infinite system with only one monopole, these problems would not arise, as it would take an infinitely long time for the system to change between degenerate configurations.

We observe the Witten effect by measuring the total charge enclosed in a sphere of radius w, centered around the location of the monopole. The precise definition of our measurement is:

$$\text{charge} = \frac{1}{L}\sum_{\tau}\sum_{x^2+y^2+z^2\leq w^2}\langle J_\tau(x,y,z,\tau)\rangle \ . \tag{4.28}$$

Note that the sphere discussed above is only a sphere in the x, y, and z directions, and we have averaged over the τ direction. We performed simulations with $L = 10$ and show the results in Fig. 4.7. At $w = 0$, we are at the location of the monopole. There is nearly no boson charge bound here. At $w = 1$, we have already included most of the screening cloud, and therefore measure an enclosed charge close to $1/2$, as expected. The fact that $w = 1$ measures a value close to one half shows that the screening length in the system is quite short. At $w = 2$, we have included the entire screening cloud, so the charge is even closer to $1/2$. As w is further increased, we start to include the screening cloud from the other monopole, which is located at a distance $L/2$ from the first one. This cancels some of the charge from the first monopole, and so the total charge starts to decrease. When $w > L/2$, the sphere encompasses the screening clouds from both external monopoles, and so there is a total charge of nearly zero. The values of charge are negative because we set the biasing parameter γ such that at the origin there is a monopole of positive charge, $Q = +1/2$, and the sign of the charge in the screening cloud is the opposite of the sign of the monopole.

In Fig. 4.7, we have found that the amount of charge at the site of the monopole ($w = 0$) is nearly zero. However, this is not universal and in fact depends on the choice of γ in Eq. (4.27). In our simulations, we find that $w = 2$ is sufficiently far from the monopole to be unaffected by the change in γ. Figure 4.8 shows simulations taken with different values of γ. We see that though the amount of charge close to the monopoles (near $w = 0$ and $w = L/2$) can be affected by changing γ, the value at $w = 2$ is always very close to one-half, regardless of what γ is used.

Various other measurements can be made to support our conclusions. Measuring the total charge on each site shows that the half-charge is distributed around the monopole in an approximately spherically symmetric way. We can also use the Witten effect to detect phase transitions out of the bosonic TI. Figure 4.9 shows the total charge on all the nearest-neighbours, as a function of K. We note that the quantized Witten effect disappears at $K = 0.6$, which is where the phase transition to the Coulomb phase is located (see Fig. 4.6). (In

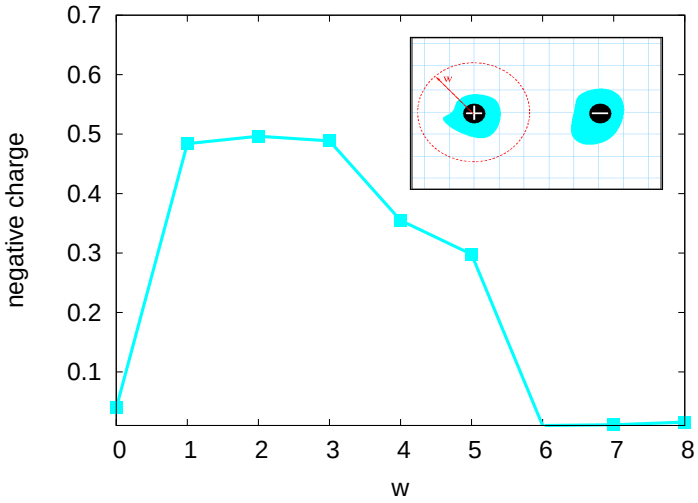

Figure 4.7: Measurement of the Witten effect. The inset shows the measurement setup. External monopoles are inserted into the system, at a distance $L/2$ apart. They carry hedgehog numbers of $\pm 1/2$, and are Debye screened by hedgehogs of equal and opposite number, which also carry half of a boson charge. The main plot shows the boson charge enclosed in a sphere of radius w. For $w \approx 1-3$, this sphere measures the boson charge in the screening cloud near the origin, and the result is $1/2$, as expected. For $w \gtrsim 5$ the sphere includes the charge from the other screening cloud, and the enclosed charge drops to zero. The system size is $L = 10$, using bulk parameters $\beta = 0.2$, $K = 0.4$, $\lambda = 8$ (cf. bottom panel in Fig. 4.6), and local biasing parameter $\gamma = 1.5$.

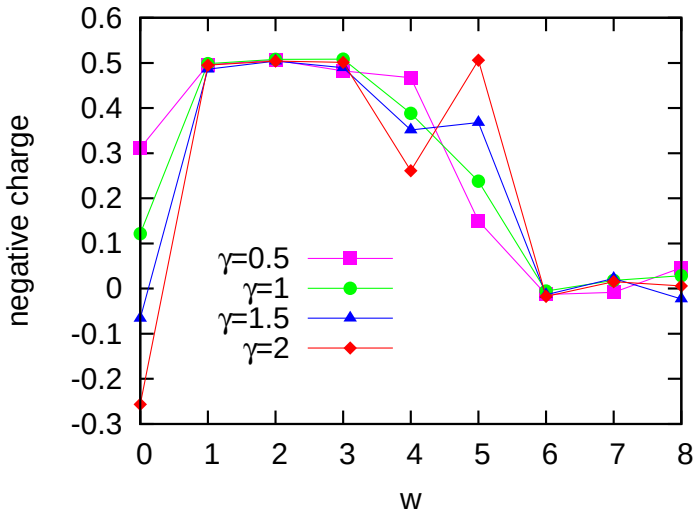

Figure 4.8: Witten effect for different values of γ, but all other parameters the same as in Fig. 4.7. We see that near $w = 2$, when we are measuring the charge inside a sphere which surrounds exactly one monopole, the amount of charge is approximately one-half, and independent of γ. At smaller w (or at $w \gtrsim 4$ when the sphere starts overlapping with the screening cloud near the second monopole), the enclosed charge does depend on γ.

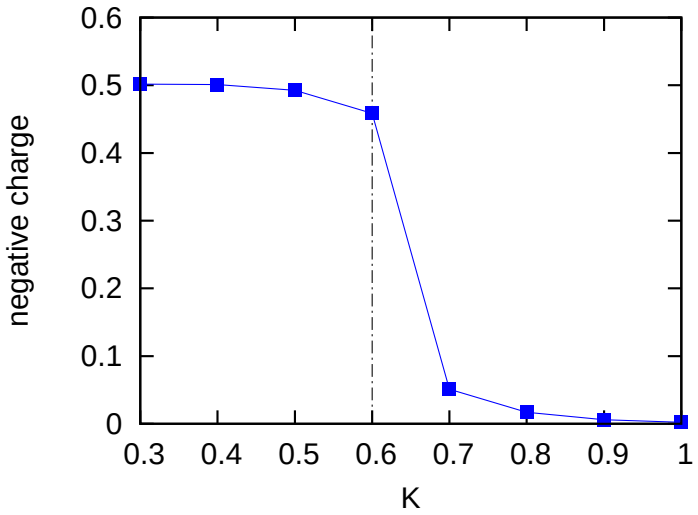

Figure 4.9: A demonstration of how the Witten effect can be used to detect phase transitions. The plot shows the amount of charge enclosed by a sphere with $w = 1$, while changing K but keeping all other parameters the same as in Fig. 4.7. We can compare to Fig. 4.6, and see that at $K = 0.6$, when the system transitions from the topological phase to the Coulomb phase, the 1/2-quantization of the enclosed charge abruptly stops.

the Coulomb phase the amount of charge isn't necessarily zero, but it is not quantized and in our simulations we found it to be zero.) We also observe the disappearance of the bound charge when the system undergoes a transition to trivial insulator as η is decreased to zero.

4.3.3 Surface Phase Diagram

The measurement of the Witten effect is evidence that our binding phase is a bosonic topological insulator. We can now study the exotic physics on the surface of this topological phase. We expect to find the surface phases predicted in Ref. [28].

We begin with some analytical arguments that provide a microscopic derivation of the surface field theory proposed in Ref. [28]. We define the surface as in Sec. 4.2.2. To uncover the exotic physics, we begin by performing a change of variables from the physical boson currents $J_\mu(r)$ to new integer-valued variables

$$G_\mu(r) \equiv J_\mu(r) - \eta(r) Q_\mu(r) \,, \tag{4.29}$$

which satisfy

$$\left(\sum_\mu \nabla_\mu G_\mu \right)(x,y,z,\tau) = \delta_{z,z_R} Q_z(x,y,z_R-1,\tau) - \delta_{z,z_L} Q_z(x,y,z_L-1,\tau) \,.$$

The action for the spins and the new $G_\mu(r)$ variables is simply

$$S = S_{\text{spin}} + \sum_{r,\mu} \frac{\lambda_\mu(r)}{2} \Big[G_\mu(r) \Big]^2 \,. \tag{4.30}$$

For simplicity, from now on we consider situation where the trivial phase region and the SPT phase region are deep in their respective phases: in particular, $\lambda_{\rm bulk}$, defined as in Eq. (4.14), is very large. At first we further simplify the situation by taking $\lambda_{\rm surf}$ to be very large, in which case we expect the variables $G_\mu(R)$ to be zero everywhere. We also assume that β is small everywhere, so the spin variables want to be deep in the disordered phase. However, near the two surfaces, the spin configurations must satisfy

$$\begin{aligned} Q_z(x,y,z_R-1,\tau)&=0,\\ Q_z(x,y,z_L-1,\tau)&=0. \end{aligned} \tag{4.31}$$

Focusing on the spins near one surface, say at z_R, we can view $Q_z(x,y,z_R-1,\tau)$ as simply hedgehog numbers in the corresponding (2+1)D spin system spanned by sites $(X,Y,Z=z_R-1/2,T)$, and the above conditions correspond to complete suppression of hedgehogs in this spin system. Such a (2+1)D Heisenberg $O(3)$ spin model with hedgehog suppression was studied in Ref. [82] and argued to be described by a *non-compact* CP^1 field theory ($NCCP^1$). On a simple (2+1)D cubic lattice, the Heisenberg model with complete hedgehog suppression actually has spontaneous magnetic order of spins even when the direct spin-spin interactions are zero.[80, 79] However, more generic such models can have a spin-disordered phase with a propagating "photon,"[79, 82] as well as other phases such as coexistence of the magnetic order and the propagating photon.[87] We will see that our findings in the present simulations on the surface of the bosonic TI region are consistent with these earlier results.

Let us now proceed more systematically and, in particular, show how we obtain a generic $NCCP^1$ model on the surface of the bosonic TI region. For simplicity, we take $\lambda_{\rm bulk}$ to be very large. For finite $\lambda_{\rm surf}$, we need to keep G_x, G_y, G_τ degrees of freedom in the (2+1)D "layer" at z_R, while all other $G_\mu(r)$ are zero. Focusing on the spin variables residing on sites $(X,Y,Z=z_R-1/2,T)$, the hedgehogs in this (2+1)D system are given precisely by $Q_z(x,y,z_R-1,\tau)$, which we will denote simply as $Q(x,y,\tau)$. The structure of the surface theory is

$$S_{\rm surface} \;=\; S_{\rm matter-gauge} + \frac{K}{2}\sum(\boldsymbol{\nabla}\times\boldsymbol{a}-2\pi\boldsymbol{B})^2 + \frac{\lambda_{\rm surf}}{2}\sum \boldsymbol{G}^2\,, \tag{4.32}$$

subject to constraints

$$\nabla_x G_x+\nabla_y G_y+\nabla_\tau G_\tau \equiv \boldsymbol{\nabla}\cdot\boldsymbol{G} = Q(x,y,\tau)\equiv \boldsymbol{\nabla}\cdot\boldsymbol{B}\,. \tag{4.33}$$

Here $S_{\rm matter-gauge}$ represents the first term in Eq. (4.19) restricted to the surface degrees of freedom. The above is a 3D statistical mechanics model, and a_μ, $(\nabla\times a)_{\mu\nu}\equiv\nabla_\mu a_\nu-\nabla_\nu a_\mu$, and $B_{\mu\nu}$ from Eq. (4.19) can be now defined as 3-vectors and are denoted by bold-face (e.g., μ-th component of $\boldsymbol{B}$ is $\frac{1}{2}\epsilon_{\mu\nu\rho}B_{\nu\rho}$). We have suppressed position indices to simplify notation.

This surface theory has spins plus integer-valued "currents" G_μ sourced and sinked by the hedgehogs of

the spin system. When the "line tension" $\lambda_{\rm surf}$ for the lines formed by these "currents" is large, we intuitively expect that the hedgehogs of the spin system are linearly confined. It is not immediately clear, however, what happens when $\lambda_{\rm surf}$ is small. Below we argue that the surface is still qualitatively described by the same "hedgehog-suppressed" field theory, which, however, can be in different regimes and have several different phases.

We can deal with the constraints in the partition sum by changing to new variables

$$\boldsymbol{B}' = \boldsymbol{B} - \boldsymbol{G}\,, \tag{4.34}$$

which satisfy

$$\boldsymbol{\nabla}\cdot\boldsymbol{B}' = 0\,. \tag{4.35}$$

The action becomes

$$S_{\rm surface} = S_{\rm matter-gauge} + \frac{K}{2}\sum(\boldsymbol{\nabla}\times\boldsymbol{a} - 2\pi\boldsymbol{B}' - 2\pi\boldsymbol{G})^2 + \frac{\lambda_{\rm surf}}{2}\sum\boldsymbol{G}^2\,.$$

There are now no constraints on the $\boldsymbol{G}$ variables, and we can formally sum these out to obtain a local action which is a function of $\boldsymbol{\nabla}\times\boldsymbol{a} - 2\pi\boldsymbol{B}'$,

$$S_{\rm surface} \quad = \quad S_{\rm matter-gauge} + S_{\rm gauge,eff}[\boldsymbol{\nabla}\times\boldsymbol{a} - 2\pi\boldsymbol{B}']. \tag{4.36}$$

However, any such action with the compact variables $\boldsymbol{a}$ and divergenceless, integer-valued $\boldsymbol{B}'$ can be formally viewed as describing a non-compact gauge field! In the limit of large $\lambda_{\rm surf}$, the effective action will have essentially lattice Maxwell form with stiffness K, while for intermediate to small $\lambda_{\rm surf}$ the gauge field energy will have more complicated but still local form. Thus, the field theory at the surface has the spinon matter fields coupled to a non-compact gauge field. In particular, we expect that the surface can be in the same phases as the (2+1)D easy-plane $NCCP^1$ model.

We can also study how the surface action is coupled to the external gauge fields introduced in Eq. (4.24). The minimal coupling between J_μ and $A^{\rm ext}_{2\mu}$, combined with the change of variables in Eq. (4.29), leads to the following term:

$$i\sum_{r,\mu} G_\mu(r)A^{\rm ext}_{2\mu}(r) + i\sum_{r,\mu}\eta(r)Q_\mu(r)A^{\rm ext}_{2\mu}(r)\,. \tag{4.37}$$

It is convenient here to represent $Q_\mu(r)$ as

$$Q_\mu(r) = \frac{1}{2}\epsilon_{\mu\nu\rho\sigma}\nabla_\nu\left(B_{\rho\sigma} - \frac{\nabla_\rho a_\sigma - \nabla_\sigma a_\rho}{2\pi}\right)\,, \tag{4.38}$$

where we have added a formal zero to the defining Eq. (4.20). Using this in the preceding equation and integrating the second term by parts, we find both an additional bulk term as well as a surface term which

results from taking a derivative of $\eta(r)$. Focusing again on the (2+1)D layer at z_R, we can write the surface contributions as

$$i\sum\left(\boldsymbol{G}+\frac{\boldsymbol{\nabla}\times\boldsymbol{a}}{2\pi}-\boldsymbol{B}\right)\cdot\boldsymbol{A}_2 = i\sum\frac{\boldsymbol{\nabla}\times\boldsymbol{\alpha}}{2\pi}\cdot\boldsymbol{A}_2\,, \tag{4.39}$$

where we defined

$$\boldsymbol{\nabla}\times\boldsymbol{\alpha}\equiv\boldsymbol{\nabla}\times\boldsymbol{a}-2\pi\boldsymbol{B}'\,, \tag{4.40}$$

which is precisely the flux of the *non-compact* gauge field identified in Eq. (4.36). When this is combined with Eq. (4.36), we are left with an effective action for the surface with schematic Lagrangian density

$$\left|\left(\boldsymbol{\nabla}-i\boldsymbol{\alpha}\mp i\frac{\boldsymbol{A}_1^{\text{ext}}}{2}\right)z_{\uparrow/\downarrow}\right|^2+\frac{\kappa}{2}(\boldsymbol{\nabla}\times\boldsymbol{\alpha})^2+i\frac{\boldsymbol{\nabla}\times\boldsymbol{\alpha}}{2\pi}\cdot\boldsymbol{A}_2\,.$$

This action, which we derived from our lattice model, has precisely the easy-plane $NCCP^1$ form proposed in Ref. [28]. In claiming that this is the correct effective action of the surface, we have neglected bulk terms which in general may also contribute to the surface response properties. We do not have an analytical justification for this choice, though from the Monte Carlo study presented in Sec. 4.3.5 we find that essentially only the surface terms given above contribute to the measured response properties, and it seems plausible that our argument applies in the limit of a sharp boundary between the topological and trivial phases deep in their respective regimes.

Note that the above arguments were based on the assumption that the $U(1)$ and $\mathbb{Z}_2^T$ symmetries were preserved in the bulk. If the $U(1)$ symmetry is broken in the bulk, the entire derivation of Eq. (4.32) based on conserved currents is invalid. On the other hand, if only the time reversal is broken in the bulk, the derivation naively holds, but in the matter-gauge sector there is no reason for $z_\uparrow$ and $z_\downarrow$ to enter symmetrically—in particular, no reason for them to carry precise $+1/2$ and $-1/2$ charges, and the field theory written above is not valid. (In fact, the system will have non-quantized σ_{xy} proportional to the length of the system in the z-direction). Since when the symmetry is broken the bulk ceases to be a topological phase, we of course should not expect exotic physics on the surface in this case.

We can confirm the above arguments, which were made in some simplifying limits, by studying the system in Monte Carlo. We can determine the phase diagram of the surface by looking at singularities in the heat capacity. We can also study the magnetization and current-current correlators as described in the previous section. In this phase diagram we set the bulk parameters so that the system is in the topological phase; specifically, we take $\beta_{\text{bulk}}=0.2$, $K_{\text{bulk}}=0.2$, and $\lambda=8$ (cf. bottom panel of Fig. 4.6). We then vary the surface parameters and obtain the phase diagram shown in Fig. 4.10, which is in good agreement with the phase diagram of the $NCCP^1$ model in the literature. Labels on the phase diagram are taken from Ref. [87], and their relation to labels in Fig. 4.3 is described below. There are three phases in the diagram. At small β_{surf} the $\phi_{\uparrow,\downarrow}$ variables are disordered, conserving the $U(1)_{\text{spin}}$ symmetry; the $U(1)_{\text{boson}}$ symmetry

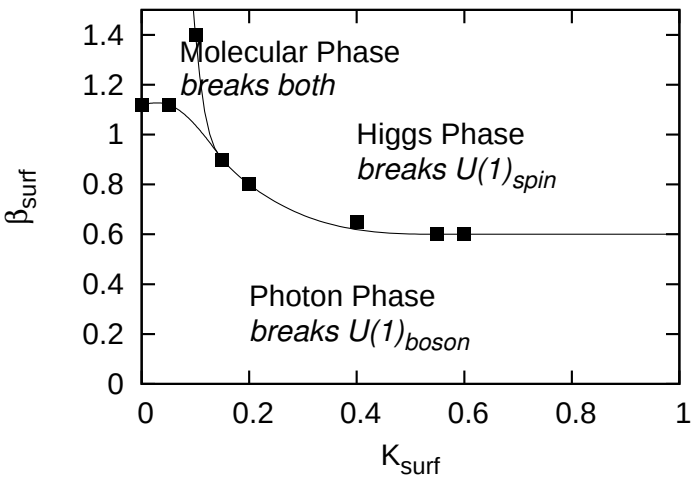

Figure 4.10: Surface phase diagram on the boundary of the SPT phase in the model with a CP^1 version of the spins. The bulk parameters are $\beta_{\rm bulk} = 0.2$, $K_{\rm bulk} = 0.2$, $\lambda = 8$, and the surface parameters are varied. The phase diagram has the same structure as the one found in the $NCCP^1$ model in Ref. [87]. The phases are the same as those in Fig. 4.3, though in this figure we have replaced the $SO(3)$ symmetry with $U(1)_{\rm spin}$, and the $\beta_{\rm surf}$ axis is oriented horizontally in Fig. 4.3 and vertically in the present figure.

is broken and the corresponding Goldstone mode is precisely the propagating photon in the $NCCP^1$ theory on the surface, hence the label "Photon Phase" in Fig. 4.10. At large $\beta_{\rm surf}$, $K_{\rm surf}$ the partons $z_\uparrow$, $z_\downarrow$ are condensed, leading to a "Higgs Phase" (in the $NCCP^1$ language) in which the $U(1)_{\rm spin}$ symmetry is broken but the $U(1)_{\rm boson}$ symmetry is preserved. Finally at large $\beta_{\rm surf}$ and small $K_{\rm surf}$ both the $U(1)_{\rm spin}$ and $U(1)_{\rm boson}$ symmetries are broken. In the $NCCP^1$ language, the individual $z_\uparrow$ and $z_\downarrow$ are gapped so the gauge field a_μ is free to fluctuate, but the "molecular field" $\Psi_{\rm mol} \sim z_\uparrow^\dagger z_\downarrow$, which is precisely the easy-plane spin field, $\Psi_{\rm mol} \sim n_a + i n_b$, becomes ordered, hence the label "Molecular Phase" in Fig. 4.10. We emphasize that the microscopic model we are simulating in (3+1)D has a compact gauge field, and we are detecting the presence or absence of $U(1)_{\rm spin}$ and $U(1)_{\rm boson}$ symmetry breaking on the surface by direct measurements. It is remarkable that the surface phase diagram is captured by the $NCCP^1$ field theory with *non-compact* gauge field!

All of the phases in Fig. 4.10 break either a $U(1)_{\rm spin}$ or a $U(1)_{\rm boson}$ symmetry and are therefore superfluids. As in the previous section, without access to the properties of their gapped excitations we cannot directly confirm that they are the predicted surface phases. As in the previous section, our phase diagram contains a direct transition between the superfluid phases, which can be viewed as providing some evidence for the proposed surface physics and is also predicted to be a deconfined critical point.[28]

4.3.4 Symmetric Surface Phase with Topological Order

Vishwanath and Senthil proposed that it is also possible to have a surface phase which is gapped and breaks no symmetries but has intrinsic topological order.[28] Since this phase is not featured in Fig. 4.10, we need to add another term to our surface action in order to push the system into this phase. The term we need to add

is the following parton "pair hopping term:"[28, 29]

$$S_{\rm pair} = -t_{\rm pair} \sum_{R,\mu} \cos[\nabla_\mu(\phi_\uparrow + \phi_\downarrow) - 2a_\mu], \tag{4.41}$$

where we have included proper coupling to the gauge fields. Note particularly that the pair field $\Psi_{\rm pair} \sim z_\uparrow z_\downarrow$ does not carry $U(1)_{\rm spin}$ charge. We can now see what happens to the surface phase diagram (Fig. 4.10) when we increase $t_{\rm pair}$ trying to induce condensation of $\Psi_{\rm pair}$. For sufficiently large $t_{\rm pair} = 2$, we get the phase diagram in Fig. 4.11. We see that a new phase has opened up at small $\beta_{\rm surf}$ and large $K_{\rm surf}$, where, as we will argue, $\Psi_{\rm pair}$ is condensed while the individual $z_\uparrow$ and $z_\downarrow$ are gapped.

When all the couplings $\beta_{\rm surf}$, $K_{\rm surf}$, and $t_{\rm pair}$ are small, there is nothing which can order the spins or gap the bosons. Therefore we are in the photon phase, which conserves $U(1)_{\rm spin}$ and breaks $U(1)_{\rm boson}$. To get a pairing phase with no broken symmetries, we need to restore the $U(1)_{\rm boson}$ symmetry without breaking the $U(1)_{\rm spin}$ symmetry, which can be acheived by condensing $\Psi_{\rm pair}$. Let us first recall how the various terms in the action change the system. The $\beta_{\rm surf}$ term allows hopping of the partons $z_{\uparrow,\downarrow}$, but even when this hopping is strong the fluctations in the gauge field a_μ when $K_{\rm surf}$ is small prevent the partons from condensing. The combination $\Psi_{\rm mol} \sim z_\uparrow^\dagger z_\downarrow$ can condense, and this breaks $U(1)_{\rm spin}$ and takes us to the molecular phase. We can see from Fig. 4.10 that the $K_{\rm surf}$ term on its own does not change the phase of the system if $\beta_{\rm surf}$ is kept small. However, when it is combined with the $\beta_{\rm surf}$ term it can prevent fluctations in the a_μ field. This gaps the photon, and allows $z_\uparrow$ and $z_\downarrow$ to condense. This gives us the Higgs phase, where the $U(1)_{\rm boson}$ symmetry has been restored, but the $U(1)_{\rm spin}$ symmetry has been broken.

With this in mind, we can see why the $t_{\rm pair}$ term brings us into the topological phase. The $t_{\rm pair}$ term is similar to the $\beta_{\rm surf}$ in that it is also a hopping term, though it hops pairs of partons. Therefore when both $t_{\rm pair}$ and $\beta_{\rm surf}$ are large the two terms cooperate, which is why the $U(1)_{\rm spin}$ symmetry breaks at lower $\beta_{\rm surf}$ in Fig. 4.11 than in Fig. 4.10. However, when $\beta_{\rm surf}$ is absent, the $t_{\rm pair}$ only hops pairs of spinons, and so it can condense $\Psi_{\rm pair}$ without condensing the individual $z_{\uparrow,\downarrow}$ or $\Psi_{\rm mol}$. When the $t_{\rm pair}$ term is combined with the $K_{\rm surf}$ term the fluctuations of a_μ are gapped. Therefore the phase at large $t_{\rm pair}$, large $K_{\rm surf}$, and small $\beta_{\rm surf}$ can restore $U(1)_{\rm boson}$ without breaking $U(1)_{\rm spin}$, and this is the phase we are looking for.

We have confirmed that the pairing phase breaks neither $U(1)$ symmetry by direct measurements in the spin and boson sectors. Also, $\Psi_{\rm pair}$ is invariant under the $\mathbb{Z}_2^T$ symmetry in Eq. (4.22), so this symmetry is not broken either, and we indeed do not observe any Hall response on the surface. Therefore we believe that this phase is the fully symmetric gapped phase envisioned by Vishwanath and Senthil, which they argued has intrinsic topological order. Specifically, we expect to have gapped spinon excitations carrying 1/2 of the $U(1)_{\rm spin}$ charge; at the same time, we also have vortices in the $\Psi_{\rm pair}$ field which carry 1/2 of the unit flux of the a_μ gauge field and hence 1/2 of the $U(1)_{\rm boson}$ charge; finally, the spinons and the vortices in $\Psi_{\rm pair}$ clearly have mutual statistics of π. Unfortunately, we do not have simple direct measurements to confirm the topological order on the surface. However, the indirect evidence for this scenario is very strong.

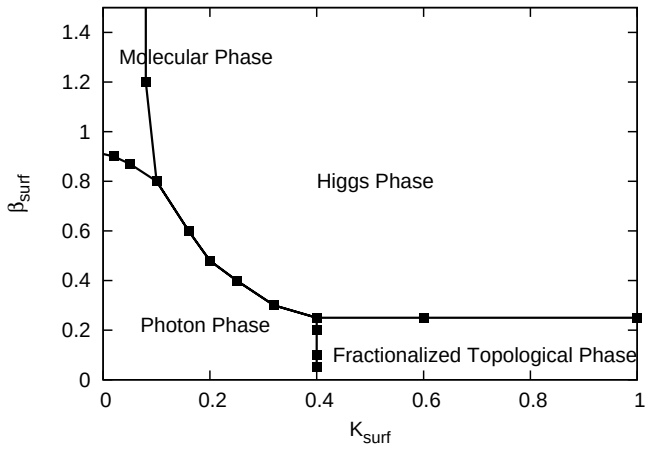

Figure 4.11: Surface phase diagram for the easy-plane CP^1 version of the model, with the additional pairing term on the surface given by Eq. (4.41). This diagram was obtained for $\beta_{\rm bulk} = 0.2$, $K_{\rm bulk} = 0.2$, $\lambda = 8$, and on the surface $t_{\rm pair} = 2$, $\beta_{\rm surf}$ and $K_{\rm surf}$ varied. Compared to Fig. 4.10, we see that there is a new phase at small $\beta_{\rm surf}$ and large $K_{\rm surf}$. We expect that this surface phase is fully symmetric and has intrinsic topological order.

Thus, it is suggestive to compare Fig. 4.11 with the phase diagram obtained in Fig. 1 of Ref. [45]. In that work, we studied a (2+1)D model with $U(1) \times U(1)$ symmetry and mutual statistics between two different species of bosons. When the mutual statistics is π, we get a phase diagram with the same topology as Fig. 4.11. The phase diagram contains a topological phase, two phases where one of the $U(1)$ symmetries is broken, and a phase where both symmetries are broken. There is a direct transition between the phases with one broken symmetry, which, if it were continuous, is a candidate for a deconfined critical transition.[48] The surface of our bosonic topological phase is thought to have a similar field theory to that in our previous work,[45, 48] and so we expect that the interpretations of the phases and phase transitions are the same in both models. We also remark that in Ref. [49] we presented a microscopic local Hamiltonian which has a topological phase with the same content of excitations. However, that phase also breaks $\mathbb{Z}_2^T$ symmetry and in particular has $\sigma_{xy} = 1/2$, while the present surface phase respects $\mathbb{Z}_2^T$ and has no Hall response.

4.3.5 Time-Reversal Breaking and Hall Effect on the Surface

Vishwanath and Senthil[28] predict another exotic phase on the surface of the bosonic topological insulator—a phase which breaks the $\mathbb{Z}_2^T$ symmetry and has a Hall conductivity quantized to an odd integer (in units of $\frac{e^2}{h}$). We can test this prediction in our Monte Carlo simulations. The first step is to break the $\mathbb{Z}_2^T$ symmetry on the surface. By examining Eq. (4.22), we see that one way to break the symmetry is to replace the parameter β in Eq. (4.19) by the parameters $\beta_\uparrow$ and $\beta_\downarrow$, which appear in the terms containing $\phi_\uparrow$ and $\phi_\downarrow$ respectively. When $\beta_\uparrow \neq \beta_\downarrow$, the $\mathbb{Z}_2^T$ symmetry is broken; this is roughly like applying the Zeeman field in Sec. 4.2.1.1.

We start with $K = 0.4$ and $\lambda = 8$ everywhere, $\beta_{\rm bulk} = 0.2$, and $\beta_\uparrow = \beta_\downarrow = 0.2$ on the surface. This system will have its bulk in the topological phase, and its surface in the photon phase. We break the $\mathbb{Z}_2^T$

symmetry on one of the surfaces by increasing $\beta_\uparrow$. We expect that a small increase will not change the properties of the system very much, since $z_\uparrow \sim e^{i\phi_\uparrow}$ and $z_\downarrow \sim e^{i\phi_\downarrow}$ will still be gapped.[82] However, as $\beta_\uparrow$ is further increased, $z_\uparrow \sim e^{i\phi_\uparrow}$ "condenses" and vortices in the $\phi_\uparrow$ variables will become gapped. In our simulations we see a singularity in the specific heat measured on the surface, indicating that the system has entered a new phase. We expect that this is the phase that will have Hall conductivity quantized at odd integer. In our simulations we also break time-reversal symmetry in the opposite direction on the other surface by increasing $\beta_\downarrow$. As discussed in Sec. 4.2.2, in this setup the top and bottom surface taken together have Hall conductivity adding to two.

We can see that unlike in the Heisenberg model, Eq. (4.19) is a differentiable function of the probing fields A_1 and A_2, and so we know how to properly couple the external gauge fields and can use linear response theory to compute the Hall conductivity. If our system has a non-zero Hall conductivity, then we can imagine integrating out the internal degrees of freedom to get the following effective action in terms of the external fields at the surface:

$$S_{\text{eff}} = i \sum_{\text{surface}} \frac{\sigma_{xy}^{12}}{4\pi} [\boldsymbol{A}_1 \cdot (\boldsymbol{\nabla} \times \boldsymbol{A}_2) + \boldsymbol{A}_2 \cdot (\boldsymbol{\nabla} \times \boldsymbol{A}_1)] \,, \tag{4.42}$$

where bold face denotes three-component vectors appropriate for the (2+1)D surface, e.g., $\boldsymbol{A}_1 = (A_{1x}, A_{1y}, A_{1\tau})$, and the above form specifies our convention for σ_{xy}^{12} (these units are such that $e^2/h = 1$). By taking, e.g., $\boldsymbol{A}_1 = (A_{1x}, 0, 0)$ and $\boldsymbol{A}_2 = (0, A_{2y}, 0)$, we have

$$S_{\text{eff}} \quad = \quad -i \sum_{\text{surface}} \frac{\sigma_{xy}^{12}}{2\pi} A_{1x} \nabla_\tau A_{2y} \,. \tag{4.43}$$

Going to momentum space, we can obtain the Hall conductivity by:

$$\sigma_{xy}^{12}(k) = \lim_{A_1, A_2 \to 0} \frac{2\pi}{2\sin(\frac{k_\tau}{2})} \frac{\partial^2 \ln Z}{\partial A_{1x}(k) \partial A_{2y}(-k)} \,, \tag{4.44}$$

where Z is the partition sum, and we also took $k = (0, 0, k_\tau)$. Note that $\boldsymbol{A}_1$ and $\boldsymbol{A}_2$ reside on lattices dual to each other, and when defining the Fourier transforms we take the convention to transform in the absolute coordinates of the origins of the links (namely, lattice sites on the dual lattice have absolute coordinates displaced from the direct lattice by half of lattice spacing). Starting from the microscopic model, we can evaluate this conductivity from the current-current correlation functions:

$$\sigma_{xy}^{12}(k) = \frac{2\pi}{2\sin(\frac{k_\tau}{2})} \langle \xi_x(-k) J_y(k) \rangle \,, \tag{4.45}$$

where the $U(1)_{\text{spin}}$ current on a link R, μ is

$$\xi_\mu(R) \equiv \frac{i}{2} \left[\beta_\uparrow \sin(\nabla_\mu \phi_\uparrow - a_\mu) - \beta_\downarrow \sin(\nabla_\mu \phi_\downarrow - a_\mu) \right] \,.$$

The measurements are performed at the smallest wave-vector $k_{\min} = (0, 0, 2\pi/L)$, as described in Section 4.2.1.

Note that the above conductivity measures the response of the $U(1)_{\text{spin}}$ currents to applied fields coupled to the bosons (or vice-versa). To study SPTs with single $U(1)$, we can take the usual approach in the literature[28] and "glue" the $U(1)_{\text{spin}}$ and $U(1)_{\text{charge}}$ by identifying A_1 and A_2 in Eq. (4.42); the conventional definition of σ_{xy} in the case with single $U(1)$ is then related to the above σ_{xy}^{12} via $\sigma_{xy} = 2\sigma_{xy}^{12}$. In particular, when the gauge fields are identified the Hall conductivity of a two-dimensional system of bosons is quantized to 2 times an integer (in units of e^2/h), while the Hall conductivity on the surface of a topological phase is an odd integer. Therefore where we present numerical values we show $2\sigma_{xy}^{12}$ so that the results can be easily compared to the literature values.

Figure 4.12 shows our numerical measurements of the Hall conductivity. The horizontal axis is the strength of the $\mathbb{Z}_2^T$ symmetry breaking, which we will loosely call Zeeman field. We see that initially there is no quantized Hall conductivity, until the Zeeman field is strong enough to forbid one species of vortex (realized here by "condensing" the corresponding spinon species). At this point the Hall conductivity increases and reaches the value of approximately 1. Though the value observed is actually slightly less than 1, we believe that a large part of this is a finite-size effect, and indeed as the system size is increased the Hall conductivity gets closer to the expected value. Note that we performed this measurement at precisely $z = z_R$. It is *a priori* possible that the Hall conductivity could be spread among several values of z near the surface, but this spreading is apparently very small, so that including additional layers does not change the result. In addition to the plot shown, we have performed the same measurement for several different values of K, β, and λ, and found that the quantized result is independent of these parameters as long as the bulk stays in the topological phase. This odd integer cannot be observed in a purely two-dimensional system with only short-ranged entanglement, and therefore this observation shows that we are measuring the Hall conductivity on the surface of a bosonic TI.

4.4 Realizing symmetry-enriched topological phases by binding multiple hedgehogs to a boson

In all of the above sections, we have studied a system where a single boson is bound to a single hedgehog. In this section we will describe the new physics which arises when our system contains bound states of a boson and multiple hedgehogs. We induce such a binding by making the following modification to Eq. (4.1):

$$S = S_{\text{spin}} + \frac{\lambda}{2} \sum_{r,\mu} [dJ_\mu(r) - Q_\mu(r)]^2. \tag{4.46}$$

Here d is an integer, and for large λ the action will bind a boson to d hedgehogs, since the λ term is minimized by $(Q, J) = (d, 1) \times$ integer.

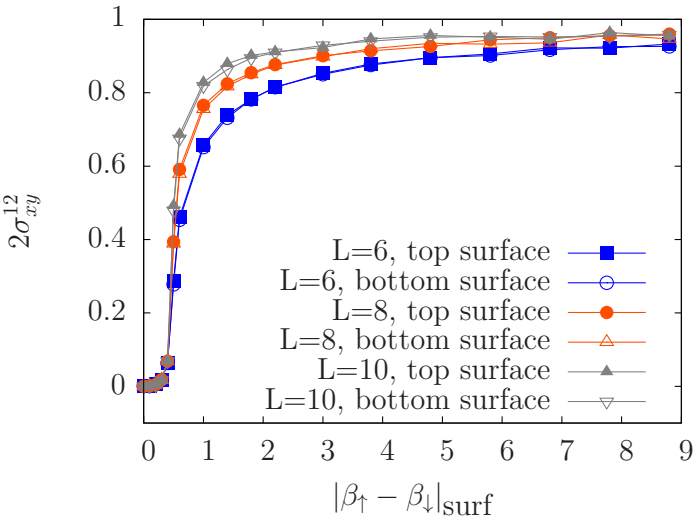

Figure 4.12: Hall conductivity on the surface of the binding phase realized in the CP^1 version of the model, measured in units of e^2/h (see text for details). On each surface we find that the conductivity is quantized to 1, and this odd-integer value shows that we are on the surface of a bosonic TI. Data was taken for $K = 0.4$, $\lambda = 8$, $\beta_\downarrow = \beta_{\rm bulk} = 0.2$. We measure the same conductivity on both the top and bottom surfaces of the topological phase.

When $d \neq 1$ the change of variables in Eq. (4.6) can no longer be applied. Therefore the phase diagram in this case will be different from the $d = 1$ case. We can determine the phase diagram by performing Monte Carlo simulations. As an example, the phase diagram for $d = 3$ is shown in Fig. 4.13. Phase boundaries were determined from singularities in the specific heat. Note that in the Heisenberg model we can define a maximum of one hedgehog per lattice site, and so this model cannot easily be used to describe the binding of multiple hedgehogs. Therefore all results for $d \neq 1$ come from the easy-plane CP^1 model for the spins.

Figure 4.13 presents the phase diagram in the variables λ and K, with fixed $\beta = 0.1$. At small λ and K, there is no energy cost for either hedgehogs or bosons, and they are independent. This leads to a paramagnet of spins and a superfluid of bosons. The $U(1)_{\rm spin}$ symmetry is preserved, and the $U(1)_{\rm boson}$ symmetry is broken. In contrast, at large λ and K both hedgehog and boson currents are forbidden, leading to a Coulomb phase of spins and an insulator of bosons. Here both the $U(1)_{\rm spin}$ and $U(1)_{\rm boson}$ symmetries are preserved, but the spin system has intrinsic topological order. At large K but small λ, the Coulomb phase of the spin system survives and the hedghogs are gapped, but the bosons are condensed breaking the $U(1)_{\rm boson}$ symmetry. On the other hand, at very small K and large λ the hedgehogs are proliferated and bosons are bound to them, and we are in the binding phase; here, neither symmetry is broken, and we will argue shortly that this is a Symmetry Enriched Topological (SET) phase.

Note that similar phase diagram (at fixed small β) for $d = 1$ contains only such four phases, where the binding phase is the SPT phase discussed in the previous sections. For $d = 1$ these are the only phases, and due to the change of variables in Eq. (4.6), the phase boundaries are all straight lines. With $d \neq 1$, we have a new phase in the middle of the diagram, and no direct transition from the phase in the lower right to

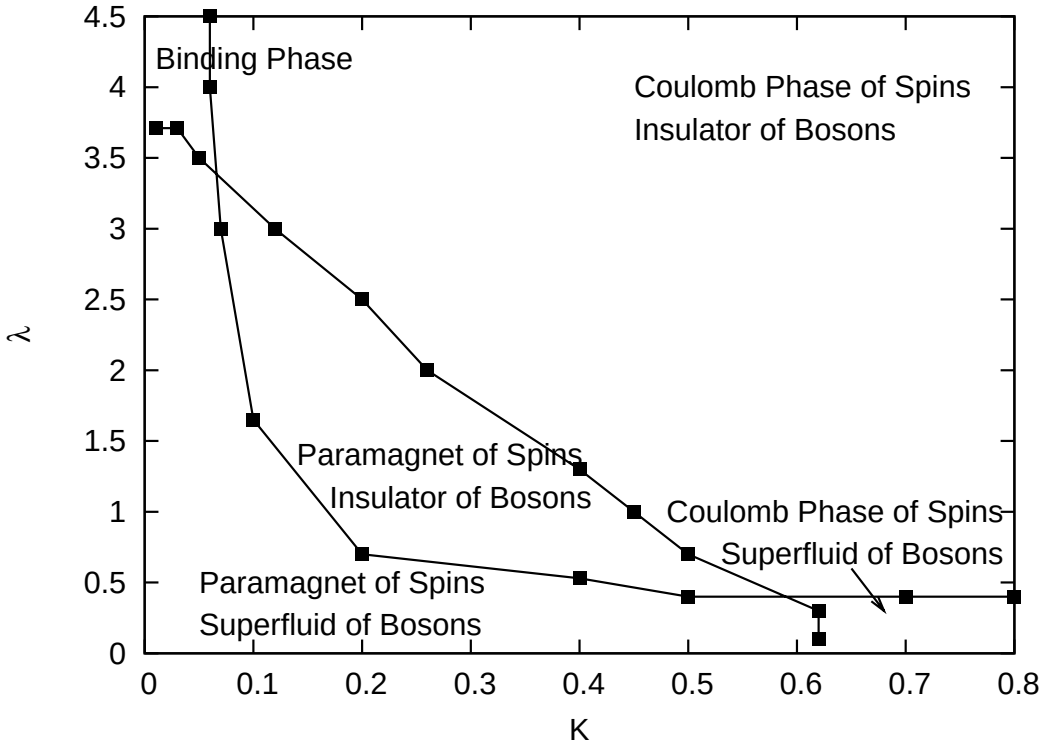

Figure 4.13: Bulk phase diagram for the model described in Eqs. (4.19) and (4.46), with $d = 3$ and small $\beta = 0.1$. We can compare this to the case of $d = 1$, where the middle phase is absent and the phase boundaries are straight vertical and horizontal lines; and to $d = 2$, where the middle phase is absent and there is a line of phase transitions between the paramagnet/superfluid phase in the lower left corner and the Coulomb/insulator phase in the upper right corner.

the binding phase. The middle phase can be understood as one in which hedgehog currents are proliferated, but their interactions are still too costly for objects with three hedgehogs and a boson to exist. Therefore such bound states are not proliferated, and individual bosons are also gapped. We expect that this phase preserves the $U(1)$ symmetries from both the spins and bosons and is conventional paramagnet/insulator. The topological phase only arises when K is lowered to the point that it does not penalize significantly objects with a hedgehog current of three and λ is increased to strongly penalize any objects other than the $(Q, J) = (3, 1)$ bound states; at this point these bound states can form and proliferate, and the system enters the topological phase. For other values of d, the phase diagram is expected to have a similar form, with the exception of $d = 2$, where in our studies of small system sizes the middle phase is not observed and there is a line of phase transitions between the lower left and upper right phases.

Let us now focus on the properties of the binding phase at large λ and small K, which binds d hedgehogs to a boson. This phase is distinct from the topological phase discussed earlier in this work. In particular, it has intrinsic topological order. Condensing bound states of d hedgehogs causes the electric field lines in the phase to fractionalize, i.e., it is possible to have electric field lines of strength $1/d$. These fractionalized electric field lines are one of the gapped excitations of the system. The other elementary gapped excitation is a single hedgehog, which binds a boson charge of $1/d$. The hedgehog has well-defined statistics as it encircles the electric field lines, and we expect it to acquire a phase of $2\pi/d$ when this happens around the elementary fractionalized line. The matter fields $z_\uparrow$ and $z_\downarrow$ are confined, but still act as sources and sinks for the electric field lines of integer strength, therefore the line topological excitations in the system are only defined up to an integer, and we can say that the system has $\mathbb{Z}_d$ topological order.[88, 52]

In the Appendix we formally demonstrate the above properties by first removing the spinon matter fields and considering a CQED$\times U(1)_{\text{boson}}$ system in which the monopoles of the compact electrodynamics are bound to bosons. Such CQED$\times U(1)_{\text{boson}}$ models allow changes of variables similar to those possible in $U(1) \times U(1)$ models demonstrating SPT and SET phases of bosons in two dimensions[49], which allow their properties to be readily determined. After the change of variables has been performed, we can couple the additional spinon matter fields to the CQED sector, and this gives us precisely the $CP^1 \times U(1)_{\text{boson}}$ model studied in this paper.

The Witten effect and Hall effect measurements can be extended to the cases with multiple hedgehogs. For the Witten effect, the amount of bound charge will be modified, since now for each hedgehog there is a boson charge of $1/d$. Therefore the screening cloud will have a charge of $1/(2d)$. We have studied the cases of $d = 2, 3$ in Monte Carlo and our results, shown in Fig. 4.14, confirm this expectation. Recall that when measuring the Witten effect we used a "biasing" term to break degeneracy between positive and negative internal monopoles. This biasing term may also introduces some excess internal monopole or boson charge at the location of the external monopole. This excess is screened by the surrounding system. In the $d = 1$ case, we found that for most values of γ, such as those shown in Fig. 4.8, the screening length is quite short and so the Witten effect can still be clearly observed. In the case of $d > 1$, the screening length seems to be

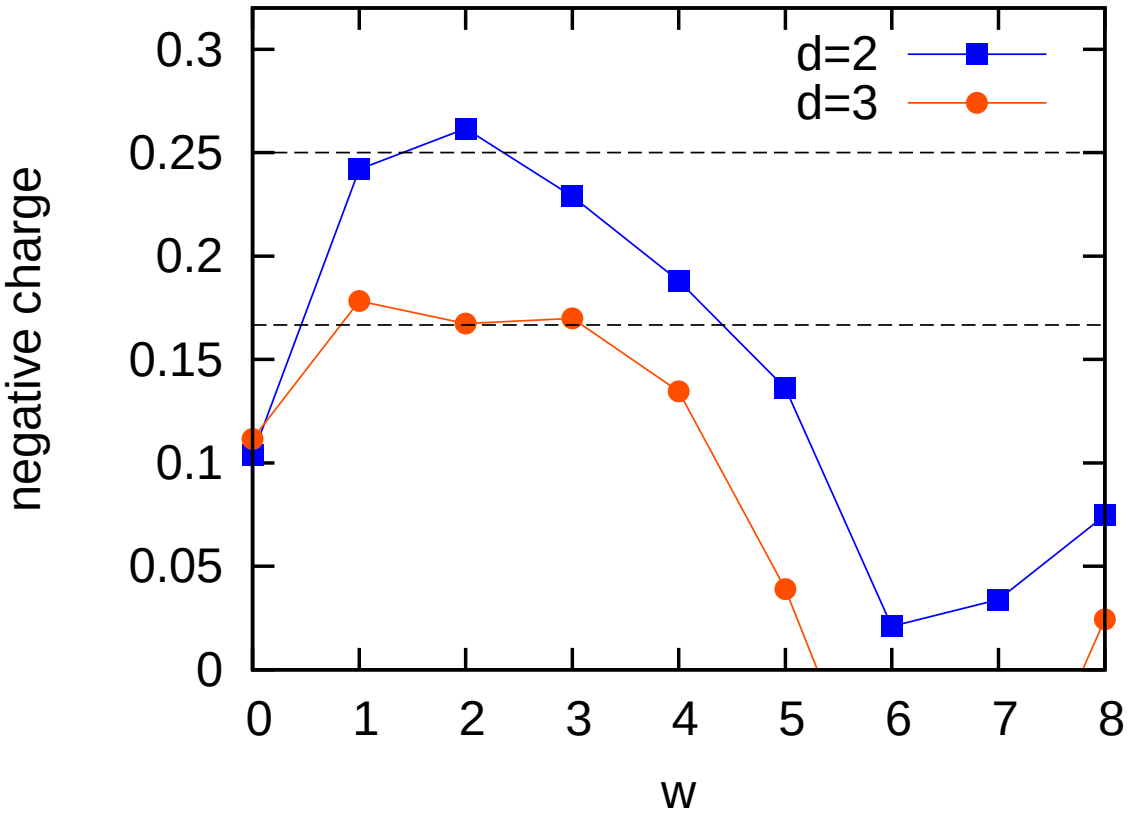

Figure 4.14: Witten effect measurement, similar to Fig. (4.7), but for the case where d hedgehogs are bound to each boson. The amount of bound charge is given by $1/(2d)$, as expected (indicated by dashed lines). Parameters K, β, and λ were chosen to put the bulk into the binding phase, while γ was chosen to minimize the amount of charge away from $w = 2$, though the value at $w = 2$ is independent of this choice.

much larger, which can lead to fluctuations of charge larger than the Witten effect we are trying to observe. We have chosen the biasing parameter in Fig. 4.14 in such a way as to minimize these fluctuations. At other values of γ the Witten effect can still be observed but the observation is less clear due to these fluctuations.

We have also measured the surface Hall effect upon breaking the $\mathbb{Z}_2^T$ symmetry on the surface by applying the Zeeman field as in Sec. 4.3.5. Our results for the Hall conductivity are shown in Fig. 4.15. We find that the surface Hall conductivity is given by $1/d$, which is one-half of the value found for a two-dimensional bosonic fractional quantum Hall effect.[49] We can again rationalize this observation by considering a slab of the binding phase as in Fig. 4.2 with the opposite Zeeman fields on the two surfaces, cf. discussion in the paragraph preceding Eq. (4.16).

4.5 Discussion and Conclusions

In this chapter we have constructed a three-dimensional bosonic topological insulator in a lattice model which can be studied in Monte Carlo. The model works by binding bosons to point topological defects (hedgehogs). We determined the phase diagram in both the bulk and on the surface of the model. We were able to numer-

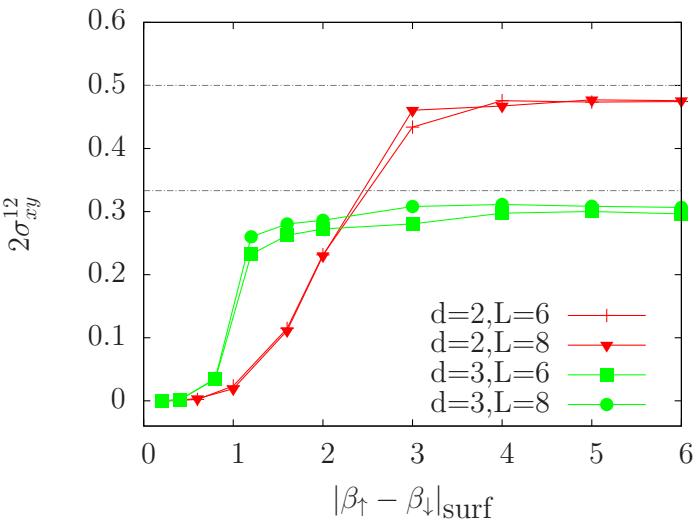

Figure 4.15: Surface Hall conductivity at a boundary of an SET phase for diffent values of d, in units of e^2/h. We see that the Hall conductivity is given by $1/d$. Both surfaces have been averaged over to improve statistics. Dashed lines are drawn at $1/d$ to guide the eye. Data was taken with $K = 0.2$, $\lambda = 8$. Different values of β_{bulk} were used for different values of d, since the phase diagram changes as d changes (see, for example, Fig. 4.13) and β_{bulk} needs to be chosen so that the system is in the topological phase.

ically extract signatures of the topological behavior: In the bulk of the model we observed a Witten effect, while on the surface with broken time-reversal symmetry we found a quantized Hall conductance with values distinct from those possible in a purely (2+1)D system. We also found other surface properties consistent with the bosonic TI, including a direct transition between surface phases with different broken symmetries, and a surface phase which breaks no symmetries and may possess topological order of a kind that would break $\mathbb{Z}_2^T$ in a purely (2+1)D system. Finally, we can also realize phases with intrinsic topological order in the bulk by binding multiple topological defects to each boson.

Our model can in principle be used to extract other properties of the bosonic topological insulator. One possible future direction is to determine the properties of the surface phase transitions, especially the transition between the two different surface superfluids. Another direction would be to find direct evidence of the exotic properties of the surface superfluids and surface topologically ordered phase. Such surface phases have generated much recent interest, as their excitations are expected to have properties not possible in a purely two-dimensional system.[28, 89, 90] It would also be interesting to investigate the surface physics of the SET phases discussed in Sec. 4.4.

In Chapter 3 on the two-dimensional bosonic topological phases, we were also able to reconstruct (starting from Euclidean space-time actions) explicit microscopic Hamiltonians which realized the bosonic integer and fractional quantum Hall effects. We have been unable to do the same in the present three-dimensional case, but this would be a very interesting result. More broadly, the idea of binding bosons to topological defects may continue to yield precise models of bosonic topological phases.

The model in the main text can be thought of as having either $U(1) \rtimes \mathbb{Z}_2^T$ or $U(1) \times \mathbb{Z}_2^T$ symmetry and in

both cases we are realizing the same phase. Based on the cohomology classification[15, 16], the symmetry $U(1) \rtimes \mathbb{Z}_2^T$ has a $\mathbb{Z}_2^2$ classification in three dimensions, i.e., there are two base phases with non-trivial topology, but one of the base phases comes from $\mathbb{Z}_2^T$ only. There is only one phase that involves $U(1)$ in a non-trivial manner, and it is this phase that we are realizing in our construction and its signature is the Witten effect, which we discuss and observe in Sec. 4.3.2. Our construction cannot access the phase that comes from the $\mathbb{Z}_2^T$ symmetry only because we require the $U(1)$ symmetry. In the $U(1) \times \mathbb{Z}_2^T$ case, the cohomology classification gives $\mathbb{Z}_2^3$, where one of the base phases is again from the $\mathbb{Z}_2^T$ alone, while the other two base phases involve $U(1)$ in a non-trivial manner. Of the latter two, again we are realizing the one which has the statistical Witten effect as its signature. The other base phase does not have the Witten effect, its signature is that the monopole is the Kramers doublet under time reversal.[28, 91] Our model in principle has more symmetries and could be also deformed to produce this other phase. We do not consider this here but it is a possible direction for future work. We are also not considering beyond cohomology phases, which bring yet another phase due to $\mathbb{Z}_2^T$ only in either case.[28, 92].

Chapter 5

DMRG study of a quantum Hall bilayer with filling $\nu = 1/3 + 1/3$

5.1 Introduction

When a two-dimensional semiconductor is placed in a strong perpendicular magnetic field, the energy of electrons in the system becomes independent of their momentum. Fermi liquid theory does not apply, and the system can realize a number of exotic phases. The integer quantum Hall effect was the first such phase to be discovered, it was also the first known example of a topological phase[2]. Not longer after this, the fractional quantum Hall effect was discovered[93], and this was the first example of a long-range entangled topological phase. The vast majority of observed fractional quantum Hall states belong to the Laughlin [18], hierarchy [94, 95] and "composite fermion" [96] states. These states realize quasiparticles which have fractional charge and statistics[18, 97, 98]. Even more exotic states, which host non-Abelian anyons, are also proposed to exist at certain quantum Hall fractions, most notably $\nu = 5/2$[39, 99, 100].

The quantum Hall states discussed above are 'single-species' quantum Hall systems, where the electrons have no internal degrees of freedom. However, "multicomponent" FQH states are ubiquitous; most obviously electrons carry spin. While the Coulomb energy scales as $e^2/\epsilon\ell_B[\mathrm{K}] \approx 50\sqrt{B[\mathrm{T}]}$, assuming free electron values for the mass and g factor in GaAs, the Zeeman splitting is only $E_Z[\mathrm{K}] \approx 0.3B[\mathrm{T}]$, suggesting that in many circumstances the ground state of the system may not be fully spin-polarized. Several classes of unpolarized FQH states have been formulated, including the so-called Halperin (mmn) states [101] and spin unpolarized composite fermion states [102, 103, 104, 105]. In materials such as AlAs or graphene, ordinary electron spin may furthermore combine with valley degrees of freedom, which can change the sequence of the observed integer and FQH states [106, 107, 108, 109, 110, 111, 112, 113, 114, 115].

In this Chapter we study an important class of multicomponent FQH systems where the internal degrees of freedom correspond to a subband or layer index, generally referred to as *pseudo-spin*. For example, if a 2DEG is confined by an infinite square well in the perpendicular z-direction, the effective Hilbert space may be restricted to several low-lying subbands of the quantum well (QW). In the most common case, the relevant

subbands are the lowest symmetric and antisymmetric subbands of the infinite square well that play the role of an effective $\mathrm{SU}(2)$ degree of freedom. Furthermore, it is possible to fabricate samples that consist of two quantum wells separated by a thin insulating barrier. We refer to the latter type of device as the quantum Hall bilayer (QHB). The interest in bilayers and quantum wells comes from their experimental flexibility that allows one to tune the parameters in the Hamiltonian to a larger degree than it is possible with ordinary spin. For example, in a QHB with finite interlayer distance, the effective Coulomb interaction is not $\mathrm{SU}(2)$ symmetric. Therefore, the "intralayer" Coulomb interaction (the potential between electrons in the same layer) is somewhat stronger than the "interlayer" Coulomb (i.e., the potential between electrons in opposite layers). The ratio between the two interaction strengths is given by the parameter d/ℓ_B, the physical distance between layers in units of magnetic length, which in experiment can be continuously tuned. The tunneling energy between the two layers (in units of the Coulomb interaction energy), $\Delta_{\mathrm{SAS}}/\frac{e^2}{\epsilon\ell_B}$, can also be tuned. The tunability of interactions in quantum Hall bilayers and quantum wells can give rise to a richer set of FQH phases that extend beyond those realized in single-layer systems. Examples of such phases occur at $\nu = 1$ and $\nu = 1/2$. They have a rich experimental history that we briefly review in Sec. 5.2.

In this Chapter we focus on the QHB at total filling factor $\nu = 1/3 + 1/3$. The early experiment by Suen *et al.* [116] measured the quasiparticle excitation gap in a wide QW as a function of Δ_{SAS}. The gap was found to close around $\Delta_{\mathrm{SAS}}/\frac{e^2}{\epsilon\ell_B} \lesssim 0.1$, with an incompressible phase on either side of the transition. A realistic model of this system [117], that included LDA calculation of the band structure, reproduced the observed behavior of the gap. A more complete phase diagram as a function of both d/ℓ_B and $\Delta_{\mathrm{SAS}}/\frac{e^2}{\epsilon\ell_B}$ was obtained in Ref. [118]. This study, however, assumed zero width for each layer and was restricted to small systems. The phase diagram was argued to consist of three phases. For small d/ℓ_B and small $\Delta_{\mathrm{SAS}}/\frac{e^2}{\epsilon\ell_B}$, the system maintains $\mathrm{SU}(2)$ symmetry and resembles the usual $\nu = 2/3$ state with spin. It has been known that the ground state in this case is a spin-singlet (112) state [119, 120, 121, 102] (for an explicit wavefunction see Refs. [118, 122]). If d/ℓ_B is large, the layers are decoupled and the system is described by the Halperin (330) state, which is the simple bilayer Laughlin state. On the other hand, large Δ_{SAS} effectively wipes out the layer degree of freedom, and the system becomes single component. This bilayer symmetric state is described by the particle-hole conjugate of Laughlin's 1/3 wavefunction (hereafter called the $\overline{1/3}$ state).

Our motivation for revisiting the problem of $\nu = 1/3 + 1/3$ QHB is twofold. First, previous theoretical studies of this system have been limited to very small systems due to the exponential cost of exact diagonalization (ED). This limitation is particularly severe in the present case because of the pseudo-spin degree of freedom. Recent work has demonstrated that to some degree this cost can be overcome by using variational methods such as the "infinite density-matrix renormalization group" (iDMRG) [42, 43]. By combining insights from ED and iDMRG, we are able to obtain a more accurate phase diagram of the $\nu = 1/3+1/3$ QHB system as a function of d and Δ_{SAS}, as shown in Fig. 5.1. Although our results are qualitatively consistent with Ref. [118], the access to significantly larger system sizes enables us to study the order of the associated phase transitions, which we find to be first order.

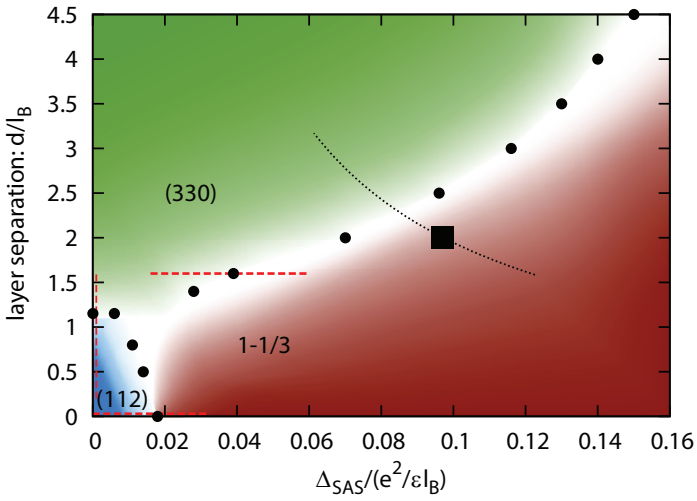

Figure 5.1: (Color online) Phase diagram of $1/3 + 1/3$ QHB in terms of dimensionless layer separation d and tunneling energy Δ_{SAS}. Data was taken with cylinder circumference $L = 14\ell_B$ and layer width $w = 0$. The dashed lines indicate sweeps performed to determine the nature of the phase transitions (see Sec. 5.4 for details). Later in this work, additional axes will be added to this plot, driving the system into a non-Abelian phase (see Fig. 5.7). The black dashed line and square mark the region studied experimentally in Ref. [123], and their observed phase transition.

Given that $1/3 + 1/3$ bilayer systems are experimentally available and allow a great deal of tunability (changing the layer width w, d or Δ_{SAS}), our second goal is to explore the possibility of realizing more exotic (non-Abelian) phases in these systems by tweaking the interaction parameters. Indeed, recently a number of trial non-Abelian states have been proposed for these systems [124, 125, 126, 41, 127, 128, 129]. At filling $\nu = 1/3 + 1/3$, the relevant candidates are the $\mathbb{Z}_4$ Read-Rezayi state [40], the bilayer Fibonacci state [129], the "intralayer-Pfaffian" and "interlayer-Pfaffian" states [125]. The latter was first introduced in Ref. [124], which showed that the phase supports Ising anyons and also exhibits spin-charge separation. We develop a diagnostic that detects spin-charge separation in the ground-state wavefunction using the entanglement spectrum. By varying the short-range Haldane pseudopotentials in the bilayer system at finite interlayer distance and tunneling, we find evidence for a non-Abelian phase that exhibits spin-charge separation and has non-trivial ground-degeneracy, consistent with the interlayer Pfaffian state. The phase is realized by either reducing the V_0 or increasing the V_1 pseudopotential component of the interaction, which may naturally occur as a consequence of strong Landau level mixing.

The remainder of this chapter is organized as follows. In Sec. 5.2 we review some of the previous experimental work in QHB and QW systems. In Sec. 5.3 we introduce the model of the QHB and discuss the numerical methods and diagnostics for identifying the FQH phases and transitions between them. Sec. 5.4 contains our main results for the phase diagram of $1/3+1/3$ QHB as a function of parameters w, d and Δ_{SAS}. We discuss in detail the three Abelian phases that occur in this system, and identify the nature of the transitions between them. In Sec. 5.5 we explore the possible new phases when the interaction is varied away from the bare Coulomb point. We establish that the modification of short-range (V_0 or V_1) pseudopotentials leads

to a robust non-Abelian phase that exhibits spin-charge separation and can be identified with the interlayer Pfaffian state. Our conclusions are presented in Sec. 5.6.

5.2 Experimental Background

In this Section we briefly review some of the important experiments on quantum Hall bilayers and wide quantum wells. As mentioned in the Introduction, one of the great advantages of studying these systems is the ability to experimentally tune parameters in the Hamiltonian, e.g., the interlayer separation and interlayer tunneling in a QHB. Different samples can be constructed with different values for these quantities. Tunneling energy is independent of layer separation since it can be varied by changing the height of the potential barrier between the layers without changing its width. Another convenient way to tune these parameters is by applying voltage bias to separate contacts made to each layer [130]; the variation of electron density ρ thus changes the effective ℓ_B at fixing filling ν via the relation $\rho = \nu/2\pi\ell_B^2$. This allows d/ℓ_B and $\Delta_{\rm SAS}/\frac{e^2}{\epsilon\ell_B}$ to be tuned continuously in a single sample.

To illustrate the typical parameter range that can be accessed, we note that at $\nu = 1/2 + 1/2$ it has been possible to vary d/ℓ_B in range 1.2–4, while the interlayer tunneling $\Delta_{\rm SAS}$ can be either completely suppressed or as large as $0.1e^2/\epsilon\ell_B$ [44]. The width of individual layers in this case is less than d. On the other hand, in wide QWs one controls independently the width of the entire well and the tunneling amplitude $\Delta_{\rm SAS}$. The latter is defined as the energy splitting between the lowest symmetric and antisymmetric subbands, and typically varies between zero and $0.2e^2/\epsilon\ell_B$. For systems where FQH can be observed, the physical width of the well is typically 30–65 nm [131]. Self-consistent numerical calculations estimate that this corresponds to an effective bilayer distance $d/\ell_B = 3$–7, with individual layer widths 1.5–$3\ell_B$ [131]. The tunability via d/ℓ_B or $\Delta_{\rm SAS}/\frac{e^2}{\epsilon\ell_B}$ can engender new physics that does not arise in a single layer quantum Hall system. Two important examples of such phenomena have been observed to occur at total filling factors $\nu = 1/2$ and $\nu = 1$.

At total filling $\nu = 1/2$, the QHB ground state is compressible in the limit of both very large and very small d/ℓ_B. At large d/ℓ_B, it is described by two decoupled $1/4 + 1/4$ "composite Fermi liquids" [132] (CFL), while around $d/\ell_B = 0$ it is the spin unpolarized $1/2$ CFL. At intermediate d/ℓ_B, an incompressible state forms when $d/\ell_B \lesssim 3$ [133, 134]. Numerical calculations performed over the years, primarily utilizing exact diagonalization [135, 136, 137, 138, 139], have confirmed that the incompressible state at vanishing interlayer tunneling is the Halperin 331 state [101]. More recently, there has been some renewed interest in the $\nu = 1/2$ two component systems [140, 131] due to the possible transition into the Moore-Read Pfaffian state as tunneling is increased [141, 142, 143]. Evidence for a tunneling-driven Moore-Read state has also been found for bosonic QHB at total filling $\nu = 1$[144]. Analogous scenario may hold for QWs at total filling $\nu = 1/4$, where the competing phases are the Halperin (553) state and the 1/4 Pfaffian state [145]. Very recently, GaAs hole systems have been shown to realize an incompressible state at $\nu = 1/2$ near the

vicinity of Landau level crossing [146].

As a second example of novel phases in QHB systems, we briefly mention the celebrated $\nu = 1$ state (for recent reviews, see Refs. [147, 44]). At large d/ℓ_B the system is compressible (two decoupled CFLs), but undergoes a transition to an incompressible state for $d/\ell_B < 2$, even at negligible interlayer tunneling. The incompressible state is represented by the Halperin (111) state, which can also be viewed as a pseudo-spin ferromagnet [148]. This wavefunction encodes the physics of exciton superfluidity, with an associated Goldstone mode [149] and vanishing of Hall resistivity in the "counterflow" measurement setup [150, 151]. The existence of an incompressible state (consistent with an exciton superfluid) has been established in numerics [152, 153, 154, 155, 156], though the questions about the details and nature of the transition, as well as the possibility of intermediate phases, remain open.

The case of total filling $\nu = 2/3$, which is the subject of this paper, has been less studied compared to previous examples. In the mentioned Ref. [116] the transition between a one-component and two-component phase was detected as a function of Δ_{SAS}, while in Ref. [117] similar data was obtained as a function of the tilt angle of the magnetic field. These experiments have been performed on a single wide QW. More recently, Refs. [123] and [157] have studied $\nu = 1/3 + 1/3$ in a QHB sample which directly corresponds to the model we study. (see Sec. 5.3) By applying a voltage bias as described above, they perform four sweeps in the d, Δ_{SAS} plane. In one sweep [123] they find a seemingly first-order transition at $d/\ell_B \approx 2$, $\Delta_{\text{SAS}}/\frac{e^2}{\epsilon \ell_B} \approx 0.1$. This sweep, and the location of the observed transition, are shown in Fig. 5.1. Another sweep entirely in the large Δ_{SAS} regime sees no phase transition, while two other sweeps are performed at small Δ_{SAS}. These sweeps see a $\nu = 2/3$ state at large d/ℓ_B which vanishes as the interlayer separation is decreased. The rest of the phase diagram remains to be fully mapped out. In our work we determine this phase diagram numerically, which can guide experiments towards realizing all the possible phases in this bilayer system. Finally, we mention that very recently [158] the stability of fractional quantum Hall states was investigated in a wide quantum well system with competing Zeeman and tunneling terms. The Zeeman splitting was controlled by an in-plane magnetic field. This system may not be fully captured by our model in Sec. 5.3 because of the potentially strong orbital effect of an in-plane field in a wide QW. It is possible, however, that the transition observed at $\nu = 5/3$ in Ref. [158] is indeed in the universality class of $\overline{1/3} \to (112)$ transition that we identify in Sec. 5.4 below.

5.3 Density Matrix Renormalization Group Applied to Quantum Hall systems

The main numerical method used in this chapter is infinite density renormalization group (iDMRG). In this section we provide a review of what this technique is and how it can be applied to quantum Hall systems. We then specialize to the case of quantum Hall bilayers, and we describe some of the numerical measurements

which will be used to distinguish between different quantum Hall phases.

5.3.1 Review of DMRG

The techniques of DMRG were developed over two decades ago by White[159] and have been extremely successful since that time in studying one-dimensional systems. Here I will give a rough introduction to how this algorithm works, readers may consult a review for a proper introduction to the method[160].

The basic idea of the algorithm is as follows. Consider the following quantum state:

$$\Psi = \sum_{\{\alpha_i\}} c_{\alpha_1\alpha_2\ldots\alpha_N} |\alpha_1\alpha_2\ldots\alpha_N\rangle . \tag{5.1}$$

Here $i \in [1, N]$ labels the sites of the one-dimensional system, and α_i is an eigenstate of that site (for example for a spin system α could be S^z). Naturally a general state is a sum over all possible eigenvalues on each site, each with a coefficient labelled c. We can think of c as being a vector, and it has d^N elements, where d is dimension of the α basis on one site. In can be useful to think of c as an $d^{N-1} \times d$ matrix instead of a d^N dimensional vector. Then we can even write c as a product of two matrices, one of size $d^{N-1} \times d$ and the other of size $d \times d$:

$$\Psi = \sum_{\{\alpha_i\}} \sum_{\beta} M_{\alpha_1\alpha_2\ldots\alpha_{N-1}\beta} \Lambda_\beta B^N_{\beta\alpha_N} |\alpha_1\alpha_2\ldots\alpha_N\rangle . \tag{5.2}$$

This equation is related to Eq. (5.1) by a singular-value decomposition (SVD), which factors the matrix c into three matrices M, Λ, B, with Λ a diagonal matrix. The matrix B contains sum over all states on site N, while M contains all the other sites. The index β, when summed over, multiplies the matrices A, Λ and B. It is called a 'virtual' degree of freedom. We can now continue this procedure, by turning A into a $d^{N-2} \times d^2$ matrix, and performing another singular value decomposition. This will leave us with a matrix B^N which contains the α_N index, a matrix B^{N-1} containing the α_{N-1} index, and a new matrix, A which contains all the other indices. There will now be two virtual dimension to sum over. We can repeat this process for the entire system. Each physical site will have a B matrix associated with it. Away from the edges of the chain, the B matrices will have approximately d^N elements. This procedure is an exact rewriting of Eq. (5.1). Note that in either the representation in terms of the B matrices, or Eq. (5.1) we have to store d^N numbers to describe our system. This will be very difficult as N becomes large, and so such a formulation cannot be used to study large systems numerically.

To understand why the above rewriting is useful, it is useful to consider the Schimdt decomposition, which states that for any quantum state defined on two subsystems A and B:

$$\Psi = \sum_{i,j} c_{ij} |i\rangle_A |j\rangle_B , \tag{5.3}$$

there is a new basis for the A and B in which the matrix c_{ij} is diagonal:

$$\Psi = \sum_a c_a \left|a\right\rangle_A \left|a\right\rangle_B , \tag{5.4}$$

where a is a label for some basis of A and B. The connection to the previous paragraph is that the Schmidt decomposition can be performed using an SVD, with c_a the elements of Λ from the SVD, and $\left|a\right\rangle_A = M \left|i\right\rangle_a$, $\left|a\right\rangle_B = B \left|j\right\rangle_B$. This is important because the c_a from the Schmidt decomposition are the eigenvalues of the reduced density matrix. For a one-dimensional gapped system, these eigenvalues are all positive numbers less than one, and they decay exponentially. Therefore we can obtain a good approximation of Ψ by truncating the matrix c_a to an exponentially small part. If we apply this to the previous paragraph, we see that each matrix B_i can be truncated as well. The size of the truncated matrix c_a is called the 'bond dimension' χ, and B_i will go from having $\sim d^N$ values to having only $\chi^2 d$. Therefore the number of numbers needed to represent Eq. (5.1) no longer grows exponentially in N, and we can represent our system on a computer. The representation on Eq. (5.1) as a product of matrices B_i is called a 'matrix product state' (MPS). The bond dimension χ represents the amount of entanglement between the subsystems on either side of the bond. The computational resources required to find the ground state are $O(\chi^3)$.

DMRG is the procedure of variationally optimizing a Hamiltonian using matrix product states as the variational ansatz. Since matrix product states can represent any one-dimensional gapped system, in one dimensions this is an excellent ansatz to use. In order to optimize the matrix product state, one needs to be able to quickly contract it with the Hamiltonian. To do this it is convenient to decompose the Hamiltonian into a 'matrix-product operator' (MPO), i.e., to write the Hamiltonian as a product of a number of matrices, each of which acts on an individual site. In general this seems like a hard problem; however, there are a number of tricks one can use to find the matrix product operators for a given Hamiltonian. For example, consider a Hamiltonian which is a product of one site operators, such as:

$$H = \sum_i S_i^z \tag{5.5}$$

The following matrix operator represents this Hamiltonian:

$$H_i = \begin{bmatrix} \mathbb{1} & 0 \\ S^z & \mathbb{1} \end{bmatrix} . \tag{5.6}$$

This matrix is in the 'virtual basis': to get the Hamiltonian this basis is summed over, which means that to get the full Hamiltonian one multiplies matrices like the above for each site. The operators in the matrix act on the physical basis at each site. One can check that multiplying out these matrices generates Eq. (5.5). Similar matrices for two-site operators such as $S_i^z S_{i+1}^z$ also exist. One can also get exponentially decaying

interactions by multiplying matrices of the form:

$$H_i = \begin{bmatrix} \mathbb{1} & 0 & 0 \\ \lambda S^z & \lambda & 0 \\ S^z & S^z & \mathbb{1} \end{bmatrix}, \tag{5.7}$$

which generates a term in the Hamiltonian of the form $\lambda^{r-r'} S^z(r) S^z(r')$.

Once the MPO for a given Hamiltonian is known one can find the ground state of that Hamiltonian by multipying all the matrix product operators and matrix product states together, except for a single matrix B_i. Then we find the B_i which has the lowest eigenvalue with respect to the operator obtained by multiplying all the other matrices. This is repeated for each B_i until convergence is achieved. The infinite DMRG (iDMRG) algorithm used in this chapter follows this algorithm, but every MPS and MPO is taken to be the same. [1]

5.3.2 DMRG applied to quantum Hall systems

In this chapter we will use the above-mentioned DMRG algorithm to study a quantum Hall system. One obvious problem is that quantum Hall systems are two-dimensional, whereas in the previous subsection DMRG was defined for a one-dimensional system. DMRG is commonly used to study two-dimensional systems by defining such systems in a quasi-one-dimensional setup such as on a strip or cylinder; in this chapter we use a cylinder. In a one-dimensional system the bond dimension χ needed to accurately approximate the system increased polynomially in system size, and this is why the problem is numerically tractable. In a quasi-1D setup the required $\chi \sim e^{L_x}$, where L_x is the diameter of the cylinder. Therefore we will only be able to deal with fairly small cylinders. This is still reasonable. The main competing numerical method used to study quantum Hall systems, exact diagonalization, has an exponential cost in both the diameter of the cylinder and its length, so DMRG can study significantly larger sizes.

To put the quantum Hall system on a cylinder, we use the Landau gauge $(A_x, A_y) = (By, 0)$. The Hamiltonian in this gauge, in the absence of interactions between electrons, is [2]

$$H_0 = \frac{\hbar^2}{2m} p_y^2 + \frac{\hbar^2}{2m} \left(p_x^2 - \frac{eB}{c} y \right)^2. \tag{5.8}$$

Where B is the magnetic field, x is the direction around the circumference of the cylinder and y is the direction along the cylinder. This Hamiltonian has a number of ground states, which are given by the following wave functions:

$$\phi_n(x, y) = \frac{e^{-ik_n x} e^{-(y - k_n \ell_B^2)^2}}{\sqrt{2 L_x \pi^{1/2}}} \quad k_n = \frac{2\pi n}{L_x}. \tag{5.9}$$

[1] More accurately, we will represent only a few sites and use periodic boundary conditions to get an 'infinite' system.

[2] This is the Hamiltonian for a single species, which will be discussed for most of this section. The generalization to more species is fairly straightforward[43].

Here $\ell_B \equiv \sqrt{\frac{\hbar}{eB}}$ is the magnetic length, which we will soon set to be 1. These wave functions are a combination of a plane wave in the x direction and the solution to a harmonic oscillator in the y direction. The above equation is for the lowest energy solution to the harmonic oscillator problem, which corresponds to the lowest Landau level. Electrons in higher Landau levels have wave functions corresponding to higher energy eigenstates of the harmonic oscillator problem.

We will perform numerics in the orbital basis, indexed by n and defined by:

$$c(r) = \sum_n \phi_n(x,y)c_n, \tag{5.10}$$

where c_n annihilates an electron in orbital n and $c(r)$ annihilates an electron at position $r = (x,y)$. Each orbital carries x-momentum k_n and is localized at position $k_n\ell_B^2$. The occupation for each orbital is either 0 or 1. Therefore in the orbital basis the quantum Hall problem reduces to a one-dimensional Hubbard model (though with some unusual interactions) and this is a problem that can be solved with DMRG.

We want to find ground states of the above Hamiltonian, including interactions

$$\delta H = \sum (r,r')V(r-r')\rho(r)\rho(r'). \tag{5.11}$$

$V(r)$ will typically be a Coulomb interaction, and $\rho(r) \equiv c^\dagger(r)c(r)$ is the electron density. Naturally the eigenstates of the full Hamiltonian may not be spanned by the basis ϕ_n, but we restrict ourselves to this basis anyways, this is projection to the lowest Landau level. In the systems considered in this chapter this is a reasonable approximation to make. The energy separation between Landau levels from H_0 is proportional to the magnetic field B, while $\delta H \sim \sqrt{B}$. Therefore at large enough fields higher Landau levels can be neglected. It has also been shown that expansions in the Landau level mixing parameter κ (which is essentially $\delta H/H_0$) are stable even for $\kappa \approx 1$. Though neglecting higher Landau levels is a reasonable approximation in this work, in other systems such as graphene, where the Landau level spacing is $\sim \sqrt{B}$, or in cases where Landau level mixing breaks a particle-hole symmetry, it cannot be neglected.

Eq. (5.11) can be written in the orbital basis as:

$$\delta H = \sum_{n,m,k} V_{mk} c^\dagger_{n+m} c^\dagger_{n+k} c_{n+m+k} c_n. \tag{5.12}$$

We see that the Coulomb Hamiltonian induces both hopping between orbitals as well as diagonal terms. Note that all of these hoppings preserve momentum in the x-direction. If V_{mk} is a Coulomb interaction then it is proportional to $|r-r'|^{-1}$. In the orbital basis, the orbitals are at positions $2\pi n\ell_B^2/L_x$, i.e., they get closer together as the diameter of the cylinder is increased, and in orbital space the Coulomb interaction gets longer-ranged as L_x is increased. The longer-ranged interaction induces more entanglement between the different orbitals, and so a larger χ is required to represent the matrix product state.

In the previous subsection we saw how to represent both on-site interactions and exponentially decaying interactions using matrix product operators. In the quantum Hall problem we have a power-law decaying operator. This can be approximated by a linear combination of exponentials, and that is the approach taken in this chapter[42].

5.3.3 The bilayer model

We label the two layers of the bilayer with the index $\mu \in \{\uparrow, \downarrow\}$, and consider Hamiltonians of the general form

$$H = \frac{1}{2}\int \mathrm{d}^2\mathbf{r}\,\mathrm{d}^2\mathbf{r}'\, V_C^{\mu\nu}(\mathbf{r}-\mathbf{r}')n^\mu(\mathbf{r})n^\nu(\mathbf{r}') - \frac{\Delta_{\mathrm{SAS}}}{2}\int \mathrm{d}^2\mathbf{r}\, c^{\mu\dagger}(\mathbf{r})\sigma^x_{\mu\nu}c^\nu(\mathbf{r}), \tag{5.13}$$

where $c^{\mu\,\dagger}(\mathbf{r})$ creates an electron in layer μ at the position $\mathbf{r} \equiv (x, y)$. The first term is the Coulomb interaction for an electron in layer μ. The precise form of the interaction term depends on the details of the bilayer. The second term encodes tunneling between the two layers. When $V_C^{\mu\nu}$ is $\mathrm{SU}(2)$ symmetric this Hamiltonian is equivalent to a $\nu = 2/3$ system with spin, and in this case Δ_{SAS} can be thought of as the Zeeman splitting.

In Eq. (5.13) we assumed that the perpendicular z coordinate has been integrated out, leading to an effective two-dimensional Hamiltonian. This is possible because the magnetic field is perpendicular to the 2DEG plane, and the transverse component of the single body wavefunctions ψ factorizes,

$$\psi^\mu(x, y, z) = \phi_z(z \pm d/2)\phi(\mathbf{r}). \tag{5.14}$$

The single-body wavefunctions depend on two length scales: the spatial separation d between the two layers in the direction $\hat{z}$, and the finite layer width w of each layer. In this work we assume $\phi_z(z)$ is set by an infinite square well of width w,

$$\phi_z(z) = \sqrt{\frac{2}{w}}\sin\left(\frac{\pi z}{w}\right). \tag{5.15}$$

The Coulomb interaction in three dimensions is given by:

$$V_{3D}(x, y, z) = \frac{e^2}{\epsilon\ell_B}\frac{\ell_B}{\sqrt{x^2+y^2+z^2}}, \tag{5.16}$$

We can then recover the Coulomb interaction part of Eq. (5.13) by integrating out the perpendicular coordinate

$$V_C^{\mu\nu}(\mathbf{r}) = \int \mathrm{d}z\,\mathrm{d}z'\,|\phi_z(z)|^2|\phi_z(z')|^2 V_{3D}(\mathbf{r}, z - z' + (1-\delta^\mu_\nu)d). \tag{5.17}$$

Throughout this work we project the Hamiltonian (5.13) into the lowest Landau level, ignoring the effects of "Landau level mixing" present at finite $\frac{e^2}{\epsilon\ell_B}/\hbar\omega_c$. In this case, it is possible to expand V_C in terms of the Haldane pseudopotentials V_α, which are the potentials felt by particles orbiting around one another in a state with relative angular momentum α. Later in this work we add additional V_α terms to V_C in order to

explore the neighboring phases. In experiment, such variations of the interaction may arise due to Landau level mixing [161, 162, 163, 164, 165, 166, 167, 43, 168].

Henceforth, we set the energy and length scales $\frac{e^2}{\epsilon \ell_B} = \ell_B = 1$ whenever units are omitted.

5.3.4 Entanglement invariants for the identification of FQH phases

All of the phases we study in this work are gapped, have quantized Hall conductance $\sigma^{xy} = \frac{2}{3}(e^2/h)$, and have no local order parameter which can be used to distinguish between them. However, these phases do have different topological orders, and we can therefore apply a number of recent developments [169, 170, 42, 171] which demonstrate how the topological order of a system can be extracted from its entanglement properties.

In a topological theory, the ground state degeneracy on both the torus and infinitely long cylinder is equal to the number of anyon types. There is a special basis for the ground state manifold, the minimally entangled basis, in which each basis state $|a\rangle$ can be identified with an anyon type a [5, 172, 169].

By measuring how various entanglement properties of $|a\rangle$ scale with the circumference L, we can measure the quantum dimensions d_a [5, 6]; the internal quantum numbers (spin, charge, etc.) of each anyon a; the "shift" $\mathcal{S}$ [173], or equivalently the bulk Hall viscosity [42]; the topological spins $\theta_a = e^{2\pi i h_a}$; and the chiral central charge c_- of the edge theory [169, 42, 171]. Below we provide a brief summary of these measurements in the context of FQH systems, and refer to Refs. [43] for a detailed discussion.

To measure entanglement properties we divide the cylinder *in orbital space* into two semi-infinite halves L/R and Schmidt decompose the state as $|\Psi\rangle = \sum_\mu \lambda_\mu |\mu\rangle_L \otimes |\mu\rangle_R$. The entanglement entropy is defined as $S = -\sum_\mu \lambda_\mu^2 \log \lambda_\mu^2$. In ground state $|a\rangle$, the entropy S_a scales as [5, 6]

$$S_a = \beta L - \log \frac{\mathcal{D}}{d_a} + \mathcal{O}(e^{-L/\tilde{\xi}}), \tag{5.18}$$

where d_a is the quantum dimension of anyon a, and $\mathcal{D}$ is the total quantum dimension of the topological phase. The corrections are set by a length scale $\tilde{\xi}$ which need not be directly related to the physical correlation length.

To measure a $\mathrm{U}(1)$ charge Q_a for anyon a, we partition the total charge operator into its components to the left / right of an entanglement cut, $\hat{Q} = \hat{Q}_L + \hat{Q}_R$. The left Schmidt states are eigenstates of $\hat{Q}_L$, $\hat{Q}_L |\mu; a\rangle_L \equiv Q_{\mu;a} |\mu; a\rangle_L$, where $|\mu; a\rangle_L$ are the Schmidt states of ground state $|a\rangle$ and $Q_{\mu;a} \in \mathbb{Z}$ in units where the elementary charge is 1. The charge Q_a of anyon a is given by the charge polarization in the ground state, which can be expressed as an "entanglement average" [42]:

$$e^{2\pi i Q_a} \equiv e^{2\pi i \sum_\mu \lambda_\mu^2 Q_{\mu;a}}. \tag{5.19}$$

Q_a is defined modulo 1. In the bilayer systems with $\mathrm{U}(1) \times \mathrm{U}(1)$ symmetry we can apply the measurement for both layers to get two charges.

FQH Phase	Ground-state degeneracy	$\mathcal{S}$	Spin-charge separation	c^-
(330)	9	3		2
(112)	3	1		0
$\overline{1/3}$	3	0		0
$\mathbb{Z}_4$ Read-Rezayi [40]	15	3		2
Interlayer-Pfaffian [124]	9	3	✓	5/2
Bonderson-Slingerland [41]	9	4	✓	5/2
Intralayer-Pfaffian [125]	27	3	✓	3
Bilayer Fibonacci [129]	6	3		14/5

Table 5.1: Possible candidate states at $\nu = 1/3 + 1/3$ and their observed properties. We call a phase "spin-charge separated" if one can consistently assign charge/spin to the excitations, with one such excitation having neutral charge and pseudo-spin $\pm 1/2$ (see Sec. 5.5).

Rotating the cylinder can also be viewed as a $\mathrm{U}(1)$ charge, whose generator is the momentum $\hat{K}$. Its eigenvalues K_a can be combined with certain analytically calculable properties of the Landau levels to recover the Berry phase for an adiabatic Dehn twist (modular transformation). Similar to the charge, the resulting phase $T_a = \exp(2\pi i M_a)$ may be computed from an entanglement average:

$$M_a = \sum_\mu \lambda_\mu^2 K_{\mu;a} + \text{analytic terms}. \tag{5.20}$$

M_a is the "momentum polarization", scaling as [42, 171]:

$$M_a = -\frac{\nu \mathcal{S}}{(4\pi \ell_B)^2} L^2 + h_a - \frac{c_-}{24} + \mathcal{O}(e^{-L/\tilde{\xi}}) \pmod 1. \tag{5.21}$$

Here $\mathcal{S}$ is the shift, h_a is the topological spin of anyon a, and c_- is the chiral central charge of the edge.

The shift $\mathcal{S}$ [173] is an constant mismatch between the number of flux N_Φ and electrons N_e required to realize the ground state of the phase on the sphere, $N_\Phi = N_e/\nu - \mathcal{S}$, and plays a particularly important role in our analysis. For the (330), (112), $\overline{1/3}$ states and the interlayer-Pfaffian (introduced in Sec. 5.5 below) the shift takes values $\mathcal{S} = 3, 1, 0, 3$ respectively (see Tab. 5.1), so distinguishes most of the phases. Because $\mathcal{S}$ in these cases is an integer and the dominant contribution to M_a, it converges very quickly and is far easier to measure than h_a, c_- or d_a.

5.4 Abelian Phase Diagram

In this Section we study the $\nu = 1/3 + 1/3$ QHB system as a function of experimentally relevant parameters: interlayer separation (d), tunneling (Δ_{SAS}), and layer width (w). We determine the phase diagram using the topological characterization explained in Sec. 5.3.4, and find three different Abelian phases [118]: decoupled $\nu = 1/3$ bilayers (330) or the bilayer Laughlin phase, a bilayer-$\mathrm{SU}(2)$ symmetric spin-singlet hierarchy state (112), and a transversely polarized particle-hole conjugate of the Laughlin state $\overline{1/3}$.

Fig. 5.1 shows the phase diagram at well width $w = 0$ and cylinder circumference $L = 14$ (which is used to all data in this section). Phase boundaries were determined at the points marked in black; these points were found by performing simulations in sweeps, changing either d or Δ_{SAS}, and plotting the results. We find points where the correlation length and entanglement entropy have either discrete jumps or peaks, and we claim that these points are the phase transitions. The upper panels of Figs. 5.4, 5.5 and 5.6 show examples of the correlation length data used to determine the locations of these transitions. The dashed lines in Fig. 5.1 show the sweeps where these data were taken. We note that the region in the vicinity of the tentative triple point is somewhat difficult to resolve, but we have have not found any evidence for additional phases. The three Abelian phases can be intuitively understood in the following limiting cases.

First, when Δ_{SAS} is small and d is large the two layers interact only weakly, and we have two decoupled Laughlin states. Second, when Δ_{SAS} is extremely large the single particle orbitals are superpositions of both layers. Both symmetric and antisymmetric superpositions are possible, but when Δ_{SAS} is very large the antisymmetric superpositions are energetically forbidden (the energy difference between the two states is Δ_{SAS}), so we can view the system as a single quantum well with $\nu = 2/3$, whose ground state is the particle-hole conjugate of the Laughlin $1/3$ state, which we call the $\overline{1/3}$ state. This state is particularly natural at $d = 0$, where the system is equivalent to a single layer with spin: the tunneling term is a Zeeman field which spin-polarizes the system along the transverse direction.

Third, when $d = 0$ and $\Delta_{\text{SAS}} = 0$ the system is equivalent to a single-layer system with spin that has full $\mathrm{SU}(2)$ symmetry. The ground state is a (112) state [102, 118, 122].

The attentive reader might note that, topologically, the (112) and $\overline{1/3}$ phases are actually the same phase, in the sense that their K matrices are related by an $\mathrm{SL}(2,\mathbb{Z})$ transformation. However, in the presence of rotational symmetry these phases have a different shift $\mathcal{S}$, and so they are not the same phase. One may be concerned that in an experiment disorder will break the rotational symmetry and allow the (112) and $\overline{1/3}$ state to be continuously connected, but this is in fact not the case, as this transition has been seen experimentally both in wide quantum wells [116], and in single-layer systems with spin [174].

5.4.1 Determination of the phases

We have determined the phases by using the entanglement invariants discussed in Sec. 5.3.4. First, we measure the momentum polarization M_a in order to compute the shift $\mathcal{S}$, which should take the values 3, 1, and 0 in the (330), (112), and $\overline{1/3}$ state, respectively. Fig. 5.2 shows the momentum polarization at three representative points in the phase diagram. We plot M_a as a function of L^2, so by Eq. (5.21) we should get straight lines with a slope proportional to $\mathcal{S}$. The green line (330) was taken at $d = 1.6$, $\Delta_{\text{SAS}} = 0$, giving $\mathcal{S} \approx 3$; the red line (112) was taken at $d = 0.2$, $\Delta_{\text{SAS}} = 0$, giving $\mathcal{S} \approx 1$; the blue line $\overline{1/3}$ was taken at $d = 2$, $\Delta_{\text{SAS}} = 0.1$, giving $\mathcal{S} \approx 0$. All of these values match those predicted for the appropriate phase.

Fig. 5.3 shows entanglement spectra for the same points as those shown in Fig. 5.2. The counting and chirality of the low-lying entanglement spectra are unique to each phase, and as elaborated in Fig. 5.3 we find

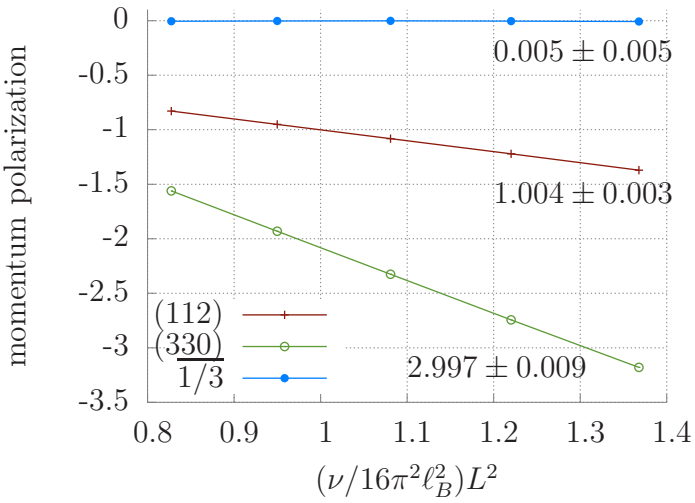

Figure 5.2: (Color online) Momentum polarization M_a for the representative points from the phases in Fig. 5.1, plotted against $\frac{\nu}{(4\pi\ell_B)^2}L^2$. The coefficient of proportionality is the shift $\mathcal{S}$, which we can read off to be 3, 1 and 0 for the (330), (112) and $\overline{1/3}$ phase respectively, as expected. Data was taken at $d = 1.6$, $\Delta_{\text{SAS}} = 0$; $d = 0.2$, $\Delta_{\text{SAS}} = 0$; and $d = 2$, $\Delta_{\text{SAS}} = 0.1$ for the (330), (112), and $\overline{1/3}$ phases, respectively. Values for the shift obtained from fitting the data are shown directly on the figure.

spectra consistent with each phase.

The phase diagram in Fig. 5.1 was taken using an infinite cylinder with a circumference $L = 14$. To assess the finite size effects, we have measured the behavior of select cuts along the phase boundaries for $L = 12$–16. We found that the location of the $(112) \to (330)$ transition changes with system size by $d < 0.02$. The $(330) \to \overline{1/3}$ and $(112) \to \overline{1/3}$ transitions do move to smaller Δ_{SAS} at larger L, with a change from $L : 12 \to 16$ of about 0.003. While the transition may continue shifting to slightly smaller Δ_{SAS} as L is further increased, at large d the change is small on the scale of the full phase diagram.

At smaller d, the critical value of Δ_{SAS} is fairly small at $L = 14$ and so we may be concerned that in the thermodynamic limit it is actually zero. We can test this at $d = 0$ by exploiting the fact that tunneling acts as a simple Zeeman field in the spin realization, so the energetics can be fully determined by the energy difference between the (112) and $\overline{1/3}$ phases at $d = 0$, $\Delta_{\text{SAS}} = 0$. Using the additional symmetries at this point we can perform accurate finite-size scaling to extract the energy difference in the thermodynamic limit, and we find that the transition occurs at $\Delta_{\text{SAS}} \approx 0.018$. Therefore, at least at small d, it appears that we have reached large enough sizes so that finite size effects do not change the location of the phase transition. Note that this system is formally equivalent to a $\nu = 2/3$ system with spin, and our value for the energy difference matches the numerical literature for the spin-polarization transition in that system.[175]

We have also assessed the sensitivity to layer width w for select cuts through the phase boundary. In the upper panels of Figs. 5.5 and 5.6, we used dashed lines to show the correlation lengths at finite widths. We see that a finite layer width shifts the location of the $(112) : (330)$ transition to larger d, while the $(330) : \overline{1/3}$ transition is shifted to smaller Δ_{SAS}. At $w = 1$ the boundaries have changed by about 10% compared to

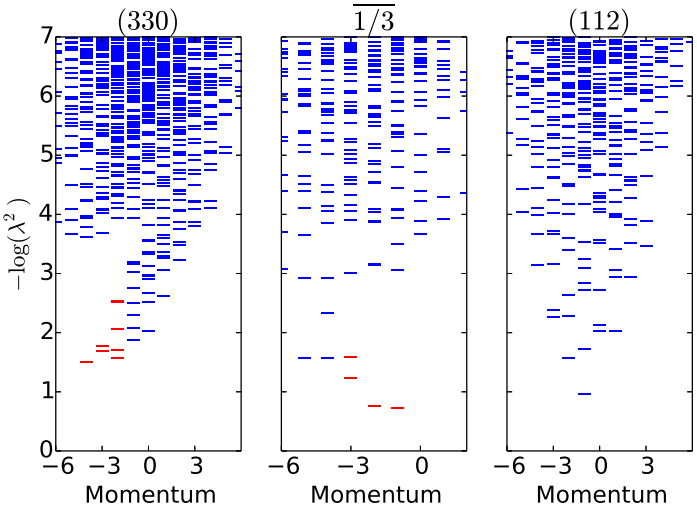

Figure 5.3: (Color online) Entanglement spectra for the phases in Fig. 5.1: the (330) state, with counting of $1, 2, 5, \ldots$ dispersing to the right; the $\overline{1/3}$ state, with counting $1, 1, 2, \ldots$ dispersing to the left; the (112) state, which has an non-chiral spectra (being a convolution of a left and right mover). These results are in agreement with the predicted values for these phases.

$w = 0$, so we don't expect any qualitative differences in the phase diagram.

Naturally there are many differences between the system we are studying numerically and those which are studied in experiments. In addition to the finite-size effects and our simplified treatment of layer width, we also neglect other factors including Landau level mixing and disorder. One can therefore ask how relevant our data is to experiments, particularly as to the quantitative locations of the phase transitions shown in Fig. 5.1. One way to address this is to compare to the experimental data which already exists. Ref. [123] studied the $(330) : \overline{1/3}$ transition and found it at approximately $d = 2$, $\Delta_{\mathrm{SAS}} = 0.1$. The location of their observed transition is shown in Fig. 5.1. We obtain $\Delta_{\mathrm{SAS}} \approx 0.07$, and this gives us reason to believe that our data can be used as a guideline for future experiments.

5.4.2 Order of the transitions

The large system sizes accessible to our DMRG simulations allow us to assess the nature of the various phase transitions in Fig. 5.1. We find strong evidence that the $(330) : \overline{1/3}$ and $(112) : \overline{1/3}$ transitions are first order. The $(330) : (112)$ transition appears to be very weakly first order, though we cannot definitely rule out a continuous transition. To determine the order of the transition we check for discontinuities in $\partial_g E$, where $g = \Delta_{\mathrm{SAS}}, d$ tunes across the transition, as well as for divergences in the correlation length and discontinuities in local observables.

The upper panel of Fig. 5.4 shows the $(112) : \overline{1/3}$ transition, at which the correlation length jumps discontinuously while remaining finite, indicating a strongly first-order transition. In the upper panels of Figs. 5.5 and 5.6 we show correlation lengths for $(330) : \overline{1/3}$ and $(330) : (112)$ transitions. The correlation length peaks as the transition is approached, suggesting either a continuous or weakly first order transition.

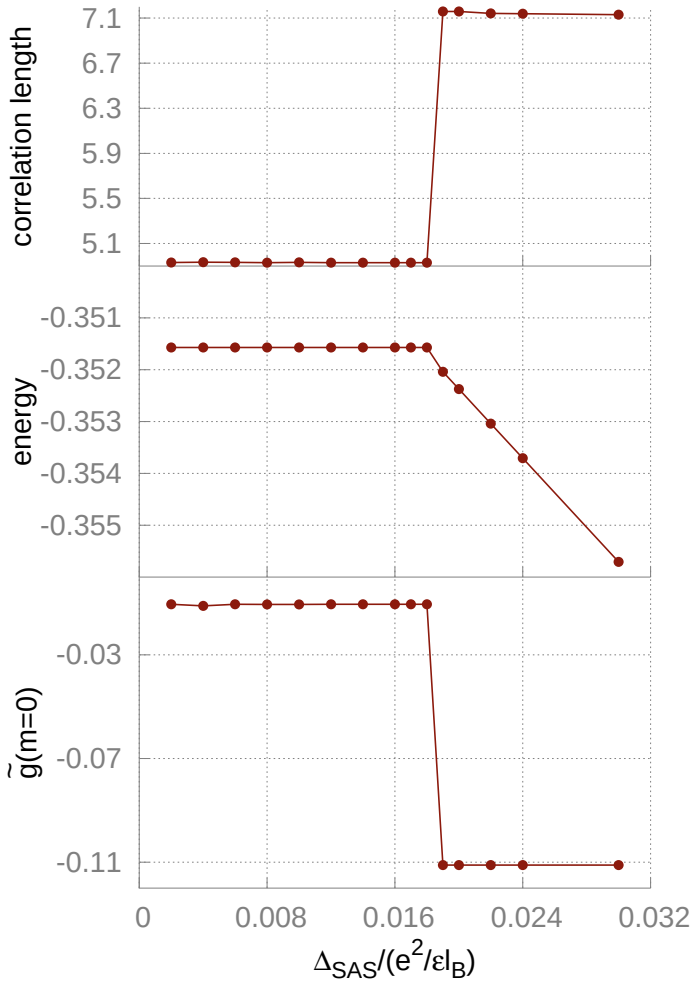

Figure 5.4: (Color online) Data as a function of tunneling strength, crossing the $(112) : \overline{1/3}$ transition. The correlation length is flat except very close to the transition, where it is discontinuous. There is also a kink in the energy and in $\tilde{g}$. This is all consistent with a first-order transition.

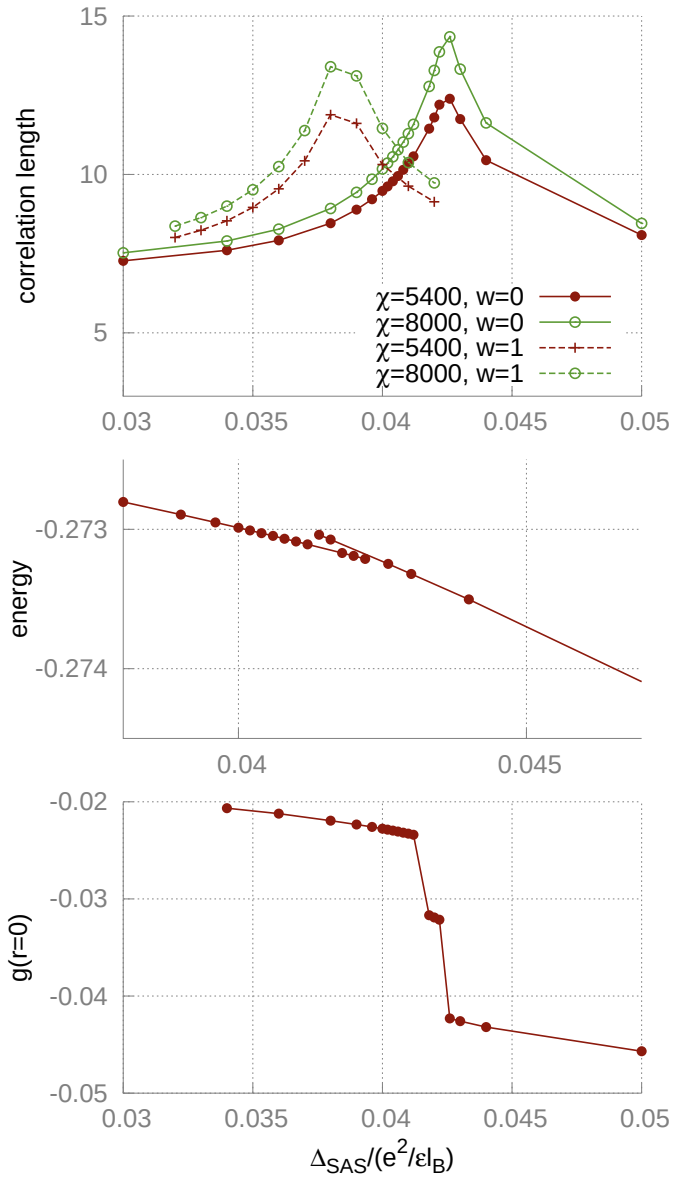

Figure 5.5: (Color online) Data as a function of tunneling strength, crossing the $(330) : \overline{1/3}$ transition. The correlation length has a peak near the transition, but this is consistent with both a first and second order transition. The middle panel shows the energy for both the (330) and $\overline{1/3}$ phases (see text), and as these lines are not parallel the systems energy has a kink. There is also a jump in $g(r = 0)$, consistent with a first-order transition.

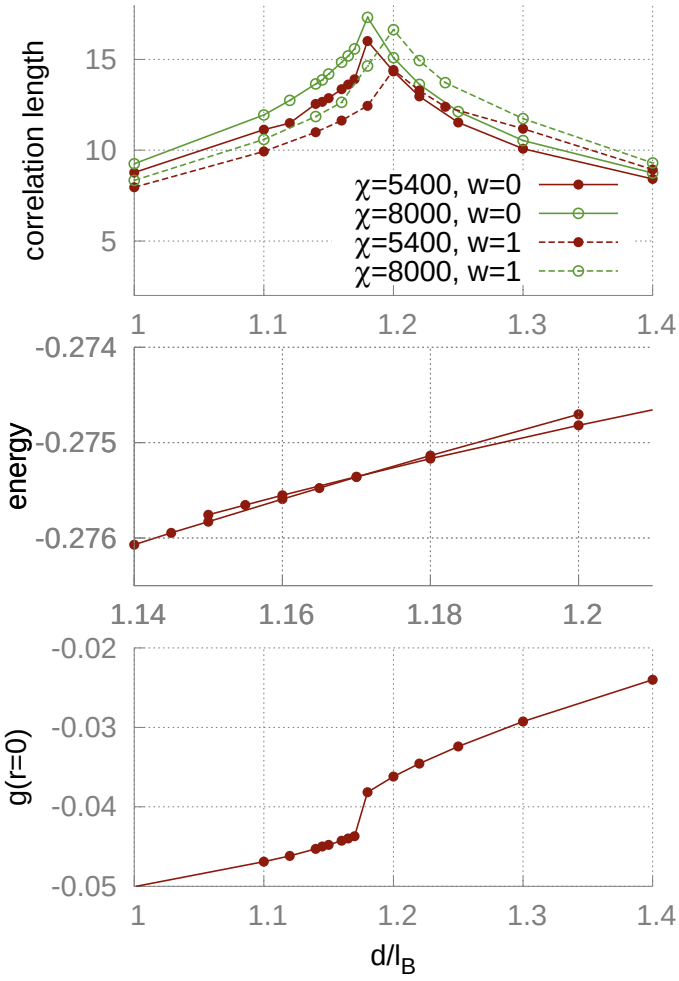

Figure 5.6: (Color online) Data as a function of interlayer separation, crossing the $(330) : (112)$ transition. The correlation length has a peak, while the energy has a kink and the $g(r = 0)$ are jumps across the transition. This is indicative of a first order transition, though the transition is weaker compared to the others in the phase diagram.

A continuous transition would be gapless, generating a large amount of entanglement which cannot be efficiently represented by an MPS; finite χ effects then cutoff the divergent ξ. Consequently we would expect a strong dependence of ξ on the MPS bond dimension χ. The different colored lines in the figure correspond to increasing χ, and we see that ξ increases with χ, which could be consistent with a continuous transition. However, a similar effect could be seen at a weakly first-order transition if χ is not large enough to capture the state. Therefore we need other ways to determine the order of these transitions.

Another approach is to look at behavior of the energy at the transition point. For a first-order transition, we expect a kink in the energy, while for a continuous transition we expect the energy to vary smoothly. The middle panels of Figs. 5.4, 5.5 and 5.6 show the energies near these transitions. The first order $(112) : \overline{1/3}$ transition has a clear kink in the energy. The $(330) : \overline{1/3}$ transition also appears of have a kink. The system

also exhibits hysteresis for both the $(112) : \overline{1/3}$ and $(330) : \overline{1/3}$ transitions: if we initialize the system in the $\overline{1/3}$ phase it will stay in that phase even if Δ_{SAS} is below its critical value. This is of course expected in a first order transition, and in the middle plot of Fig. 5.5 we plot two separate lines, which are the energy of the (330) and $\overline{1/3}$ phases (the actual energy of the system is whichever of these energies is lower). We can see that these lines are not parallel, which clearly shows that there is a kink in the system's energy and therefore the transition is first order. At the $(330) : (112)$ transition we find a very weak kink, so we tentatively conclude all three transitions are first order.

It is also useful to look at the behavior of local correlations, such as the real space density-density correlation between electrons in different layers:

$$g(\mathbf{r}) = \langle n^{\uparrow}(\mathbf{r}) n^{\downarrow}(0) \rangle - \langle n^{\uparrow}(\mathbf{r}) \rangle \langle n^{\downarrow}(0) \rangle \,, \tag{5.22}$$

where $n^{\mu}(\mathbf{r}) = (c^{\mu})^{\dagger}(\mathbf{r}) c^{\mu}(\mathbf{r})$. In the (330) phase, the layers are uncorrelated, and this quantity should be approximately zero. In the other phases, at small $\mathbf{r}$ the electrons repel and so $g(\mathbf{r})$ should be negative. We can also look at the same correlation function in orbital space instead of real space:

$$\begin{aligned} \tilde{g}(m) &= \langle n_m^{\uparrow} n_0^{\downarrow} \rangle - \langle n_m^{\uparrow} \rangle \langle n_0^{\downarrow} \rangle \,, \\ n_m^{\mu} &\equiv {c_m^{\mu}}^{\dagger} c_m^{\mu}. \end{aligned} \tag{5.23}$$

For $m = 0$, this quantity will be negative in the $\overline{1/3}$ phase, but it will be small in the other phases. When the above quantities have different values on either side of a phase transition, we expect them to jump discontinuously for a first-order transition and to vary continuously for a second-order transition.

We plot these quantities in the bottom panels of Figs. 5.4, 5.5, and 5.6, and see discrete jumps in all cases. Based on the results of this section we can claim that all the transitions in the diagram are first order, with the strongest first order transition being the $(112) : \overline{1/3}$ transition. The $(330) : (112)$ transition has only a slight kink in the energy and the jump in $g(r)$ is smaller than the other transitions, so this is the weakest first order transition in the diagram.

In Ref. [157], four experimental sweeps in our phase diagram were performed. Two of these sweeps had small Δ_{SAS}, and had $d \approx 1.4 - 2.8$. These sweeps found a $\nu = 2/3$ state which we take to be the (330) state at large d, but below $d \approx 1.8$ they find no QH state. We believe that this is because their experiments were taken at layer width $w/\ell_B \approx 2$, which would move the $(330) : (112)$ transition to larger d, putting it near where they observe the vanishing QH state. Furthermore, we have found that the $(330) : (112)$ transition is weakly first-order, implying that at the transition there is a small energy gap. We surmise that the quantum Hall state is not observed in experiment because the gap is very small near the transition, and so the transition point is being smeared by finite temperature and disorder effects.

5.4.3 Spin polarization

In addition to the bilayer degree of freedom, electrons carry spin, resulting in a four-component system. Thus far we have assumed the spin is polarized by the external magnetic field, an assumption we can test with our simulations.

The spin-polarized $\overline{1/3}$ phase at $d = 0, w = 0$ and large Δ_{SAS} is essentially a one-component system with filling $2/3$, while the competing spin-unpolarized state is a two component (spin) system with each component having filling $1/3$. The spin-unpolarized case has a lower Coulomb energy proportional to $\ell_B^{-1} \propto B^{1/2}$ (this is why we find (112) in the equivalent bilayer problem), while the spin-polarized state gains a Zeeman energy proportional to the applied field B. For systems at fixed $\nu = 2/3$, for a small perpendicular magnetic field (and proportionally small density), the system will be in a spin-unpolarized state, while for large magnetic field (and density) the system will spin polarize. The spin base case been studied both numerically [175] and experimentally [174], but the results to not agree, with the numerics predicting a critical magnetic field of $\approx 11\,\text{T}$ and experiments measuring $\approx 3\,\text{T}$. It has been proposed that the difference between these values is due to the finite layer width of the samples [174]. We are in a position to confirm this, and indeed we find that increasing the layer width does decrease the critical magnetic field, with a layer width of ≈ 5 magnetic lengths being sufficient to bring experiment and simulation into agreement. Thus, in context to the bilayer set up, whether the $\overline{1/3}$ state is completely spin-polarized will depend on the bilayer separation (d) and the strength of the magnetic field.

For the bilayer-(112) point at $d = 0, w = 0$ we compute the energy of an $\text{SU}(4)$ symmetric four-component system (bilayer + spin) with each component having filling $1/6$. The resulting state is gapless, which means that our DMRG performs poorly and we can only obtain a rough estimate for the energy. However, it appears that the magnetic field required to spin-polarize the system is approximately an order of magnitude less than that required to polarize the $\overline{1/3}$ phase, so this phase should be spin-polarized even at small magnetic fields.

In the large-d (330) phase, the problem reduces to decoupled layers, and it is well known that $\nu = 1/3$ system spin-spin polarizes, so we expect this will remain true for all d into the (112) phase.

Also note that experimental studies [123, 157] on this system have observed a spin-polarized system at all the tunneling strengths and interlayer separations accessed, for magnetic fields $B \approx 4$–$11\,\text{T}$.

5.5 Non-Abelian phase

In addition to the Abelian phases shown in Fig. 5.1, a number of non-Abelian candidates have been proposed to appear in the $1/3 + 1/3$ system. These include the $\mathbb{Z}_4$ Read-Rezayi state [40], the "interlayer-Pfaffian" (iPf) [124] and "intralayer-Pfaffian" states [125], and the bilayer Fibonacci state [129]. While we find no signature of these non-Abelian phases when restricting to the lowest Landau level and tuning the parameters d, w, and Δ_{SAS}, experimental samples certainly contain further tuning parameters we have neglected. To

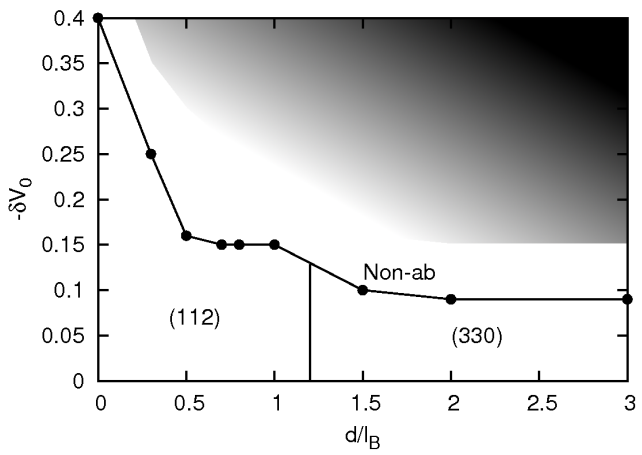

Figure 5.7: Phase diagram as a function of interlayer separation d and the modification of the Haldane potential δV_0. We find that as $-\delta V_0$ is increased, a new phase appears which we believe is a bilayer-spin charge separated non-Abelian phase. Data is taken with zero tunneling $\Delta_{\text{SAS}} = 0$ and layer width $w = 0$.

account for those, we have further perturbed the model with Haldane pseudopotentials V_0 and V_1. Remarkably, we find that a modification of the interlayer interaction, either through an attractive hard core $-\delta V_0$ or repulsive hollow-core δV_1, is sufficient to drive the system into a non-Abelian phase over a range of layer separations d. In Fig. 5.7 we show the phase diagram at fixed $\Delta_{\text{SAS}} = 0$, $w = 0$, as we scan d and the interlayer perturbation $-\delta V_0$. We find that for all interlayer separations d it is possible to reduce V_0 enough to reach a new phase consistent with the interlayer-Pfaffian (iPf) state, the evidence for which we present in this section.

Fig. 5.8 shows a plot of correlation length and energy as a function of δV_0 for $d = 0.5$. There is clearly a peak in the correlation length and a kink in the energy at $\delta V_0 \approx 0.16$, indicative of a first-order phase transition. The other points in Fig. 5.7 were determined from similar data. As $-\delta V_0$ is increased much further, we see that the correlation length continuously increases, and eventually the iDMRG becomes unstable [shaded area in Fig. 5.7]. Based on small systems studied by ED, in this regime we expect a strongly-paired phase where electrons form tightly bound pairs in real space [101, 176]. Upon even further increase of $-\delta V_0$ [not shown in Fig. 5.7], using ED we find symmetry-broken, CDW and clustered phases [177].

In the new intermediate δV_0 phase the iDMRG finds two nearly-degenerate ground states which we label $|\Omega^1\rangle$ and $|\Omega^2\rangle$. These states in fact triple the unit cell along the cylinder, so by translating $|\Omega^1\rangle$, $|\Omega^2\rangle$ we know there are *at least* six ground states in total. This must be understood as a lower bound on the degeneracy, as there is no general way to guarantee iDMRG finds all possible ground states.

Our evidence for identifying the novel phase with the iPf is five-fold.

1. The shift is $\mathcal{S} = 3$, as determined by the momentum polarization.

2. From the ground state $|\Omega^2\rangle$ we deduce there is a anyonic excitation that carries pseudo-spin $\pm\frac{1}{2}$ yet is

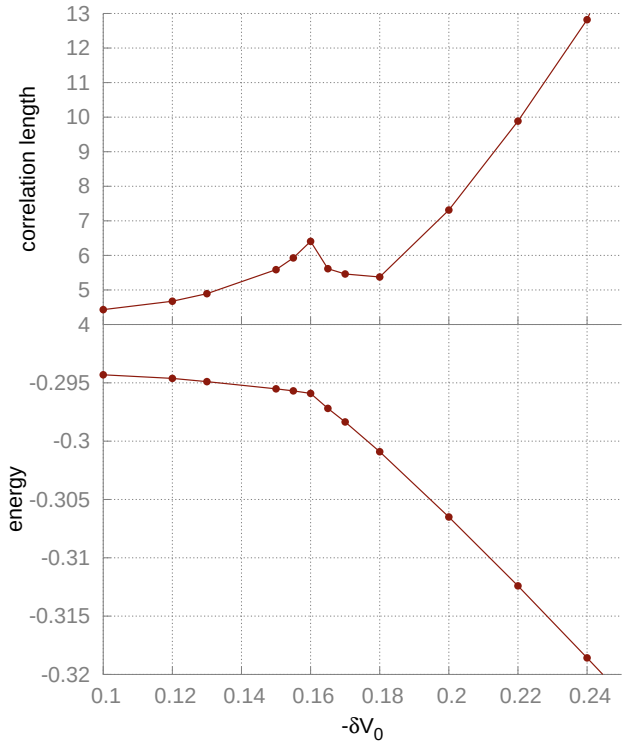

Figure 5.8: (Color online) Correlation length and energy for the spin-charge separated state as a function of δV_0 for $d = 0.5$, showing a clear first-order transition at $\delta V_0 \approx 0.16$. Note that correlation length increases rapidly as V_0 is made further negative.

charge neutral. Hence the phase is "spin-charge separated", and we call this excitation the spinon.

3. The spinon excitation is non-Abelian, with quantum dimension $d_{\Omega^2} \approx 1.4$ consistent with the iPf but not the intralayer-Pfaffian.

4. The momentum polarization of the two ground states differ by $h_{\Omega^2} - h_{\Omega^1} \approx -0.21$, which corresponds to the difference in the topological spins of the associated anyons.

5. The ground states exhibit a purely chiral entanglement spectra with counting that varies with charge sector.

A summary of the possible candidates is listed in Tab. 5.1 These observations eliminate all other known candidates for the $1/3 + 1/3$ system. In the following Sections, we give a brief description of the iPf phase (Sec. 5.5.1), compute overlaps against the model wavefunction using ED (Sec. 5.5.2), and present evidence for spin-charge separation (Sec. 5.5.3) and non-Abelian statistics (Sec. 5.5.4).

5.5.1 The interlayer-Pfaffian state

The iPf phase was first introduced and extensively discussed in Ref. [124], and coined the interlayer-Pfaffian in Ref. [125]. Similar to the Moore-Read phase relevant at $\nu = 5/2$, the interlayer-Pfaffian has non-Abelian Ising anyon excitations, which behave like unpaired Majorana zero modes. But the iPf phase is even more interesting than the Moore-Read phase as it is "spin-charge separated". Here we treat the two layers as an effective spin system and label them as $\uparrow$ and $\downarrow$. The total charge is the sum $Q = Q^{\uparrow} + Q^{\downarrow}$ while the "pseudo-spin" is the difference $S^z = \frac{1}{2}(Q^{\uparrow} - Q^{\downarrow})$. The *local* excitations are built up from neutral excitons and electrons. The neutral bilayer-excitons have $Q = 0$ and carry integral $S^z = 0, \pm 1, \pm 2, \ldots$, while the $Q = 1$ electrons carry $S^z = \pm\frac{1}{2}$. Thus local excitations obey the relation $Q \equiv 2S^z \pmod 2$, "locking" spin and charge together. In the iPf phase the electron can fractionalize into a neutral non-Abelian "spinon" carrying $Q = 0, S^z = \frac{1}{2}$ and three non-Abelian "chargons" carrying $Q = \frac{1}{3}, S^z = 0$. Thus when including fractional excitations there are no constraints between charge and spin.

A representative (model) wavefunction for the iPf phase is given by [124]

$$\Psi(\{z\},\{w\}) = \mathrm{Pf}\left(\frac{1}{x_i - x_j}\right)\Psi_{221}(\{z\},\{w\}). \tag{5.24}$$

Here $\{z\}$ and $\{w\}$ denote complex 2D coordinates of electrons in two layers, while $\{x\} = \{z, w\}$ stands for coordinates of all electrons, regardless of their layer index. The (221) state is defined as

$$\Psi_{221} = \prod_{a<b}(z_a - z_b)^2 \prod_{a<b}(w_a - w_b)^2 \prod_{a,b}(z_a - w_b) \times e^{-\frac{1}{4}\sum_a |z_a|^2} e^{-\frac{1}{4}\sum_a |w_a|^2}. \tag{5.25}$$

There are nine anyon types in the iPf phase, which break up into three sets of three. Three of these anyons are over-all charge neutral and form the Ising theory: the trivial sector $\mathbb{1}$, a neutral fermion ψ which carries

fermion parity but no charge, and the non-Abelian spinon excitation ϕ_s, which carries pseudo-spin $S^z = \pm\frac{1}{2}$ but no charge [3]. In addition, threading 2π flux quanta induces a charge $Q = \frac{1}{3} + \frac{1}{3}$ Abelian anyon we denote by Φ. The fusion rules are

$$\phi_s \times \psi = \phi_s, \qquad \phi_s \times \phi_s = \mathbb{1} + \psi, \qquad \Phi^3 = \mathbb{1}. \tag{5.26}$$

By combining fluxes Φ with the Ising sector, we obtain the nine anyon types:

		charge Q		
		0	$\frac{2}{3}$	$\frac{4}{3}$
spin S^z	0	$\mathbb{1}$	Φ	Φ^2
	0	ψ	$\psi\Phi$	$\psi\Phi^2$
	$\frac{1}{2}$	ϕ_s	$\phi_s\Phi$	$\phi_s\Phi^2$

(5.27)

Corresponding to the nine anyon types we should obtain nine degenerate ground states on the torus or an infinite cylinder. Using the 3-body parent Hamiltonian [178, 179] for the model wavefunction in Eq. (5.24), we have verified this is indeed the case on the torus. By performing exact diagonalization of this Hamiltonian, we find three ground states with zero momentum, each being 3-fold degenerate due to center-of-mass translations (i.e., inserting Φ), which yields nine ground states in total.

In the "thin-torus" limit [180, 181, 182] the cylinder is effectively a one-dimensional spin-full fermion chain, the ground states reduce to the "root configurations".

$$|\mathbb{1}\rangle: \quad |\cdots 0\,2\,0\,0\,2\,0\,0\,2\,0\cdots\rangle\,, \tag{5.28a}$$

$$|\psi\rangle: \quad |\cdots \overbrace{\uparrow\ 0\ \downarrow}\overbrace{\uparrow\ 0\ \downarrow}\overbrace{\uparrow\ 0\ \downarrow}\cdots\rangle\,, \tag{5.28b}$$

$$|\phi_s\rangle: \quad |\cdots \overbrace{\uparrow}0\overbrace{\downarrow}\overbrace{\uparrow}0\overbrace{\downarrow}\overbrace{\uparrow}0\overbrace{\downarrow}\cdots\rangle\,. \tag{5.28c}$$

Here a 2/0 denotes a doubly occupied/empty site, and the bracket $\overbrace{\uparrow\downarrow} = (\uparrow\downarrow - \downarrow\uparrow)/\sqrt{2}$ denotes electrons placed in a spin-singlet. We have verified the thin torus wavefunctions by performing exact diagonalization of the model Hamiltonian in the thin-torus limit [183].

5.5.2 Exact-diagonalization overlaps

In small systems accessible by ED, the overlap with iPf model wavefunction becomes large in the novel phase identified in Fig. 5.7. For small systems up to 10 particles, we can obtain the complete set of exact ground states on the torus corresponding to Eq. 5.24, and overlap those with the same number of lowest states of

[3] Technically the list of anyons are sets of excitations, rather than a single excitation. What we've described here are the properties of a representative excitation within each set, with all other excitations related by the addition/removal of electrons.

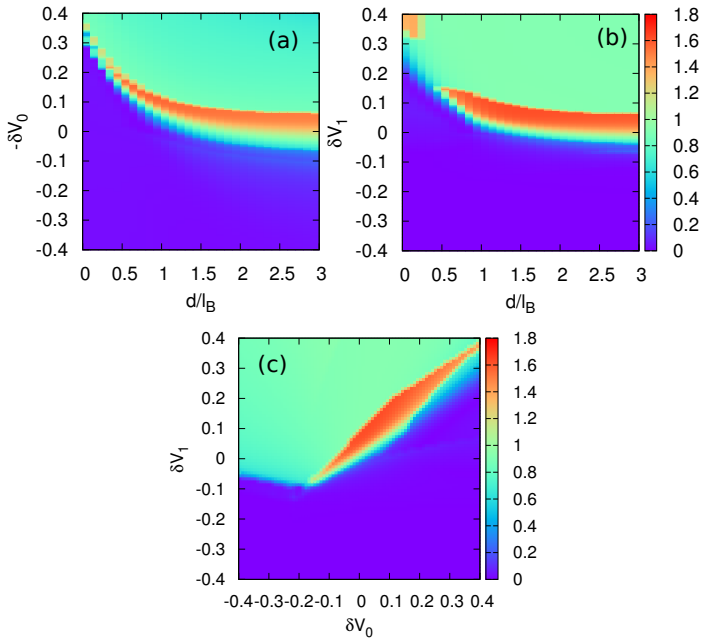

Figure 5.9: (Color online) Overlap between the iPf state and the ground state of Coulomb interaction with modified short-range pseudopotentials from ED. The system contains 8 electrons and 12 flux quanta, on a torus with a hexagonal unit cell. The color scale indicates the sum of singular values of the 3×3 overlap matrix defined in the main text. (a) The interaction is varied by changing d/ℓ_B and adding δV_0 pseudopotential. (b) The interaction is varied by changing d/ℓ_B and adding δV_1 pseudopotential. The same amount of δV_1 is added to both intralayer and interlayer Coulomb. (c) The effect of varying both V_0 and V_1 at fixed bilayer distance $d = 1.5\ell_B$. Note that the iPf phase is located in the narrow red strip, and can be stabilized by either the reduction in V_0 (a), the increase in V_1 (b), or the increase of both δV_0 and δV_1 (c).

the Coulomb interaction (possibly with some short-range pseudopotentials added). This defines an overlap matrix. The sum of singular values of the overlap matrix can serve as a rough indicator if the system is in the iPf phase or not. For example, singular values close to zero would indicate the system being far from the iPf phase. In a finite system, singular values that can be considered "non-zero" are those larger than $1/\sqrt{\dim \mathcal{H}}$, where $\dim \mathcal{H}$ is the dimension of the Hilbert space. Note that because of the invariance under the center-of-mass translation, it is sufficient to restrict only to the three ground states with momentum equal to zero, i.e., we obtain a 3×3 overlap matrix.

Fig. 5.9 summarizes the effect of varying short-range V_0 and V_1 components of the Coulomb interactions inferred from the overlap of the ground state (obtained by ED) and the model wavefunction, Eq. (5.24). We plot the sum of singular values of the overlap matrix between the exact ground state of the Coulomb interaction (with modified short-range components) and the iPf state. In Fig. 5.9(a),(b) we vary the bilayer distance d and add V_0 (a) or V_1 pseudopotential (b) to the Coulomb interaction. The system contains 8 electrons and 12 flux quanta on a torus with a hexagonal unit cell. We first note that the largest value of the overlap occurs in the narrow red strip, corresponding to intermediate values of d and the reduction of V_0 or, conversely, the increase of V_1. The non-zero overlap in this region suggests that the system is in the iPf

phase. The ED result in Fig. 5.9(a) can be directly compared with the phase diagram obtained by DMRG in Fig. 5.7. We note that the variation δV_1 in Fig. 5.9(b) assumes adding the same amount of δV_1 to both intralayer and interlayer Coulomb pseudopotential. Another possibility is to add δV_1 to interlayer Coulomb only. This yields a qualitatively similar result to Fig. 5.9(b) but with somewhat stronger finite-size effects.

Finally, in Fig. 5.9(c) we consider a combined effect of simultaneously varying V_0 and V_1. The starting point is Coulomb interaction at fixed bilayer distance $d = 1.5$ in the (330) phase. In this case we find the iPf phase to be stabilized for positive δV_0 as well as positive δV_1. Note that the largest overlap (i.e., sum of singular values of the overlap matrix) is roughly the same in all cases shown in Fig. 5.9. Although the magnitude of the overlap with the iPf is significant, it is relatively moderate (at maximum 1.8 compared to the "perfect" value of 3). The reason for this is the difficulty in fully resolving the complete set of iPf ground states in small finite systems. For example, finding only two out of three ground states will significantly reduce the overlaps in Fig. 5.9. This is responsible for small overlaps in at least part of the green region in Fig. 5.9, and leads to a somewhat narrower iPf phase compared to the DMRG result in Fig. 5.7.

5.5.3 Spin-charge separation

We now demonstrate how we can extract the charges (Q, S^z) of an anyon a from entanglement spectrum of its associated ground state $|a\rangle$. Partition the cylinder with a cut along the circumference into "left" and "right" semi-infinite halves. Each left Schmidt state $|\beta; a\rangle$ of the MES $|a\rangle$ has quantum numbers $Q^{\uparrow/\downarrow}_{\beta;a}$. By coarse graining the Schmidt spectrum $\lambda_{\beta;a}$ over quantum-number sectors, we can look at the probability distribution P_a for charge Q_L or spin S^z_L to fluctuate to the left of the cut:

$$1 = \sum_{Q_L, S^z_L} P_a(Q_L, S^z_L), \tag{5.29a}$$

$$\langle \hat{Q}_L \rangle_a = \sum_{Q_L, S^z_L} P_a(Q_L, S^z_L) Q_L, \tag{5.29b}$$

$$\langle \hat{S}^z_L \rangle_a = \sum_{Q_L, S^z_L} P_a(Q_L, S^z_L) S^z_L. \tag{5.29c}$$

The first equation expresses normalization. The "entanglement averages" in the second and third equation determine the charge and pseudo-spin of the anyon a (modulo local excitations). In Fig. 5.10, we have plotted this probability distribution in the spin-charge plane for the states $|\Omega^1\rangle$, $|\Omega^2\rangle$ (for cylinders with circumference $L = 14$). Intuitively the $|\Omega^1\rangle$ has a probability distribution associated with a completely neutral object, plus some number of electrons; in contrast $|\Omega^2\rangle$ has a probability distribution associated with a $Q = 0$, $S^z = \pm\frac{1}{2}$ object, plus some number of electrons. The anyon associated with the latter ground state is what we identify with the spinon (ϕ_s).

Referring to the thin-torus wavefunctions of Eq. (5.28c), we indeed see that the symmetric entanglement cut in the ϕ_s sector splits a singlet, leading to the two-fold degenerate $P_\sigma(Q_L, S^z_L)$ just discussed.

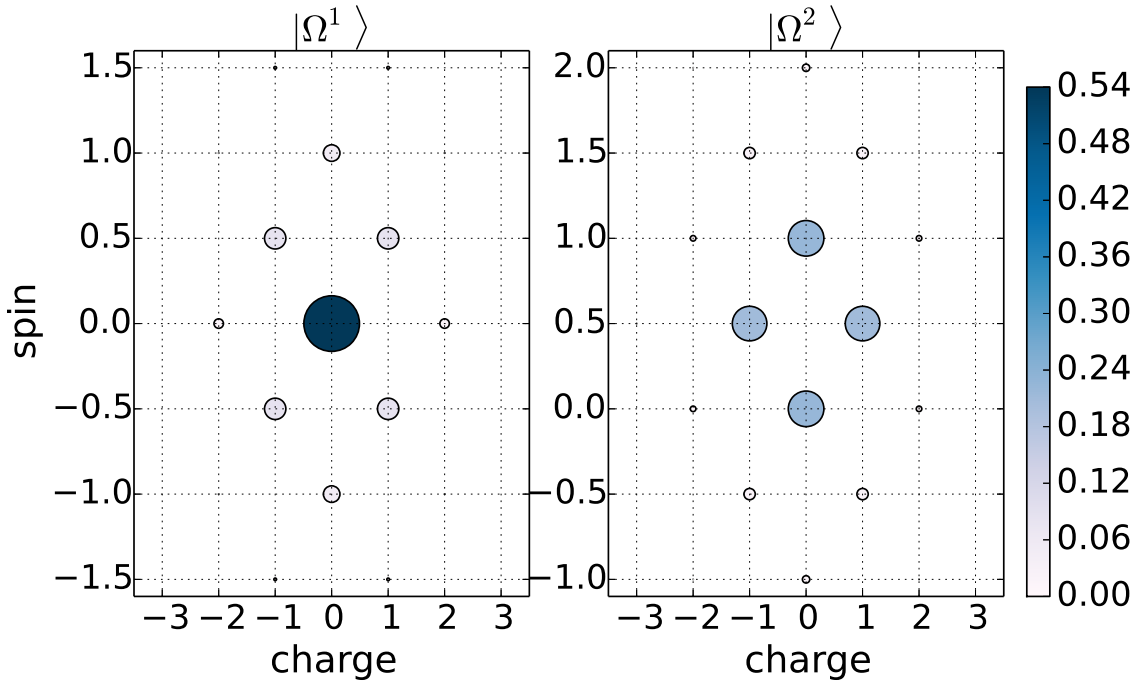

Figure 5.10: (Color online) Entanglement of for spin-charge separation in the non-Abelian phase. We plot the probability $P_a(Q_L, S^z_L)$ for charges Q_L, S^z_L to fluctuate to the left of the cut in ground states $a = \Omega_1/\Omega_2$. The center of this distribution gives the charge and spin of the anyon associated with the ground state. We see that ground state Ω_1 corresponds to a quasiparticle with $S^z = 0$ and $Q = 0$, consistent with either the $\mathbb{1}$ or ψ sector; in the other ground state there is a quasiparticle with $S^z = 1/2$ and $Q = 0$, consistent with the ϕ_s sector.

Our interpretation can be made rigorous by viewing the cylinder wavefunction as a 1D fermion chain and appealing to the theory of 1D symmetry-protected topological (SPT) phases. The internal symmetry group of the bilayer is $G = (\mathrm{U}(1) \times \mathrm{U}(1)) \rtimes \mathbb{Z}_2$, coming from particle conservation in each layer and the interchange of the two layers. In addition, there is a 180-degree inversion symmetry $\mathcal{I}$, which we denote by $\mathbb{Z}_2^{\mathcal{I}}$. As discussed in Sec. 5.3.4, the global symmetry group can be restricted to the left half of the system in order to determine how it acts on left Schmidt states. In a 1D symmetry-protected topological (SPT) phases, the symmetry G may be represented *projectively* on the Schmidt states. The classification of 1D-SPT phases is given by the distinct possible projective representations, which are in turned classified by the second group cohomology classes [19]:

$$\text{1D } G\text{-symm. phases} \;\leftrightarrow\; \text{elements of } H^2\big(G, \mathrm{U}(1)\big). \tag{5.30}$$

For our symmetry the group cohomology contains a particular $\mathbb{Z}_2$ component we identify with spin-charge-

separation:

$$\mathbb{Z}_2 \in H^2\big((\mathrm{U}(1)^2 \rtimes \mathbb{Z}_2) \times \mathbb{Z}_2^{\mathcal{I}}, \mathrm{U}(1)^{\mathcal{I}}\big). \tag{5.31}$$

Here, $\mathrm{U}(1)^{\mathcal{I}}$ denotes that there is "G-action", since the inversion $\mathcal{I}$ acts on the coefficients via complex conjugation. We identify the two phases classified by this $\mathbb{Z}_2$ with trivial and spin-charge separated.

We will identify the $\mathbb{Z}_2$ invariant by examining how the symmetry relations are realized projectively on the Schmidt states. Following established techniques [184, 19, 185], let $U_{\mathcal{I}}$ denote the action of inversion and $U_{\theta_{\uparrow/\downarrow}}$ the $\mathrm{U}(1)$ symmetries of the upper/lower layer when acting on Schmidt states. A priori, these U have $\mathrm{U}(1)$ phase ambiguities, which we will gauge fix as follows. We first choose a gauge in which $U_{\theta_\sigma} U_{\theta'_\sigma} = U_{\theta_\sigma + \theta'_\sigma}$ for $\theta_\sigma + \theta'_\sigma \in [0, 2\pi)$, which fixes U_{θ_σ} up to a single $\mathrm{U}(1)$ ambiguity $U_{\theta_\sigma} \to U_{\theta_\sigma} e^{i\theta_\sigma m_\sigma}$ for some m_σ. Next, we further gauge-fix U_{θ_σ} by requiring that

$$U_{\mathcal{I}} U_{\theta_\sigma}^* = U_{\theta_\sigma} U_{\mathcal{I}}. \tag{5.32}$$

This *fully* fixes the gauge of U_{θ_σ}.

Combining the group relations $U_{2\pi_\sigma} \propto \mathbb{1}$ with the gauge choice established by Eq. (5.32), we find $\mathbb{Z}_2$ invariants

$$U_{2\pi_\sigma} \equiv P_\sigma = \pm 1. \tag{5.33}$$

Because of the $\mathbb{Z}_2$ bilayer symmetry, we must have $P_\uparrow = P_\downarrow$. Thus we find two possibilities:

$$(P_\uparrow, P_\downarrow) = (+1, +1) \quad \text{(trivial)} \tag{5.34}$$

$$(P_\uparrow, P_\downarrow) = (-1, -1) \quad \text{(spin-charge separated)} \tag{5.35}$$

The physical interpretation is as follows. In the spin-charge separated scenario, $2S^z + 1 = Q \mod 2$, or equivalently $Q_\uparrow - Q_\downarrow + 1 = Q_\uparrow + Q_\downarrow \mod 2$. It follows that $\frac{1}{2} = Q_\downarrow \mod 1$ and $\frac{1}{2} = Q_\uparrow \mod 1$. The half-integral nature of Q_σ is revealed in the entanglement spectrum via the projective relation $U_{2\pi_\sigma} = e^{2\pi i Q_\sigma} = P_\sigma = -1$. Thus $P_\sigma = -1$ is a quantized signature of spin-charge separation. Each anyon in the system has a P_σ, and they must obey the fusion rules. Based on Fig. 5.10 we assign $P_\sigma(\mathbb{1}) = 1$, $P_\sigma(\psi) = 1$, $P_\sigma(\phi_s) = -1$, which is clearly consistent with the fusion rules in Eq. (5.26). Also note that having an anyon with $P_\sigma = -1$ is inconsistent with some fusion rules, in particular it is inconsistent with the fusion rules for the Fibonacci phase.

We have explicitly checked the symmetry properties of the Schmidt states to verify that the MES $|\phi_s\rangle$ has non-trivial 1D-SPT order under G, while $|\mathbb{1}\rangle$ and $|\psi\rangle$ are trivial, which is why we identify $\phi_s \leftrightarrow \Omega^2$. Pictorially, referring back to Fig. 5.10 we see that $|\Omega^2\rangle$ has a 2-fold degenerate probability distribution,

which is a tell-tale signature of a 1D-SPT phase.

In summary, we have shown the state has an excitation with quantum numbers $Q = 0, S^z = \pm\frac{1}{2}$, which rules out the (330), $\mathbb{Z}_4$ Read-Rezayi, and Fibonacci phases. In light of this data, we find that $|\Omega^2\rangle$ is consistent with $|\phi_s\rangle$, while $|\Omega^1\rangle$ is consistent with either $|\mathbb{1}\rangle$ or $|\psi\rangle$. The absence of either the $\mathbb{1}$-family or ψ-family from our numerics is not terribly troubling, as $\mathbb{1}$ and ψ have no symmetry properties which distinguish them; even a slight energetic splitting of the topological degeneracy may consistently bias the iDMRG towards the latter.

The intralayer-Pfaffian also has a $Q = 0$, $S^z = \pm\frac{1}{2}$ spinon, but it can be distinguished from the spinon of the interlayer-Pfaffian by its quantum dimension.

5.5.4 Non-Abelian signatures

In order to directly confirm the non-Abelian nature of the novel phase, we measure the quantum dimension of the spinon. In the iPf phase, the spinon has quantum dimension $d_{\phi_s} = \sqrt{2}$. In contrast, the intralayer-Pfaffian phase has two kinds of ϕ_s excitations, each of which lives in only the top or bottom layers. In this phase the observed quasiparticle with spin-charge separation is a product of a spinon in each layer, and it therefore has quantum dimension $d = 2$. Our measurements of the quantum dimension therefore allow us to rule out the intralayer-Pfaffian.

To make this measurement, we compute the difference in the entanglement entropy between $|\Omega^1\rangle$ and $|\Omega^2\rangle$. From Eq. (5.18) [5, 6],

$$S_{\Omega^2}(L) - S_{\Omega^1}(L) = \log(d_{\Omega^2}/d_{\Omega^1}) + \mathcal{O}(e^{-L/\tilde{\xi}}), \tag{5.36}$$

from which we obtain the ratio of quantum dimensions $d_{\Omega_2}/d_{\Omega_1}$. Assuming $|\Omega^1\rangle$ corresponds to a Abelian anyon ($d_{\Omega^1} = 1$), and provided the finite-size effects are small enough, we extract the quantum dimension of the spin-charge separated anyon. In Fig. 5.11 we show the results of this subtraction, for $L = 12$–17, for several different combinations of d, δV_0, and δV_1. Finite-size and finite-χ effects introduce significant systematic errors into our calculation of this quantity, leading to results for $\Delta S = S_{\Omega^2} - S_{\Omega^1}$ which vary from 0.1–0.5 for different measurements. Though this prevents us from determining the quantum dimension precisely, we can still say that our results are consistent with $d_{\phi_s} = \sqrt{2}$ (as shown by the blue dashed line in Fig. 5.11), and inconsistent with the intralayer Pfaffian value $d = 2$ (as shown by the green dashed line), and the Abelian value of $d = 1$.

Furthermore, we can use a similar subtraction scheme to extract the (relative) topological spin of the spinon (Ω^2) compared to the neutral (Ω^1) via the momentum polarization [Eq. (5.21)]. Taking the difference of the momentum polarizations of the ground states

$$M_{\Omega^2} - M_{\Omega^1} = h_{\Omega^2} - h_{\Omega^1} + \mathcal{O}(e^{-L/\tilde{\xi}}) \pmod 1, \tag{5.37}$$

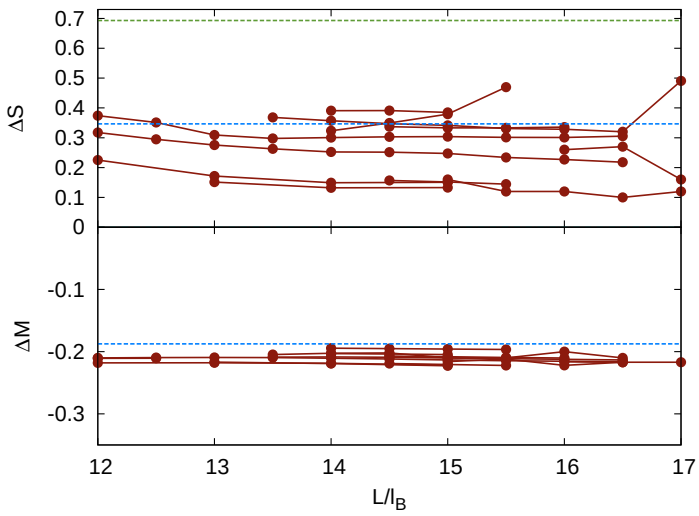

Figure 5.11: (Color online) Differences in entanglement entropy and momentum polarization for the two degenerate states as a function of circumference. Data was taken at a variety of different interlayer separations, δV_0 and δV_1. The blue dashed lines show the expected values for the iPf phase, at $S_{\phi_s} - S_\psi = \log\sqrt{2}$ and $h_{\phi_s} - h_\psi = -\frac{3}{16}$.

we can extract the difference in topological spin $\Delta h = h_{\Omega^2} - h_{\Omega^1}$. As shown in Fig. 5.11, we get $\Delta h \approx -0.21$ for a number of points in phase space. This is consistent with the identification $\Omega^1 = \psi$, $\Omega^2 = \phi_s$, as $h_{\phi_s} - h_\psi = \frac{5}{16} - \frac{1}{2} = -0.1875$ in the iPf phase. We attribute the difference between the observed and expected values to finite-size and finite-χ systematic errors. (Note that $h_{\mathbb{1}} = 0$, and thus we can conclude $\Omega^1 \neq \mathbb{1}$.)

Further support for our identification of ground states can be found in the entanglement spectrum. We first give the theoretical orbital entanglement spectra for the ground states of the iPf phase, which depends on both the ground state $|a\rangle$ and the charge across the entanglement cut. (Note that so far in this work, we have given the entanglement spectra for only one value of electric charge crossing the entanglement cut, and we chose the value of charge which has the lowest lying entanglement states. Henceforth we will be explicit about the charges.) For any of the nine MES and fixed charge (Q, S^z) across the entanglement cut, the entanglement spectra counting follows one of three possible sequences.

$$\begin{aligned} s_1 &: 1, 2, 6, 13, \ldots, \\ s_\sigma &: 1, 3, 8, 19, \ldots, \\ s_\chi &: 1, 3, 8, 18, \ldots. \end{aligned} \tag{5.38}$$

For state $|\mathbb{1}\rangle$, the entanglement spectrum follows the s_1 sequence for even Q, and s_χ sequence for odd Q. For state $|\psi\rangle$, the spectrum follows s_χ and s_1 for even and odd Q, respectively. For state $|\phi_s\rangle$, the entanglement spectrum always follows s_σ.

We attempt to match up the low-lying states of the ground states $|\Omega^1\rangle$ and $|\Omega^2\rangle$, shown in Fig. 5.12 for sys-

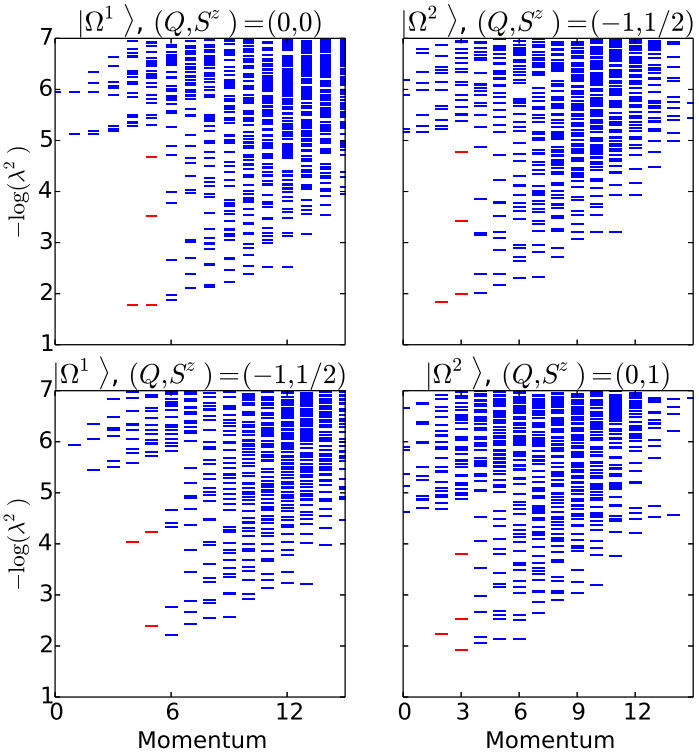

Figure 5.12: (Color online) Entanglement spectra for the putative iPf state. The left two panels show the entanglement spectra for the $|\Omega^1\rangle$ state, for the charge sectors with the lowest-lying and second lowest-lying entanglement states, the counting for these states is $1, 3, ...$ and $1, 2, ...$, as expected if $|\Omega^1\rangle = |\psi\rangle$. The right panel shows spectra for the $|\Omega^2\rangle$ state. There are two degenerate charge sectors with lowest lying states. Here we show one example from each of the two sectors with the lowest-lying entanglement states, and we find counting of $1, 3, \ldots$ in both, as expected if $|\Omega^2\rangle = |\phi_s\rangle$.

tem size $L = 24$–26, to those expected for the iPf phase. Typically one defines the "low-lying" entanglement states as those below the "entanglement gap", which is a window devoid of states as the circumference is increased. In practice, at finite system size we observe multiple regions without states which could be called the entanglement gap, which makes it difficult to specify which levels should be counted. We have highlighted in the figures to indicate the presumed counting of iPf, but in full honesty other assignments are possible. The left panels shows the entanglement spectra for $|\Omega^1\rangle$, with $(Q, S^z) = (0, 0)$ (top) and $(Q, S^z) = (-1, \frac{1}{2})$ (bottom). Assuming states with $-\log(\lambda^2) < 5$ are the low-lying states, we observe the counting $1, 3, \ldots$ and $1, 2, \ldots$ for the two charge sectors, respectively. This suggests that $|\Omega^1\rangle = |\psi\rangle$, consistent with the momentum polarization data above. On the right panels, we showed the entanglement spectra for $|\Omega^2\rangle$ (for the same charges), which seem to indicate the counting $1, 3, \ldots$ regardless of charge, also consistent with the identification $|\Omega^2\rangle = |\phi_s\rangle$.

In summary, the well-established spin-charge separation shown in Fig. 5.10 rules out all currently proposed wavefunctions besides the intralayer-Pfaffian and iPf phase. The entanglement properties and the overlaps, though not conclusive, are incompatible with the intralayer-Pfaffian state, but appear consistent with the iPf state.

5.6 Conclusion

In this work, we use iDMRG and exact diagonalization techniques to study a bilayer quantum Hall system with filling $1/3$ in each layer. We find a phase diagram in terms of the experimentally accessible parameters: layer separation, interlayer tunneling, and layer width. We find three different phases: a phase with decoupled layers, a bilayer-spin singlet phase, and a bilayer-symmetric phase. We confirm the nature of these phases and study the transitions between them.

We also explore the phase diagram for Coulomb interaction with modified short-range components (V_0 and V_1). We find a non-Abelian phase over a wide region of parameter space. This phase has anyons which carry spin $1/2$ and no charge. This observation, coupled with a study of additional entanglement properties and wavefunction overlaps, leads us to conclude that the non-Abelian phase is interlayer-Pfaffian. Our data for the non-Abelian phase is inconsistent with all other known non-Abelian candidates. However, it is possible that a novel non-Abelian state could be constructed that can reproduce our results.

Although it is experimentally not feasible to directly modify a given pseudopotential, there are many realistic ways to change the Coulomb interaction in a quantum Hall system. The simplest one is varying the chemical potential to place the system in a higher Landau level, effectively at filling $\nu = 8/3$, where FQHE has been seen [186, 187, 188]. More recent sample fabrication techniques also allow to access the regime of large Landau level mixing (with the mixing parameter $\kappa \gtrsim 2$ [189, 190]), which is expected to strongly modify the short-range components of the Coulomb interaction. Finally, tilting the magnetic field or explicitly screening the Coulomb potential may serve as additional experimental knobs to probe the non-

Abelian physics at $\nu = 1/3 + 1/3$. Since all of these perturbations can ultimately be expanded in terms of V_α's, the phase diagram we find here may be helpful in guiding future experimental studies towards a realization of the non-Abelian phase.

Chapter 6

Conclusions and Future Directions

In this thesis we have seen a number of examples of topological systems that can be studied numerically. In Chapter 3 we constructed lattice models of integer and fractional quantum Hall effects for bosons, and studied these models using Monte Carlo simulations. In Chapter 4 we used a similar procedure to construct a lattice model for a bosonic topological insulator in three dimensions. In other works not explicitly outlined in this thesis similar techniques have also been used to construct one-dimensional symmetry-protected topological phases, and to construct topological phases of lattice gauge theories. These lattice models provide concrete realizations of phases which had previously been only understood at the level of an effective field theory. Since the models can be studied numerically, they allow us to answer questions, for example about the nature of phase transitions, which may not be accessible to other methods. These models can also allow us to find microscopic Hamiltonians which realize this physics, and which may lead towards experimental realizations in cold atomic systems.

There are a number of directions research like this can take in the future. One possible direction would be to try to realize other topological phases with similar lattice models. One could try to realize the discrete-symmetry phases described in Ref.[191], which would provide a more concrete understanding of the abstract concepts described there. Such an effort may also tell us which SPTs can be described by models of the type described in this thesis. One might also try to construct some of the other bosonic topological insulators described in Ref. [192].

Another direction would be to use the models already constructed to learn more about the phases they describe. For example, we have studied the phase transitions between different bosonic FQHE plateaus. The Hamiltonian for the bosonic FQHE, which we presented in Sec. 3.6, is quite distant from what can be accomplished experimentally in cold atoms, but we can try to make the Hamiltonian more realistic, for example by replacing the harmonic oscillators in the Hamiltonian with simple clock variables. We could then perform the Trotter decomposition on the resulting Hamiltonian and see if it still realizes a topological phase. We can also try to learn more about the entanglement properties of the phases we have constructed, for example by computing their entanglement entropies and Hall viscosities. Recently there have been a number of proposals for realizing interesting physics in the bosonic FQHE (e.g., Ref. [193]), and we could try to

realize these proposals in our lattice models.

In Chapter 5 we used a different numerical technique, DMRG, to study bilayer fractional quantum Hall effect systems (of fermions) with a realistic Hamiltonian. We were able to determine the phase diagram in terms of experimentally accessible parameters. We also found a non-Abelian phase, the interlayer Pfaffian, and determined what modifications to the Coulomb interaction realize this phase.

There are a number of future directions in which similar techniques can be used. We are currently studying using the same numerical method to study the composite fermi liquid phase thought to exist at $\nu = 1/2$. It seems that we are able to simulate this phase on much larger system sizes than have been done before, and because of this we can potentially answer a number of different questions about this phase. One question we are interested in immediately is whether or not the phase is particle-hole symmetric. We can also look at other quantum Hall systems, such as bilayer systems at other filling fractions, or graphene. The quality of FQHE samples in both GaAs and graphene continues to increase, and this will likely lead to the discovery of more phenomena which cannot be easily explained. The DMRG methods described in this work are a very powerful tool which can be used to address these problems.

The study of topological phases has dominated condensed matter physics for many years. During that time the majority of the literature has focussed on phases of free fermions, and as a result the supply of interesting phenomena that can be discovered in the free-fermion context is running out. In order to continue to discover new topological physics, we must turn to interacting systems. In these systems it will be necessary to develop new techniques, especially numerical techniques. The techniques developed and applied in this thesis are examples of this philosophy, which should continue to yield interesting results for interacting topological phases.

Bibliography

[1] X.-G. Wen, *Quantum field theory of many-body systems: from the origin of sound to an origin of light and electrons*. Oxford: Oxford University Press, 2007.

[2] K. v. Klitzing, G. Dorda, and M. Pepper, "New method for high-accuracy determination of the fine-structure constant based on quantized hall resistance," *Phys. Rev. Lett.*, vol. 45, pp. 494–497, Aug 1980.

[3] A. M. Turner and A. Vishwanath, "Beyond Band Insulators: Topology of Semi-metals and Interacting Phases," *ArXiv e-prints*, Jan. 2013.

[4] A. Einstein, B. Podolsky, and N. Rosen, "Can quantum-mechanical description of physical reality be considered complete?," *Phys. Rev.*, vol. 47, pp. 777–780, May 1935.

[5] A. Kitaev and J. Preskill, "Topological entanglement entropy," *Phys. Rev. Lett.*, vol. 96, p. 110404, Mar 2006.

[6] M. Levin and X.-G. Wen, "Detecting topological order in a ground state wave function," *Phys. Rev. Lett.*, vol. 96, p. 110405, Mar 2006.

[7] J. Maciejko, T. L. Hughes, and S.-C. Zhang, "The quantum spin hall effect," *Annual Review of Condensed Matter Physics*, vol. 2, pp. 31–53, 2011.

[8] M. Z. Hasan and C. L. Kane, "¡i¿colloquium¡/i¿: Topological insulators," *Rev. Mod. Phys.*, vol. 82, pp. 3045–3067, Nov 2010.

[9] X.-L. Qi and S.-C. Zhang, "Topological insulators and superconductors," *Rev. Mod. Phys.*, vol. 83, pp. 1057–1110, Oct 2011.

[10] L. Fu and C. L. Kane, "Time reversal polarization and a Z_2 adiabatic spin pump," *Phys. Rev. B*, vol. 74, p. 195312, Nov 2006.

[11] X.-L. Qi, T. L. Hughes, and S.-C. Zhang, "Topological field theory of time-reversal invariant insulators," *Phys. Rev. B*, vol. 78, p. 195424, Nov 2008.

[12] H. Nielsen and Ninomiya, "A no-go theorem for regularizing chiral fermions," *Phys. Lett. B*, vol. 105, pp. 219–223, 1981.

[13] A. Kitaev, "Periodic table for topological insulators and superconductors," *arXiv:cond-mat*, p. 0901.2686, 2009.

[14] A. P. Schnyder, S. Ryu, A. Furusaki, and A. W. W. Ludwig, "Classification of topological insulators and superconductors in three spatial dimensions," *Phys. Rev. B*, vol. 78, p. 195125, Nov 2008.

[15] X. Chen, Z.-C. Gu, Z.-X. Liu, and X.-G. Wen, "Symmetry-protected topological orders in interacting bosonic systems," *Science*, vol. 338, no. 6114, pp. 1604–1606, 2012.

[16] X. Chen, Z.-C. Gu, Z.-X. Liu, and X.-G. Wen, "Symmetry protected topological orders and the group cohomology of their symmetry group," *Phys. Rev. B*, vol. 87, p. 155114, Apr 2013.

[17] A. Kapustin and R. Thorngren *arXiV/hep-th*, p. 1309.4721, 2013.

[18] R. B. Laughlin, "Anomalous quantum hall effect: An incompressible quantum fluid with fractionally charged excitations," *Phys. Rev. Lett.*, vol. 50, pp. 1395–1398, May 1983.

[19] L. Fidkowski and A. Kitaev, "Topological phases of fermions in one dimension," *Phys. Rev. B*, vol. 83, p. 075103, Feb 2011.

[20] C. Wang and T. Senthil, "Interacting fermionic topological insulators/superconductors in three dimensions," *Phys. Rev. B*, vol. 89, p. 195124, May 2014.

[21] Y.-M. Lu and A. Vishwanath, "Theory and classification of interacting integer topological phases in two dimensions: A chern-simons approach," *Phys. Rev. B*, vol. 86, p. 125119, Sep 2012.

[22] A. Kitaev and C. Laumann, "Topological phases and quantum computation," *arXiv:c*, p. 0904.2771, 2009.

[23] M. Levin and Z.-C. Gu, "Braiding statistics approach to symmetry-protected topological phases," *Phys. Rev. B*, vol. 86, p. 115109, Sep 2012.

[24] K. Walker and Z. Wang, "(3+1)-tqfts and topological insulators," *arXiv:cond-mat*, p. 1104.2636, 2011.

[25] C. W. von Keyserlingk and F. J. Burnell, "Walker-Wang models and axion electrodynamics," *ArXiv e-prints*, 2014.

[26] T. Senthil and M. Levin, "Integer quantum hall effect for bosons," *Phys. Rev. Lett.*, vol. 110, p. 046801, Jan 2013.

[27] G. Rosenberg and M. Franz, "Witten effect in a crystalline topological insulator," *Phys. Rev. B*, vol. 82, p. 035105, Jul 2010.

[28] A. Vishwanath and T. Senthil, "Physics of three-dimensional bosonic topological insulators: Surface-deconfined criticality and quantized magnetoelectric effect," *Phys. Rev. X*, vol. 3, p. 011016, Feb 2013.

[29] M. Metlitski and M. P. A. Fisher *unpublished notes*, 2013.

[30] M. A. Metlitski, C. L. Kane, and M. P. A. Fisher, "Bosonic topological insulator in three dimensions and the statistical witten effect," *Phys. Rev. B*, vol. 88, p. 035131, Jul 2013.

[31] M. Freedman, M. Larsen, and Z. Wang, "A modular functor which is universal for quantum computation," *Commun. Math. Physics.*, vol. 227, p. 605, 2002.

[32] S. Vijay, T. Hsieh, and L. Fu, "Majorana fermion surface code for universal quantum computation," *arXiv:cond-mat*, vol. 1504.01724, 2015.

[33] A. Y. Kitaev, "Unpaired Majorana fermions in quantum wires," vol. 44, p. 131, Oct. 2001.

[34] S. X. Cui and Z. Wang, "Universal quantum computation with metaplectic anyons," *arXiv:con*, p. 1405.7778, 2014.

[35] J. Alicea, "New directions in the pursuit of majorana fermions in solid state systems," *Rep. Prog. Phys.*, vol. 75, p. 076501, 2012.

[36] V. Mourik, K. Zuo, S. M. Frolov, S. R. Plissard, E. P. A. M. Bakkers, and L. P. Kouwenhoven, "Signatures of Majorana Fermions in Hybrid Superconductor-Semiconductor Nanowire Devices," *Science*, vol. 336, pp. 1003–1007, Apr. 2012.

[37] S. Nadj-Perge, I. K. Drozdov, J. Li, H. Chen, S. Jeon, J. Seo, A. H. MacDonald, B. A. Bernevig, and A. Yazdani, "Observation of Majorana fermions in ferromagnetic atomic chains on a superconductor," *Science*, vol. 346, pp. 602–607, Oct. 2014.

[38] K. Mong, Roger S. D. J. Clarke, J. Alicea, N. H. Lindner, P. Fendley, C. Nayak, Y. Oreg, A. Stern, E. Berg, K. Shtengel, and A. Fisher, Matthew P. "Universal topological quantum computation from a superconductor-abelian quantum hall heterostructure," *Phys. Rev. X*, vol. 4, p. 011036, Mar 2014.

[39] G. Moore and N. Read, "Nonabelions in the fractional quantum Hall effect," *Nucl. Phys. B*, vol. 360, pp. 362–396, Aug. 1991.

[40] N. Read and E. Rezayi, "Beyond paired quantum hall states: Parafermions and incompressible states in the first excited landau level," *Phys. Rev. B*, vol. 59, pp. 8084–8092, Mar 1999.

[41] P. Bonderson and J. K. Slingerland, "Fractional quantum hall hierarchy and the second landau level," *Phys. Rev. B*, vol. 78, p. 125323, Sep 2008.

[42] M. P. Zaletel, R. S. K. Mong, and F. Pollmann, "Topological characterization of fractional quantum hall ground states from microscopic hamiltonians," *Phys. Rev. Lett.*, vol. 110, p. 236801, Jun 2013.

[43] M. P. Zaletel, R. S. K. Mong, F. Pollmann, and E. H. Rezayi, "Infinite density matrix renormalization group for multicomponent quantum hall systems," *Phys. Rev. B*, vol. 91, p. 045115, Jan 2015.

[44] J. P. Eisenstein, "Exciton condensation in bilayer quantum hall systems," *Ann. Rev. Cond. Mat.*, vol. 5, no. 1, pp. 159–181, 2014.

[45] S. D. Geraedts and O. I. Motrunich, "Monte carlo study of a $u(1) \times u(1)$ system with π-statistical interaction," *Phys. Rev. B*, vol. 85, p. 045114, Jan 2012.

[46] S. D. Geraedts and O. I. Motrunich, "Line of continuous phase transitions in a three-dimensional u(1) loop model with $1/r^2$ current-current interactions," *Phys. Rev. B*, vol. 85, p. 144303, Apr 2012.

[47] S. D. Geraedts and O. I. Motrunich, "Phases and phase transitions in a $u(1) \times u(1)$ system with $\theta = 2\pi/3$ mutual statistics," *Phys. Rev. B*, vol. 86, p. 045106, Jul 2012.

[48] S. D. Geraedts and O. I. Motrunich, "Monte carlo study of a $u(1) \times u(1)$ loop model with modular invariance," *Phys. Rev. B*, vol. 86, p. 245121, Dec 2012.

[49] S. D. Geraedts and O. I. Motrunich, "Exact realization of integer and fractional quantum hall phases in models in," *Annals of Physics*, vol. 334, no. 0, pp. 288 – 315, 2013.

[50] S. Geraedts and O. Motrunich, "Exact models for symmetry-protected topological phases in one dimension," *arXiv:cond-mat*, p. 1410.1580, 2014.

[51] S. D. Geraedts and O. I. Motrunich, "Model realization and numerical studies of a three-dimensional bosonic topological insulator and symmetry-enriched topological phases," *Phys. Rev. X*, vol. 4, p. 041049, Dec 2014.

[52] S. D. Geraedts and O. I. Motrunich, "Model of fractionalization of faraday lines in compact electrodynamics," *Phys. Rev. B*, vol. 90, p. 214505, Dec 2014.

[53] J. Y. Lee, S. Geraedts, and O. Motrunich *TBD*.

[54] S. Geraedts, M. Zaletel, Z. Papić, and R. Mong *accepted in PRB*.

[55] A. M. Polyakov, *Gauge Fields and Strings*. Hardwood Academic Publishers, 1987.

[56] M. E. Peskin, "Mandelstam-'t hooft duality in abelian lattice models," *Annals of Physics*, vol. 113, no. 1, pp. 122 – 152, 1978.

[57] C. Dasgupta and B. I. Halperin, "Phase transition in a lattice model of superconductivity," *Phys. Rev. Lett.*, vol. 47, pp. 1556–1560, Nov 1981.

[58] M. P. A. Fisher and D. H. Lee, "Correspondence between two-dimensional bosons and a bulk superconductor in a magnetic field," *Phys. Rev. B*, vol. 39, pp. 2756–2759, Feb 1989.

[59] D.-H. Lee and M. P. A. Fisher, "Anyon superconductivity and the fractional quantum hall effect," *Phys. Rev. Lett.*, vol. 63, pp. 903–906, Aug 1989.

[60] O. I. Motrunich and T. Senthil, "Origin of artificial electrodynamics in three-dimensional bosonic models," *Phys. Rev. B*, vol. 71, p. 125102, 2005.

[61] F. Alet and E. S. Sørensen, "Cluster monte carlo algorithm for the quantum rotor model," *Phys. Rev. E*, vol. 67, p. 015701, Jan 2003.

[62] A. M. Essin and M. Hermele, "Classifying fractionalization: Symmetry classification of gapped Z_2 spin liquids in two dimensions," *Phys. Rev. B*, vol. 87, p. 104406, Mar 2013.

[63] Y.-M. Lu and A. Vishwanath, "Theory and classification of interacting integer topological phases in two dimensions: A chern-simons approach," *Phys. Rev. B*, vol. 86, p. 125119, Sep 2012.

[64] T. Grover and A. Vishwanath, "Quantum Phase Transition between Integer Quantum Hall States of Bosons," *ArXiv e-prints*, Oct. 2012.

[65] Y.-M. Lu and D.-H. Lee, "Quantum phase transitions between bosonic symmetry protected topological phases in two dimensions: emergent \$QED_3\$ and anyon superfluid," *ArXiv e-prints*, Oct. 2012.

[66] Y.-M. Lu and D.-H. Lee, "Spin quantum Hall effects in featureless non-fractionalized spin-1 magnets," *ArXiv e-prints*, Dec. 2012.

[67] L. Balents, M. P. A. Fisher, and C. Nayak, "Dual order parameter for the nodal liquid," *Phys. Rev. B*, vol. 60, pp. 1654–1667, Jul 1999.

[68] T. Senthil and M. P. A. Fisher, "z_2 gauge theory of electron fractionalization in strongly correlated systems," *Phys. Rev. B*, vol. 62, no. 12, pp. 7850–7881, 2000.

[69] We are grateful to T. Senthil and Ashvin Vishwanath for motivating us to study edge states in such topological phases.

[70] M.-C. Cha, M. P. A. Fisher, S. M. Girvin, M. Wallin, and A. P. Young, "Universal conductivity of two-dimensional films at the superconductor-insulator transition," *Phys. Rev. B*, vol. 44, pp. 6883–6902, Oct 1991.

[71] We are grateful to Matthew Fisher and Alexei Kitaev for emphasizing the question of whether our model can be realized as a path integral of a local Hamiltonian and for sharing their insights about the fractionalized phases.

[72] Such toric-code-like structure was suggested to us by Alexei Kitaev.

[73] A. Vishwanath and T. Senthil, "Physics of three dimensional bosonic topological insulators: Surface Deconfined Criticality and Quantized Magnetoelectric Effect," *ArXiv e-prints*, Sept. 2012.

[74] C. W. von Keyserlingk, F. J. Burnell, and S. H. Simon, "Three-dimensional topological lattice models with surface anyons," *Phys. Rev. B*, vol. 87, p. 045107, Jan 2013.

[75] C. Xu and T. Senthil, "Wave Functions of Bosonic Symmetry Protected Topological Phases," *ArXiv e-prints*, Jan. 2013.

[76] X.-G. Wen, "Topological invariants of symmetry-protected and symmetry-enriched topological phases of interacting bosons or fermions," *ArXiv e-prints*, Jan. 2013.

[77] P. Ye and X.-G. Wen, "Constructing symmetric topological phases of bosons in three dimensions via fermionic projective construction and dyon condensation," *Phys. Rev. B*, vol. 89, p. 045127, 2014.

[78] P. Ye and J. Wang, "Symmetry-protected topological phases with charge and spin symmetries: Response theory and dynamical gauge theory in two and three dimensions," *Phys. Rev. B*, vol. 88, p. 235109, 2013.

[79] M. Kamal and G. Murthy, "New o(3) transition in three dimensions," *Phys. Rev. Lett.*, vol. 71, p. 1911, 1993.

[80] M.-h. Lau and C. Dasgupta, "Numerical investigation of the role of topological defects in the three-dimensional heisenberg transition," *Phys. Rev. B*, vol. 39, pp. 7212–7222, Apr 1989.

[81] S. Sachdev and K. Park *Annals of Physics N. Y.*, vol. 298, p. 58, 2002.

[82] O. I. Motrunich and A. Vishwanath, "Emergent photons and transitions in the ¡span class="aps-inline-formula"¿¡math display="inline" baseline="-0.5"¿¡mrow¿¡mi mathvariant="normal"¿o¡/mi¿¡mo¿(¡/mo¿¡mn¿3¡/mn¿¡mo¿)¡/mo¿¡/mrow¿¡/math¿¡/span¿ sigma model with hedgehog suppression," *Phys. Rev. B*, vol. 70, p. 075104, Aug 2004.

[83] S. McKenzie, C. Domb, and D. L. Hunter *J. Phys. A. Math. Gen.*, vol. 15, pp. 3909–3914, 1982.

[84] O. I. Motrunich and T. Senthil, "Exotic order in simple models of bosonic systems," *Phys. Rev. Lett.*, vol. 89, p. 277004, Dec 2002.

[85] Z. Bi, A. Rasmussen, and C. Xu *arXiv*, p. 1309.0515, 2013.

[86] M. Hermele, M. P. A. Fisher, and L. Balents, "Pyrochlore photons: The $u(1)$ spin liquid in a $s = \frac{1}{2}$ three-dimensional frustrated magnet," *Phys. Rev. B*, vol. 69, p. 064404, 2004.

[87] O. I. Motrunich and A. Vishwanath *arXiv:0805:1494*, 2008.

[88] S. Gukov and A. Kapustin *arXiv/hep-th*, p. 1307.4793, 2013.

[89] X. Chen, F. Burnell, A. Vishwanath, and L. Fidkowski *arXiv*, p. 1403.6491, 2014.

[90] G. Cho, J. Teo, and S. Ryu *arXiv*, p. 1403.2018, 2014.

[91] Z. Bi, A. Rasmussen, and C. Xu *arXiv:cond-mat*, p. 1309.0515, 2013.

[92] A. Kapustin *arXiv:cond-mat*, p. 1404.6659, 2014.

[93] D. C. Tsui, H. L. Stormer, and A. C. Gossard, "Two-dimensional magnetotransport in the extreme quantum limit," *Phys. Rev. Lett.*, vol. 48, pp. 1559–1562, May 1982.

[94] F. D. M. Haldane, "Fractional quantization of the hall effect: A hierarchy of incompressible quantum fluid states," *Phys. Rev. Lett.*, vol. 51, pp. 605–608, Aug 1983.

[95] B. I. Halperin, "Statistics of quasiparticles and the hierarchy of fractional quantized hall states," *Phys. Rev. Lett.*, vol. 52, pp. 1583–1586, Apr 1984.

[96] J. K. Jain, "Composite-fermion approach for the fractional quantum hall effect," *Phys. Rev. Lett.*, vol. 63, pp. 199–202, Jul 1989.

[97] J. M. Leinaas and J. Myrheim, "On the theory of identical particles," *Il Nuovo Cimento B*, vol. 37, pp. 1–23, 1977.

[98] D. Arovas, J. R. Schrieffer, and F. Wilczek, "Fractional statistics and the quantum hall effect," *Phys. Rev. Lett.*, vol. 53, pp. 722–723, Aug 1984.

[99] M. Greiter, X.-G. Wen, and F. Wilczek, "Paired hall state at half filling," *Phys. Rev. Lett.*, vol. 66, pp. 3205–3208, Jun 1991.

[100] M. Greiter, X.-G. Wen, and F. Wilczek *Nucl. Phys. B*, vol. 374, p. 567, 1992.

[101] B. I. Halperin, "Theory of quantized Hall conductance," *Helv. Phys. Acta.*, vol. 56, pp. 75–102, Mar. 1983.

[102] X. G. Wu, G. Dev, and J. K. Jain, "Mixed-spin incompressible states in the fractional quantum hall effect," *Phys. Rev. Lett.*, vol. 71, pp. 153–156, Jul 1993.

[103] X. G. Wu and J. K. Jain, "Fractional quantum hall states in the low-zeeman-energy limit," *Phys. Rev. B*, vol. 49, pp. 7515–7519, Mar 1994.

[104] S. C. Davenport and S. H. Simon, "Spinful composite fermions in a negative effective field," *Phys. Rev. B*, vol. 85, p. 245303, Jun 2012.

[105] A. C. Balram, C. Tőke, A. Wójs, and J. K. Jain, "Phase diagram of fractional quantum hall effect of composite fermions in multicomponent systems," *Phys. Rev. B*, vol. 91, p. 045109, Jan 2015.

[106] N. C. Bishop, M. Padmanabhan, K. Vakili, Y. P. Shkolnikov, E. P. De Poortere, and M. Shayegan, "Valley polarization and susceptibility of composite fermions around a filling factor nu=3/2," *Phys. Rev. Lett.*, vol. 98, p. 266404, Jun 2007.

[107] M. Padmanabhan, T. Gokmen, and M. Shayegan, "Density dependence of valley polarization energy for composite fermions," *Phys. Rev. B*, vol. 80, p. 035423, Jul 2009.

[108] T. Gokmen, M. Padmanabhan, and M. Shayegan *Nat. Phys.*, vol. 6, p. 621, 2010.

[109] K. S. Novoselov, A. K. Geim, S. V. Morosov, D. Jiang, M. I. Katsnelson, I. V. Grigorieva, S. V. Dubonos, and A. A. Firsov *Nature*, vol. 438, p. 197, 2005.

[110] Y. Zhang, Y.-W. Tan, H. L. Stormer, and P. Kim *Nature*, vol. 438, p. 201, 2005.

[111] X. Du, I. Skachko, F. Duerr, A. Luican, and E. Y. Andrei *Nature*, vol. 462, p. 192, 2009.

[112] K. I. Bolotin, F. Ghahari, M. D. Shulman, H. L. Stormer, and P. Kim *Nature*, vol. 462, p. 196, 2009.

[113] F. Ghahari, Y. Zhao, P. Cadden-Zimansky, K. Bolotin, and P. Kim, "Measurement of the nu=1/3 fractional quantum hall energy gap in suspended graphene," *Phys. Rev. Lett.*, vol. 106, p. 046801, Jan 2011.

[114] C. R. Dean, A. F. Young, P. Cadden-Zimansky, L. Wang, H. Ren, K. Watanabe, T. Taniguchi, P. Kim, J. Hone, and K. L. Shepard *Nat. Phys.*, vol. 7, p. 693, 2011.

[115] B. E. Feldman, B. Krauss, J. H. Smet, and A. Yacoby *Science*, vol. 337, p. 1196, 2012.

[116] Y. W. Suen, H. C. Manoharan, X. Ying, M. B. Santos, and M. Shayegan, "Origin of the nu=1/2 fractional quantum hall state in wide single quantum wells," *Phys. Rev. Lett.*, vol. 72, pp. 3405–3408, May 1994.

[117] T. S. Lay, T. Jungwirth, L. Smrčka, and M. Shayegan, "One-component to two-component transition of the nu=2/3 fractional quantum hall effect in a wide quantum well induced by an in-plane magnetic field," *Phys. Rev. B*, vol. 56, pp. R7092–R7095, Sep 1997.

[118] I. McDonald and F. Haldane, "Topological phase transition in the nu=2/3 quantum hall effect," *Phys. Rev. B*, vol. 53, pp. 15845–15855, 1996.

[119] T. Chakraborty and F. C. Zhang, "Role of reversed spins in the correlated ground state for the fractional quantum hall effect," *Phys. Rev. B*, vol. 29, pp. 7032–7033, Jun 1984.

[120] E. H. Rezayi, "Reversed-spin excitations of the fractionally quantized hall effect from finite-size calculations," *Phys. Rev. B*, vol. 36, pp. 5454–5457, Oct 1987.

[121] P. A. Maksym *J. Phys. Condens. Matter*, vol. 1, p. 6299, 1989.

[122] J. E. Moore and F. D. M. Haldane, "Edge excitations of the nu= spin-singlet quantum hall state," *Phys. Rev. B*, vol. 55, pp. 7818–7823, Mar 1997.

[123] N. Kumada, D. Terasawa, Y. Shimoda, H. Azuhata, A. Sawada, Z. F. Ezawa, K. Muraki, T. Saku, and Y. Hirayama, "Phase diagram of interacting composite fermions in the bilayer $\nu = 2/3$ quantum hall effect," *Phys. Rev. Lett.*, vol. 89, p. 116802, Aug 2002.

[124] E. Ardonne, F. J. M. vanLankvelt, A. W. W. Ludwig, and K. Schoutens, "Separation of spin and charge in paired spin-singlet quantum hall states," *Phys. Rev. B*, vol. 65, p. 041305, Jan 2002.

[125] M. Barkeshli and X.-G. Wen, "Non-abelian two-component fractional quantum hall states," *Phys. Rev. B*, vol. 82, p. 233301, Dec 2010.

[126] E. H. Rezayi, X.-G. Wen, and N. Read unpublished, 2010.

[127] M. Barkeshli and X.-G. Wen, "Bilayer quantum hall phase transitions and the orbifold non-abelian fractional quantum hall states," *Phys. Rev. B*, vol. 84, p. 115121, Sep 2011.

[128] M. Barkeshli and X.-L. Qi, "Synthetic topological qubits in conventional bilayer quantum hall systems," *Phys. Rev. X*, vol. 4, p. 041035, Nov 2014.

[129] A. Vaezi and M. Barkeshli, "Fibonacci anyons from abelian bilayer quantum hall states," *Phys. Rev. Lett.*, vol. 113, p. 236804, Dec 2014.

[130] J. P. Eisenstein, L. N. Pfeiffer, and K. W. West *Appl. Phys. Lett.*, vol. 57, no. 22, p. 2324, 1990.

[131] J. Shabani, Y. Liu, M. Shayegan, L. N. Pfeiffer, K. W. West, and K. W. Baldwin, "Phase diagrams for the stability of the nu=1/2 fractional quantum hall effect in electron systems confined to symmetric, wide gaas quantum wells," *Phys. Rev. B*, vol. 88, p. 245413, Dec 2013.

[132] B. I. Halperin, P. A. Lee, and N. Read, "Theory of the half-filled landau level," *Phys. Rev. B*, vol. 47, pp. 7312–7343, Mar 1993.

[133] Y. W. Suen, L. W. Engel, M. B. Santos, M. Shayegan, and D. C. Tsui, "Observation of a nu=1/2 fractional quantum hall state in a double-layer electron system," *Phys. Rev. Lett.*, vol. 68, pp. 1379–1382, Mar 1992.

[134] J. P. Eisenstein, G. S. Boebinger, L. N. Pfeiffer, K. W. West, and S. He, "New fractional quantum hall state in double-layer two-dimensional electron systems," *Phys. Rev. Lett.*, vol. 68, pp. 1383–1386, Mar 1992.

[135] T. Chakraborty and P. Pietiläinen, "Fractional quantum hall effect at half-filled landau level in a multiple-layer electron system," *Phys. Rev. Lett.*, vol. 59, pp. 2784–2787, Dec 1987.

[136] D. Yoshioka, A. H. MacDonald, and S. M. Girvin, "Fractional quantum hall effect in two-layered systems," *Phys. Rev. B*, vol. 39, pp. 1932–1935, Jan 1989.

[137] S. He, S. Das Sarma, and X. C. Xie, "Quantized hall effect and quantum phase transitions in coupled two-layer electron systems," *Phys. Rev. B*, vol. 47, pp. 4394–4412, Feb 1993.

[138] V. W. Scarola and J. K. Jain, "Phase diagram of bilayer composite fermion states," *Phys. Rev. B*, vol. 64, p. 085313, Aug 2001.

[139] M. R. Peterson and S. Das Sarma, "Quantum hall phase diagram of half-filled bilayers in the lowest and the second orbital landau levels: Abelian versus non-abelian incompressible fractional quantum hall states," *Phys. Rev. B*, vol. 81, p. 165304, Apr 2010.

[140] J. Shabani, T. Gokmen, Y. T. Chiu, and M. Shayegan, "Evidence for developing fractional quantum hall states at even denominator 1/2 and 1/4 fillings in asymmetric wide quantum wells," *Phys. Rev. Lett.*, vol. 103, p. 256802, Dec 2009.

[141] K. Nomura and D. Yoshioka, "Gap evolution in nu=1/2 bilayer quantum hall systems," *Journal of the Physical Society of Japan*, vol. 73, no. 10, pp. 2612–2615, 2004.

[142] Z. Papić, M. O. Goerbig, N. Regnault, and M. V. Milovanović, "Tunneling-driven breakdown of the 331 state and the emergent pfaffian and composite fermi liquid phases," *Phys. Rev. B*, vol. 82, p. 075302, Aug 2010.

[143] M. R. Peterson, Z. Papić, and S. Das Sarma, "Fractional quantum hall effects in bilayers in the presence of interlayer tunneling and charge imbalance," *Phys. Rev. B*, vol. 82, p. 235312, Dec 2010.

[144] W. Zhu, S. Gong, D. N. Sheng, and L. Sheng unpublished, 2015.

[145] Z. Papić, G. Möller, M. V. Milovanović, N. Regnault, and M. O. Goerbig, "Fractional quantum hall state at nu=1/4 in a wide quantum well," *Phys. Rev. B*, vol. 79, p. 245325, Jun 2009.

[146] Y. Liu, A. L. Graninger, S. Hasdemir, M. Shayegan, L. N. Pfeiffer, K. W. West, K. W. Baldwin, and R. Winkler, "Fractional quantum hall effect at nu=1/2 in hole systems confined to gaas quantum wells," *Phys. Rev. Lett.*, vol. 112, p. 046804, Jan 2014.

[147] J. P. Eisenstein and A. H. MacDonald, "Boseeinstein condensation of excitons in bilayer electron systems," *Nature*, vol. 432, pp. 691–694, 2004.

[148] S. M. Girvin and A. H. Macdonald, "Multi-component quantum hall systems : The sum of their parts and more," in *in Novel Quantum Liquids in Low-Dimensional Semiconductor Structures, S.D. Sarma and A. Pinczuk Eds*, Wiley (New York), 1995.

[149] I. B. Spielman, J. P. Eisenstein, L. N. Pfeiffer, and K. W. West, "Resonantly enhanced tunneling in a double layer quantum hall ferromagnet," *Phys. Rev. Lett.*, vol. 84, pp. 5808–5811, Jun 2000.

[150] M. Kellogg, J. P. Eisenstein, L. N. Pfeiffer, and K. W. West, "Vanishing hall resistance at high magnetic field in a double-layer two-dimensional electron system," *Phys. Rev. Lett.*, vol. 93, p. 036801, Jul 2004.

[151] E. Tutuc, M. Shayegan, and D. A. Huse, "Counterflow measurements in strongly correlated gaas hole bilayers: Evidence for electron-hole pairing," *Phys. Rev. Lett.*, vol. 93, p. 036802, Jul 2004.

[152] J. Schliemann, S. M. Girvin, and A. H. MacDonald, "Strong correlation to weak correlation phase transition in bilayer quantum hall systems," *Phys. Rev. Lett.*, vol. 86, pp. 1849–1852, Feb 2001.

[153] S. H. Simon, E. H. Rezayi, and M. V. Milovanovic, "Coexistence of composite bosons and composite fermions in nu=1/2+1/2 quantum hall bilayers," *Phys. Rev. Lett.*, vol. 91, p. 046803, Jul 2003.

[154] N. Shibata and D. Yoshioka, "Ground state of nu=1 bilayer quantum hall systems," *Journal of the Physical Society of Japan*, vol. 75, no. 4, p. 043712, 2006.

[155] G. Möller, S. H. Simon, and E. H. Rezayi, "Paired composite fermion phase of quantum hall bilayers at nu=1/2+1/2," *Phys. Rev. Lett.*, vol. 101, p. 176803, Oct 2008.

[156] Z. Papić and M. Milovanović, "p-wave pairing in quantum hall bilayers," *Advances in Condensed Matter Physics*, vol. 2011, p. 614173, 2011.

[157] N. Kumada, D. Terasawa, M. Morino, K. Tagashira, A. Sawada, Z. F. Ezawa, K. Muraki, Y. Hirayama, and T. Saku, "Phase diagrams of $\nu = 2$ and $\nu = \frac{2}{3}$ quantum hall states in bilayer systems," *Phys. Rev. B*, vol. 69, p. 155319, Apr 2004.

[158] Y. Liu, S. Hasdemir, J. Shabani, M. Shayegan, L. N. Pfeiffer, K. W. West, and K. W. Baldwin unpublished, 2015.

[159] S. R. White, "Density matrix formulation for quantum renormalization groups," *Phys. Rev. Lett.*, vol. 69, pp. 2863–2866, Nov 1992.

[160] U. Schollwck, "The density-matrix renormalization group in the age of matrix product states," *Annals of Physics*, vol. 326, no. 1, pp. 96 – 192, 2011. January 2011 Special Issue.

[161] W. Bishara and C. Nayak, "Effect of landau level mixing on the effective interaction between electrons in the fractional quantum hall regime," *Phys. Rev. B*, vol. 80, p. 121302, Sep 2009.

[162] A. Wójs, C. Tőke, and J. K. Jain, "Landau-level mixing and the emergence of pfaffian excitations for the 5/2 fractional quantum hall effect," *Phys. Rev. Lett.*, vol. 105, p. 096802, Aug 2010.

[163] E. H. Rezayi and S. H. Simon, "Breaking of particle-hole symmetry by landau level mixing in the nu=5/2 quantized hall state," *Phys. Rev. Lett.*, vol. 106, p. 116801, Mar 2011.

[164] Z. Papić, F. D. M. Haldane, and E. H. Rezayi, "Quantum phase transitions and the nu=5/2 fractional hall state in wide quantum wells," *Phys. Rev. Lett.*, vol. 109, p. 266806, Dec 2012.

[165] I. Sodemann and A. MacDonald, "Landau level mixing and the fractional quantum hall effect," *Phys. Rev. B*, vol. 87, p. 245425, Jun 2013.

[166] M. Peterson and C. Nayak, "More realistic hamiltonians for the fractional quantum hall regime in gaas and graphene," *Phys. Rev. B*, vol. 87, p. 245129, Jun 2013.

[167] S. H. Simon and E. H. Rezayi, "Landau level mixing in the perturbative limit," *Phys. Rev. B*, vol. 87, p. 155426, Apr 2013.

[168] K. Pakrouski, M. R. Peterson, T. Jolicoeur, V. W. Scarola, C. Nayak, and M. Troyer unpublished, 2014.

[169] Y. Zhang, T. Grover, A. Turner, M. Oshikawa, and A. Vishwanath, "Quasiparticle statistics and braiding from ground-state entanglement," *Phys. Rev. B*, vol. 85, p. 235151, Jun 2012.

[170] L. Cincio and G. Vidal, "Characterizing topological order by studying the ground states on an infinite cylinder," *Phys. Rev. Lett.*, vol. 110, p. 067208, Feb 2013.

[171] H.-H. Tu, Y. Zhang, and X.-L. Qi, "Momentum polarization: An entanglement measure of topological spin and chiral central charge," *Phys. Rev. B*, vol. 88, p. 195412, Nov 2013.

[172] H. Li and F. Haldane, "Entanglement spectrum as a generalization of entanglement entropy: Identification of topological order in non-abelian fractional quantum hall effect states," *Phys. Rev. Lett.*, vol. 101, p. 010504, Jul 2008.

[173] X. G. Wen and A. Zee, "Shift and spin vector: New topological quantum numbers for the hall fluids," *Phys. Rev. Lett.*, vol. 69, pp. 953–956, Aug 1992.

[174] J. P. Eisenstein, H. L. Stormer, L. N. Pfeiffer, and K. W. West, "Evidence for a spin transition in the nu=2/3 fractional quantum hall effect," *Phys. Rev. B*, vol. 41, pp. 7910–7913, Apr 1990.

[175] X. C. Xie, Y. Guo, and F. C. Zhang, "Fractional quantum hall effect with spin reversal," *Phys. Rev. B*, vol. 40, pp. 3487–3490, Aug 1989.

[176] N. Read and D. Green, "Paired states of fermions in two dimensions with breaking of parity and time-reversal symmetries and the fractional quantum hall effect," *Phys. Rev. B*, vol. 61, pp. 10267–10297, Apr 2000.

[177] Y. Zhang, E. H. Rezayi, and K. Yang, "Existence of strong-pairing quantum hall phase in bilayer cold-atom systems with dipolar interactions," *Phys. Rev. B*, vol. 90, p. 165102, Oct 2014.

[178] F. J. M. van Lankvelt, *PhD thesis*. University of Amsterdam, 2004.

[179] C.-H. Lee, Z. Papić, and R. Thomale (to appear), 2015.

[180] R. Tao and D. J. Thouless, "Fractional quantization of hall conductance," vol. 28, pp. 1142–1144, July 1983.

[181] A. Seidel, H. Fu, D.-H. Lee, J. M. Leinaas, and J. Moore, "Incompressible quantum liquids and new conservation laws," *Phys. Rev. Lett.*, vol. 95, p. 266405, Dec 2005.

[182] E. J. Bergholtz and A. Karlhede, "Quantum hall system in tao-thouless limit," *Phys. Rev. B*, vol. 77, p. 155308, Apr 2008.

[183] E. Ardonne and N. Regnault, "Structure of spinful quantum hall states: A squeezing perspective," *Phys. Rev. B*, vol. 84, p. 205134, Nov 2011.

[184] F. Pollmann, A. M. Turner, E. Berg, and M. Oshikawa, "Entanglement spectrum of a topological phase in one dimension," *Phys. Rev. B*, vol. 81, p. 064439, Feb 2010.

[185] X. Chen, Z.-C. Gu, and X.-G. Wen, "Complete classification of one-dimensional gapped quantum phases in interacting spin systems," *Phys. Rev. B*, vol. 84, p. 235128, Dec 2011.

[186] W. Pan, J. S. Xia, H. L. Stormer, D. C. Tsui, C. Vicente, E. D. Adams, N. S. Sullivan, L. N. Pfeiffer, K. W. Baldwin, and K. W. West, "Experimental studies of the fractional quantum hall effect in the first excited landau level," *Phys. Rev. B*, vol. 77, p. 075307, Feb 2008.

[187] H. C. Choi, W. Kang, S. Das Sarma, L. N. Pfeiffer, and K. W. West, "Activation gaps of fractional quantum hall effect in the second landau level," *Phys. Rev. B*, vol. 77, p. 081301, Feb 2008.

[188] M. Dolev, Y. Gross, R. Sabo, I. Gurman, M. Heiblum, V. Umansky, and D. Mahalu, "Characterizing neutral modes of fractional states in the second landau level," *Phys. Rev. Lett.*, vol. 107, p. 036805, Jul 2011.

[189] A. Kumar, N. Samkharadze, G. A. Csáthy, M. J. Manfra, L. N. Pfeiffer, and K. W. West, "Particle-hole asymmetry of fractional quantum hall states in the second landau level of a two-dimensional hole system," *Phys. Rev. B*, vol. 83, p. 201305, May 2011.

[190] N. Samkharadze, J. D. Watson, G. Gardner, M. J. Manfra, L. N. Pfeiffer, K. W. West, and G. A. Csáthy, "Quantitative analysis of the disorder broadening and the intrinsic gap for the $\nu = \frac{5}{2}$ fractional quantum hall state," *Phys. Rev. B*, vol. 84, p. 121305, Sep 2011.

[191] J. C. Wang, Z.-C. Gu, and X.-G. Wen, "Field-theory representation of gauge-gravity symmetry-protected topological invariants, group cohomology, and beyond," *Phys. Rev. Lett.*, vol. 114, p. 031601, Jan 2015.

[192] T. Senthil *arXiv:cond-mat*, p. 1405.4015, 2014.

[193] M. F. Maghrebi, S. Ganeshan, D. J. Clarke, A. V. Gorshkov, and J. D. Sau, "Parafermionic zero modes in ultracold bosonic systems," *arXiv:cond-mat*, p. 1504.04012, 2015.